AD-A127 719 A GEOMETRIC OPTICS MODEL FOR CALCULATING THE FIELD STRENGTH OF ELECTROMAG..(U) AIR FORCE WRIGHT AERONAUTICAL LABS WRIGHT-PATTERSON AFB OH R P WASKY 1/3

UNCLASSIFIED DEC 77 F/G 20/14 NL

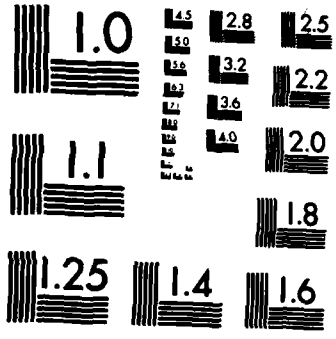


MICROCOPY RESOLUTION TEST CHART
NATIONAL BUREAU OF STANDARDS-1963-A

PHOTOGRAPH THIS SHEET

AD A127719

DTIC ACCESSION NUMBER

II

LEVEL

INVENTORY

AFWAL-TR-83-1061

DOCUMENT IDENTIFICATION

Final, Apr. 77-Dec 77

Wasky, Raymond

Dec 77

DISTRIBUTION STATEMENT A

Approved for public release;
Distribution Unlimited

DISTRIBUTION STATEMENT

| ACCESSION FOR | | |
|---|---|---|
| NTIS | GRA&I | ☒ |
| DTIC | TAB | ☐ |
| UNANNOUNCED | | ☐ |
| JUSTIFICATION | | |
| | | |
| | | |
| | | |
| BY | | |
| DISTRIBUTION / | | |
| AVAILABILITY CODES | | |
| DIST | AVAIL AND/OR SPECIAL | |
| A | | |

DISTRIBUTION STAMP

DTIC
ELECTE
S MAY 2 1983 D
D

DATE ACCESSIONED

DTIC COPY INSPECTED 2

83 04 28 086

DATE RECEIVED IN DTIC

PHOTOGRAPH THIS SHEET AND RETURN TO DTIC-DDA-2

DTIC FORM OCT 79 70A

DOCUMENT PROCESSING SHEET

AFWAL-TR-83-1061

# A GEOMETRIC OPTICS MODEL FOR CALCULATING THE FIELD STRENGTH OF ELECTROMAGNETIC WAVES IN THE PRESENCE OF A TROPOSPHERIC DUCT

Raymond P. Wasky

AD A127719

December 1977

Final Report for Period April - December 1977

Approved for Public Release; Distribution Unlimited.

AVIONICS LABORATORY
AIR FORCE WRIGHT AERONAUTICAL LABORATORY
AIR FORCE SYSTEMS COMMAND
WRIGHT-PATTERSON AIR FORCE BASE, OHIO 45433

*NOTICE*

*When Government drawings, specifications, or other data are used for any purpose other than in connection with a definitely related Government procurement operation, the United States Government thereby incurs no responsibility nor any obligation whatsoever; and the fact that the government may have formulated, furnished, or in any way supplied the said drawings, specifications, or other data, is not to be regarded by implication or otherwise as in any manner licensing the holder or any other person or corporation, or conveying any rights or permission to manufacture use, or sell any patented invention that may in any way be related thereto.*

*This report has been reviewed by the Office of Public Affairs (ASD/PA) and is releasable to the National Technical Information Service (NTIS). At NTIS, it will be available to the general public, including foreign nations.*

*This technical report has been reviewed and is approved for publication.*

MARVIN SPECTOR, Chief
Applications Branch
Mission Avionics Division
Avionics Laboratory

*FOR THE COMMANDER*

ROBERT E. DEAL, Assistant Chief
Mission Avionics Division
Avionics Laboratory

*"If your address has changed, if you wish to be removed from our mailing list, or if the addressee is no longer employed by your organization please notify* AFWAL/AART, *W-PAFB, OH 45433 to help us maintain a current mailing list".*

*Copies of this report should not be returned unless return is required by security considerations, contractual obligations, or notice on a specific document.*

UNCLASSIFIED

SECURITY CLASSIFICATION OF THIS PAGE (When Data Entered)

# REPORT DOCUMENTATION PAGE

READ INSTRUCTIONS BEFORE COMPLETING FORM

1. REPORT NUMBER: AFWAL-TR-83-1061

2. GOVT ACCESSION NO.

3. RECIPIENT'S CATALOG NUMBER

4. TITLE (and Subtitle): A Geometric Optics Model for Calculating the Field Strength of Electromagnetic Waves in the Presence of a Tropospheric Duct

5. TYPE OF REPORT & PERIOD COVERED: Final Report Apr 77 - Dec 77

6. PERFORMING ORG. REPORT NUMBER

7. AUTHOR(s): Raymond Wasky

8. CONTRACT OR GRANT NUMBER(s): N/A

9. PERFORMING ORGANIZATION NAME AND ADDRESS: Air Force Avionics Laboratory (AART), Air Force Wright Aeronautical Laboratories, Wright-Patterson AFB, OH 45433

10. PROGRAM ELEMENT, PROJECT, TASK AREA & WORK UNIT NUMBERS: 611A0605

11. CONTROLLING OFFICE NAME AND ADDRESS: Air Force Avionics Laboratory (AART), Air Force Wright Aeronautical Laboratories, Wright-Patterson AFB, OH 45433

12. REPORT DATE: December 1977

13. NUMBER OF PAGES: 188 pages

14. MONITORING AGENCY NAME & ADDRESS (if different from Controlling Office)

15. SECURITY CLASS. (of this report): UNCLASSIFIED

15a. DECLASSIFICATION/DOWNGRADING SCHEDULE

16. DISTRIBUTION STATEMENT (of this Report): Approved for public release; distribution unlimited.

17. DISTRIBUTION STATEMENT (of the abstract entered in Block 20, if different from Report)

18. SUPPLEMENTARY NOTES

19. KEY WORDS (Continue on reverse side if necessary and identify by block number)

Atmospheric Refraction
Ducting
Geometrical Optics
Microwave
Propagation
Radio Frequency
Ray Tracing
Troposphere

20. ABSTRACT (Continue on reverse side if necessary and identify by block number)

The theory and development of a geometric optics model for analyzing the effects of anomalous atmospheric refraction on the field strength of radio frequency emitters is presented. The model is derived from Fermat's principle which defines the Euler-Lagrange equations of a ray and the ray optical path length. This model is applicable to radio propagation above 30MHz where ionosphere effects are generally negligible. Given an isotropic emitter of known frequency, polarization, pulse width, and altitude, (OVER)

DD FORM 1 JAN 73 1473 EDITION OF 1 NOV 65 IS OBSOLETE

UNCLASSIFIED

SECURITY CLASSIFICATION OF THIS PAGE (When Data Entered)

BLOCK 20 CONTINUED:

the free space normalized power density and field strength are calculated as a function of altitude and distance along the earth's surface.

Results obtained with this model are compared to experimental and waveguide mode theory field strength calculations for a low altitude super-refractive atmospheric layer, or tropospheric duct, lying along a 280 nautical mile path off the California coast between San Diego and Guadalupe Island. Field strength calculations are presented at 65, 170, 520, and 3300 MHz first using the average measured refractive index profile for the Guadalupe Island duct and then a trilinear approximation to that profile.

# A GEOMETRIC OPTICS MODEL FOR CALCULATING THE FIELD STRENGTH OF ELECTROMAGNETIC WAVES IN THE PRESENCE OF A TROPOSPHERIC DUCT

Thesis

Submitted to

The School of Engineering of the

UNIVERSITY OF DAYTON

In Partial Fulfillment of the Requirements for

The Degree

Master of Science in Electrical Engineering

by

Raymond P. Wasky

UNIVERSITY OF DAYTON

Dayton, Ohio

December, 1977

.S 08249

APPROVED BY:

Bernard M Schmidt
Chairman, Advisory Committee

Associate Dean for Graduate
Studies and Research

David C. Kroft
Dean, School of Engineering

ABSTRACT

A GEOMETRIC OPTICS MODEL FOR CALCULATING THE FIELD STRENGTH OF ELECTROMAGNETIC WAVES IN THE PRESENCE OF A TROPOSPHERIC DUCT

Raymond P. Masky
University of Dayton, 1977

Major Professor: Dr. B. M. Schmidt

The theory and development of a geometric optics model for analyzing the effects of anomalous atmospheric refraction on the field strength of radio frequency emitters is presented. The model is derived from Fermat's principle which defines the Euler-Lagrange equations of a ray and the ray optical path length. This model is applicable to radio propagation above 30 MHz where ionospheric effects are generally negligible. Given an isotropic emitter of known frequency, polarization, pulse width, and altitude, the free space normalized power density and field strength are calculated as a function of altitude and distance along the earth's surface. Computations are made by constructing a ray trace and utilizing the Jacobian of the transformation between ray space coordinates and wavefront surface coordinates to solve for the time-averaged free space normalized Poynting vector.

The atmosphere is treated as a non-magnetic inhomogeneous medium which is otherwise linear ($\mu$ and $\epsilon$ are independent of the fields) and isotropic ($\mu$ and $\epsilon$ are scalars). The atmospheric refractive index is modeled as a function of altitude above a spherical earth surface by either a standard Central Radio Propagation Laboratory (CRPL) exponential

function or by measured profiles obtained from meteorological soundings (horizontal homogeneity in the refractive index may be assumed over relatively large distances). Fields that are incident upon the earth's surface are specularly reflected and attenuated by a Fresnel reflection coefficient and a surface roughness factor which is dependent upon the angle of incidence and standard deviation of the surface about a mean height.

Results obtained with this model are compared to experimental and waveguide mode theory field strength calculations for a low altitude superrefractive atmospheric layer, or tropospheric duct, lying along a 280 nautical mile path off the California coast between San Diego and Guadalupe Island. Field strength calculations are presented at 65, 170, 520, and 3300 MHz first using the average measured refractive index profile for the Guadalupe Island duct and then a trilinear approximation to that profile. The results show a fair amount of agreement with the experimental and waveguide data at the lower frequencies, with good to excellent comparisons at 520 and 3300 MHz especially when the Guadalupe Island refractive index profile is used. Calculations are restricted to the region within the duct because of limitations in the geometric optics method, which are discussed at length.

TABLE OF CONTENTS

ABSTRACT . . . . . iii

TABLE OF CONTENTS . . . . . v

LIST OF ILLUSTRATIONS . . . . . vii

LIST OF TABLES . . . . . xi

ACKNOWLEDGEMENTS . . . . . xii

CHAPTER

I. INTRODUCTION AND DISCUSSION OF THE THESIS . . . . . 1

Background
Statement of the Problem
Method of Approach

II. RADIO REFRACTIVITY OF AIR . . . . . 8

III. THEORY OF GEOMETRIC OPTICS . . . . . 14

Euler-Lagrange Equations of a Ray
Algorithm Development

IV. PROPERTIES OF GEOMETRIC OPTICS . . . . . 25

Wave and Eikonal Equations
Jacobian and Power Density
Restrictions of Ray Theory

V. COMPUTER SIMULATION DESCRIPTION . . . . . 40

General Characteristics
Refractivity Models
Ray Algorithms
Power Density and Field Strength Algorithms
Earth Reflection Model

VI. RESULTS . . . . . 76

Introduction
Simulation Results
Comparison of Results

VII. SUMMARY AND CONCLUSIONS . . . . . 135

APPENDIX . . . . . 139

REFERENCES . . . . . 174

## LIST OF ILLUSTRATIONS


1. Variation of a curve C between two points . . . . . 14

2. Ray geometry in polar coordinates . . . . . 19

3. Ray trajectory for a double valued solution to Eq. (55) . . . 22

4. The volume element $d\gamma$ bounded by rays and surfaces of constant phase . . . . . 30

5. Geometry for ray curvature in polar coordinates . . . . . 37

6. The volume element $d\gamma$ bounded by rays and surfaces of constant phase for a spherical wavefront element radiated from an isotropic emitter at point O . . . . . 45

7. The angular subtense of a line segment $dl_v$ at the emitter O as seen in free space and in a refractive atmosphere . . . . . 46

8. Geometry for the free space ray elevation angle $\epsilon_{oi}$ . . . . . 48

9. Ray geometry at the vertical line segment $dl_v$ within a refractive atmosphere . . . . . 50

10. Reflection of uniform plane waves at a plane boundary for parallel and perpendicular polarizations . . . . . 57

11. Wavelength dependence of $\epsilon_{cr}'$ and $\epsilon_{cr}''$ for sea water at $17^\circ$ C . . . . . 62

12. Magnitude of the reflection coefficient as a function of incident grazing angle for a smooth sea at $10^\circ$ C . . . . . 64

13. Expanded plot of Fig. 12 for incident grazing angles between 0 and 10 degrees . . . . . 64

14. Phase of the reflection coefficient as a function of incident grazing angle for a smooth sea at $10^\circ$ C . . . . . 65

15. Expanded plot of Fig. 14 for incident grazing angles between 0 and 10 degrees . . . . . 65

16. Magnitude of the reflection coefficient as a function of incident grazing angle for smooth average land where $\epsilon_{cr}' = 10$ and $\sigma = 0.0016$ mho/m . . . . . 66

17. Phase of the reflection coefficient as a function of incident grazing angle for smooth average land where $\epsilon_{cr}' = 10$ and $\sigma = 0.0016$ mho/m . . . . . 66

18. Geometry of the divergence factor D . . . . . 69

19. Mean square $< R^2 >$ of the surface roughness factor R versus phase deviation . . . . . 72

20. Refractivity profiles and height gain curves for the Guadalupe Island ground based duct . . . . . 78

21. Comparison of atmospheric refractivity profiles . . . . . 82

22. Comparison of atmospheric refractivity gradient profiles . . . . . 83

23. N and dN/dh profiles for free space . . . . . 86

24. Ray trace for a 100 ft high emitter in free space . . . . . 87

25. N and dN/dh profiles for the CRPL exponential atmosphere model . . . . . 88

26. Ray trace for a 100 ft emitter in the CRPL exponential atmosphere . . . . . 89

27. Ray trace for a 100 ft emitter in the Guadalupe Island duct . . . . . 91

28. N and dN/dh profiles for the Guadalupe Island duct (expanded from Fig. (21a)) . . . . . 96

29. Ray trace for the 100 ft emitter in the Guadalupe Island duct (expanded from Fig. (27)) . . . . . 97

30. Height gain curves at 65 MHz, from Figs. (28) and (29) . . . . . 98

31. Height gain curves at 170 MHz, from Figs. (28) and (29) . . . . 99

32. Height gain curves at 520 MHz, from Figs. (28) and (29) . . . . 100

33. Height gain curves at 3300 MHz, from Figs. (28) and (29) . . . . . 101

34. Ray trace for the 500 ft emitter in the Guadalupe Island duct . . . . . 102

35. Height gain curves at 65 MHz, from Figs. (28) and (34) . . . . . 103

36. Height gain curves at 170 MHz, from Figs. (28) and (34) . . . . 104

37. Height gain curves at 520 MHz, from Figs. (28) and (34) . . . . 105

38. Height gain curves at 3300 MHz, from Figs. (38) and (34) . . . . 106

39. N and dN/dh profiles for the trilinear ground based duct (expanded from Fig. (21b)) . . . . . 107

40. Ray trace for the 100 ft emitter in the trilinear duct . . . . 108

41. Height gain curves at 65 MHz, from Figs. (39) and (40) . . . . 109

42. Height gain curves at 170 MHz, from Figs. (39) and (40) . . . . 110

43. Height gain curves at 520 MHz, from Figs. (39) and (40) . . . . 111

44. Height gain curves at 3300 MHz, from Figs. (39) and (40) . . . 112

45. Ray trace for the 500 ft emitter in the trilinear duct . . . . 113

46. Height gain curves at 65 MHz, from Figs. (39) and (45) . . . . 114

47. Height gain curves at 170 MHz, from Figs. (39) and (45) . . . . 115

48. Height gain curves at 520 MHz, from Figs. (39) and (45) . . . . 116

49. Height gain curves at 3300 MHz, from Figs. (39) and (45) . . . 117

50. Height gain curves at 65 MHz, for $h_o$ = 500 ft and x = 60 naut mi . . . . . 125

51. Height gain curves at 65 MHz, for $h_o$ = 100 ft and x = 120 naut mi . . . . . 126

52. Height gain curves at 65 MHz, for $h_o$ = 500 ft and x = 120 naut mi . . . . . 127

53. Height gain curves at 170 MHz, for $h_o$ = 100 ft and x = 120 naut mi . . . . . 128

54. Height gain curves at 170 MHz, for $h_o$ = 500 ft and x = 120 naut mi . . . . . 129

55. Height gain curves at 520 MHz, for $h_o$ = 100 ft and x = 120 naut mi . . . . . 130

56. Height gain curves at 520 MHz, for $h_o$ = 500 ft and x = 120 naut mi . . . . . 131

57. Height gain curves at 3.3 GHz, for $h_o$ = 100 ft and x = 60 naut mi . . . . . 132

58. Height gain curves at 3.3 GHz, for $h_o$ = 100 ft and x = 120 naut mi . . . . . 133

59. Height gain curves at 3.3 GHz, for $h_o$ = 500 ft and x = 120 naut mi . . . . . 134

60. Computer program flow diagram . . . . . 140

61. Program listing . . . . . 141

## LIST OF TABLES


1. Approximate electromagnetic properties of soil and water . . . . . 61

2. Electromagnetic properties of soil and water models . . . . . 68

3. Sea state and wave height . . . . . 73

4. Land surface deviations . . . . . 73

5. Standard deviation of heights for sea surfaces . . . . . 74

6. Standard deviation of heights for land surfaces . . . . . 75

7. Atmospheric refractivity profile for the Guadalupe Island duct . . . . . 80

8. Atmospheric refractivity profile for the trilinear duct . . . . . 80

9. Maximum launch angles of trapped rays . . . . . 95

10. Card input data . . . . . 166

11. Sample input for the 100 ft high emitter in the trilinear duct . . . . . 170

12. Sample output for the 100 ft high emitter in the trilinear duct . . . . . 172

## ACKNOWLEDGMENTS

The author would like to thank Mr. J. E. Valstar for his many valuable comments and Mrs. D. T. Law for her excellent typing of this thesis.

# CHAPTER I

# INTRODUCTION AND DISCUSSION OF THE THESIS

## Background

The beginning of large scale research in electromagnetic wave propagation over the surface of the earth was prompted by Marconi's demonstration in 1901 that signals could be transmitted across the Atlantic Ocean. Much of the work concentrated on providing a description of four mechanisms that had been proposed to account for over-the-horizon transmission: diffraction by the earth, reflection from an elevated layer of ionized gases (i.e., the ionosphere), atmospheric refraction, and surface waves at the boundary between differing dielectric media.[1] Papers by Zenneck, Sommerfeld, and Watson concluded that long distance propagation up to 30 MHz was explainable in terms of all of these mechanisms except atmospheric refraction, which was found to have a negligible effect.[1, 2]

During the period immediately preceding and following World War II, the useable radio spectrum was extended from 30 MHz to approximately 300 GHz. In this region the effects of surface waves, earth diffraction, and ionospheric reflection are generally absent, while refraction by the lower atmosphere or troposphere, becomes the central mechanism which enables long distance signal transmission.[3] As will be shown in Chapters II and IV, it is not the absolute value of the refractive index of air that is important in describing radio propagation at these wavelengths, but rather its rate of change.

Under "standard" conditions the atmospheric index of refraction remains essentially constant in horizontal directions while decreasing exponentially with increasing altitude.[1, 4] From Snell's law of optics (Chapter III) this negative gradient in the refractive index normally bends horizontally launched radio waves around the curvature of the earth so that the radio horizon is about 4/3 the distance to the geometric horizon. If the gradient has a greater than normal magnitude the waves will be refracted even further around the earth's surface, thus extending the radar horizon. When the gradient becomes sufficiently large, the waves may have the same curvature as that of the earth and follow the earth's surface indefinitely, a condition referred to as superrefraction, trapping, or ducting. Conversely, a smaller than usual change in the refractive index results in substandard propagation or subrefraction.[1]

The refractive index of air at radio frequencies is a function of total atmospheric pressure, water vapor content, and temperature (Chapter II) and is therefore subject to local meteorological conditions. Greater than normal refraction generally occurs when the temperature increases or the humidity decreases rapidly with height, such as when a warm dry air mass from the land is blown out over a cooler sea surface, or when heat is radiated from the earth's surface at night and the ground is moist. Such conditions are called temperature and humidity inversions, with humidity inversions usually being the dominant factor in determining atmospheric refraction properties. As a result, superrefractive and nearly superrefractive propagating conditions are more prevalent over oceans than over land surfaces.[5, 6, 7] Superrefractive conditions, when they do exist over land, tend to exhibit more pronounced daily variations than over the sea, since land masses change temperature more

rapidly than do sea bodies. In either case, superrefraction occurs most frequently under fair weather conditions when the atmosphere is vertically stratified and there is little or no air mixing due to turbulence. Propagation is more nearly normal when the atmosphere is cold or stormy or when very rough terrain and high winds contribute to the mixing process.[7]

Long distance propagation due to superrefraction is possible with only a relatively small change in the refractive index. A mere gradient of $(-1.57)10^{-7}$ parts per meter in altitude for the index will result in ducting. However, as Skolnik[7] illustrates, the results may be dramatic, as in the case of a ground based 200 MHz radar in Bombay, India, which frequently received target echoes from points in Arabia at ranges of 1000 to 1500 miles during World War II. Such extremely long distance operation is possible since the atmospheric duct behaves like a leaky waveguide, with the ground plus the thermal or humidity inversion layers acting as lossy waveguide walls. While most ducts are bounded by the earth on the bottom and an upper inversion layer usually not more than several hundred feet high, elevated earth-detached ducts have been reported up to altitudes of several thousand feet.[7, 8, 9]

As an example of subrefractive conditions, Skolnik[7] cites an instance when radars off Fisher's Island, New York, were unable to see Block Island only 22 miles away, although it was optically visible. This occurred because the refractive index gradient, rather than bending the signals around the earth's curvature, refracted the signals away from the earth, thus reducing the range to the radar horizon. Under certain circumstances subrefraction may result from a low flying fog for which part of the water in the air changes from a gaseous to a liquid state. Although the total amount of water in the air remains unchanged, only the

water in a vapor form contributes significantly to the air's refractive index, making the index lower than normal at the surface, and consequently yielding substandard propagation conditions.[7]

## Statement of the Problem

While surveying the literature for the effects of refraction on propagation at radio frequencies, it becomes evident that the vast majority of analytical work in this area has been conducted by using propagation models that are either extremely simplistic or exceedingly complex and specialized. The simpler approaches generally assume some form of "standard" vertical refractive index profile[10, 11] such as a constant gradient index or "4/3 effective earth radius" model (Chapter II), which is not representative of superrefractive or subrefractive atmospheric conditions. The more complex methods, which use waveguide mode theory to solve for tropospheric refraction,[12, 13] are generally limited to atmospheric structures having only one or two inversion layers since the difficulty of solution increases rapidly with the number of changes in the vertical profile. In either case, measured refractive index data is usually replaced by approximate profile models which, as Chapter VI indicates, may have a noticeable effect on results.

The purpose of this thesis is to present the theory and development of an accurate yet practical model for analyzing the effects of atmospheric refraction on the field strength of radio frequency emitters in the 30 MHz to 100 GHz spectrum. Results obtained from this model are compared with theoretical and experimental data recently reported by Pappert and Goodhart[14] for a ground-based tropospheric duct lying along a 280 nautical mile path between San Diego and Guadalupe Island. Field strength calculations are made at 65, 170, 520, and 3300 MHz using the

measured refractive index profile and a trilinear approximation to that profile.

Since this is a study of refraction effects, no attempt is made to include signal attenuation due to precipitation scattering or gaseous absorption, both of which are widely discussed in the literature. Furthermore, the choice of frequency range in this study eliminates the problem of partial penetration and reflection from ionized layers in the atmosphere. Consequently, the atmosphere is treated as an isotropic and linear medium (i.e., the permeability and permittivity are scalar quantities that are independent of the fields in the medium) which would not be the case if ionospheric effects were present.

## Method of Approach

One of the major concerns that arose early in this study regarded the selection of a suitable approach for modeling propagation through a refractive medium. Classically the solutions for radio propagation problems fall into two general categories: geometric optics or ray theory, and physical optics or wave theory. Each has its advantages and limitations, depending on the type of problem being addressed.

Geometric optics is usually a simpler approach than physical optics since it describes the propagation of waves along rays according to elementary geometric laws without regard to wavelengths or phases. The rays are defined as normals to the surfaces of constant phase of the wavefront. When the medium is isotropic, the index of refraction may be regarded to be a real quantity, and the rays are found to lie along the direction of energy propagation. For anisotropic media, however, the refractive index becomes complex and the rays may not follow the direction of energy flow.[15]

The attractiveness of geometric optics is that it retains its simplicity even for complicated refractive index structures, while generating easily interpreted ray patterns which show the effect of refraction on an emitter's radiation pattern. However its main drawbacks are that it is not valid for diffraction or complex scattering problems, nor is it suitable in regions of rapid refractive index changes (within a wavelength of distance) or rapid ray divergence, such as near sources or focal points. Any use of ray optics must therefore include careful consideration of its limitations, with the knowledge that it is only a limiting form of physical optics.[1, 15]

Physical optics, by contrast, results from a solution of the wave equation, and introduces wavelengths, phases, and mode concepts. It is valid for all diffraction and scattering problems and is unaffected by rapid changes in the refractive index or by the presence of sources or focal points.[16] Unfortunately this method rapidly becomes unmanageable for complicated atmospheric structures to the point where it is nearly useless. Furthermore, while presenting "exact" solutions to propagation problems, its accuracy generally exceeds that of available measured refractivity data. Even for complex scattering problems it becomes so difficult an approach that many analytic methods still rely on the approximations of ray theory whenever feasible.[1, 17]

Considering the applicability of ray versus wave theory, the former was selected for use in this study because of its inherent simplicity. Since earth diffraction is not regarded as a significant contributor to long range propagation at the wavelengths being considered, it may be eliminated as an obstacle to the use of geometric optics. Scattering in this paper is limited to specular reflection from the earth, since diffuse reflection becomes an extremely complicated function of incidence

angle, wavelength, polarization, surface roughness, and surface electrical properties. The problem of modeling diffuse scattering from rough surfaces is so difficult that many authors choose to describe it in terms of a summation of specular reflections from randomly oriented plane facet surfaces.[17, 18] Specular reflection on the other hand, may be included in the geometric optics approach by assigning complex specular scattering coefficients to the reflected signal, as shown in Chapter V.

Numerous geometric optics models exist which use a variety of techniques to compute field strength from the ray trajectories of a refracted field.[19-22] Each of these, however, has considerable limitations either in the selection of atmospheric models, method of field strength calculation, absence of a reasonable earth reflection model, or general lack of versatility. Consequently it was necessary to develop a new computer program for this thesis (Chapter V) which solves the ray trajectory equations derived in Chapter III and calculates emitter field strength as a function of height and distance along the earth's surface. While this simulation represents original work, portions of the field strength and numerical integration algorithms were obtained from a computer program described in Reference 21.

## CHAPTER II

## RADIO REFRACTIVITY OF AIR

As previously mentioned, long range propagation at radio frequencies above 30 MHz is mainly attributable to vertical changes in the refractive index of air. Refractive index is defined as the ratio of the velocity of light in free space c to the phase velocity $v_p$ of a field traveling through a given medium. Thus the refractive index of air is

$$n = \frac{c}{v_p} = \frac{\sqrt{\mu\epsilon}}{\sqrt{\mu_o\epsilon_o}} \tag{1}$$

where $\mu$ and $\epsilon$ are the permeability and permittivity of air, and $\mu_o$, $\epsilon_o$ are the respective quantities in free space.

For good dielectric and non-magnetic media such as air

$$\mu = \mu_o\mu_r \approx \mu_o \tag{2}$$

$$\epsilon = \epsilon_o\epsilon_r \tag{3}$$

where $\mu_r$ and $\epsilon_r$ are the relative permeability and permittivity. Eq. (1) then may be written

$$n = \frac{c}{v_p} = \frac{\sqrt{\mu_o\mu_r\epsilon_o\epsilon_r}}{\sqrt{\mu_o\epsilon_o}} = \sqrt{\mu_r\epsilon_r} \approx \sqrt{\epsilon_r} \tag{4}$$

Since $n \approx 1$ for air, Eq. (4) may be approximated by the binomial series

$$\sqrt{1 + x} = 1 + \frac{x}{2} - \frac{x^2}{8} + \frac{3x^3}{48} - \cdots \quad ; -1 < x \leq 1 \tag{5}$$

such that

$$n = \sqrt{1 + (\epsilon_r - 1)} \approx 1 + \frac{\epsilon_r - 1}{2} \tag{6}$$

Eq. (6) is generally rewritten to define the refractivity N of air as

$$N = (n - 1)\cdot 10^6 \tag{7}$$

The use of N is widespread in radio meteorology since it reflects the difference between the refractive indices of air and vacuum in units that range from zero to several hundreds. At sea level the value of n is approximately n = 1.00031, which corresponds to an N value of 310.

Other commonly used units include the "modified indices" given by

$$B = (n - 1 + \frac{h}{4a})\cdot 10^6 \tag{8}$$

and

$$M = (n - 1 + \frac{h}{a})\cdot 10^6 \tag{9}$$

where h is height above the earth's surface and a is the radius of the earth. As will be shown in Chapter IV, the radius of curvature of a nearly horizontal traveling wave is inversely proportional to the vertical gradient dn/dh of the air's refractive index. Since -1/4a is close to the observed gradient of n at low altitudes under standard atmospheric conditions,[23] the B-unit serves to eliminate this standard decrease of N by adding the quantity $(h/4a)\cdot 10^6$ to N. Thus a positive, zero, or negative valued B-gradient represents below standard, standard, or above standard refractive conditions, respectively. For ducting, when a signal's radius of curvature is equal to that of the earth, dn/dh = -1/a. Adding $(h/a)\cdot 10^6$ to N yields the M unit, so that M-gradients are always positive except for ducting conditions, when the gradients assume zero or negative values. The major advantage of using refractivity, or N-units,

lies in the fact that N is not modified by any altitude term and therefore reflects the true distribution of the refractive index n with respect to altitude. The gradient of N is generally negative even for some conditions of subrefraction. For ducting the gradient must satisfy

$$\frac{dN}{dh} \leq -\frac{1}{a} = -157 \text{ N-units/km} \tag{10}$$

The refractivity of air is a function of atmospheric temperature, pressure, and water vapor content. While N varies with frequency in general, it is essentially frequency independent over the radio spectrum being considered (30 MHz to 100 GHz). Numerous studies have been conducted to accurately describe the radio refractivity of air in terms of atmospheric properties. The generally used expression for N comes from the work by Smith and Weintraub[24] and is given by

$$N = 77.6 \frac{P_d}{T} + 72 \frac{e}{T} + (3.75)\cdot 10^5 \frac{e}{T^2} \tag{11}$$

where $P_d$ is the pressure of dry air in millibars (mbar), T is the temperature in degrees Kelvin ($^{o}$K), and e is the partial pressure of water vapor in mbar. According to Smith and Weintraub, Eq. (11) has an overall accuracy of $\pm$ 0.5 percent of N for frequencies up to 30 GHz (excluding refractivity dispersion at the 22 GHz water vapor resonance lines) and for normally encountered ranges of pressure, temperature, and humidity. This accuracy also includes errors due to rounding the constants to three significant figures. The constants of Eq. (11) are in basic agreement with the results of many experimenters whose work extends up to approximately 100 GHz.[23]

Under most conditions the total atmospheric pressure P is

$$P = P_c + P_d + e \approx P_d + e \tag{12}$$

where $P_c$ is the partial pressure of carbon dioxide.[23] Eq. (11) may be written

$$N = 77.6 \frac{P}{T} - 5.6 \frac{e}{T} + (3.75)\cdot 10^5 \frac{e}{T^2} \tag{13}$$

which for $T \approx 273\ ^{o}K$ ($\approx 0^{o}$ C) may be simplified to

$$N = 77.6 \frac{P}{T} + (3.73)\cdot 10^5 \frac{e}{T^2} \tag{14}$$

or

$$N = \frac{77.6}{T} (P + 4810 \frac{e}{T}) \tag{15}$$

Ideally the refractive index is directly measurable by using radio refractometers which are sensitive to the velocity of propagation through the air. However refractometers are expensive and often difficult to maintain and are therefore not in general use. The bulk of refractive index measurements are made indirectly from meteorological observations of atmospheric pressure, temperature, and humidity, which are then converted to units of refractivity through Eqs. (14) or (15). These measurements are typically made by radiosondes which are sent aloft on weather balloons at thousands of weather stations around the world, usually at six- or twelve-hour intervals.

Radiosondes, which carry sensors that detect changes in pressure, temperature, and humidity, transmit their data to the ground as they rise with what is usually assumed to be a constant rate of ascent. Unfortunately the radiosonde sensors suffer from response lags and sometimes rapid component aging, which can adversely affect the accuracy of their data. Furthermore, the problem of refractivity measurement is complicated by the fact that three sets of data are required, each of which contains its own sensor errors. Thus the errors in the data

generally outweigh any discrepancies in the constants used in Eqs. (14) or (15).[23]

Numerous models of "standard" or mean atmospheres exist. They range in complexity from the often used "4/3 earth radius" model to exponential and bi-exponential models. Each has its inherent strengths and weaknesses and its range of applications. For example, the 4/3 earth radius model (named because it uses an effective earth whose radius is 4/3 the normal earth radius) assumes an atmosphere of constant N-gradient with respect to altitude. This model is convenient because of its computational simplicity and because it allows signals to propagate along straight instead of curved lines. However a major disadvantage is that the model becomes highly inaccurate at altitudes above one or two kilometers, a fact that is often overlooked by many of its users.

The model which most generally and accurately represents standard atmospheric refractivity is the exponential function

$$N = N_s \, e^{-[c_e(h - h_s)]} \tag{16}$$

where $N_s$ is the refractivity at the earth's surface, $c_e$ is the exponential decay rate of N, h is height above sea level, and $h_s$ is the surface altitude above sea level at which $N_s$ is measured. This model has been adopted for use by the National Bureau of Standards Central Radio Propagation Laboratory (CRPL) along with a table of values for $N_s$ and $c_e$.[25] This model and its associated constants from the CRPL Exponential Reference Atmosphere (1958) is in agreement with data collected by the Rocket Panel[26] and the Air Force Research and Development Command.[27] Using the mean values of $N_s$, $c_e$, and $h_s$ for the United States, Eq. (16) becomes

$$N = 313e^{-(0.1439h)} \tag{17}$$

where h is in kilometers. Eq. (17) is the model used to represent a

standard reference atmosphere in this paper. A variant of Eq. (17) is the bi-exponential model which has a humidity dependent term and a pressure and temperature dependent term. The bi-exponential model while providing some additional modeling flexibility especially in regions of significant humidity changes, does not differ appreciably from the single term model for most general cases.[23] In any event, Eq. (17) merely serves as a useful analytic standard since it cannot represent the structure of N for any given location, season, or time of day. Thus to realistically study the effects of atmospheric refraction on an emitter's field distribution for a given set of meteorological conditions, it becomes necessary to use measured N profiles.[28]

Finally, the discussion of refractivity structure has centered upon the relationship of N to altitude, and has neglected changes in the horizontal direction. An examination of climatic data indicates that this is reasonable since the horizontal changes in refractivity are slow as compared to the vertical changes. Bean[23] indicates that it would be necessary to compare sea level meteorological stations located 500 kilometers apart in order to detect a difference in refractivity values that would be comparable to ascending merely one kilometer above the location of either station. There are, as Bean reports, several special cases where the horizontal gradient of N may become large, and these must be treated on an individual basis. However the data available indicates that the effect of horizontal changes in N is generally small and can usually be omitted from consideration.

## CHAPTER III

## THEORY OF GEOMETRIC OPTICS

The most common approach to developing the theory of geometric optics is from the use of Snell's law. However, considerable insight may be gained by following Kelso's[15] derivation of the differential ray equations (Euler-Lagrange equations) from Fermat's principle in optics. This approach directly presents solutions for the optical path length of a ray, the time of propagation along a ray, and the relationship of ray height to its projected distance along the earth's surface, as well as deriving Snell's law.

### Euler-Lagrange Equations of a Ray

Consider a curve C joining two points A and B as shown in Fig. (1). The time t required for a wave surface of constant phase, or phase front, to travel along C with phase velocity $v_p$ is

$$t = \int_A^B (1/v_p)\, ds \tag{18}$$

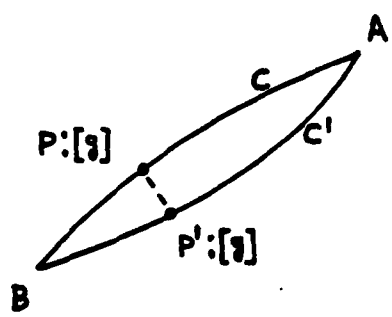


Fig. 1. Variation of a curve C between two points

where ds is an increment of arc length. Substituting $v_p = c/n$ from Eq. (1) for a given medium into Eq. (18) gives

$$t = (1/c) \int_A^B nds \tag{19}$$

The distance that the phase front would travel in the medium is called the optical path length L, and is given as

$$L = ct = \int_A^B nds \tag{20}$$

Fermat's principle is stated as follows: When light travels from a point A to a point B, it travels along a path for which the optical path length has a stationary value. From the calculus of variations this "stationary value" is usually expressed as a variation $\delta$ of the path length integral, which is taken to be a minimum. Thus Fermat's principle may be given by

$$\delta L = \delta \int_A^B nds = 0 \tag{21}$$

Suppose the curve C joining points A and B is defined by

$$x(g),\ y(g),\ z(g) \tag{22}$$

where g is some parameter along the curve. The element of arc length ds along C is then

$$ds = \left[ \left(\frac{dx}{dg}\right)^2 + \left(\frac{dy}{dg}\right)^2 + \left(\frac{dz}{dg}\right)^2 \right]^{1/2} dg$$

$$= \left[x'^2 + y'^2 + z'^2\right]^{1/2} dg \tag{23}$$

where the prime denotes differentiation with respect to g. Substituting Eq. (23) into Eq. (20) gives

$$L = \int_A^B wdg \tag{24}$$

where

$$w = w(x,y,z,x',y',z') = n(x,y,z)[x'^2 + y'^2 + z'^2]^{1/2} \tag{25}$$

Consider now a neighboring curve C' having the same end points A and B, which is also defined in terms of $g$ as shown in Fig. (1). The variation of w in passing from a point P on the curve C to a point P' on curve C' which corresponds to the same value of $g$ is

$$\delta w = \sum_{i=1}^{3} \frac{\partial w}{\partial x_i} \delta x_i + \sum_{i=1}^{3} \frac{\partial w}{\partial x_i'} \delta x_i' \tag{26}$$

where the notation $x_1$, $x_2$, $x_3$, $x_1'$, $x_2'$, $x_3'$ is used to denote x, y, z, x', y', z' respectively. Taking the variation of Eq. (24), noting that the integral sign and variational symbol $\delta$ are commutable, and substituting Eq. (26), $\delta L$ becomes

$$\delta L = \delta \int_A^B w dg = \int_A^B (\delta w) dg$$

$$= \int_A^B \left[ \sum_{i=1}^{3} \frac{\partial w}{\partial x_i} \delta x_i + \sum_{i=1}^{3} \frac{\partial w}{\partial x_i'} \delta x_i' \right] dg \tag{27}$$

Since the derivative d and the variation $\delta$ are likewise commutable, then

$$\delta x_i' = \delta(dx_i/dg) = (d/dg)(\delta x_i) \tag{28}$$

Substituting Eq. (28) into Eq. (27) giv es

$$\delta L = \int_A^B \left[ \sum_{i=1}^{3} \frac{\partial w}{\partial x_i} \delta x_i + \sum_{i=1}^{3} \frac{\partial w}{\partial x_i'} \frac{d}{dg} (\delta x_i) \right] dg \tag{29}$$

Integrating the second term on the right hand side of the equation by parts yields

$$\int_A^B \sum_{i=1}^{3} \frac{\partial w}{\partial x_i'} \frac{d}{dg} (\delta x_i)\, dg = \sum_{i=1}^{3} \frac{\partial w}{\partial x_i'} \delta x_i \Big|_A^B$$

$$- \int_A^B \sum_{i=1}^{3} \frac{d}{dg} \left(\frac{\partial w}{\partial x_i'}\right) \delta x_i \, dg \tag{30}$$

Since the curves C and C' have common end points A and B, then the variations $\delta x_i$ vanish at the end points. Thus the first term on the right hand side of Eq. (30) vanishes, which results in Eq. (29) being written as

$$\delta L = \int_A^B \sum_{i=1}^{3} \left[\frac{\partial w}{\partial x_i} - \frac{d}{dg} \left(\frac{\partial w}{\partial x_i'}\right)\right] \delta x_i \, dg \tag{31}$$

Fermat's principle requires that this variation must be zero if curve C is the path along which light travels from point A to point B. That is, Eq. (21) must be satisfied for curve C to be a ray. Setting Eq. (31) equal to zero and reversing the terms gives

$$\delta L = \int_A^B \sum_{i=1}^{3} \left[\frac{d}{dg} \left(\frac{\partial w}{\partial x_i'}\right) - \frac{\partial w}{\partial x_i}\right] \delta x_i \, dg = 0 \tag{32}$$

Since all $\delta x_i$ were introduced as completely generalized functions, the integrand of Eq. (32) must vanish to avoid trivial solutions in which all $\delta x_i = 0$ or $dg = 0$. Thus the component differential equations

$$\frac{d}{dg} \left(\frac{\partial w}{\partial x'}\right) - \frac{\partial w}{\partial x} = 0 \tag{33a}$$

$$\frac{d}{dg} \left(\frac{\partial w}{\partial y'}\right) - \frac{\partial w}{\partial y} = 0 \tag{33b}$$

$$\frac{d}{dg} \left(\frac{\partial w}{\partial z'}\right) - \frac{\partial w}{\partial z} = 0 \tag{33c}$$

must be satisfied by a ray, which are also known as the Euler-Lagrange equations.

Eqs. (33) are valid for propagation over short distances where the effects of earth and atmospheric curvature are nil. However for longer ranges (> 100 nautical miles) it is necessary to consider the more general case of a spherical earth and a spherically stratified atmosphere.

Let two points in space P and P' be located a short distance apart. The arc length ds between the points is given in spherical coordinates as

$$ds = \left[\left(\frac{dr}{dg}\right)^2 + \left(\frac{rd\theta}{dg}\right)^2 + \left(\frac{rd}{dg}\right)^2\right]^{1/2} dg$$

$$= [(r')^2 + (r\theta')^2 + (r\phi')^2]^{1/2}\, dg \qquad (34)$$

Letting

$$w = n(r, \theta, \phi)[(r')^2 + (r\theta')^2 + (r\phi')^2]^{1/2} \qquad (35)$$

then following the previous development, the Euler-Lagrange equations of a ray in spherical coordinates are

$$\frac{d}{dg}\left(\frac{\partial w}{\partial r'}\right) - \frac{\partial w}{\partial r} = 0 \qquad (36a)$$

$$\frac{d}{dg}\left(\frac{\partial w}{\partial \theta'}\right) - \frac{\partial w}{\partial \theta} = 0 \qquad (36b)$$

$$\frac{d}{dg}\left(\frac{\partial w}{\partial \phi'}\right) - \frac{\partial w}{\partial \phi} = 0 \qquad (36c)$$

## Algorithm Development

Having derived the general equations of a ray in a spherically stratified medium, it is now desirable to solve for ray height versus distance. For the sake of simplicity in computational as well as graphical representation of the ray, consider any arbitrary $\phi$ = constant plane in the atmosphere as shown in Fig. (2). Let the ray lie in the $\phi$ = constant plane and let the refractive index vary as a function of radial distance r for r > a, where a is the earth's radius.

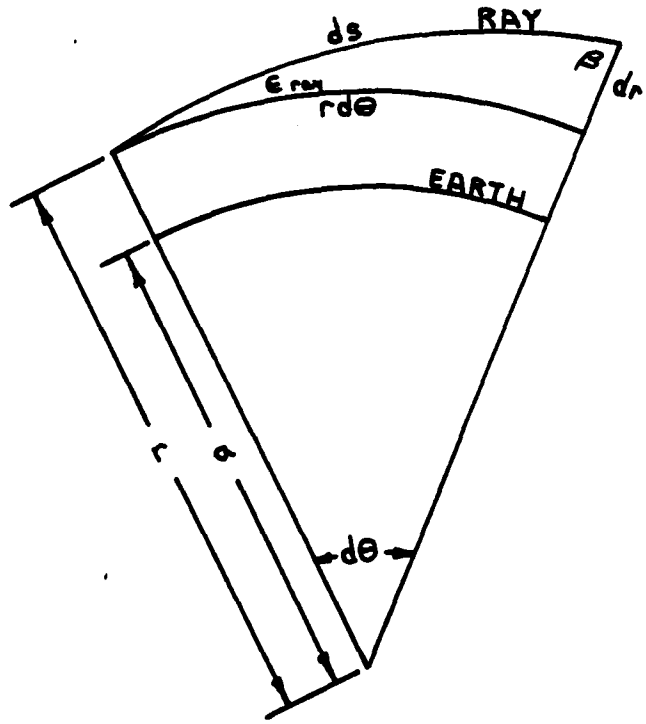


Fig. 2. Ray geometry in polar coordinates.

Substituting $g = r$ into Eqs. (34) and (35) gives

$$ds = \left[ 1 + \left(r \frac{d\theta}{dr}\right)^2 \right]^{1/2} dr \tag{37}$$

$$w = n(r) \left[ 1 + \left(r \frac{d\theta}{dr}\right)^2 \right]^{1/2} \tag{38}$$

Inserting Eq. (38) into Eqs. (36) gives

$$\frac{d}{dr} \left[ \frac{\partial w}{\partial \left(\frac{d\theta}{dr}\right)} \right] - \frac{\partial w}{\partial \theta} = 0 \tag{39}$$

From the geometry of Fig. (2) it should be noted that

$$r = r(\theta) \tag{40a}$$

$$\theta = \theta(r) \tag{40b}$$

However, Eq. (38) is an explicit function only of r and $d\theta/dr$, or

$$w = w(r, \theta') \tag{41}$$

where the prime denotes differentiation with respect to r (or g). The derivative of w is written

$$dw = \frac{\partial w}{\partial r}\, dr + \frac{\partial w}{\partial \theta'}\, d\theta' \tag{42}$$

Thus while the total derivative $dw/d\theta$ may exist for Eq. (42), the partial derivative $\partial w/\partial\theta$ does not. Therefore

$$\frac{\partial w}{\partial \theta} = 0 \tag{43}$$

Combining Eqs. (39) and (43) yields an Euler-Lagrange equation in polar coordinates given by

$$\frac{d}{dr}\left[\frac{\partial w}{\partial\left(\frac{d\theta}{dr}\right)}\right] = 0 \tag{44}$$

Similarly letting $g = \theta$ in Eqs. (34) and (35) gives

$$ds = \left[\left(\frac{dr}{d\theta}\right)^2 + r^2\right]^{1/2} d\theta \tag{45}$$

$$w = n(r)\left[\left(\frac{dr}{d\theta}\right)^2 + r^2\right]^{1/2} \tag{46}$$

Substituting Eq. (46) into Eqs. (36) yields

$$\frac{d}{d\theta}\left[\frac{\partial w}{\partial\left(\frac{dr}{d\theta}\right)}\right] - \frac{\partial w}{\partial r} = 0 \tag{47}$$

In this case Eq. (46) is an explicit function only of r and $dr/d\theta$, or

$$w = w(r, r') \tag{48}$$

where the prime indicates differentiation with respect to $\theta$ (or g). The derivative then becomes

$$dw = \frac{\partial w}{\partial r}\, dr + \frac{\partial w}{\partial r'}\, dr' \tag{49}$$

Since both $dw/dr$ and $\partial w/\partial r$ exist for Eq. (49), then Eq. (47) remains unchanged, thus providing a second Euler-Lagrange equation.

Eq. (44) is useful since it produces a form of Snell's law for spherically concentric refractive media, and Eq. (47) is important because it results in a second order differential equation which defines the trajectory of a ray in a polar coordinate system.

Substituting Eq. (38) into Eq. (44) and integrating Eq. (44) gives

$$\frac{\partial}{\partial\left(\frac{d\theta}{dr}\right)}\left[n(r)\left[1+\left(r\frac{d\theta}{dr}\right)^2\right]^{1/2}\right]=K \tag{50}$$

which becomes

$$\frac{r^2 n(r)\frac{d\theta}{dr}}{\left[1+\left(r\frac{d\theta}{dr}\right)^2\right]^{1/2}}=K \tag{51}$$

where K is a constant of integration. From Fig. (2) it may be seen that

$$\sin\beta=\frac{r d\theta}{\left[(dr)^2+(r d\theta)^2\right]^{1/2}}$$

$$=\frac{r\frac{d\theta}{dr}}{\left[1+\left(r\frac{d\theta}{dr}\right)^2\right]^{1/2}} \tag{52}$$

where $\beta$ is the angle between the ray and the radius vector r. Substituting Eq. (52) into Eq. (51) gives

$$rn(r)\sin\beta=K \tag{53}$$

which is Snell's law for spherically concentric media. Evaluating K at some known point (e.g., the emitter) yields

$$rn(r)\sin\beta=r_o n(r_o)\sin\beta_o \tag{54}$$

where the zero subscript refers to known values at the emitter.

Substituting Eq. (54) into Eq. (52), solving for $d\theta/dr$, and integrating gives

$$\theta = r_o n(r_o) \sin \beta_o \int_{r_o}^{r} \frac{dr}{r[(rn(r))^2 - (r_o n(r_o) \sin \beta_o)^2]^{1/2}} \qquad (55)$$

Eq. (55) could be used to calculate the ray trajectory except for the fact that, as Fig. (3) illustrates, $\theta$ may become a double valued function of r.

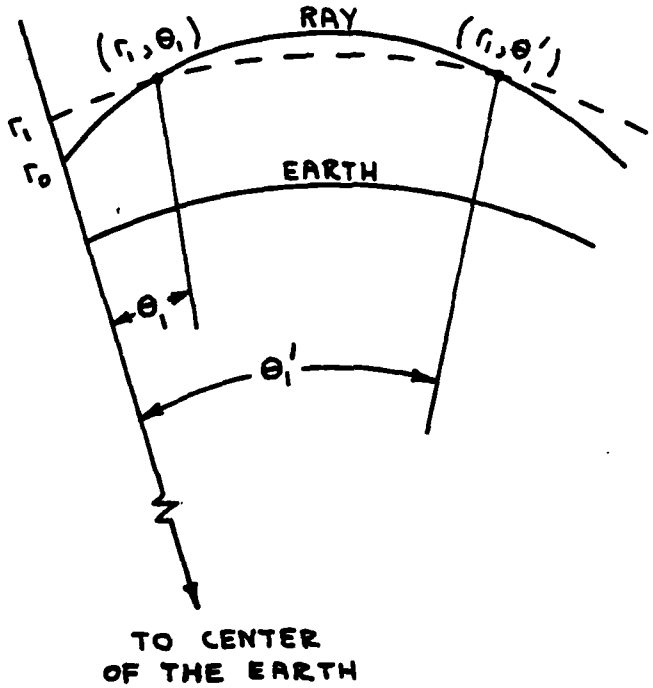


Fig. 3. Ray trajectory for a double valued solution to Eq. (55). An initially rising ray is refracted downward toward the earth resulting in two possible values of $\theta$ ($\theta_1$ and $\theta_1'$) for a single value of $r = r_1$.

A more satisfactory approach to determining the ray trajectory is to expand Eq. (47) since it permits the solution of r as a function of $\theta$. Substituting Eq. (46) into Eq. (47) gives

$$\frac{d}{d\theta}\left[\frac{\partial}{\partial(\frac{dr}{d\theta})}\left[n(r)\left[(\frac{dr}{d\theta})^2 + r^2\right]^{1/2}\right]\right]$$

$$- \frac{\partial}{\partial r}\left[n(r)\left[(\frac{dr}{d\theta})^2 + r^2\right]^{1/2}\right] = 0 \qquad (56)$$

Carrying out the differentiation and rearranging the terms yields

$$\frac{d^2r}{d\theta^2} = \frac{2}{r}\left(\frac{dr}{d\theta}\right)^2 + \frac{r^2}{n(r)}\frac{\partial[n(r)]}{\partial r}\left[\left(\frac{1}{r}\frac{dr}{d\theta}\right)^2 + 1\right]^2 + r \tag{57}$$

Substituting the relationship

$$\frac{\partial}{\partial r}[\ln(u)] = \frac{1}{u}\frac{\partial u}{\partial r} \tag{58}$$

into Eq. (57) gives

$$\frac{d^2r}{d\theta^2} = \frac{2}{r}\left(\frac{dr}{d\theta}\right)^2 + r^2\frac{\partial}{\partial r}(\ln[n(r)])\left[\left(\frac{1}{r}\frac{dr}{d\theta}\right)^2 + 1\right]^2 + r \tag{59}$$

Eq. (59) is more useful when it is changed from polar coordinates $(r, \theta)$ to the coordinates of distance over the earth's surface and altitude above the earth's surface $(x, h)$. Letting

$$r = a + h \tag{60a}$$

$$\theta = \frac{x}{a} \tag{60b}$$

Eq. (59) may be written

$$\frac{d^2h}{dx^2} = \frac{(a+h)}{a^2}\left[2\left[\left(\frac{a}{a+h}\right)\frac{dh}{dx}\right]^2 + (a+h)\frac{\partial}{\partial h}(\ln[n(h)])\left(\left[\left(\frac{a}{a+h}\right)\frac{dh}{dx}\right]^2 + 1\right)^2 + 1\right] \tag{61}$$

Eq. (61) forms the basis for all ray trajectory computations throughout this paper, and is in agreement with the ray equations developed by Hartree et al[22] for use on an analog differential analyzer. The results presented in this thesis are obtained by numerically integrating Eq. (61) on a digital computer by using a standard fourth order Runge-Kutta integration algorithm.

Now that the ray trajectory may be found, it is useful to derive a solution for the time of propagation along the ray path. Eq. (19) gives

the time it takes for a wave front to travel between two points along a specified curve C. If C is the ray path which satisfies the Euler-Lagrange equations in a polar coordinate system (Eqs. (36) for a $\phi$ = constant plane) then substituting Eqs. (37) and (45) into Eq. (19) yields

$$t = \frac{1}{c} \int_{r_o}^{r} n(r) \left[ 1 + \left(r\frac{d\theta}{dr}\right)^2 \right]^{1/2} dr \tag{62}$$

and

$$t = \frac{1}{c} n(r) \int_{\theta_o}^{\theta} \left[ \left(\frac{dr}{d\theta}\right)^2 + r^2 \right]^{1/2} d\theta \tag{63}$$

where $(r_o, \theta_o)$ are the emitter coordinates and $(r, \theta)$ are the coordinates of a point on the ray. Both solutions are valid although as in the case of Eq. (55), Eq. (62) may be double valued for some ray trajectories.

Differentiating Eq. (63) and substituting the coordinate relationships of Eqs. (60) gives

$$\frac{dt}{dx} = \frac{1}{c} n(h) \left[ \left(\frac{dh}{dx}\right)^2 + \left(\frac{a + h}{a}\right)^2 \right]^{1/2} \tag{64}$$

Eq. (64) is useful since it provides the phase information necessary to calculate the total field in regions of signal interference. It is integrated with Eq. (61) to provide the position and time coordinates (x, h, t) of each ray.

## CHAPTER IV

## PROPERTIES OF GEOMETRIC OPTICS

While the method of geometric optics is a simple technique for solving many propagation problems, there exist a number of conditions which limit its useage. One way of presenting these restrictions and other related properties is to examine the wave equation and its solution in both homogeneous and inhomogeneous media.[1, 15]

### Wave and Eikonal Equations

Consider a nearly perfect dielectric medium that is charge-free (no sources exist), unbounded (infinite in extent), linear (the permeability $\mu$ and permittivity $\epsilon$ of the medium are independent of the fields), homogeneous ($\mu$ and $\epsilon$ are independent of position), and isotropic ($\mu$ and $\epsilon$ are scalar). The wave equation is then given as

$$\nabla^2 \vec{E} + k^2 \vec{E} = 0 \tag{65}$$

where $\vec{E}$ is the electric field intensity vector and k is the propagation constant of the medium. From elementary electromagnetic theory it is known that for a nearly perfect dielectric medium

$$k = 2\pi/\lambda = \omega/v_p = \omega\sqrt{\mu\epsilon} \tag{66}$$

where $\lambda$ is the wavelength, $\omega$ is the radian frequency, and $v_p$ is the phase velocity of the field in the medium. The free space propagation constant is

$$k_o = 2\pi/\lambda_o = \omega/c = \omega\sqrt{\mu_o\epsilon_o} \tag{67}$$

where the zero subscript denotes free space values and c is the speed of light in vacuum.

Substituting Eqs. (2) and (3) for a non-magnetic medium into Eq. (66) gives

$$k = \omega\sqrt{\mu_o \epsilon_o \epsilon_r} = k_o\sqrt{\epsilon_r} \tag{68}$$

where $\epsilon_r$ is the relative permittivity. The wave equation may now be written as

$$\nabla^2 \vec{E} + k_o^2 \epsilon_r \vec{E} = 0 \tag{69}$$

Finally, substituting Eq. (4) into Eq. (68) yields

$$k = k_o n \tag{70}$$

and Eq. (65) becomes

$$\nabla^2 \vec{E} + k_o^2 n^2 \vec{E} = 0 \tag{71}$$

Thus Eqs. (65), (69), and (71) give three forms of the wave equation for $\vec{E}$ in terms of the propagation constant, relative permittivity, and index of refraction of the medium.

Eq. (71) is particularly interesting since it explicitly contains the refractive index. Using rectangular coordinates to simplify the treatment of plane waves, Eq. (71) may be expressed in terms of its scalar component fields

$$\nabla^2 E_x + k_o^2 n^2 E_x = 0 \tag{72a}$$

$$\nabla^2 E_y + k_o^2 n^2 E_y = 0 \tag{72b}$$

$$\nabla^2 E_z + k_o^2 n^2 E_z = 0 \tag{72c}$$

For a homogeneous medium where n is constant, the plane wave solution for Eqs. (72) will have the form

$$E = Ae^{-j(\vec{k}_o n)\cdot\vec{r}}$$

$$= Ae^{-jk_o n(\hat{n}\cdot\vec{r})} \tag{73}$$

where $\vec{k}_o$ is the free space propagation vector which is normal to the wavefront and pointed in the direction of motion of the planes of constant phase, $\hat{n}$ is the unit vector in the direction of $\vec{k}_o$, and $\vec{r}$ is the position vector of the point in space at which the field is to be calculated.

In reality, atmospheric refractive index is not a constant but varies slightly with position so that Eq. (73) is no longer valid. However a solution to the wave equation does exist in a form very similar to Eq. (73). Replacing A and n by Q and S, which are real functions of position, the solution becomes

$$E = Qe^{-jk_o S} \tag{74}$$

Substituting Eq. (74) into any of the component fields of Eqs. (72) yields

$$[\nabla^2 Q - k_o^2 Q(\nabla S)^2 - jk_o Q\nabla^2 S - j2k_o\ \nabla Q\cdot\nabla S]e^{-jk_o S} + k_o^2 n^2 Qe^{-jk_o S} = 0 \tag{75}$$

Rearranging the terms, dividing by $Qk_o^{\ 2}$, and dropping the exponent, this becomes

$$n^2 - (\nabla S)^2 = (j/k_o)[\nabla^2 S + 2\nabla Q\cdot\nabla S/Q] - \nabla^2 Q/Qk_o^{\ 2} \tag{76}$$

Now if $k_o$ is sufficiently large such that the following two conditions are satisfied:

$$\frac{\nabla^2 Q}{k_o^{\ 2} Q} \ll n^2 \tag{77}$$

$$\nabla^2 S + \frac{2\nabla Q\cdot\nabla S}{Q} \ll k_o \tag{78}$$

then Eq. (76) reduces to

$$n^2 = (\nabla S)^2 \tag{79}$$

which is called the equation of the eikonal. While Eq. (79) may be used directly to construct the ray paths of geometric optics,[1] it will be used here to derive the relationship of ray density to the power density of the field and to present the limitations of ray optics.

## The Jacobian and Power Density

Consider the transformation of a point in space between the coordinates (x, y, z) and (u, v, w). Let the coordinates (x, y, z) be definable in terms of (u, v, w) such that

$$x = x(u, v, w) \tag{80a}$$

$$y = y(u, v, w) \tag{80b}$$

$$z = z\ (u, v, w) \tag{80c}$$

If at a given point $P_o$ where $(x_o, y_o, z_o) = (u_o, v_o, w_o)$ the Jacobian of the transformation

$$J = \frac{\partial(x, y, z)}{\partial(u, v, w)} = \begin{vmatrix} \frac{\partial x}{\partial u} & \frac{\partial x}{\partial v} & \frac{\partial x}{\partial w} \\ \frac{\partial y}{\partial u} & \frac{\partial y}{\partial v} & \frac{\partial y}{\partial w} \\ \frac{\partial z}{\partial u} & \frac{\partial z}{\partial v} & \frac{\partial z}{\partial w} \end{vmatrix} \tag{81}$$

is not zero, and if all the partial derivatives in Eq. (81) are continuous throughout some region which includes $P_o$, then Eqs. (80) may be solved uniquely for u, v, and w in terms of x, y, and z in this region. Holding each of the variables u, v, and w constant in turn gives three parametric, or coordinate, surfaces through a point in space. Furthermore, holding any pair of the variables constant yields a parametric, or coordinate, curve passing through the point.[29]

Consider next a volume element $d\gamma$ bounded by a bundle or "pencil" of

rays and surfaces of constant phase as shown in Fig. (4).[1] Let the volume be defined by the surfaces $u = u_1$, $u = u_1 + du$, $v = v_1$, $v = v_1 + dv$, $w = w_1$, and $w = w_1 + dw$, where the variables u, v, and w are solvable within the volume such that

$$u = u(x, y, z) \tag{82a}$$

$$v = v(x, y, z) \tag{82b}$$

$$w = w(x, y, z) \tag{82c}$$

If the surfaces of constant phase are given by

$$w = w_1 = S_1 \tag{83}$$

and

$$w = w_1 + dw = S_1 + dS \tag{84}$$

where $S_1$ and dS represent the phase angle and phase angle increment for Eq. (74), then Eqs. (82b) and (82c) produce two families of surfaces whose intersections are the rays between $S_1$ and dS. It should be noted that these families are not uniquely determined by the ray pattern since it is possible to construct an infinite number of families having the same intersections as Eqs. (82b) and (82c).

Equating the imaginary part of Eq. (76) to zero yields

$$\nabla^2 S + \frac{2(\nabla Q \cdot \nabla S)}{Q} = 0 \tag{85}$$

Combining Eq. (85) with the vector relationship

$$\nabla \cdot (Q^2 \nabla S) = 2Q(\nabla Q \cdot \nabla S) + Q^2 \nabla^2 S \tag{86}$$

gives

$$\nabla \cdot (Q^2 \nabla S) = 0 \tag{87}$$

Since $Q^2 \nabla S$ is solenoidal (i.e., its divergence is zero), there exists a vector $\vec{U}$ such that

$$Q^2 \nabla S = \nabla \times \vec{U} \tag{88}$$

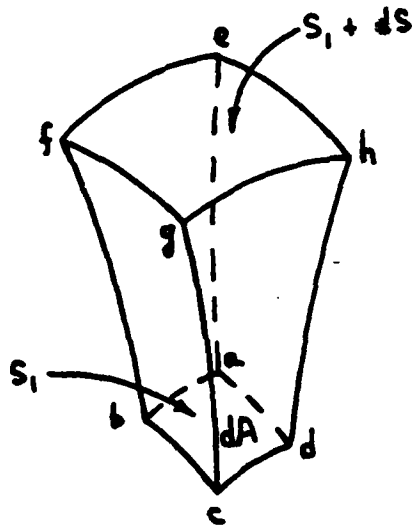


Fig. 4. The volume element $d\gamma$ bounded by rays and surfaces of constant phase. The face abcd lies on the surface $w = S_1$, and the face efgh lies on the surface $w = S_1 + dS$. Similarly abfe and dcgh are portions of the surfaces $v = v_1$, and $v = v_1 + dv$, respectively. The remaining two faces adhe and bcgf lie on the surfaces $u = u_1$, and $u = u_1 + du$, respectively.

where the curl of $\vec{U}$ lies in the direction of $\nabla S$. By correctly choosing $\vec{U}$, the surfaces u and v may be found which satisfy the wave equation and the rays within $d\gamma$, although surface families other than those of u and v may also exist.

It was stated in Chapter I that rays are perpendicular to the wavefronts, or surfaces of constant phase, which are propagating in an isotropic medium.[16] Since $\nabla S$ defines the normal to a wavefront, then for the surfaces of u and v to intersect along the ray paths, $\nabla u$ and $\nabla v$ must be normal to $\nabla S$, and the vector $\nabla u \times \nabla v$ must be parallel to $\nabla S$. This latter vector is used in the identity

$$\nabla \times (u\nabla v) = \nabla u \times \nabla v + u[\nabla \times (\nabla v)]$$
$$= \nabla u \times \nabla v \qquad (89)$$

where the term $u[\nabla \times (\nabla v)]$ vanishes since, from vector calculus, the curl of a gradient is zero when continuous mixed partial derivatives are assumed so that the order of differentiation is immaterial. Allowing u and

v to be well behaved functions with continuous derivatives, Eq. (89) gives

$$\vec{U} = u\nabla v \tag{90}$$

where the curl of $\vec{U}$ lies in the direction of $\nabla S$. Substituting Eq. (90) into Eq. (88) yields

$$Q^2\nabla S = \nabla \times (u\nabla v) = \nabla u \times \nabla v \tag{91}$$

Taking the dot product of each side of Eq. (91) with $\nabla S$ and substituting Eq. (79) gives

$$Q^2 = \frac{(\nabla u \times \nabla v)\cdot\nabla S}{n^2} \tag{92}$$

for which the numerator may be written

$$(\nabla u \times \nabla v)\cdot\nabla S = \begin{vmatrix} \frac{\partial u}{\partial x} & \frac{\partial u}{\partial y} & \frac{\partial u}{\partial z} \\ \frac{\partial v}{\partial x} & \frac{\partial v}{\partial y} & \frac{\partial v}{\partial z} \\ \frac{\partial w}{\partial x} & \frac{\partial w}{\partial y} & \frac{\partial w}{\partial z} \end{vmatrix} = \frac{\partial(u,v,w)}{\partial(x,y,z)} = \frac{1}{J} \tag{93}$$

where J is the Jacobian of x, y, and z with respect to u, v, and w. Thus Eq. (92) may be written

$$Q^2 = \frac{1}{Jn^2} \tag{94}$$

The volume increment of $d\gamma$ may be expressed in terms of the Jacobian by

$$d\gamma = J(u, v, w)\, dudvdS \tag{95}$$

Let dA be the element of area on the surface $w = S_1$ which is bounded by the surfaces u = constant and v = constant as shown in Fig. (4). Since the rays are normal to their respective wavefronts, Eq. (95) may be approximated by

$$d\gamma = dA d\sigma \tag{96}$$

where $d\sigma$ is used to denote the arc length along a ray. Combining Eqs. (95) and (96) yields

$$J = \frac{dA d\sigma}{du dv dS} \tag{97}$$

From the definition of the gradient of a scalar function

$$\frac{dS}{d\sigma} = |\nabla S| = n \tag{98}$$

Thus Eq. (97) becomes

$$J = \frac{dA}{n du dv} \tag{99}$$

Turning momentarily to Maxwell's equations for time-varying fields in a source-free medium,

$$\nabla \times \vec{E} = -\frac{\partial \vec{B}}{\partial t} \tag{100a}$$

$$\nabla \times \vec{H} = \frac{\partial \vec{D}}{\partial t} \tag{100b}$$

$$\nabla \cdot \vec{D} = 0 \tag{100c}$$

$$\nabla \cdot \vec{B} = 0 \tag{100d}$$

where $\vec{E}$ and $\vec{H}$ are the electric and magnetic field intensity vectors, and $\vec{D}$ and $\vec{B}$ are the electric and magnetic flux density vectors, respectively. In simple linear media

$$\vec{D} = \epsilon \vec{E} \tag{101a}$$

$$\vec{B} = \mu \vec{H} \tag{101b}$$

For a plane sinusoidal wave propagating through an infinite homogeneous or inhomogeneous medium, Eqs. (100) dictate that $\vec{E}$ and $\vec{H}$ are transverse

or perpendicular to the propagation vector $\vec{k}$ of the field, and normal to each other. From Eqs. (100) and (101) this relationship is written

$$\vec{H} = \sqrt{\epsilon/\mu}\ \hat{n} \times \vec{E} \tag{102}$$

where $\hat{n}$ is the unit vector in the direction of $\vec{k}$.

The density of the outward flux of energy, or power density, for a time-varying field passing through a closed surface is given by the Poynting vector $\vec{P}$, where

$$\vec{P} = \vec{E} \times \vec{H} \tag{103}$$

Following the standard convention that physically meaningful electric and magnetic fields are represented by the real part of complex quantities (i.e., $\cos\theta = \mathrm{Re}[e^{j\theta}]$), the time-averaged Poynting vector for sinusoidal fields is written

$$\vec{P}_{av} = \frac{1}{2}\,\mathrm{Re}[\vec{P}_c] = \frac{1}{2}\,\mathrm{Re}[\vec{E} \times \vec{H}^*] \tag{104}$$

where $\vec{H}^*$ denotes the complex conjugate of $\vec{H}$ and the operator Re means "the real part" of the complex Poynting vector $\vec{P}_c = \vec{E} \times \vec{H}^*$. Substituting Eq. (102) into Eq. (104) gives

$$\vec{P}_{av} = \frac{1}{2}\sqrt{\epsilon/\mu}\ \left|\vec{E}\right|^2 \hat{n} \tag{105}$$

which may be integrated to determine the average outward energy flux or average power p through a closed surface S', such that

$$p = \oint_{S'} \vec{P}_{av} \cdot d\vec{s}' \tag{106}$$

Substituting Eq. (99) into Eq. (94) and using $n^2 = \nabla S \cdot \nabla S$ from Eq. (79) yields

$$du\,dv = Q^2 n\,dA = Q^2 \nabla S \cdot (\nabla S/n)\ dA = Q^2 \nabla S \cdot \hat{n}\,dA \tag{107}$$

where $\nabla S/n = \hat{n}$ is the unit vector normal to the wavefront at the surface element dA. Integrating Eq. (107) over a closed surface S' which includes

the wavefront surface $S_1$ gives

$$\oiint_{S'} dudv = \oiint_{S'} Q^2 \nabla S \cdot \hat{n} dA$$

$$= \oiint_{S'} Q^2 \nabla S \cdot d\vec{s}' \tag{108}$$

Noting from Eq. (74) that $|Q^2 \nabla S|$ is proportional to $|\vec{E}|^2$ and lies in the direction of $\hat{n}$, then a comparison of Eqs. (105), (106), and (108) indicates that $\oiint_{S'} dudv$ is the total outward power radiated through the surface S'. Thus the element dudv, which is bounded by the ray bundle of Fig. (4), is the time-averaged energy flux of the Poynting vector $\vec{P}_{av} = Q^2 \nabla S$ through the wavefront surface increment dA, or

$$dudv = Q^2 \nabla S \cdot \hat{n} dA = \vec{P}_{av} \cdot \hat{n} dA \tag{109}$$

It is this relationship of the ray bundle element dudv to the average power density at the wavefront which is used in the power density and field strength calculations presented in Chapter VI of the thesis.

## Restrictions of Ray Theory

The restrictions in the use of geometric optics result from the inequality of Eq. (77). Using the vector identity

$$\nabla \cdot \left(\frac{\nabla Q}{nQ}\right) = \frac{\nabla^2 Q}{nQ} + \nabla Q \cdot \nabla\left(\frac{1}{nQ}\right) \tag{110}$$

Eq. (77) may be written

$$\frac{\nabla^2 Q}{k_o^2 n^2 Q} = \frac{1}{k_o n} \nabla \cdot \left(\frac{\nabla Q}{k_o n Q}\right) + \frac{1}{k_o n} \left(\frac{\nabla n}{n}\right) \cdot \left(\frac{\nabla Q}{k_o n Q}\right) + \left(\frac{\nabla Q}{k_o n Q}\right) \cdot \left(\frac{\nabla Q}{k_o n Q}\right) \ll 1 \tag{111}$$

Taking the square root of Eq. (94) and substituting it into $\nabla Q / k_o n Q$ gives

$$\frac{\nabla Q}{k_o n Q} = -\left[\frac{\nabla (J^{1/2})}{k_o n (J^{1/2})} + \frac{1}{k_o n} \frac{\nabla n}{n}\right] \tag{112}$$

Combining Eqs. (111) and (112) yields

$$\frac{\nabla^2 Q}{k_o^2 n^2 Q} = \left[\frac{\nabla(J^{1/2})}{k_o n(J^{1/2})}\right] \cdot \left[\frac{1}{k_o n}\left(\frac{\nabla n}{n}\right)\right] + \left[\frac{\nabla(J^{1/2})}{k_o n(J^{1/2})}\right]^2$$

$$- \frac{1}{k_o n} \nabla \cdot \left[\frac{\nabla(J^{1/2})}{k_o n(J^{1/2})}\right] - \frac{1}{k_o n} \nabla \cdot \left[\frac{1}{k_o n}\left(\frac{\nabla n}{n}\right)\right] \ll 1 \qquad (113)$$

which is satisfied only when

$$\frac{1}{k_o n} \frac{|\nabla n|}{n} \ll 1 \qquad (114)$$

and

$$\frac{1}{k_o n} \frac{|\nabla(J^{1/2})|}{(J^{1/2})} \ll 1 \qquad (115)$$

Furthermore, Eq. (113) requires that $(1/k_o n)(\nabla n/n)$ and $(1/k_o n)[\nabla(J^{1/2})/(J^{1/2})]$ be smooth so that their divergences are likewise small.

Eqs. (114) and (115) specify the conditions governing the use of ray optics. Recalling that $k_o = 2\pi/\lambda_o$ and $n = k_o/k = \lambda_o/\lambda$, Eq. (114) may be written

$$\frac{\lambda_o}{2\pi n}\left(\frac{\nabla n}{n}\right) = \frac{\lambda}{2\pi}\left(\frac{\nabla n}{n}\right) \ll 1 \qquad (116)$$

which states that the relative change in the refractive index over a distance approximately equal to a wavelength of radiation must be small compared with unity. Thus Eq. (114) becomes a better approximation as wavelength decreases, and is perfectly satisfied in a homogeneous medium where $\nabla n = 0$. On the other hand, a medium with sharp discontinuities in the refractive index violates Eq. (114) at the discontinuities. Therefore while rays obey Snell's law on either side of a discontinuity in the refractive index (e.g., either side of the boundary between two dielectric media), the region at the discontinuity itself cannot be described by geometric optics, but instead must be treated by the more general wave

or physical optics theory.

Eq. (114) also implies that the radius of curvature of a ray must be much greater than a wavelength of radiation. Consider a ray passing from point A to point A' as shown in Fig. (5). Let the refractive index vary as a function of radial distance r from the center of the earth, and let $\rho$ be the radius of ray curvature between A and A'. Next consider a small wavefront increment AB which is normal to the ray at point A at time $t_o$. The wavefront arrives at A'B' when the time is $t_o + t$. Since the wavefront must travel from A to A' in the same amount of time t that it takes to travel from B to B', the arc lengths between the two paths may be written as

$$\sigma = vt \tag{117}$$

and

$$\sigma + d\sigma = (v + dv)t \tag{118}$$

where v is the phase velocity between A and A'. Thus the angle $\psi$ between the two wavefront positions becomes

$$\psi = \frac{\sigma}{\rho} = \frac{\sigma + d\sigma}{\rho + d\rho}$$

$$= \frac{vt}{\rho} = \frac{(v + dv)t}{\rho + d\rho} \tag{119}$$

or simply

$$\frac{d\rho}{\rho} = \frac{dv}{v} \tag{120}$$

Substituting

$$v = \frac{c}{n} \tag{121}$$

from Eq. (1) and

$$dv = -\frac{c}{n^2}\, dv \tag{122}$$

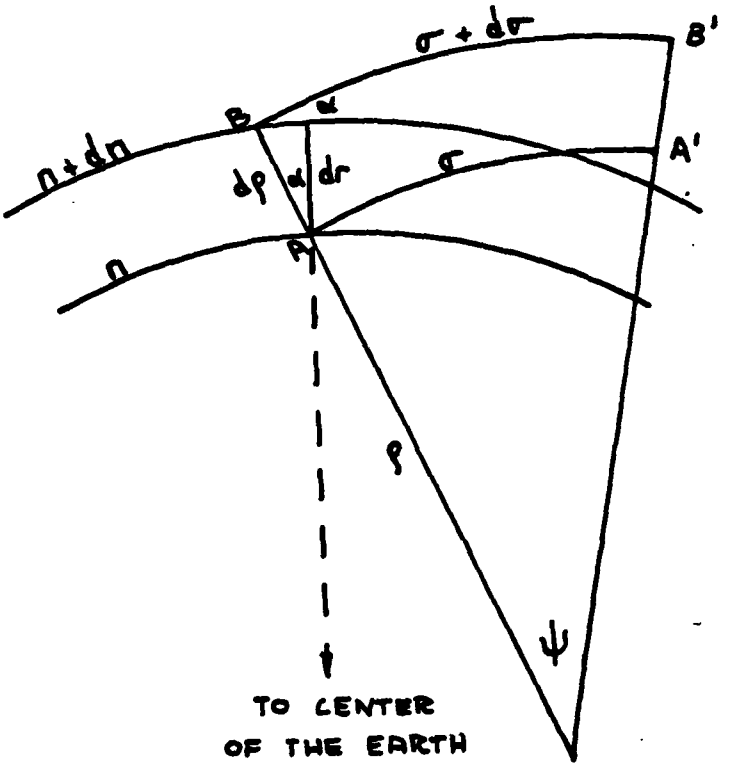


Fig. 5. Geometry for ray curvature in polar coordinates

into Eq. (120) gives

$$\frac{d\rho}{\rho} = -\frac{dn}{n} \tag{123}$$

From Fig. (5) it may be seen that the incremental radial displacement dr of the ray as measured from the center of the earth is approximately

$$dr = d\rho \cdot \cos\alpha \tag{124}$$

where $\alpha$ is the angle between the earth radius vector $\vec{r}$ and the wavefront. $\alpha$ is also the angle of ray elevation with respect to the local horizontal plane (i.e., the plane normal to $\vec{r}$) drawn at point A. Solving for $d\rho$ in Eq. (124) and substituting into Eq. (123) yields

$$\frac{1}{\rho} = -\frac{1}{n}\frac{dn}{dr}\cos\alpha \tag{125}$$

Since the refractive index is a function only of r, dn/dr may be replaced by $\nabla n$ so that

$$\frac{1}{\rho} = -\frac{\nabla n}{n} \cos \alpha \tag{126}$$

Thus the requirement of Eq. (114) that $\nabla n/n$ be small as compared to a wavelength of distance forces the radius of ray curvature in Eq. (126) to be large over the same distance. Furthermore, Eq. (126) clearly indicates that ray bending is dependent upon the relative change in the refractive index of the medium. For a ray to follow the curvature of the earth as in the case of wave trapping or ducting, Eq. (126) yields the condition

$$\nabla n = -\frac{1}{a} \tag{127}$$

where $\rho = a$ is the earth's radius, $n \approx 1$ for air, and $\alpha = 0$. In free space where $\nabla n = 0$, then

$$\rho = \infty \tag{128}$$

which enables the rays to travel in straight lines.

Returning to the second major condition of geometric optics, Eq. (99) indicates that J is directly proportional to the cross section dA of the ray bundle, thus implying that $J^{1/2}$ is related to the spacing between neighboring rays. Therefore Eq. (115) states that the fractional change in the spacing between neighboring rays over a wavelength of distance must also be small compared with unity. This condition is violated where rays either converge or diverge rapidly as is often the case along the edge of a reflected or refracted envelope of rays. Such a region, known as a caustic, is generally characterized by a ray density which increases steadily up to the edge of the ray envelope and then sharply decreases to zero beyond the envelope boundary. Furthermore, Eq. (115) is violated whenever the cross section of a ray pencil vanishes as it does

when the pencil emerges from a point source or passes through a focal point or caustic. Thus point source regions, focal points, and caustics must be excluded from any meaningful consideration in ray optics, although like discontinuities in the medium, they may be handled by wave theory.[1, 13, 15]

Finally, since ray curvature is affected only by the relative change in the refractive index and the angle of ray elevation in the medium, there is no mechanism within classical geometric optics to account for the phenomenon of wavefront diffraction around the edges, corners, or vertices of boundary surfaces. Modifications to the theory, which are generally referred to as the Geometrical Theory of Diffraction (GTD), have been made in recent years to overcome this deficiency.[30] While the GTD lies beyond the scope of the thesis, it is worth noting that this extension of ordinary ray optics is also based upon Fermat's principle and the equation of the eikonal in modified form.

# CHAPTER V

# COMPUTER SIMULATION DESCRIPTION

## General Characteristics

The previous discussion of refractivity and geometric optics theory provides a model of radio wave propagation through a non-ionized and time invariant atmospheric medium that is radially stratified with respect to the earth's center. The model follows the polar coordinate convention of Fig. (2), which assumes azimuthal symmetry in the atmosphere about the emitter. A computer program which uses this model was developed for the thesis to serve as an analytic tool in comparing the field calculated from ray theory, with available experimental data for an isotropic emitter. A description of the program and its algorithms is presented here, with specific details regarding program useage given in the Appendices.

Program ATREF (atmospheric refractivity) is written in Extended FORTRAN language for the CDC 6600 digital computer system. It requires approximately 65,000 octal words of memory and 15 seconds of central processor time for execution of a run. Output is provided by a standard 132 column line printer and an on-line CALCOMP plotter.

Given the following input in card image form:

a) Atmospheric refractivity versus altitude

b) Emitter parameters (frequency, polarization, pulse width, beam upper and lower angle limits, altitude)

c) Earth surface parameters (land or sea, surface height variation)

the program calculates the ray trajectories and the time of propagation along each ray path from Eqs. (61) and (64), respectively. The rays are launched in the vertical (i.e., elevation) plane with a 0.02 degree angular separation to ensure a reasonable ray density at long ranges. The program allows the rays to be launched within a beam whose total angular width is a maximum of one degree, although this beam width may be enlarged by increasing the array dimensions and thus the computer memory requirement.

The coordinates of distance along the earth's surface, height above the surface, and time of propagation (x, h, t) are stored for each ray at regular intervals of dx. These coordinates are then employed in an algorithm based upon Eq. (109) which computes the given emitter's relative power density and field strength, normalized to free space (vacuum) values. Each ray that intersects the earth is reflected in the specular direction and is assigned a complex scattering coefficient which is a function of the incidence angle, emitter frequency and polarization, terrain type, and surface roughness. The scattering coefficients of each ray are then entered into the power density and field calculations to model the attenuation and phase change of earth reflected signals.

The computer simulation provides the user the option to select any or all of the following items for output in either printed or plotted form, or both:

a) Profile of refractivity N versus altitude

b) Profile of the vertical gradient of N versus altitude

c) Ray trajectories (plotted only)

d) Relative field strength versus altitude and distance along the earth's surface

e) Relative power density versus altitude and distance along the

earth's surface.

The plotted output of options (d) and (e) shows the relative field strength (or power density) of the total $\vec{E}$ field in space, whereas the printed output permits a more detailed breakout of the total field and each of its components, as in the case of multipath interference where the field in space is the resultant of the fields from the main propagating wave plus a wave component which has been reflected from the earth. The program also prints the time difference of arrival between the main and multipath wavefronts (which is useful in some radar problems) and the number of wave components in the field strength and power density calculations.

## Refractivity Models

While the simulation is generally used with card input refractivity profiles, the user may select either of two reference refractivity models which are stored in the simulation. Both are based on the Central Radio Propagation Laboratory (CRPL) model given by Eq. (16). Since all calculations in the simulation are in the units of feet, the constants in Eq. (16) become

$$N_s = 313.0 \tag{129a}$$

$$c_e = 0.0000438 \text{ ft}^{-1} \tag{129b}$$

for the stored exponential refractivity model and

$$N_s = 0.0 \tag{130a}$$

$$c_e = 0.0 \text{ ft}^{-1} \tag{130b}$$

for the stored free space model. If the program is used with an input refractivity profile, a curve fit is made to Eqs. (16) and (129) to model atmospheric refractivity for altitudes which lie above the highest point

in the profile.

## Ray Algorithms

The simulation uses a standard fourth order Runge-Kutta integration algorithm to solve the ray trajectory and time of propagation equations given in Chapter III by Eqs. (61) and (64), respectively. The integration step size used in the Runge-Kutta algorithm is equal to one tenth the distance along the earth's surface that the user has specified for printing or plotting output data. For example, if the user wants data printed or plotted every X nautical miles, then the step size becomes X/10 nautical miles.

Eqs. (61) and (64) are written in state variable notation for numerical integration. Letting the ray altitude above mean sea level be given in state notation, then $h = h_1$, $dh/dx = h_1'$, and $d^2h/dx^2 = h_1'' = h_2'$. The second order differential equation of Eq. (61) becomes a pair of first order state equations which are given by

$$h_2' = \frac{a + h_1}{a^2}\left[2\left[\left(\frac{a}{a + h_1}\right) h_1'\right]^2 + (a + h_1)\frac{\partial}{\partial h_1}(\ln[n(h_1)]\left[\left[\left(\frac{a}{a + h_1}\right) h_1'\right]^2 + 1\right]^2 + 1\right] \quad (131)$$

and

$$h_1' = h_2 \quad (132)$$

where $n(h_1) = N(h_1)\cdot 10^{-6} + 1$ is described by either a piece-wise linear function connecting the input refractivity profile data points, or the stored function of Eq. (16). Similarly, Eq. (64) becomes

$$t_1' = \frac{1}{c}\, n(h_1)\left[(h_1')^2 + \left(\frac{a + h_1}{a}\right)^2\right]^{1/2} \quad (133)$$

where the values of $h_1$ and $h_1'$ are obtained from the integration of Eqs. (131) and (132).

## Power Density and Field Strength Algorithms

The calculation of the power density of a field is based upon Eq. (109) which states that the power density is directly related to the element of flux dudv bounded by a ray bundle through an incremental area dA on the wavefront surface. While Eq. (109) was developed for propagating plane waves, it is possible to arrive at the same result for spherical waves from an isotropic emitter by making plane wave approximations over small elements on the wavefront surface.

Let the volume element $d\gamma$ in Fig. (6) be bounded by surfaces $r = S_1$, $r = S_1 + dS$, $\epsilon = \epsilon_1$, $\epsilon = \epsilon_1 + d\epsilon$, $\nu = \nu_1$, and $\nu = \nu_1 + d\nu$, where $(r, \epsilon, \nu)$ is analogous to the spherical coordinate system $(r, \theta, \phi)$ centered at the emitter. If $d\epsilon$ and $d\nu$ are sufficiently small, then the spherical wavefront elements $S_1$ and $S_1 + dS$ may be approximated by plane wave elements. Following the development in Chapter IV, Eq. (109) may be written

$$d\epsilon d\nu = \vec{P}_{av} \cdot \hat{n}\, dA \tag{134}$$

where $d\epsilon d\nu$ is the element of energy flux of the time-averaged Poynting vector $\vec{P}_{av}$ at the wavefront surface dA.

The program calculates relative power density (i.e., normalized to the power density in free space with no earth surface present) by taking the ratio of $d\epsilon d\nu$ in the atmosphere to $d\epsilon_o d\nu_o$ in vacuum. Since the atmosphere generally has a refractive index gradient which varies with altitude, Eq. (126) predicts that the rays will have differing radii of curvature depending upon the local values of ray slope and $\nabla n/n$. This variation in ray curvature causes the rays to converge and diverge

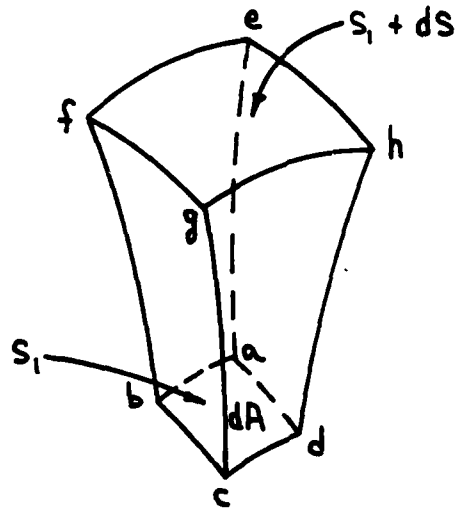


Fig. 6. The volume element $d\gamma$ bounded by rays and surfaces of constant phase for a spherical wavefront element radiated from an isotropic emitter at point 0. The face abcd lies on the surface $r = S_1$ and the face efgh lies on the surface $r = S_1 + dS$. Faces abfe and dcgh are portions of the surfaces $\epsilon = \epsilon_1$ and $\epsilon = \epsilon_1 + d\epsilon$, respectively. The remaining two faces adhe and bcgf lie on the surfaces $\nu = \nu_1$ and $\nu = \nu_1 + d\nu$, respectively.

throughout the atmosphere, resulting in $d\epsilon d\nu \neq d\epsilon_o d\nu_o$ for a given wavefront element dA. However since the atmosphere is assumed to have azimuthal symmetry about the emitter, then $\nabla n = 0$ in the $\nu$ direction, which yields $d\nu = d\nu_o$. Thus the surface element dA contributes to the flux ratio only in the $\hat{\epsilon}$ direction. Replacing dA with its projection dl along $\hat{\epsilon}$, the flux ratio then becomes

$$\frac{d\epsilon}{d\epsilon_o} = \frac{\vec{P}_{av} \cdot \hat{n} dl}{\vec{P}_{avo} \cdot \hat{n} dl} \tag{135}$$

Eq. (35) is solved by the following process, part of which has been adapted from a ray tracing program developed by the MITRE Corporation.[9] At regular intervals along the earth's surface, which are selected by the user, the simulation divides the altitude difference between the highest and lowest rays into 100 slightly overlapping vertical segments,

each of which is used to calculate the relative power density. Fig. (7) shows one such vertical (i.e., radial from the center of the earth at a distance x from the transmitter) segment whose length is $dl_v$. The angular subtense of the ray bundle which passes through $dl_v$ in free space is $d\epsilon_o$, while the subtense of the ray bundle through $dl_v$ in a refractive medium is $d\epsilon$. Stated differently, $d\epsilon_o$ and $d\epsilon$ represent the angular subtense of the element $dl_v$ as seen by the emitter at point 0 both in free space and in a refractive atmosphere, respectively.

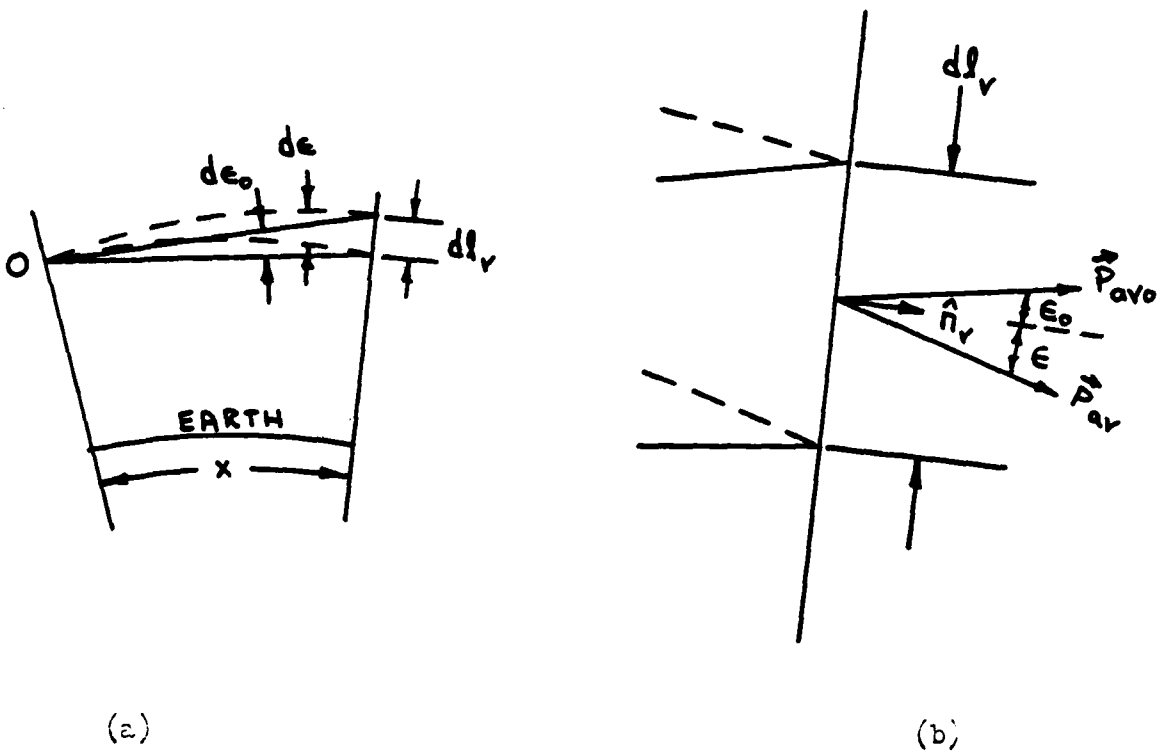


Fig. 7. The angular subtense of a line segment $dl_v$ at the emitter 0 as seen in free space and in a refractive atmosphere. Fig. (7a) shows $d\epsilon_o$ and $d\epsilon$ above a spherical earth surface, and Fig. (7b) gives an enlarged view at segment $dl_v$.

Replacing $\hat{n}dl$ in Eq. (135) with the line vector $\hat{n}_v dl_v$ gives the flux ratio as

$$\frac{d\epsilon}{d\epsilon_o} = \frac{\vec{P}_{av}\cdot\hat{n}_v dl_v}{\vec{P}_{avo}\cdot\hat{n}_v dl_v} = \frac{P_{av} dl_v \cos\epsilon}{P_{avo} dl_v \cos\epsilon_o} = \frac{P_{av}\cos\epsilon}{P_{avo}\cos\epsilon_o} \tag{136}$$

where $\hat{n}_v$ is the unit vector normal to $dl_v$ which defines the local horizontal reference axis, and $\epsilon_o$ and $\epsilon$ are the respective elevation angles of the Poynting vectors $\vec{P}_{avo}$ and $\vec{P}_{av}$ at $dl_v$. Solving Eq. (136) for the average relative power density gives

$$P_{avr} = \frac{P_{av}}{P_{avo}} = \frac{d\epsilon}{d\epsilon_o}\cdot\frac{\cos\epsilon_o}{\cos\epsilon} \tag{137}$$

The angles $d\epsilon_o$ and $\epsilon_o$ in Eq. (137) are obtained from the free space geometry of Fig. (8), where a is the radius of the earth, $h_o$ and h are the known respective altitudes above the earth's surface of the emitter and a given ray, $r_o$ and r are the radial distances to the emitter and ray ($r_o = a + h_o$ and $r = a + h$), x is the distance along the earth's surface, and $\theta = x/a$ is the angle subtended by x at the center of the earth. A right triangle is constructed having the sides b and c such that

$$b = r_o \tan\theta \tag{138}$$

and

$$c = \frac{r_o}{\cos\theta} \tag{139}$$

where side b forms the local horizontal reference axis at the emitter. The distance d between the ray and emitter is given by the law of cosines as

$$d = [r_o^2 + r^2 - 2rr_o\cos\theta]^{1/2} \tag{140}$$

Similarly

$$f = [b^2 + d^2 - 2bd\cos|\epsilon_{oi}|]^{1/2} = |c - r| \tag{141}$$

where $\epsilon_{oi}$ is the free space elevation angle of the ray with respect to horizontal at the emit ter (i.e., the initial or "launch" elevation angle at the emitter. Squaring both sides of Eq. (141) and solving for $|\epsilon_{oi}|$ gives

$$|\epsilon_{oi}| = \cos^{-1}\left[\frac{b^2 + d^2 - (c - r)^2}{2bd}\right] \tag{142}$$

where Fig. (8) indicates that $\epsilon_{oi}$ is negative for $c > r$ and positive for $r > c$.

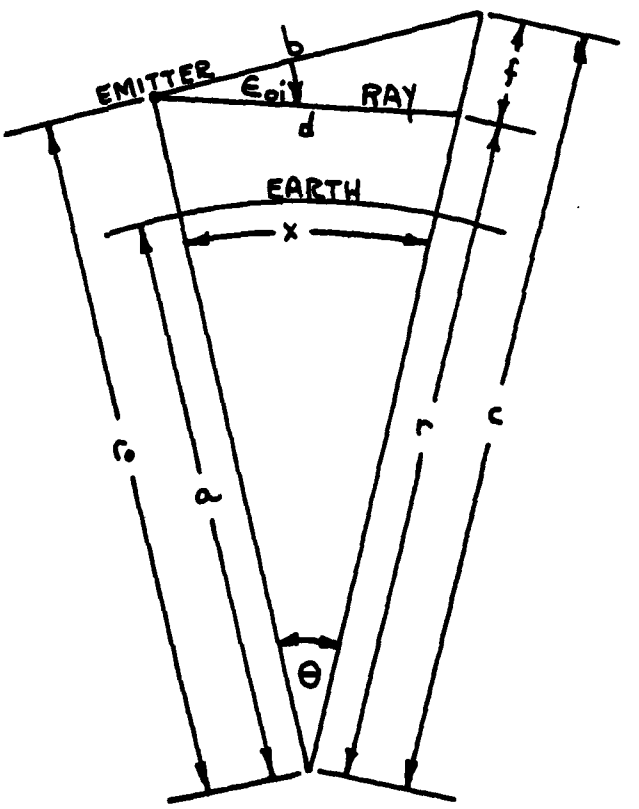


Fig. 8. Geometry for the free space ray elevation angle $\epsilon_{oi}$

The upper and lower ray angle limits $\epsilon_{Uo}$ and $\epsilon_{Lo}$ of the free space flux angle element $d\epsilon_o$ are calculated from Eq. (142) by alternately

setting $h = h_U$ and $h = h_L$, where $h_U$ and $h_L$ are the known upper and lower height limits of the vertical line segment $dl_v$ in Fig. (7). Thus

$$d\epsilon_o = \epsilon_{Uo} - \epsilon_{Lo} \tag{143}$$

The angle $\epsilon_o$ between $\vec{P}_{avo}$ and $\hat{n}_v$ is found by reversing the positions of the emitter and ray in Fig. (8) (i.e., by interchanging $h_o$ with h and $r_o$ with r), and replacing $\epsilon_{oi}$ with $\epsilon_o$. Since the waves within the flux angular element $d\epsilon_o$ are approximately plane, the Poynting vector $\vec{P}_{avo}$ in Fig. (7) points radially outward from the emitter and through the center of the wavefront surface element within $d\epsilon_o$. Thus setting $h = h_c$ in Eq. (142) where $h_c$ is the known height of the center of $dl_v$, yields

$$\epsilon_o = \cos^{-1}\left[\frac{b^2 + d^2 - (c - r_o)^2}{2bd}\right]^{1/2} \tag{144}$$

where b and c are given by Eqs. (138) and (139) with r replacing $r_o$, and d remaining unchanged. With the reversal of the emitter and ray positions in Fig. (8), the line b now lies in the direction of $\hat{n}_v$, while line d lies along $\vec{P}_{avo}$. Thus Eq. (144) gives the angle between the two vectors, both of which are pointing to the left in Fig. (8).

The problem of obtaining the flux angle increment $d\epsilon$ in Eq. (137) is different from that of finding $d\epsilon_o$, where the elevation angles are computed directly from the ray altitudes passing through the upper and lower limits of $dl_v$. Here a simple geometric transformation between altitude and ray angle is not possible since ray curvature is not easily modeled along each ray path. Instead a linear interpolation is made between the known initial elevation angles of the rays which pass through and on either side of the line segment $dl_v$.

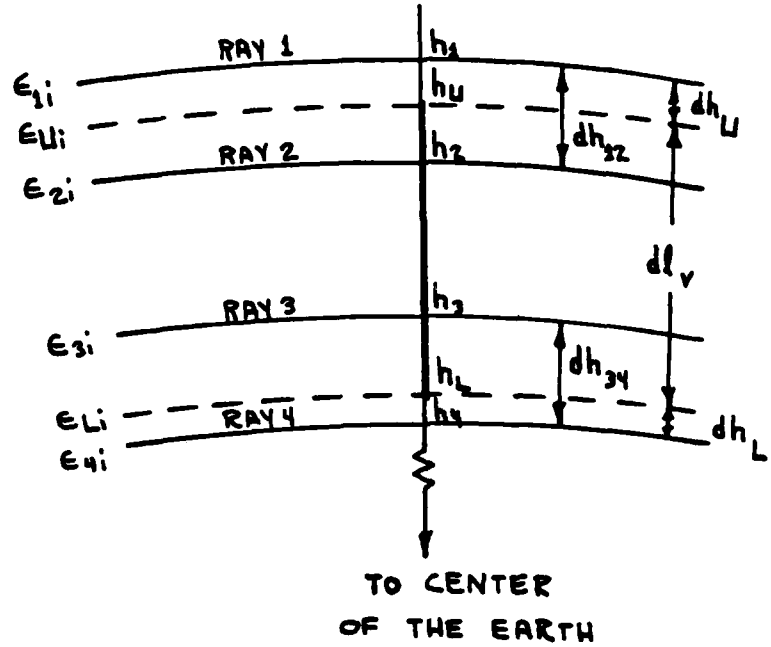


Fig. 9. Ray geometry at the vertical line segment $dl_v$ within a refractive atmosphere

Consider the set of four rays shown in Fig. (9) which have initial elevation angles of $\epsilon_{1i}$, $\epsilon_{2i}$, $\epsilon_{3i}$, and $\epsilon_{4i}$ at the emitter. The ray altitudes at the segment $dl_v$ are $h_1$, $h_2$, $h_3$, and $h_4$, and the local ray elevation angles are $\epsilon_1$, $\epsilon_2$, $\epsilon_3$, and $\epsilon_4$, respectively. The angles $\epsilon_{Ui}$ and $\epsilon_{Li}$ denote the launch angles of rays passing through the limits of $dl_v$ at heights $h_U$ and $h_L$. Both $\epsilon_{Ui}$ and $\epsilon_{Li}$ are approximated by linearly interpolating between the launch angles of the rays which lie immediately above and below $h_U$ (rays 1 and 2) and those which lie immediately above and below $h_L$ (rays 3 and 4), respectively. The interpolation uses the relative spacing between the rays and the line segment limits according to the relationships

$$\epsilon_{Ui} = \epsilon_{1i} - \Delta\epsilon \frac{dh_U}{dh_{12}}$$

$$= \epsilon_{1i} - \Delta\epsilon \frac{(h_1 - h_U)}{(h_1 - h_2)} \tag{145}$$

and

$$\epsilon_{Li} = \epsilon_{3i} - \Delta\epsilon \frac{dh_L}{dh_{34}}$$

$$= \epsilon_{3i} - \Delta\epsilon \frac{(h_3 - h_L)}{(h_3 - h_4)} \tag{146}$$

where $\Delta\epsilon$ (= 0.02 degree) is the equal angular separation between the initial ray elevation angles, and $dh_U/dh_{12}$ and $dh_L/dh_{34}$ are the fractional differences in altitude between the rays and the limits of $dl_v$. The flux angle for the refractive atmospheric medium is then computed from Eqs. (145) and (146) by

$$d\epsilon = \epsilon_{Ui} - \epsilon_{Li} \tag{147}$$

It should be noted that Eqs. (145) and (146) are valid regardless of the number of rays passing through $dl_v$ in Fig. (9). For instance if rays 2 and 3 were absent, the ratios for $\epsilon_{Ui}$ and $\epsilon_{Li}$ would be $\epsilon_{Ui} = \epsilon_{1i} - \Delta\epsilon(dh_U/dh_{14})$ and $\epsilon_{Li} = \epsilon_{1i} - \Delta\epsilon(dh_L/dh_{14})$ where $dh_U = h_1 - h_U$, $dh_L = h_1 - h_L$, and $dh_{14} = h_1 - h_4$. The presence of rays 2 and 3 merely adds to the accuracy of the interpolations in regions where the ray altitudes are not equally spaced.

Finally, the angle $\epsilon$ between $\vec{P}_{av}$ and $\hat{n}_v$ is obtained by taking the mean value of the angles $\epsilon_1$, $\epsilon_2$, $\epsilon_3$, and $\epsilon_4$, since the Poynting vector is again assumed to be pointing radially outward from the emitter along the direction of the rays and through the center of the flux element $d\epsilon$. That is, the mean elevation angle $\epsilon$ defines the elevation angle of $\vec{P}_{av}$ at the segment $dl_v$.

The elevation angle $\epsilon_{ray}$ of a ray in polar coordinates is obtained from Fig. (2), where

$$\tan \epsilon_{ray} = \frac{1}{r} \frac{dr}{d\theta} \tag{148}$$

Substituting $\rho = x/a$ from Eq. (60b) and solving Eq. (148) for $\epsilon_{ray}$ gives

$$\epsilon_{ray} = \tan^{-1}\left[\frac{a}{r}\frac{dr}{dx}\right] = \tan^{-1}\left[\frac{a}{a+h}\frac{dh}{dx}\right] \tag{149}$$

where h and dh/dx are solved in the computer program by integrating Eqs. (131) and (132) along the ray path. Using Eq. (149) to find the elevation angles of the rays at $dl_v$, the mean value of $\epsilon$ becomes

$$\epsilon = \frac{\epsilon_1 + \epsilon_2 + \epsilon_3 + \epsilon_4}{4} \tag{150}$$

which, like $d\epsilon$, improves in accuracy as the number of rays passing through $dl_v$ increases.

Eqs. (142) through (150) are used in the simulation to solve for the relative average power density in Eq. (137) for each of the 100 vertical line segments of length $dl_v$. Similarly, the program calculates the magnitude of the relative field strength by means of the relationship between power density and field strength shown in Eq. (105). Substituting Eqs. (2), (3), (4), and (105) (where $\epsilon$, $\epsilon_o$ and $\epsilon_r$ denote permittivities) into Eq. (137) gives

$$P_{avr} = n\frac{\left|\vec{E}\right|^2}{\left|\vec{E}_o\right|^2}$$

$$= n\left|\frac{E}{E_o}\right|^2 = \frac{d\epsilon}{d\epsilon_o}\cdot\frac{\cos\epsilon_o}{\cos\epsilon} \tag{151}$$

where n is the mean refractive index of air taken at the center of $dl_v$, and E and $E_o$ are the amplitudes of the electric field intensity vectors in the refractive atmosphere and in free space, respectively. Solving for $\left|E/E_o\right|$ gives

$$E_r = \left| \frac{E}{E_o} \right| = \left[ \frac{d\epsilon \cos\epsilon_o}{n\, d\epsilon_o \cos\epsilon} \right]^{1/2}$$

$$\approx \left[ \frac{d\epsilon \cos\epsilon_o}{d\epsilon_o \cos\epsilon} \right]^{1/2} \tag{152}$$

where $E_r$ is the magnitude of the relative field strength and $\sqrt{n} \approx 1$ in air.

If more than one wavefront from a given emitter arrives at $dl_v$ because of strong atmospheric refraction or reflection from the earth, the program computes the relative power density and field strength for the resultant field and for the field of each component wavefront at $dl_v$. Furthermore, if the emitter radiates pulsed rather than continuous waves (as in the case of most radars) the calculations for the resultant field include only those component waves whose pulses overlap in time with the pulses of the direct (line-of-sight) propagating wave. Since the optical path length, and hence the time of propagation, from the emitter to $dl_v$ is generally different for each component wave, this overlap will not extend over the full pulse width of the line-of-sight wave, given that the pulse widths of each wave are equal. Therefore all calculations for the resultant field at $dl_v$ denote maximum values of $P_{avr}$ and $E_r$ when all pulses overlap with the pulse of the line-of-sight wave.

Consider the case of M waves originating from the same emitter which arrive at the vertical line segment $dl_v$ at some time t. Let the emitter be linearly polarized so that the electric field of each wave will be polarized in the same direction (to eliminate elliptical and circular polarizations). Since Eqs. (151) and (152) apply to those field components whose Poynting vectors are perpendicular to $dl_v$, the

resultant or total field which is propagating normally to $dl_v$ may be written as

$$E_T e^{-j\theta_T} = \sum_{m=1}^{M} E_m e^{-j\theta_m} \tag{153}$$

where $E_m$ and $\theta_m$ are the amplitude and phase of each field component propagating normally to $dl_v$.

For the purpose of simulation, all field magnitudes and phases are represented by

$$E_m = \rho_m E_m' \tag{154}$$

and

$$\theta_m = \delta_m + \phi_m \tag{155}$$

where $\rho_m$ is the reflection coefficient of the earth's surface, $E_m'$ is the field strength due to atmospheric refraction, $\delta_m$ is the wavefront phase at $dl_v$, and $\phi_m$ is the phase shift due to reflection. The wavefront phase is computed from

$$\delta_m = kL_m - (k_o n)(ct_m) \tag{156}$$

where the optical path length $L_m$ between the emitter and $dl_v$ is obtained by multiplying the speed of light c in vacuum times the total wavefront propagation time $t_m$ as given by Eq. (133).

In the simulation $\rho_m = 1$ and $\phi_m = 0$ for each wavefront until it is reflected from the earth's surface, at which point $\rho_m$ and $\phi_m$ are calculated as functions of emitter frequency and polarization, terrain composition, surface roughness, and wave incidence angle at the ground. In the case of multiple reflections, both terms are altered accordingly, with $\rho_m$ equal to the product of the reflection coefficient magnitudes at each reflection point and $\phi_m$ equal to the sum of the

reflection phase shifts.

Taking the ratio of the total electric field in Eq. (153) to the free space electric field (without the earth's surface) gives the total relative field

$$E_{Tr}e^{-j\theta_{Tr}} = \frac{E_T e^{-j\theta_T}}{E_o e^{-j\theta_o}} = \sum_{m=1}^{M} \frac{\rho_m E_m' e^{-j(\delta_m + \phi_m)}}{E_o e^{-j\delta_o}} \tag{157}$$

where $\rho_o = 1$ and $\alpha_o = 0$ for the free space field. Substituting Eq. (152) for $E_m'/E_o$ in Eq. (157) gives

$$E_{Tr}e^{-j\theta_{Tr}} = \sum_{m=1}^{M} \left[ \rho_m \left[ \frac{d\epsilon_m \cos\epsilon_o}{d\epsilon_o \cos\epsilon_m} \right]^{1/2} e^{-j(\delta_m + \phi_m - \delta_o)} \right]$$

$$= \left[ \frac{\cos\epsilon_o}{d\epsilon_o} \right]^{1/2} \left[ e^{j\delta_o} \right] \sum_{m=1}^{M} \left[ \rho_m \left[ \frac{d\epsilon_m}{\cos\epsilon_m} \right]^{1/2} e^{-j(\delta_m + \phi_m)} \right] \tag{158}$$

Since $E_{Tr}$ is the magnitude of the total relative field at $dl_v$, the average relative power density may be found from Eq. (151) as

$$P_{Tavr} = n \left| E_{Tr} \right|^2 \approx E_{Tr}^2 \tag{159}$$

Eqs. (158) and (159), which are merely extensions of Eqs. (152) and (151), are used in the simulation for all relative field strength and power density calculations. The coefficients $\rho_m$, $\phi_m$ and $\delta_m$ for each reflected wave crossing $dl_v$ are found in much the same manner as the wave elevation angle $\epsilon$ in Eq. (150). Consider the rays from a reflected wavefront which pass through and on either side of $dl_v$ as shown in Fig. (9). Since the restriction of Eq. (115) in Chapter IV requires that adjacent rays be nearly parallel (i.e., the relative spacing between adjacent rays

must not change appreciably over a wavelength of distance), the rays through a small wavefront element may be expected to intersect the earth at approximately the same angle of incidence. Thus the wavefront reflection coefficients $\rho_m$ and $\phi_m$, which are dependent upon the angle of wave incidence, may be obtained by taking the mean of the reflection coefficients $\rho_{mp}$ and $\phi_{mp}$ which are calculated at the ray incidence angles. For the four rays in Fig. (9), the magnitude of the wavefront reflection coefficient $\rho_m$ becomes

$$\rho_m = \frac{\rho_{m1} + \rho_{m2} + \rho_{m3} + \rho_{m4}}{4} = \sum_{p=1}^{4} \frac{\rho_{mp}}{4} \tag{160}$$

with similar expressions existing for $\phi_m$ and the time of propagation $t_m$ used in Eq. (156) to obtain the phase $\delta_m$. The reflection model which computes the values of $\rho_{mp}$ and $\phi_{mp}$ is presented in the following section.

## Earth Reflection Model

Consider a uniform plane wave which is incident upon a plane boundary between two media as shown in Fig. (10). Let the incident wave be polarized so that its electric field vector is either parallel to or perpendicular to the plane of incidence (i.e., the plane containing the wave propagation vector $\vec{k}$ and the normal to the boundary). The ratio of the reflected to the incident field gives the reflection coefficient $\gamma$ which is derived in any standard electromagnetics text.[31, 32] For parallel polarization this becomes

$$\gamma_{par} = \left(\frac{E_r}{E_i}\right)_{par} = \frac{\eta_2 \cos \beta_2 - \eta_1 \cos \beta_1}{\eta_2 \cos \beta_2 + \eta_1 \cos \beta_1} \tag{161}$$

and for perpendicular polarization

$$\gamma_{perp} = \left(\frac{E_r}{E_i}\right)_{perp} = \frac{\eta_2 \sec\beta_2 - \eta_1 \sec\beta_1}{\eta_2 \sec\beta_2 + \eta_1 \sec\beta_1} \tag{162}$$

where $\eta$ is the intrinsic impedance of each medium, and $\beta$ denotes the angle of incidence and transmission for media 1 and 2 as shown in Fig. (10). For simple non-magnetic media the intrinsic impedance may be

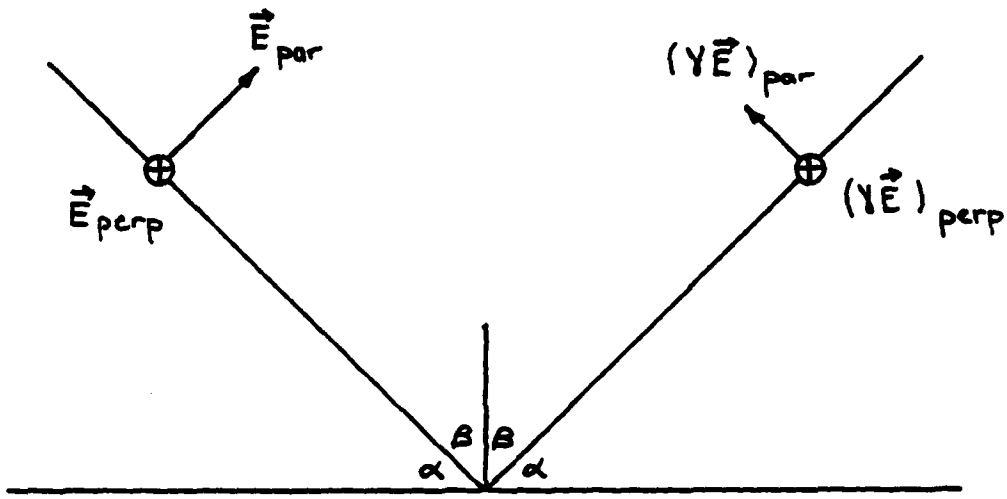


Fig. 10. Reflection of uniform plane waves at a plane boundary for parallel and perpendicular polarizations.

written as

$$\eta = \left[\frac{j\omega\mu}{\sigma + j\omega\epsilon}\right]^{1/2} \tag{163}$$

where $\mu$, $\epsilon$, and $\sigma$ are the permeability, permittivity, and conductivity of the medium, and are treated as real quantities. Note that $\epsilon$ is used here as a material property, rather than an angular quantity as in the preceding section.

For problems involving the reflection of a field from the surface of the earth, Eqs. (161) and (162) are frequently written in a form which is dependent only upon the angle of grazing incidence $\alpha_1$ where $\alpha_1 = \pi/2 - \beta_1$,

and the complex permittivity $\epsilon_c$ of the earth where $\epsilon$, which is also called the "a-c capacitivity" in some texts, is the real part of $\epsilon_c$. To derive these equations, which are known as Fresnel's equations for a smooth plane surface, it is necessary to give the relationships between the index of refraction, permittivity, and wave propagation constant of general non-magnetic media such as most land and sea surfaces of the earth. These relationships are analogous to Eqs. (4) and (68) for the nearly perfect dielectric medium of air.

In general both the permittivity and permeability of a medium are complex quantities. However for magnetically lossless media such as land and sea bodies, these quantities may be given by

$$\mu_c = \mu' - j\mu'' \approx \mu' = \mu_o\mu_r \approx \mu_o \tag{164a}$$

$$\epsilon_c = \epsilon' - j\epsilon'' = \epsilon_o\epsilon_r - j\epsilon'' = \epsilon - j\epsilon'' \tag{164b}$$

where the imaginary term $\epsilon''$ is the dielectric loss factor. Substituting Eqs. (164) into Eq. (4) gives the refractive index as

$$n = \frac{V_p}{c} = \left[\frac{\mu_o(\epsilon' - j\epsilon'')}{\mu_o\epsilon_o}\right]^{1/2} = \left[\frac{\epsilon' - j\epsilon''}{\epsilon_o}\right]^{1/2}$$

$$= \sqrt{\epsilon_c/\epsilon_o} = \sqrt{\epsilon_{cr}} \tag{165}$$

where $\epsilon_{cr}$ is the relative complex permittivity, or complex dielectric constant, and is merely the complex form of the relative permittivity $\epsilon_r$ or (real) dielectric constant of Eq. (4).

A similar relationship exists between the complex dielectric constant and the wave propagation constant of Eq. (68). Noting that the general form of the wave constant is given by

$$k = \sqrt{-j\omega\mu(\sigma + j\omega\epsilon)} \tag{166}$$

then taking the square of Eq. (70), solving for n, and substituting Eqs. (67), (164), (165), and (166) yields

$$\epsilon_{cr} = \frac{\epsilon_c}{\epsilon_o} = \left(\frac{k}{k_o}\right)^2 = \frac{\omega^2\mu_o\epsilon - j\omega\mu_o\sigma}{\omega^2\mu_o\epsilon_o}$$

$$= \frac{\epsilon - j\sigma/\omega}{\epsilon_o} = \frac{\epsilon' - j\epsilon''}{\epsilon_o} \tag{167}$$

where $\epsilon'' = \sigma/\omega$ . Eq. (167) is frequently expressed in mks units as

$$\epsilon_{cr} \approx \frac{\epsilon}{\epsilon_o} - j\ 60\ \lambda\sigma = \epsilon_{cr}' - j\epsilon_{cr}'' \tag{168}$$

where the wavelength $\lambda$ is in meters and the conductivity $\sigma$ is in mhos/meter.

Returning to the reflection coefficient for parallel polarized fields and letting the subscripts 1 and 2 denote the air and earth media in Eq. (161), the respective intrinsic impedances become

$$\eta_{air} = \eta_1 = \left[\frac{\mu_o}{\epsilon_1}\right]^{1/2} = \left[\frac{\mu_o}{\epsilon_o\epsilon_{r1}}\right]^{1/2} \tag{169}$$

since $\sigma_{air} = \sigma_1 \approx 0$, and

$$\eta_{earth} = \eta_2 = \left[\frac{j\omega\mu_o}{\sigma_2 + j\omega\epsilon_2}\right]^{1/2} \tag{170}$$

Applying Snell's law for plane dielectric media at the earth surface boundary and solving in terms of $\beta_2$ gives

$$\sin\beta_2 = \left(\frac{n_1}{n_2}\right)\sin\beta_1 \tag{171}$$

which may be rewritten as

$$\cos \beta_2 = \left[ 1 - \left(\frac{n_1}{n_2}\right)^2 \sin^2 \beta_1 \right]^{1/2} \tag{172}$$

Substituting Eqs. (4) and (165), for media 1 and 2 respectively, into Eq. (172) gives

$$\cos \beta_2 = \left[ 1 - \left(\frac{\epsilon_{r1}}{\epsilon_{cr2}}\right) \sin^2 \beta_1 \right]^{1/2} \tag{173}$$

Multiplying the numerator and denominator of Eq. (161) by $\eta_1/\eta_2^2$ gives the reflection coefficient for parallel polarized fields as

$$\gamma_{par} = \frac{(\eta_1/\eta_2) \cos \beta_2 - (\eta_1/\eta_2)^2 \cos \beta_1}{(\eta_1/\eta_2)\cos \beta_2 + (\eta_1/\eta_2)^2 \cos \beta_1} \tag{174}$$

Noting that the impedance ratio at the earth surface boundary is

$$\frac{\eta_1}{\eta_2} = \left[\frac{\mu_o}{\epsilon_o \epsilon_{r1}} \quad \frac{\sigma_2 + j\omega\epsilon_2}{j\omega\mu_o}\right]^{1/2}$$

$$= \left[\frac{1}{\epsilon_{r1}} \quad \frac{\epsilon_2 - j\sigma_2/\omega}{\epsilon_o}\right]^{1/2} = \sqrt{\epsilon_{cr2}/\epsilon_{r1}} \tag{175}$$

then substituting Eqs. (173) and (174) into Eq. (175) yields

$$\gamma_{par} = \frac{\left[\left(\frac{\epsilon_{cr2}}{\epsilon_{r1}}\right) - \sin^2 \beta_1\right]^{1/2} - \left(\frac{\epsilon_{cr2}}{\epsilon_{r1}}\right) \cos \beta_1}{\left[\left(\frac{\epsilon_{cr2}}{\epsilon_{r1}}\right) - \sin^2 \beta_1\right]^{1/2} + \left(\frac{\epsilon_{cr2}}{\epsilon_{r1}}\right) \cos \beta_1} \tag{176}$$

Following the same type of procedure for Eq. (162), the reflection coefficient for perpendicular polarized fields becomes

$$\gamma_{perp} = \frac{\cos \beta_1 - \left[\left(\frac{\epsilon_{cr2}}{\epsilon_{r1}}\right) - \sin^2 \beta_1\right]^{1/2}}{\cos \beta_1 + \left[\left(\frac{\epsilon_{cr2}}{\epsilon_{r1}}\right) - \sin^2 \beta_1\right]^{1/2}} \tag{177}$$

Table (1), which is taken from Kerr,[1] gives typical values of the real $\epsilon_{cr}'$ and imaginary $\epsilon_{cr}''$ terms of the complex dielectric constant for various water and soil types at several different frequencies. While these values are not intended to be a complete set of earth parameters, they do represent values obtained from a variety of sources which serve as a useful guide for the complex dielectric constant of earth surfaces.

TABLE 1

APPROXIMATE ELECTROMAGNETIC PROPERTIES OF SOIL AND WATER[1]

| Medium | $\lambda$ | $\sigma$ ohm/m | $\epsilon_{cr}'$ | $\epsilon_{cr}''$ |
|---|---|---|---|---|
| Sea water | 3 m | 4.3 | 80 | 774 |
| | 20 cm | 4.3 | 80 | 52 |
| $20^\circ$ - $25^\circ$ C | 10 cm | 6.5 | 69 | 39 |
| $28^\circ$ C | 3.2 cm | 16 | 65 | 30.7 |
| Distilled water, $23^\circ$ C | 3.2 cm | 12 | 67 | 23 |
| Fresh water lakes | 1 m | 0.001 | 80 | 0.06 |
| | 1 m | 0.01 | 80 | 0.60 |
| Very dry sandy loam | 9 cm | 0.03 | 2 | 1.62 |
| Very wet sandy loam | 9 cm | 0.6 | 24 | 32.4 |
| Very dry ground | 1 m | 0.0001 | 4 | 0.006 |
| Moist ground | 1 m | 0.01 | 30 | 0.6 |
| Arizona soil | 3.2 cm | 0.10 | 3.2 | 0.19 |
| Austin, Tex. soil, very dry | 3.2 cm | 0.0074 | 2.8 | 0.014 |

As Table (1) indicates, the properties of sea water ($\epsilon_{cr}'$ and $\sigma$) are independent of wavelength for wavelengths greater than 20 cm. Since $\epsilon_{cr}'' = \sigma/\omega\,\epsilon_o \approx 60\,\sigma\lambda$ from Eq. (168), then $\epsilon_{cr}''$ is found to vary only with wavelength and not sea conductivity. However at shorter wavelengths $\sigma$ is dependent on wavelength, which affects the value of $\epsilon_{cr}''$ as shown in Fig. (11). Furthermore, $\epsilon_{cr}'$ and $\sigma$ are highly dependent on temperature with $\epsilon_{cr}'$ decreasing and $\sigma$ increasing with higher temperatures. Further

evidence of the temperature dependence of $\epsilon_{cr}'$ and $\epsilon_{cr}''$ for sea and fresh water is given by Burrows and Attwood[33] and by Saxton.[34]

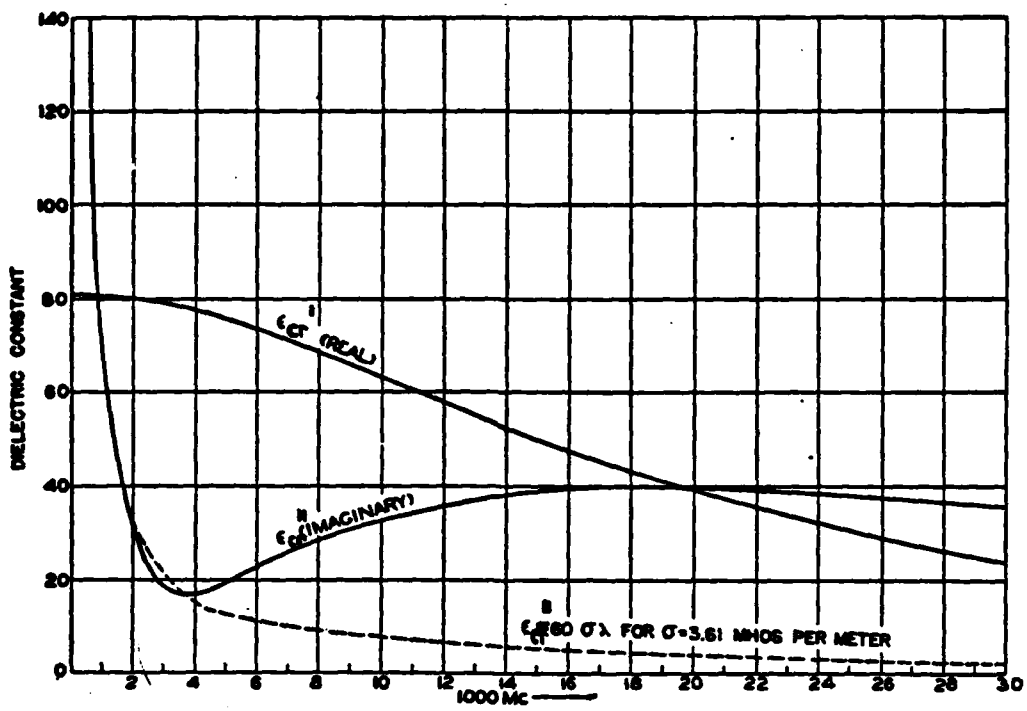


Fig. 11. Wavelength dependence of $\epsilon_{cr}'$ and $\epsilon_{cr}''$ for sea water at 17° C, from Burrows and Attwood.[33] The dotted line for $\epsilon_{cr}''$ is for a constant $\sigma = 3.61$ mho/m, while the solid $\epsilon_{cr}''$ curve results from the dependence of $\sigma$ on wavelength for wavelengths shorter than 20 cm.

For land surfaces both $\epsilon_{cr}'$ and $\sigma$ are much lower than for water, with the smaller values associated with dry, rocky, or sandy soil, and the higher values occurring with moist and rich soil. As Kerr points out in his discussion of the values in Table (1), the wide range in $\epsilon_{cr}'$ and $\sigma$ produces a considerable variation in $\epsilon_{cr}$ which in turn largely effects the reflection coefficient, especially for parallel polarization. On the other hand, the reflection coefficient for either polarization is not appreciably affected even if medium 1 is assumed to be free space ($\epsilon_{r1} = 1$), since the mean relative permittivity of air at sea level is

$$\epsilon_{r(air)} = \epsilon_{r1} = n_1^{\,2} = (1.00031)^2 \approx 1 \tag{178}$$

and $|\epsilon_{cr}| > 1$ for extremely dry soil and $|\epsilon_{cr}| \gg 1$ for all other soil and water surfaces in Table (1).

Frequently the coefficient of reflection is described in terms of the grazing incidence angle shown in Fig. (10) as $\alpha_1 = \pi/2 - \phi_1$, and the polarization of the electric field with respect to the earth's surface where the terms "vertical" and "horizontal" polarization are synonymous with parallel and perpendicular polarization. Taking note that $\epsilon_{r1} \approx 1$, Eqs. (176) and (177) may then be written as

$$\gamma_v = \rho_v e^{-j\phi_v} = \frac{[\epsilon_{cr2} - \cos^2 \alpha_1]^{1/2} - \epsilon_{cr2} \sin \alpha_1}{[\epsilon_{cr2} - \cos^2 \alpha_1]^{1/2} + \epsilon_{cr2} \sin \alpha_1} \tag{179}$$

and

$$\gamma_h = \rho_h e^{-j\phi_h} = \frac{\sin \alpha_1 - [\epsilon_{cr2} - \cos^2 \alpha_1]^{1/2}}{\sin \alpha_1 + [\epsilon_{cr2} - \cos^2 \alpha_1]^{1/2}} \tag{180}$$

where the subscripts v and h denote vertical (parallel) and horizontal (perpendicular) polarizations, and $\rho$ and $\phi$ are the magnitude and phase of the reflection coefficients.

Figs. (12) through (17), which are taken from Long[35] and Povejsil, Raven, and Waterman,[36] show the amplitude and phase of the Fresnel reflection coefficient of Eqs. (179) and (180) for both vertical and horizontal polarizations. Figs. (12) through (15) are for a smooth sea surface at $10^\circ$ C with $\epsilon_{cr}'$ and $\sigma$ having values comparable to those of Table (1). The most pronounced feature is the insensitivity of reflected horizontally polarized fields to grazing angle as compared to vertically polarized fields. For vertical polarizations, the reflection coefficient magnitude is at a minimum when $\phi_v = \pi/2$. The corresponding grazing

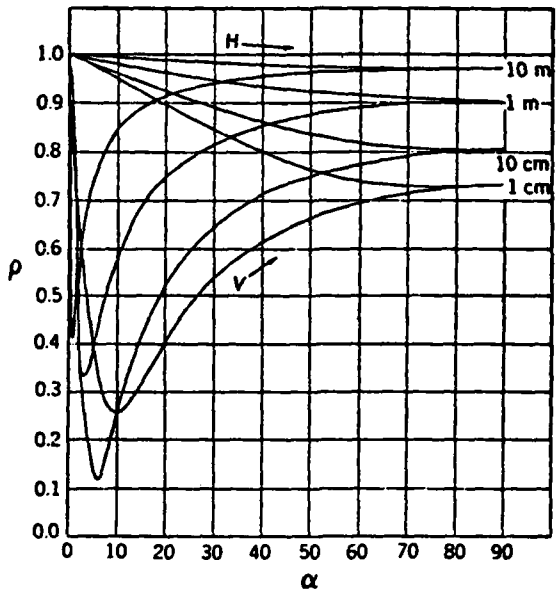


Fig. 12. Magnitude of the reflection coefficient as a function of incident grazing angle for a smooth sea at 10° C, from Long[35] and Povejsil, Raven, and Waterman.[36] Parameters on the curves refer to polarization and wavelength.

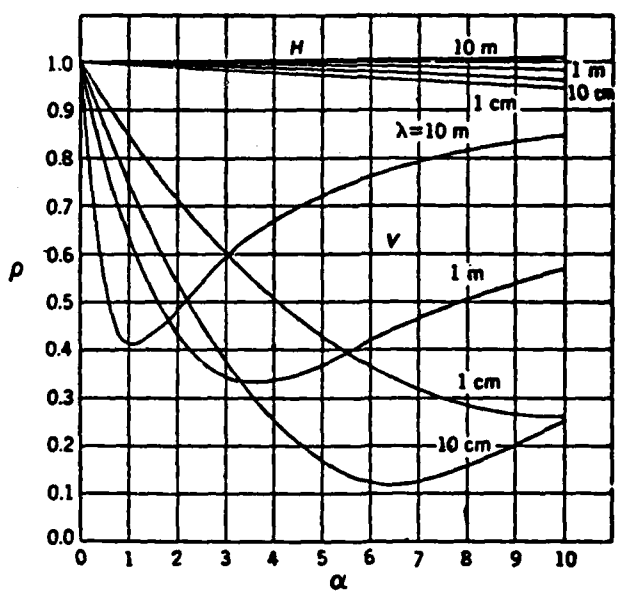


Fig. 13. Expanded plot of Fig. 12 for incident grazing angles between 0 and 10 degrees [35, 36]

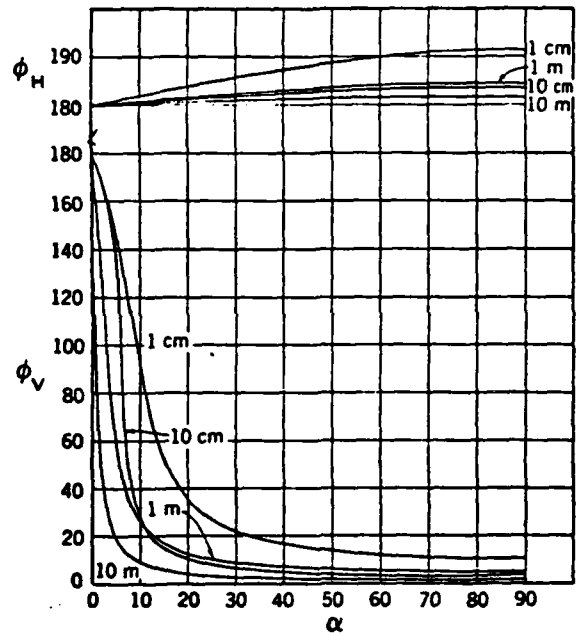


Fig. 14. Phase of the reflection coefficient as a function of incident grazing angle for a smooth sea at 10° C [35, 36]

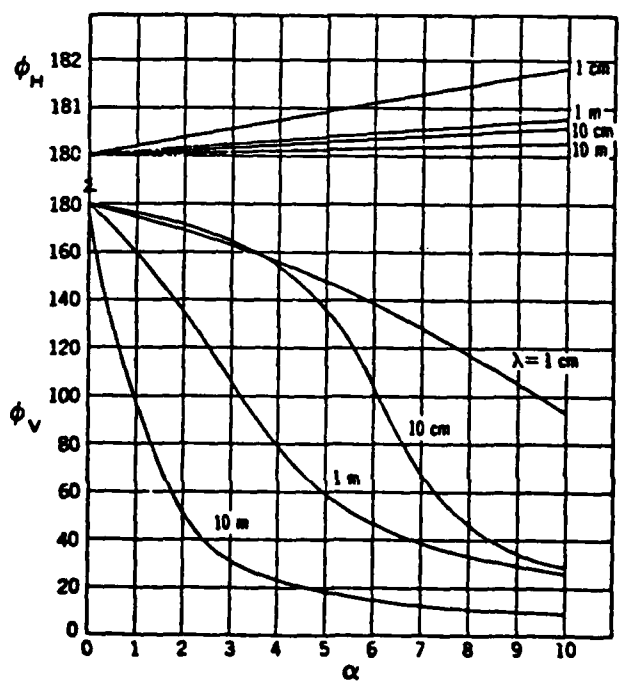


Fig. 15. Expanded plot of Fig. 14 for incident grazing angles between 0 and 10 degrees [35, 36]

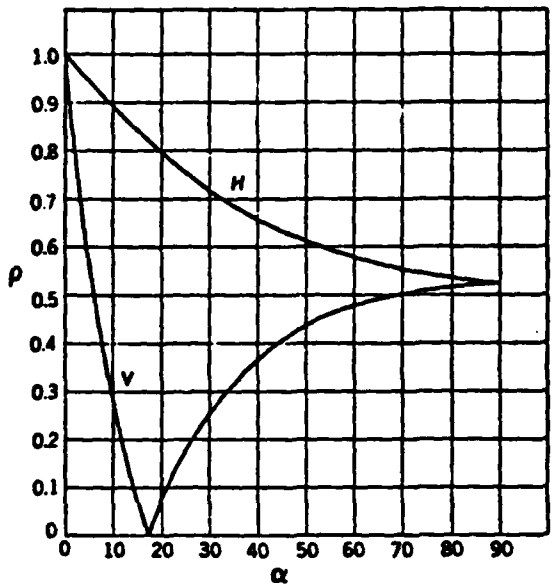


Fig. 16. Magnitude of the reflection coefficient as a function of incident grazing angle for smooth average land where $\epsilon'_{cr} = 10$ and $\sigma = .0016$ mho/m [35, 36]

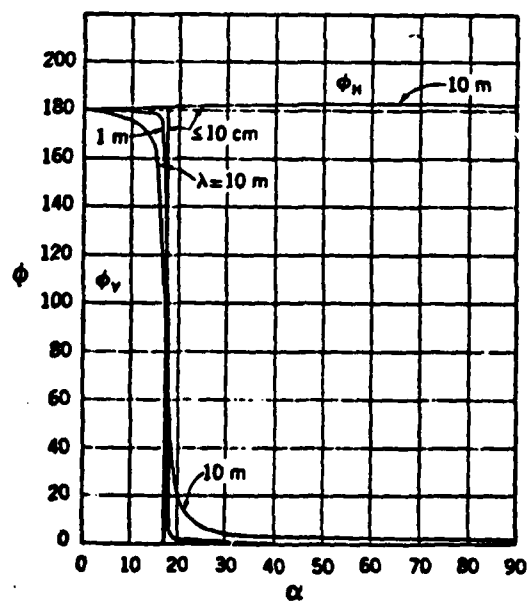


Fig. 17. Phase of the reflection coefficient as a function of incident grazing angle for smooth average land where $\epsilon'_{cr} = 10$ and $\sigma = .0016$ mho/m [35, 36]

angle $\alpha$ is known as Brewster's angle which represents the angle of incidence for which transmission into the sea is maximized. Since the impedance ratio of Eq. (175) is $\eta_1/\eta_2 = \sqrt{\epsilon_{cr2}/\epsilon_{r1}} \approx \sqrt{\epsilon_{cr2}}$ and since $|\epsilon_{cr2}| \gg 1$ for sea water, the impedance mismatch at the air and sea boundary will always result in wave reflections even at the Brewster angle.

As previously mentioned, the values of $\epsilon_{cr}'$ and $\sigma$ are much smaller for land surfaces than for sea or fresh water surfaces. Land is generally a better dielectric material than water and yields a considerably improved impedance match at the surface. This is evident in Figs. (16) and (17) where the values $\epsilon_{cr}' = 10$ and $\sigma = 0.0016$ mho/m are used. Fig. (16) shows that $\rho$ is nearly zero for vertically polarized fields incident on smooth average land at the Brewster angle. This contrasts with values of approximately $\rho = 0.1$ to $\rho = 0.4$ at the Brewster angle for smooth sea surfaces. Furthermore, the smaller value of $|\epsilon_{cr}|$ results in a general decrease in $\rho$ for both horizontal and vertical polarizations and a nearly instantaneous phase change at Brewster's angle for vertically polarized fields.

Since the earth's electrical properties vary so considerably, several surfaces are modeled in the simulation by using representative values of $\epsilon_{cr}'$ and $\sigma$ as shown in Table (2). The sea models are divided into three wavelength regions whereas the land models are relatively independent of wavelength but dependent upon the moisture content of the ground. All values are averages obtained from a number of sources and are therefore only approximate.[1, 33, 34, 36]

In reality, the Fresnel coefficients are of limited use in describing reflected fields since few earth surfaces may be regarded as being either plane or smooth. Consequently, a modification to Eqs. (179) and

TABLE 2

ELECTROMAGNETIC PROPERTIES
OF SOIL AND WATER MODELS

| Medium | $\lambda$ | $\sigma$ mho/m | $\epsilon_{cr}'$ |
|---|---|---|---|
| Sea water | 10 m - 20 cm | 4.3 | 80.0 |
| | 20 cm - 6 cm | 6.5 | 69.0 |
| | 6 cm - 1 cm | 16.0 | 65.0 |
| Wet ground | 10 m - 1 cm | .01 | 30.0 |
| Average ground | 10 m - 1 cm | .0016 | 10.0 |
| Dry ground | 10 m - 1 cm | .0001 | 4.0 |

(180) is required for most applications. Kerr,[1] Beckmann and Spizzichino,[17] and Barton[18] present such a theory which is summarized in the following discussion.

Reflection from any generalized surface is usually described in terms of specular and diffuse scattering, where "specular" scattering means that the angle of incidence equals the angle of reflection and "diffuse" scattering implies reflection in all other directions. However diffuse scattering is a highly complicated function of incidence angle, surface electrical properties, surface roughness, wavelength, and geometry. As such it does not lend itself to a simple expression which is valid for all angles and wavelengths, and therefore lies beyond the scope of this thesis. Specular reflection, on the other hand, is the dominant type in most applications and is also readily solvable.

The coefficient of specular reflection for the earth's surface is generally given by

$$\gamma = \rho e^{-j\phi} = \gamma_{v,h} DR = \rho_{v,h} DRe^{-j\phi_{v,h}} \tag{181}$$

where $\gamma_{v,h} = \rho_{v,h} e^{-j\phi_{v,h}}$ is the Fresnel coefficient for vertical and horizontal polarizations, D is a divergence factor which describes the reduction in reflection caused by the earth's curvature, and R is a

factor of surface roughness. D has values which range between 1 and 0 which, depending on the geometry between the emitter, earth, and receiver, correspond to the cases in which the earth may be regarded as flat or highly curved. The roughness factor R likewise ranges from 1 to 0 depending on whether the surface is perfectly smooth or extremely rough.

The geometric spreading of wavefronts due to reflection from a spherical earth surface is illustrated in Fig. (18). This wave divergence is already accounted for in the simulation since all ray trajectories are calculated in polar coordinates and are reflected from a spherical earth. Thus the total specular reflection coefficient used in the simulation becomes

$$\gamma = \rho e^{-j\phi} = \rho_{v,h} R e^{-j\phi_{v,h}} \tag{182}$$

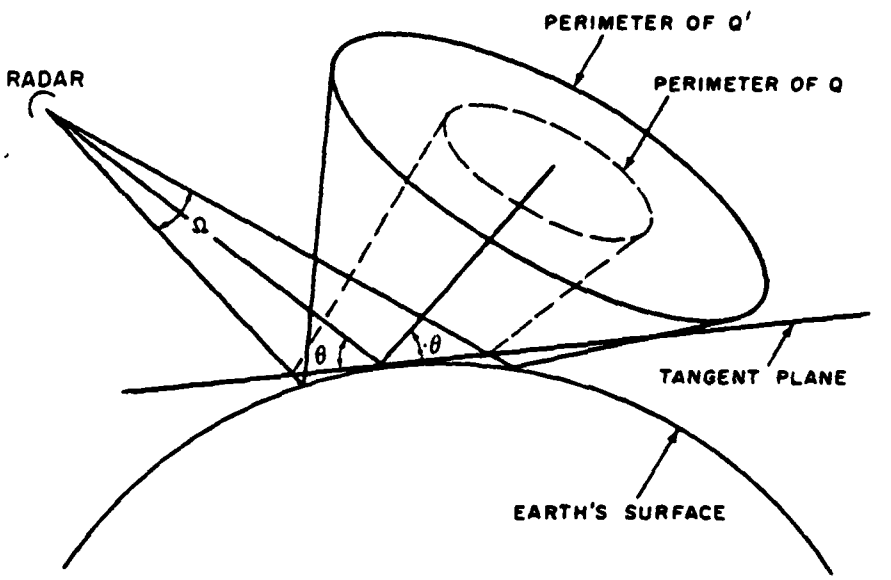


Fig. 18. Geometry of the divergence factor D, from Long.[35] The dotted perimeter Q represents the cone of rays having an initial angular separation of Ω which are reflected from a tangent plane at the center of the cone. The solid perimeter Q' shows the additional ray divergence due to reflection from the curved earth surface.

Unlike divergence, surface smoothness is considerably more difficult to quantify. In general a smooth surface is defined as one which satisfies the condition established by Lord Rayleigh given by[17, 35]

$$\delta h < \frac{1}{8} \frac{\lambda}{\sin\alpha} \tag{183}$$

where $\delta h$ is the height of surface irregularities, $\lambda$ is the wavelength, and $\alpha$ is the incident grazing angle between the ray and a plane surface representing the average of the surface irregularities. Some authors replace the factor 8 with 16 in Eq. (183) due to the difficulty of clearly defining smooth versus rough surfaces. Nonetheless, the Rayleigh criterion states that the variations in height must become smaller as wavelength decreases and grazing angle increases, for a surface to be considered smooth. For example, if $\lambda = 1$ m then $\delta h$ must be less than approximately 7.1 m at a grazing angle of 1 degree, and less than 1.4 m at a grazing angle of 5 degrees. If $\lambda = 1$ cm then the maximum values of $\delta h$ become 7.1 cm and 1.4 cm for grazing angles of 1 and 5 degrees respectively. Thus a calm sea might be expected to appear as more of a smooth surface than most land for wavelengths ranging from the radio spectrum to the microwave region.

In practice it is found that the earth's surface may usually be described in terms of a Gaussian distribution of surface heights about a local mean height.[17, 35, 37] Ament[38] and Beckmann and Spizzichino[17] have calculated the mean square value of the specular roughness factor R for a Gaussian surface (neglecting shadowing and sharp edge diffraction effects) as

$$< R^2 > = e^{-(\Delta\phi)^2} \tag{184}$$

$$\Delta\phi = \frac{4\pi\Delta h \cdot \sin\alpha}{\lambda} \tag{185}$$

where < > denotes the mean value of a function, $\Delta h$ is the standard deviation of the Gaussian distribution of heights, $\alpha$ is the incident grazing angle, and $\lambda$ is the wavelength of the incident field. Fig. (19) shows the relationship of $< R^2 >$ to $\Delta\phi$, with Eq. (184) plotted as a solid line and experimental data from sea and land surfaces (both plane and hilly conditions) represented by crosses. Spizzichino states that the correlation of $< R^2 >$ with $\Delta\phi$ is good considering that the reflection data were often given with little precision and the values used for $\Delta h$ were merely estimated.

Frequently land and sea surface profiles are reported only in terms of the largest observed height variations, rather than as a distribution of height measurements. The data in Tables (3) and (4),[35, 39] while representing surface descriptions that can be regarded as loosely quantitative at best, often provide the only basis available from which $\Delta h$ may be obtained. For example, the Douglas sea scale listed in Table (3) defines wave height as the average of the peak-to-trough heights of the one-third highest waves in a given observation. Even if the one-third highest waves are predominant, there is rarely any statistical measure established for smaller waves in most observations, thereby rendering an accurate measurement of $\Delta h$ impossible.

Similar difficulty exists in establishing $\Delta h$ for land surfaces where the irregularities easily become an order of magnitude greater than those of the roughest seas. Table (4) gives the average of the peak-to-mean height variations, or deviations from the mean, of the largest scale surface features for several types of terrain. Land roughness is often described in terms of the surface height deviation from the local mean

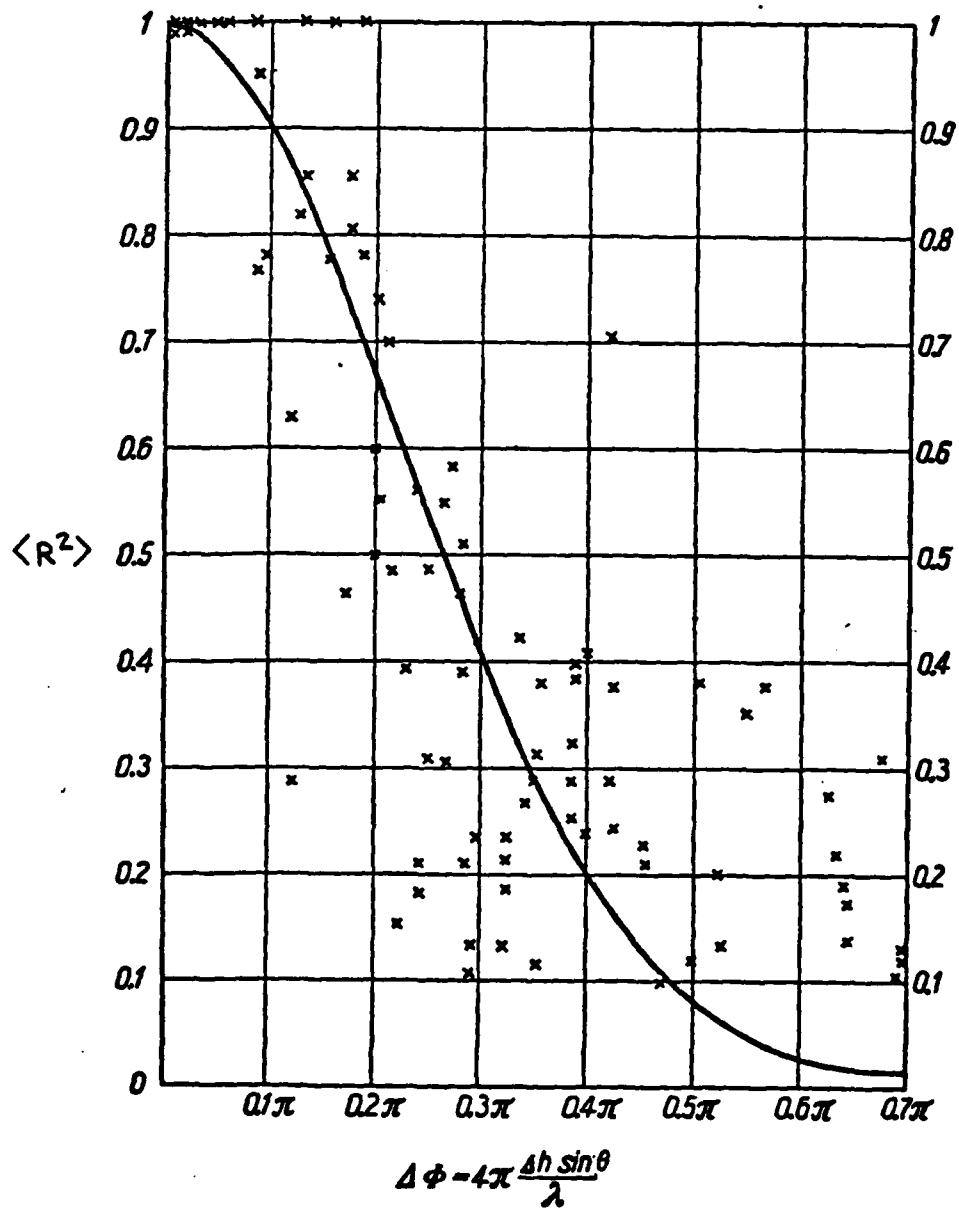


Fig. 19. Mean square $< R^2 >$ of the surface roughness factor R versus phase deviation $\Delta\phi$, from Beckmann and Spizzichino[17].

TABLE 3

SEA STATE AND WAVE HEIGHT[35]

| Douglas Sea State | Description | Peak-to-Trough Wave Height (feet) | Wave Height Deviation $\Delta h_m$ (feet) |
|---|---|---|---|
| 1 | Smooth | 0 - 1 | 0 - .5 |
| 2 | Slight | 1 - 3 | .5 - 1.5 |
| 3 | Moderate | 3 - 5 | 1.5 - 2.5 |
| 4 | Rough | 5 - 8 | 2.5 - 4.0 |
| 5 | Very rough | 8 - 12 | 4.0 - 6.0 |
| 6 | High | 12 - 20 | 6.0 - 10.0 |
| 7 | Very high | 20 - 40 | 10.0 - 20.0 |
| 8 | Precipitous | 40 - 60 | 20.0 - 30.0 |

TABLE 4

LAND SURFACE DEVIATIONS[39]

| Description | Surface Height Deviation $\Delta h_m$ (feet) |
|---|---|
| Very smooth plains | 0 - 20 |
| Smooth plains | 20 - 70 |
| Slightly rolling plains | 70 - 130 |
| Rolling plains | 130 - 260 |
| Hills | 260 - 500 |
| Mountains | 500 - 1000 |
| Rugged mountains | 1000 - 3000 |
| Extremely rugged mountains | 3000 and above |

surface altitude ($\Delta h_m = h - \langle h \rangle$) because of the asymmetrical nature of terrain irregularities.

Given that most earth surface profiles are approximately Gaussian, the data of Tables (3) and (4) may be interpreted as upper values of their respective height distributions. Bullington[40] and other authors[17, 37] suggest letting the maximum height deviation $\Delta h_M$ of a surface profile represent the amplitude of the surface irregularity which is exceeded less than 1 per cent of the time over the path between the emitter

and receiver. Using this criterion, the maximum surface deviations in Tables (3) and (4) will include 98 per cent of all height variations (49 per cent above and below the mean surface height).

It may be shown from any set of statistical tables that 98 per cent of all possible random variables having a standard normal or Gaussian distribution will be found within 2.33 standard deviations of the mean. Thus letting $\Delta h_M$ be the maximum surface deviation about the mean such that $\Delta h_M$ is exceeded less than 1 per cent of the time, then

$$\Delta h_M = h_M - \langle h \rangle = 2.33 \Delta h \tag{186}$$

where $h_M$ is the maximum surface height in any observation. Values of $\Delta h_M$ and $\Delta h$ used in the simulation are given in Tables (5) and (6), where $\Delta h_M$ is chosen as the maximum height deviation listed in Tables (3) and (4) for each surface description.

TABLE 5

STANDARD DEVIATION OF HEIGHTS FOR SEA SURFACES

| Douglas Sea State | Description | $\Delta h_M$ (feet) | $\Delta h$ (feet) |
|---|---|---|---|
| 1 | Smooth | .5 | .2 |
| 2 | Slight | 1.5 | .6 |
| 3 | Moderate | 2.5 | 1.1 |
| 4 | Rough | 4.0 | 1.7 |
| 5 | Very rough | 6.0 | 2.6 |
| 6 | High | 10.0 | 4.3 |
| 7 | Very high | 20.0 | 8.6 |
| 8 | Precipitous | 30.0 | 12.9 |

Combining Eqs. (179) through (186) and Tables (2), (5), and (6), the total specular reflection coefficient becomes

$$\gamma = \rho e^{-j\phi} = \rho_{v,h} R e^{-j\phi_{v,h}} = \rho_{v,h} \sqrt{\langle R^2 \rangle}\, e^{-j\phi_{v,h}}$$

$$= \rho_{v,h} \left[ e^{-(\Delta\phi)^2/2} \right] e^{-j\phi_{v,h}} \tag{187}$$

TABLE 6

STANDARD DEVIATION OF HEIGHTS FOR LAND SURFACES

| Description | $\Delta h_M$ (feet) | $\Delta h$ (feet) |
|---|---|---|
| Very smooth plains | 20 | 9 |
| Smooth plains | 70 | 30 |
| Slightly rolling plains | 130 | 56 |
| Rolling plains | 260 | 112 |
| Hills | 500 | 214 |
| Mountains | 1000 | 429 |
| Rugged mountains | 3000 | 1288 |
| Extremely rugged mountains | 5000 | 2146 |

where $R = R_{rms} = \sqrt{< R^2 >}$. Because of the assumed Gaussian nature of the surface profile, the Fresnel reflection phase $\phi_{v,h}$ is the only explicit term in Eq. (187) which contributes to a phase shift in the reflected field. While a given surface deviation will alternate the reflected field by an equal amount regardless of whether it lies above or below the mean surface height, the difference in path length, and hence the phase shift, between fields reflected from the mean and the surface variation will differ in sign according to whether the height deviation lies above or below the mean. Thus the phase changes due to equally sized surface deviations above and below the mean surface height will be equal but opposite in sign. Assuming a Gaussian surface therefore results in random phase shifts having a zero mean value which do not contribute to the phase of the total reflection coefficient of Eq. (187).

# CHAPTER VI

# RESULTS

## Introduction

In an examination of over-the-horizon radio propagation, Pappert and Goodhart[14] recently presented an excellent comparison of theoretical and experimental results for long range tropospheric propagation due to ducting conditions off the San Diego, California, coast. A ground based duct was analyzed by means of waveguide mode theory and field strength measurements at 65, 170, 520, and 3300 MHz using variable emitter and receiver heights, while an elevated, or earth detached, duct was studied at the single frequency of 3087.7 MHz.

The data presented by Pappert and Goodhart were used to point out the relative merits of using waveguide concepts to describe anomalous propagation. A similar comparison is made in this thesis to evaluate the ability of geometric optics to predict the field in a layered atmospheric structure such as a duct. However, validation of the thesis geometric optics model is restricted to the case studies of the ground based duct since Pappert and Goodhart presented results for the elevated duct that were limited to a single set of transmitter and receiver heights and only one frequency.

The presence of tropospheric ducts off the California coast is a well known phenomenon that is largely caused by strong temperature inversions ranging in height from near sea level to 4000 feet.[1, 23] The air below these inversions is usually moist and well mixed while the air

above is warmer and much drier. A rapid decrease in the refractive index, as indicated by Eq. (15), occurs in a thin layer between these two contrasting types of air, and results in the kind of ducting shown in the Guadalupe Island case studies.

The experimental data considered in this thesis were obtained from field strength measurements taken by the U. S. Naval Electronics Laboratory Center across a 280 nautical mile over-water path between San Diego and Guadalupe Island. A receiver located at heights of 100 and 500 ft above mean sea level at San Diego recorded the signal of a horizontally polarized airborne transmitter which was flown in and out of a ground based duct lying between these two locations.

The measured data, which are shown in Fig. (20) for the 100 ft receiver, are plotted as the received field strength normalized to the free space field (in decibels) versus transmitter height. These data, commonly referred to as height gain curves, are given at 20 naut mi intervals (measured along the surface of the earth) between the emitter and receiver. Also shown is the approximate flight path of the transmitter and the meteorological profiles of atmospheric refractivity. The distance from the San Diego receiver to the geometric horizon is given with each set of height gain curves to illustrate that the measured field results from over-the-horizon propagation due to tropospheric ducting.

Although the data in Fig. (20) were obtained in 1948, they represent some of the best case studies of field measurements and supporting meteorological data that are available today.[14] The meteorological profiles shown along the San Diego to Guadalupe Island path are recordings of the atmospheric refractive index structure given in B-units (Chapter II). These profiles are easily converted to the more conventional refractivity

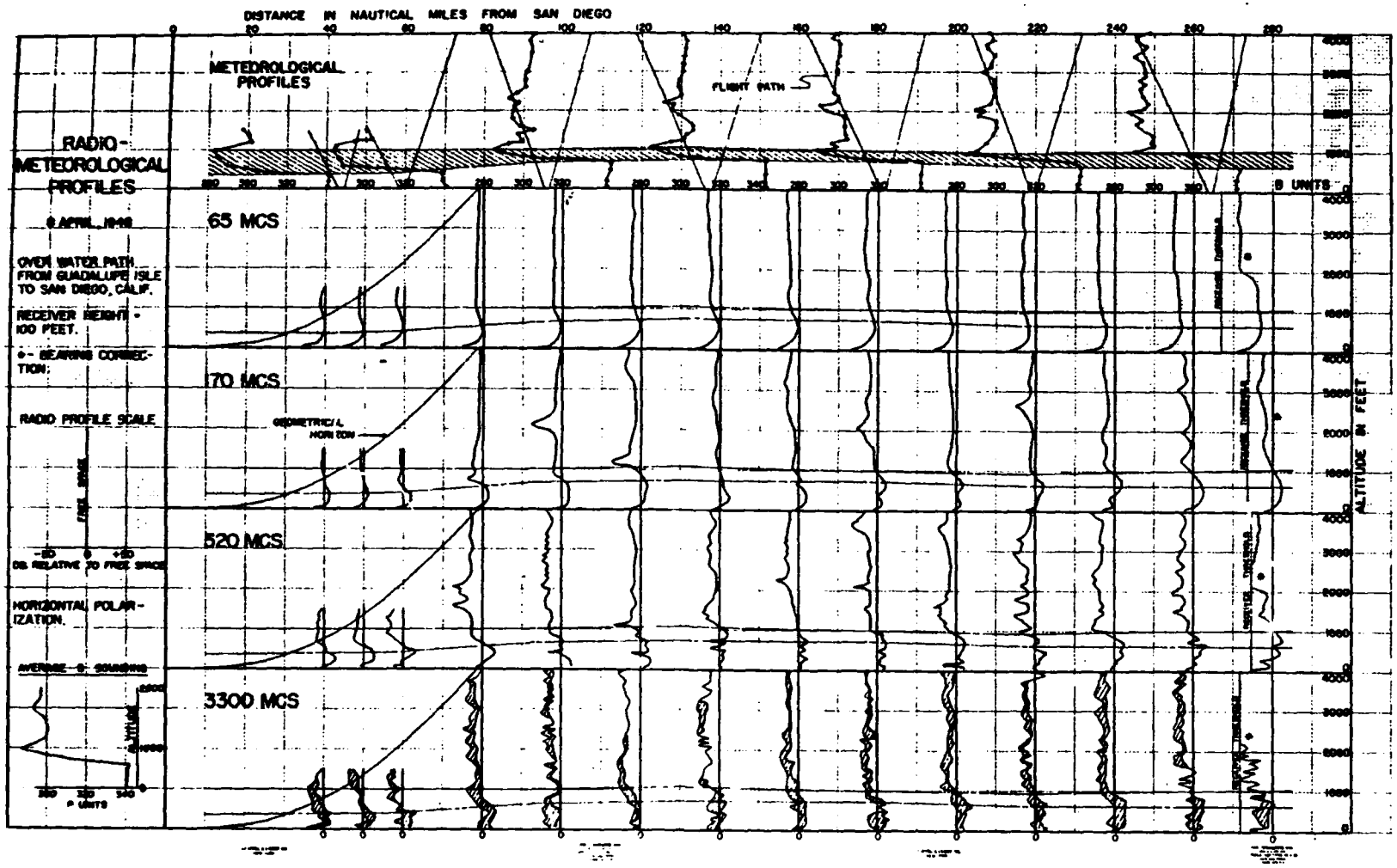


Fig. 20. Refractivity profiles and height gain curves for the Guadalupe Island ground based duct.

or N-units by combining Eqs. (7) and (8) to yield

$$N = B - \frac{h}{4a} \cdot 10^6 \tag{188}$$

An examination of Fig. (20) indicates that the layer structure varied temporally or spatially or both. None the less, a strong gradient of -22 B-units/1000 ft (-22 B-units/kft) or -232 N-units/kft exists from approximately 600 to 1000 ft in altitude, which exceeds the -47.85 N-units/kft (-157 N-units/km) criterion for ducting given by Eq. (10). An average B-profile, shown in the lower left hand corner of Fig. (20) and listed in Table (7), is used in the thesis simulation to represent the refractivity profile along the entire San Diego to Guadalupe Island path.

A trilinear approximation to the Guadalupe Island refractivity profile was similarly used in the waveguide computations of Pappert and Goodhart. The trilinear model, which was originally given in modified index or M-units, is converted to N-units by combining Eqs. (7) and (9) such that

$$N = M - \frac{h}{a} \cdot 10^6 \tag{189}$$

and is listed in Table (8). Both profiles are used in the simulation with the assumption that the atmospheric refractivity structure is reasonably stationary and homogeneous in the horizontal direction.

Comparisons of the two profile models and their N-gradients are given in Figs. (21) and (22). Both models have extremely large negative gradients from 600 to 1000 ft in height and positive gradients between 1000 and 1300 ft, which correspond respectively to superrefractive and subrefractive regions. It is this superrefractive layer and the sea surface which act as waveguide walls to trap horizontally traveling waves,

AD-A127 719 A GEOMETRIC OPTICS MODEL FOR CALCULATING THE FIELD STRENGTH OF ELECTROMAG..(U) AIR FORCE WRIGHT AERONAUTICAL LABS WRIGHT-PATTERSON AFB OH R P WASKY 2/3

UNCLASSIFIED DEC 77 F/G 20/14 NL

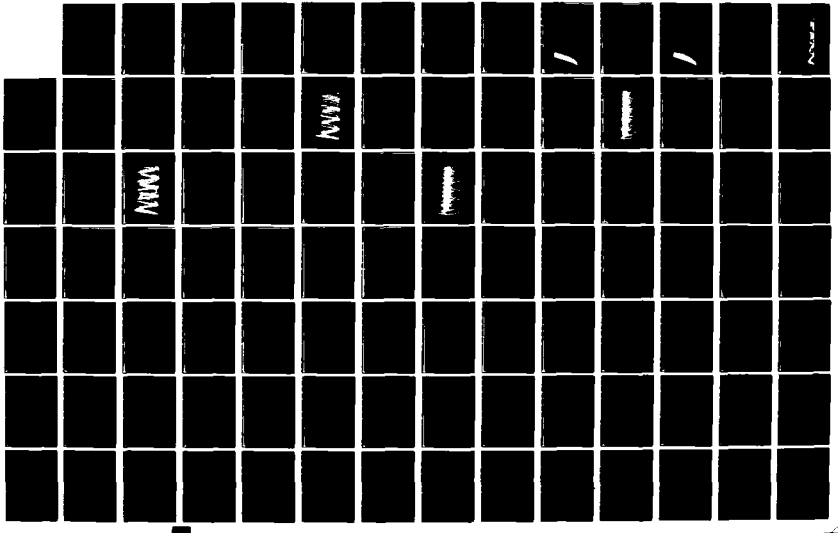

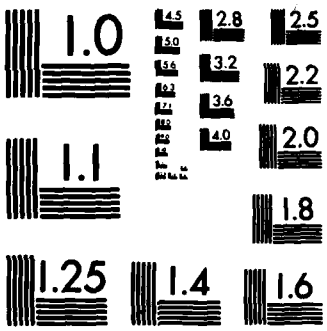


MICROCOPY RESOLUTION TEST CHART
NATIONAL BUREAU OF STANDARDS-1963-A

TABLE 7

ATMOSPHERIC REFRACTIVITY PROFILE FOR THE GUADALUPE ISLAND DUCT

| Height above mean sea level (ft) | Atmospheric Refractivity B-units | N-units |
|---|---|---|
| 0 | 341.0 | 341.0 |
| 100 | 341.0 | 338.8 |
| 200 | 341.0 | 337.6 |
| 400 | 341.0 | 336.2 |
| 600 | 342.0 | 334.8 |
| 700 | 320.0 | 311.6 |
| 800 | 305.0 | 295.4 |
| 900 | 296.0 | 285.2 |
| 1000 | 287.0 | 275.0 |
| 1100 | 294.0 | 280.8 |
| 1200 | 298.0 | 283.6 |
| 1300 | 300.0 | 284.4 |
| 1450 | 301.0 | 283.6 |
| 1600 | 300.0 | 280.8 |
| 1700 | 299.0 | 278.6 |
| 1800 | 298.0 | 276.4 |
| 1900 | 296.0 | 273.3 |
| 2000 | 293.0 | 269.1 |
| 2100 | 294.0 | 268.9 |
| 2200 | 296.0 | 269.7 |
| 2300 | 297.0 | 269.5 |
| 2500 | 297.0 | 267.1 |

TABLE 8

ATMOSPHERIC REFRACTIVITY PROFILE FOR THE TRILINEAR DUCT

| Height above mean sea level (ft) | Atmospheric Refractivity M-units | N-units |
|---|---|---|
| 0 | 341.0 | 341.0 |
| 600 | 365.0 | 336.3 |
| 1000 | 323.0 | 275.1 |
| 1300 | 349.0 | 286.8 |
| 2000 | 371.0 | 275.3 |

thus enabling wave propagation over the horizon. While the trilinear model is a good approximation of the Guadalupe Island duct, it underestimates the strong N-gradient existing from 800 to 1000 ft. Fortunately this difference is not crucial since both models, whose maximum gradients at this layer are -232 N-units/kft (Guadalupe Island) and -153 N-units/kft (trilinear), satisfy the -47.85 N-units/kft gradient required for ducting. A second layer, extending from 1900 to 2000 ft in the Guadalupe Island profile, is shown to be highly refractive (-42 N-units/kft) although there is no evidence in either the height gain curves of Fig. (20) or in the simulation results that this layer causes any significant trapping.

The theoretical calculations of Pappert and Goodhart are based upon the modal wave solution for a planar waveguide as developed by Budden.[14, 16] In this solution the transverse electric (TE) wave propagating in a trilinear medium, such as the one in Fig. (21), is obtained from the plane wave reflection coefficients at the boundaries of the medium. The reflection coefficients are given as functions of the eigenvalues of the incident grazing angle for each propagating mode at the medium boundaries. Each reflection coefficient is then expressed in terms of modified Hankel functions of order one third and their derivatives. Entering into these coefficients are the Fresnel reflection coefficient and surface roughness factor given by Eqs. (170) through (185). In all of their calculations Pappert and Goodhart use a surface height standard deviation ($\Delta h$) of 1 ft, which corresponds to a sea state of 3 in Table (5). Furthermore, the waveguide calculations require the solution of from one to a hundred modes depending on the height of the ducting layer, the frequency, and the emitter location within the ducting layer.

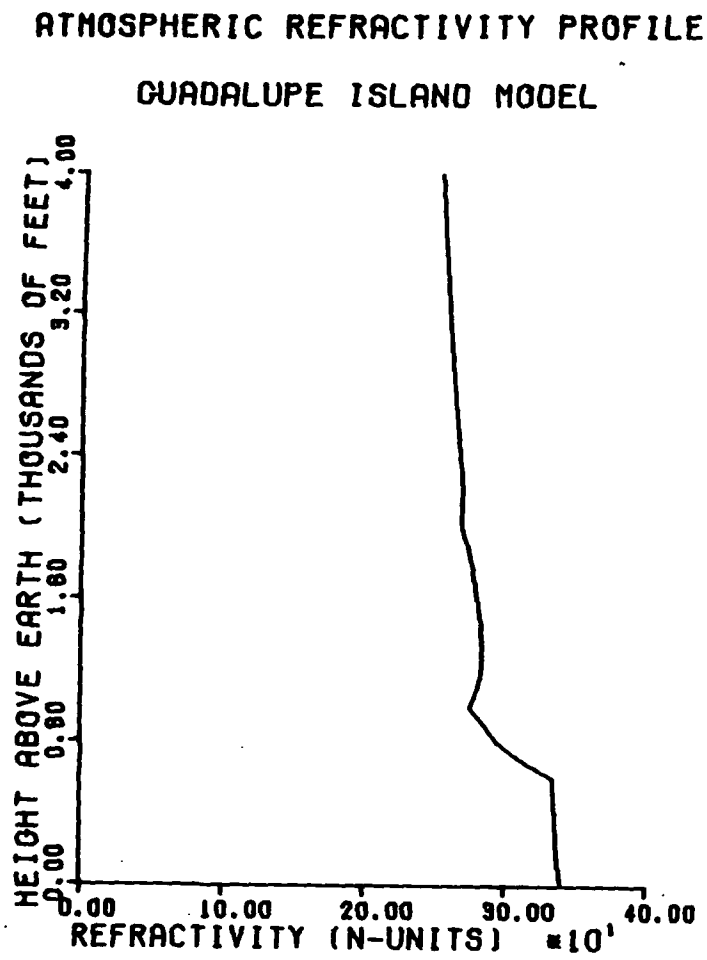


(a)

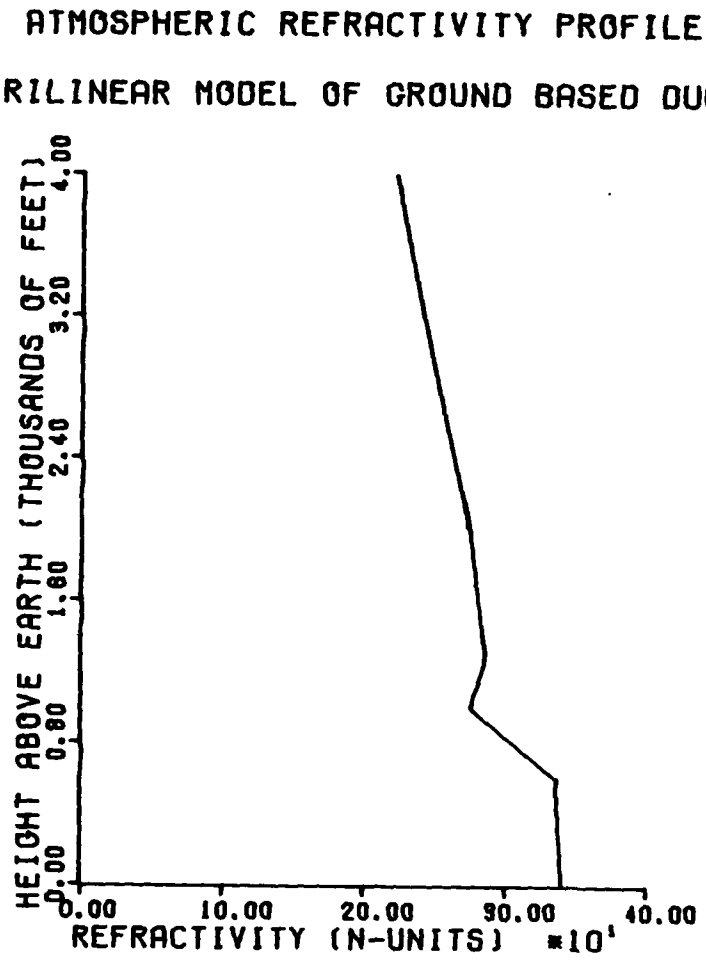


(b)

Fig. 21. Comparison of atmospheric refractivity profiles

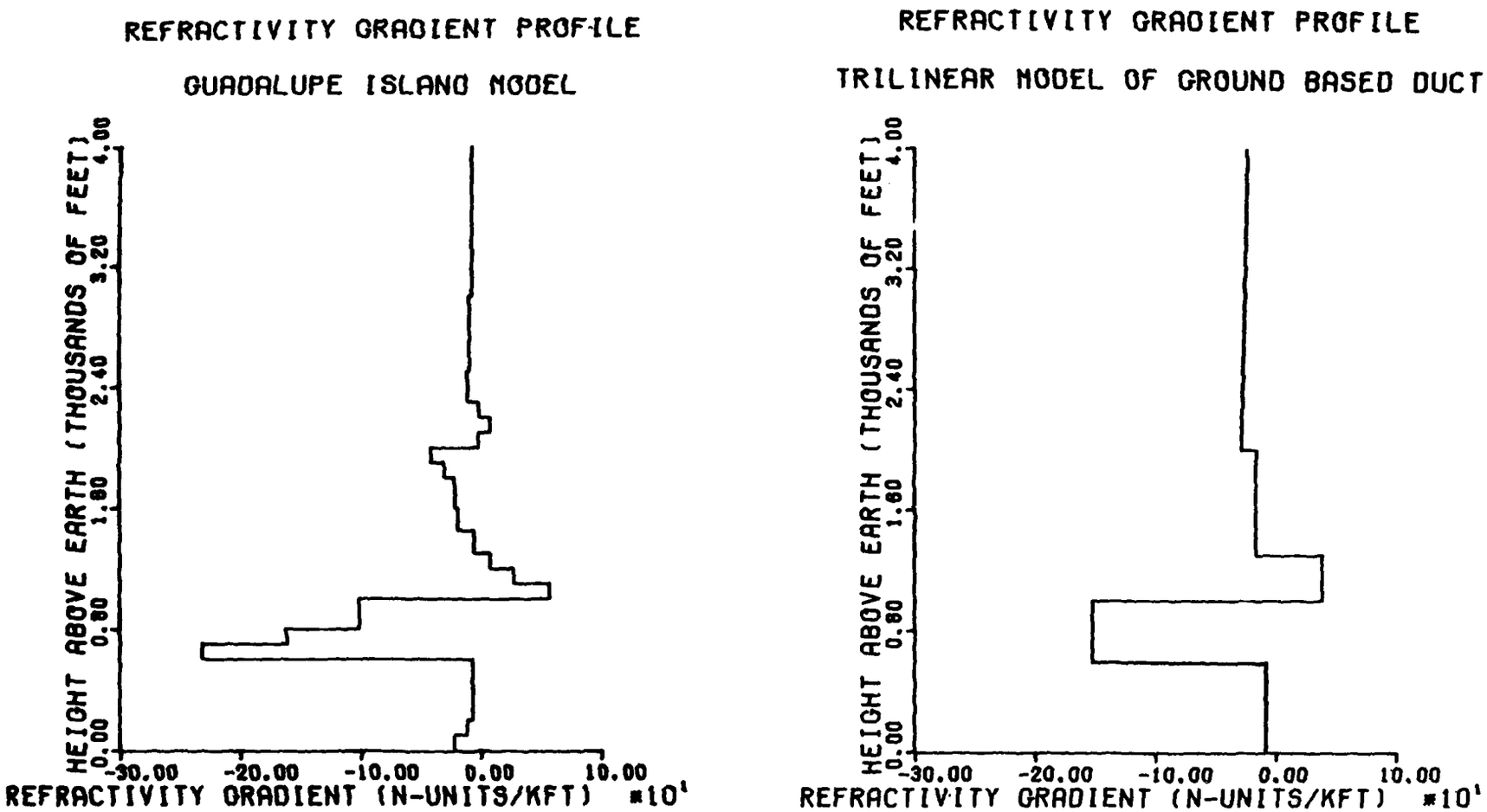


(a) (b)

Fig. 22. Comparison of atmospheric refractivity gradient profiles

## Simulation Results

Results obtained from the geometric optics computer simulation described in Chapter V are presented in this section for both the Guadalupe Island and trilinear ground based duct refractivity profiles. A moderate sea surface (sea state 3) is used to approximate the surface model used by Pappert and Goodhart. A perfectly smooth sea could have been assumed, however, since the surface roughness factor of Eq. (184) is very nearly unity (0.959) at the highest frequency (3300 MHz) and largest grazing angle (0.359 deg) encountered in this study. The emitter characteristics are the same as for the Guadalupe Island measurements, namely a horizontally polarized radiating pattern at 65, 170, 520, and 3300 MHz.

Since the atmosphere is considered to be a linear and isotropic medium, the theorem of reciprocity may be applied.[31] Reciprocity states that for a linear and isotropic medium the transmitter and receiver may be interchanged without affecting the response of either. Thus the transmitter and receiver positions are reversed in the simulation with the emitter located at 100 and 500 ft altitudes and the receiver moving vertically into and out of the duct along the flight profile of Fig. (20).

Before examining the simulation results for propagation within a ground based duct, consider the case of an isotropic emitter in free space (vacuum) which is at a height $h_o$ of 100 ft above mean sea level. Fig. (23) shows the refractivity and refractivity gradient profiles of free space, which are of course zero since the index of refraction n in Eq. (7) is unity throughout free space.

Ray trajectories, which are computed by the simulation and shown in Fig. (24), are launched from the emitter at 0.02 deg increments between the angles of +0.50 and -0.50 deg in elevation. This ray density of 50

rays/deg resulted from an investigation during the early development of the simulation which indicated that the field strength calculations, while being highly sensitive to ray spacings greater than 0.05 deg, tended to converge rapidly for spacings of 0.035 or less. A ray separation of 0.02 deg was then selected to ensure the accuracy and consistency of the simulation field strength results.

The rays in Fig. (24) are shown with an artificial upward curvature that results from plotting the earth's surface along a linear rather than a curved axis. This curvature is actually 1/a where a is the mean radius of the earth. If the rays were drawn in a spherical coordinate system they would be correctly shown to be straight lines. The choice of a rectangular coordinate system was made, however, for ease of comparison between simulation results, waveguide calculations, and the Guadalupe Island measurements of Fig. (20). Another point to be made is that the rays appear to be traveling upward at a rapid rate because of the enormous scale compression along the abscissa (approximately 228 times that of the ordinate axis).

The ray shown farthest to the right in Fig. (24) defines the geometric horizon seen by the transmitter. For an emitter in free space whose altitude is 100 ft, the horizon appears 0.18 deg below the local horizontal at the transmitter, given that the earth's surface is perfectly smooth. Rays launched below this angle will be reflected from the earth as shown in the ray trace figure.

Figs. (25) and (26) show the refractivity profiles and ray trajectories for the same emitter using the standard C.R.P.L. exponential atmosphere given by Eqs. (17) and (129). A comparison of Figs. (24) and (26) shows that the negative N-gradient of the exponential atmosphere (-13.65

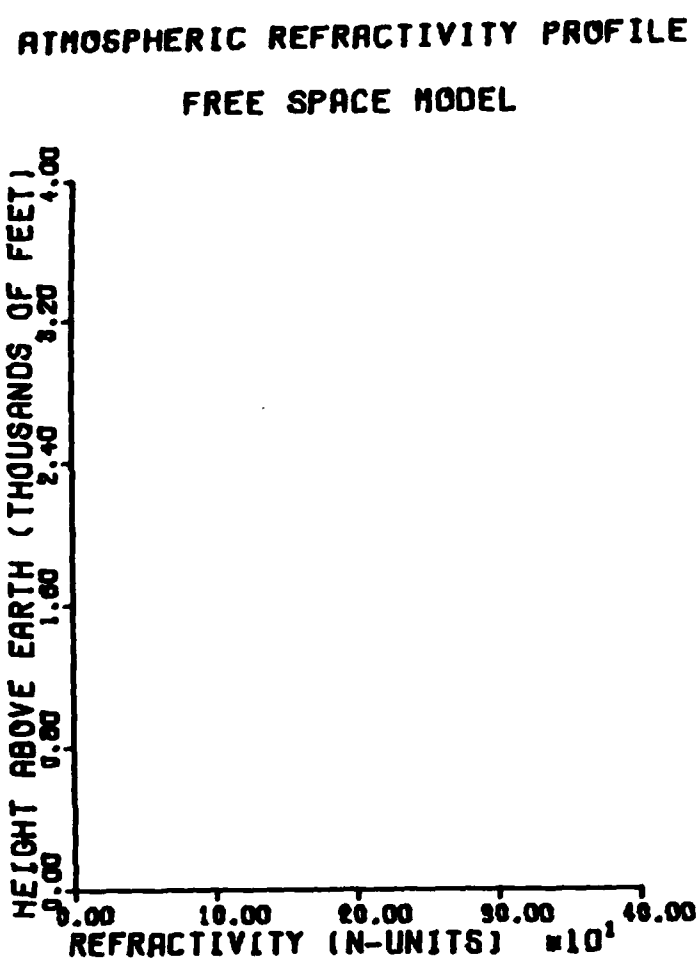


(a)

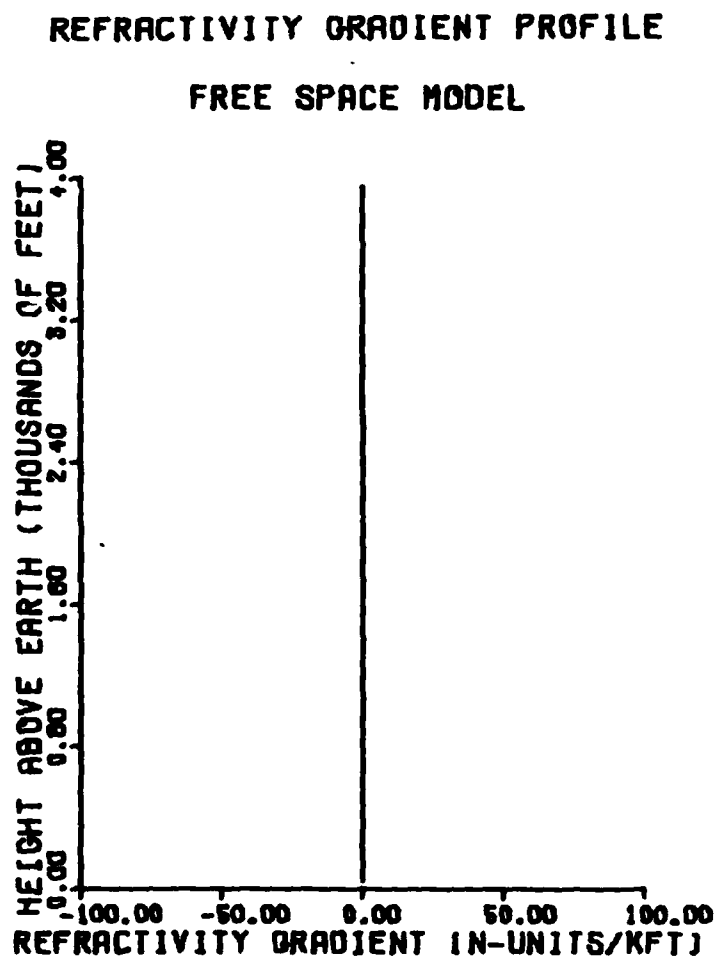


(b)

Fig. 23. N and dN/dh profiles for free space

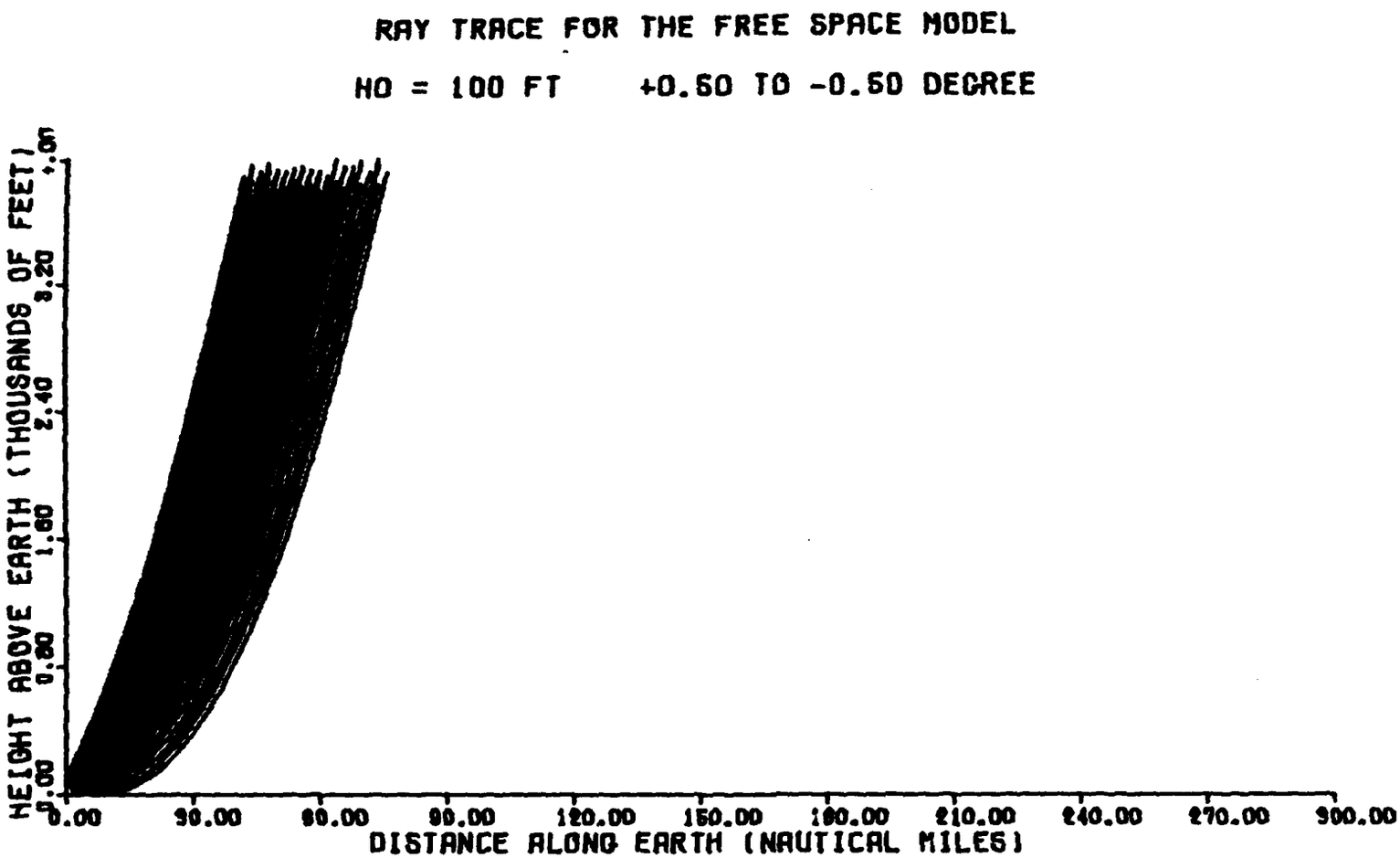


Fig. 24. Ray trace for a 100 ft high emitter in free space

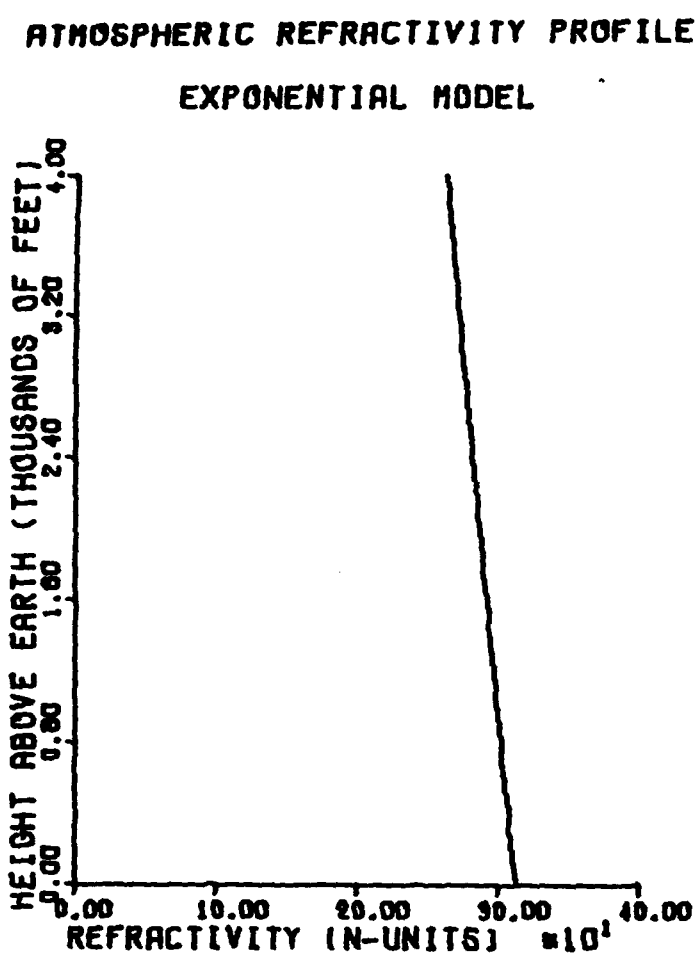


(a)

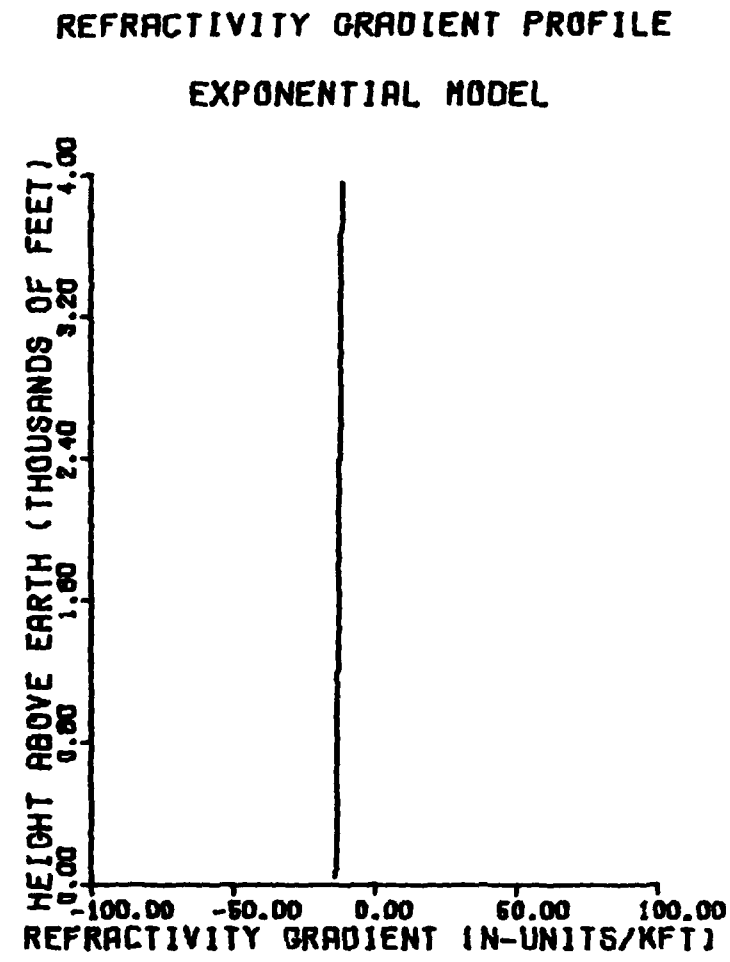


(b)

Fig. 25. N and dN/dh profiles for the CNPL exponential atmosphere model

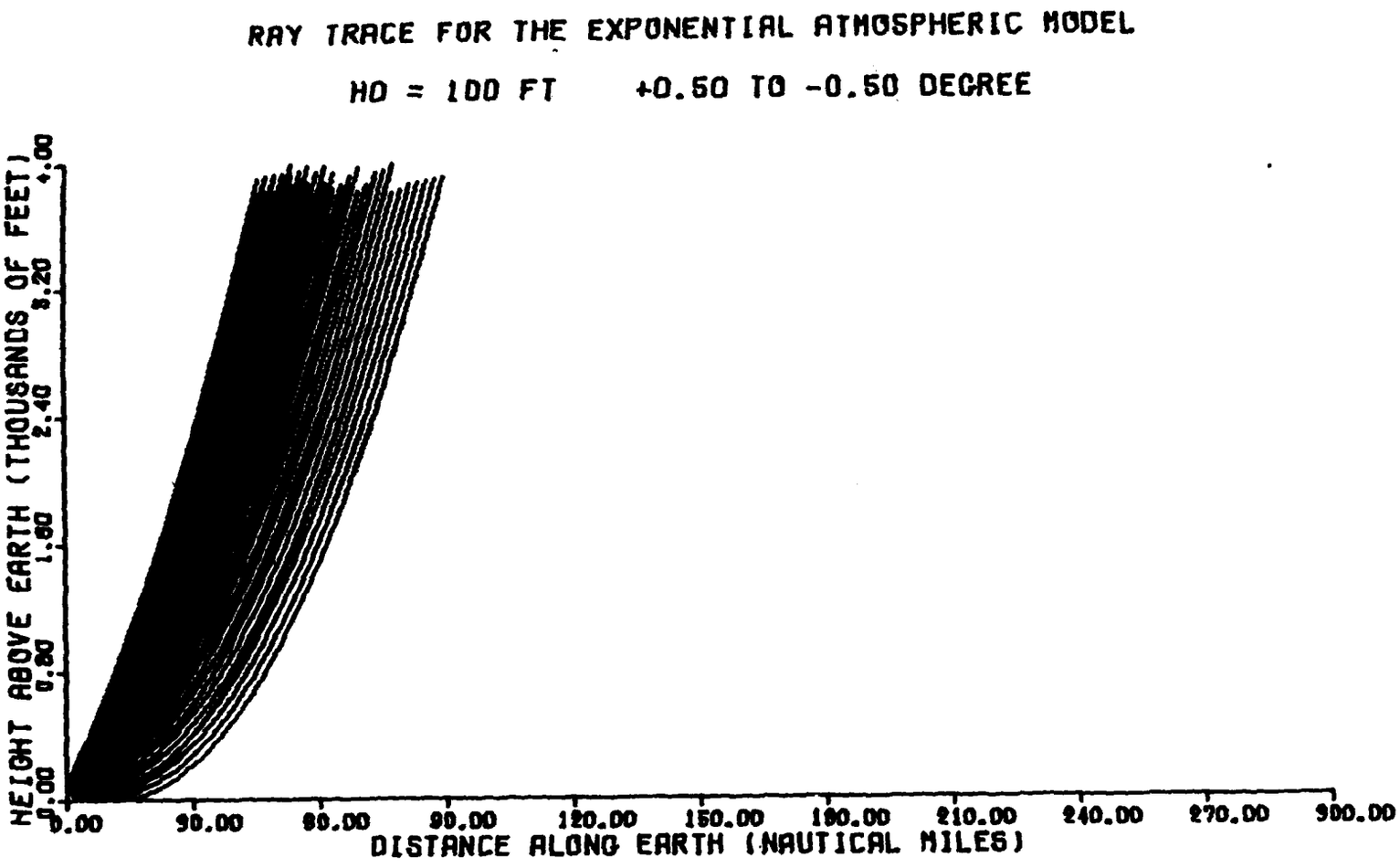


Fig. 26. Ray trace for the 100 ft emitter in the CRPL exponential atmosphere

N-units/kft at a height of 100 ft) causes the rays to refract beyond the geometric horizon such that the distance to the horizon is extended approximately 1.33 times the horizon distance in free space.

Turning now to the Guadalupe Island duct, Figs. (27) through (33) show simulation results obtained with the average measured refractivity profile of Table (7) and Fig. (21a). Fig. (27) shows the trajectories of rays launched between +0.50 and -0.50 deg from the 100 ft high emitter. Only those rays whose elevation angles are less than or equal to some critical angle are trapped between the earth and the 1000 ft top of the duct. The maximum launch angle for trapped rays may be found from Snell's law, which is given by Eq. (54) for spherically concentric media. Rewriting Eq. (54) in terms of ray elevation angles (i.e., the angular complement of $\beta$ and $\beta_o$) gives

$$rn(r)\cos\epsilon = r_o n(r_o)\cos\epsilon_o \tag{190}$$

where r, n(r), and $\epsilon$ denote values at the point of refraction, and $r_o$, $n(r_o)$, and $\epsilon_o$ are measured at some known point, such as at the emitter. Setting $\epsilon = 0$ for total internal reflection (trapping) at the maximum height of the duct, substituting the coordinate change of Eq. (60a) and solving for $\epsilon_o$, the critical launch angle for trapped rays becomes

$$\epsilon_o = \cos^{-1}\left[\frac{(a+h)n(h)}{(a+h_o)n(h_o)}\right] \tag{191}$$

where h and $h_o$ are the altitudes of the top of the duct and the transmitter (measured from mean sea level) and $a = 2.0925\cdot 10^7$ ft is the mean radius of the earth. For a 100 ft transmitter in the Guadalupe Island duct, the maximum launch angles are $|\epsilon_o| = 0.369$ deg for ray trapping at the top of the duct (h = 1000 ft) and $|\epsilon_o| = 0.255$ deg for ray trapping at the intermediate 800 ft layer in the duct. Fig. (27) shows that ray trapping occurs mainly between these two heights. On the other hand, Eq.

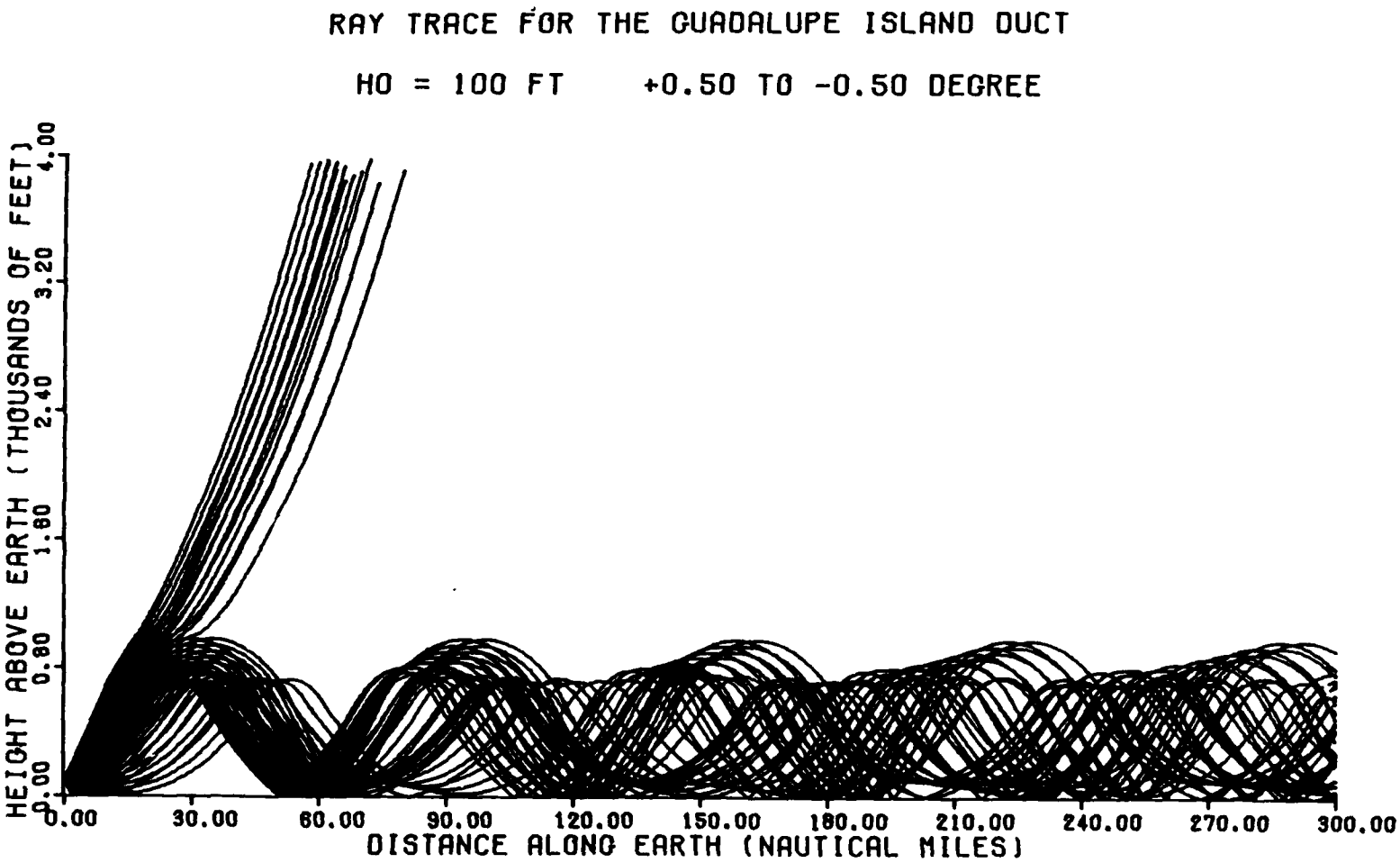


Fig. 27. Ray trace for a 100 ft emitter in the Guadalupe Island duct

(191) indicates that ray trapping does not occur at the 2000 ft high layer shown in Figs. (21a) and (22a) for any value of $\epsilon_o$.

Fig. (27) shows a number of regions where there is a distinct absence of rays, particularly the area above the duct and the low altitude hole extending from 10 to 50 naut mi within the duct. The hole represents the region beyond the earth's horizon where rays are unable to penetrate and is frequently referred to as the earth shadow region. While geometric optics predicts that there is no field present in either of these regions, the experimental results and waveguide mode theory calculations presented in the following section indicate that just the opposite is true. This discrepancy arises from the fact that classical geometric optics, because it does not make explicit use of wavelength and phase, is not able to solve for diffracted fields or fields resulting from evanescent and leaky modes which are often present in atmospheric ducts.[1, 12, 14, 16] A further discussion of these mode types and their fields will be given in the latter part of this chapter.

The wavelike ray structure shown near the top of the duct in Fig. (27) forms several caustics, or regions where the ray density increases rapidly and then falls off abruptly to zero (Chapter IV). Caustics must be excluded from consideration since they violate the requirement of Eq. (115) that the relative spacing between adjacent rays, and hence the ray density in a volume of space, must not change appreciably over a wavelength of distance.

Rays that intersect the earth in Fig. (27) are reflected from surfaces that are locally plane and tangent to a smooth spherical earth at the point of reflection (Chapter V). Thus ray divergence due to reflection from a curved earth is provided for in the ray trace diagram. Surface roughness becomes a consideration only when calculating the field of a

reflected wave by means of Eqs. (184) and (185).

Figs. (28) and (29) show an expanded view of the Guadalupe Island refractivity and refractivity gradient profiles of Figs. (21a) and (21b) and the ray trace plot of Fig. (27) for heights of 0 to 1000 ft within the duct, since the region above the duct is not modeled correctly by geometric optics. Figs. (30) through (33) present height gain curves computed by the simulation at 65, 170, 520, and 3300 MHz for the 100 ft high emitter, using the Guadalupe Island refractivity profile and a moderate sea surface ($\Delta h$ = 1.1 ft) model. Vertical reference axes are drawn at 20 naut mi intervals to represent the zero db gain level of field strength relative to free space values. A scale for measuring relative field strength is given in the upper right hand corner of each plot.

The most notable features of the height gain curves are the peaks and nulls which result from mutual interference between the refracted and reflected wavefronts propagating through the duct. Unlike standard microwave waveguides, the duct has a height which is several orders of magnitude greater than a wavelength of radiation, and thus is capable of sustaining a vertical standing wave pattern with numerous minima and maxima. Furthermore, since the medium within the duct is not homogeneous and since the boundaries of the duct are considerably different (the earth surface causes an amplitude and phase change in reflected fields while the more amorphous upper "boundary" of the duct does not) the interference patterns are not symmetric either with respect to height or to the zero db reference axes. Finally, the number of peaks and nulls in the height gain curves is seen to increase with emitter frequency. This is in agreement with elementary optics theory which states that the distance between the minima and maxima of interfering fields is inversely proportional to frequency. Thus more peaks and nulls appear as this distance decreases.

Simulation results for the 500 ft transmitter are shown in Figs. (34) through (38). In this case the rays are launched between +0.54 and -0.46 deg to permit the simulation to detect the caustics at the top of the duct and thus exclude them from the field strength calculations (at least two adjacent rays must lie above a caustic to enable its location by the computer program).

The ray trace of Fig. (34) is considerably different from that of Fig. (29) with many of the rays trapped between the emitter and the bottom edge of the ducting layer. From Snell's law and Fig. (34) it may be shown that rays having $0 < \epsilon_o < 0.0987$ deg are trapped between 500 and 630 ft, while those for which $|\epsilon_o| < 0.411$ deg are trapped at 800 ft and those launched at $|\epsilon_o| < 0.490$ deg are trapped at 1000 ft. The difference in ray trapping at the two emitter heights may be explained by Eq. (191). Assume for the moment that the ratio $n(h)/n(h_o)$ does not change over some range of altitude h. Eq. (191) states that as h becomes larger, $\epsilon_o$ will become smaller until at some point the right hand side of the equation exceeds unity and no rays may be trapped. Thus the greater the separation between the layer and emitter altitudes (i.e., h and $h_o$) the smaller the launch angle must become to remain trapped. Of course changing n(h) significantly will alter this result, but in the case of trapping at the 800 and 1000 ft levels, the ratio of $n(h)/n(h_o)$ remains relatively constant as compared to the ratio of $(a + h)/(a + h_o)$ when solving Eq. (191) at $h_o = 100$ ft and $h_o = 500$ ft. Similarly Eq. (191) indicates that no ray trapping will occur along the bottom edge of the duct for the 100 ft emitter, as confirmed by Fig. (29).

Figs. (35) through (38) show simulated height gain curves for the 500 ft emitter above the same moderately rough (sea state 3) surface. As with

the 100 ft emitter, the peaks and nulls in the height gain curves become more pronounced at higher frequencies.

Finally, the simulation results using the trilinear ground based duct model of Pappert and Goodhart are presented in Figs. (39) through (49). Rays are again launched from +0.50 to -0.50 deg in elevation for the 100 ft emitter and from +0.54 to -0.46 deg for the 500 ft emitter. A comparison of critical angles for ray trapping within the Guadalupe Island and trilinear duct models is given in Table (9).

TABLE 9

MAXIMUM LAUNCH ANGLES OF TRAPPED RAYS

| Model | Emitter Height (ft) | Trapping Height (ft) | Maximum Launch Angle (deg) |
|---|---|---|---|
| Guadalupe Island | 100 | 1000 | ± 0.369 |
| | | 800 | ± 0.255 |
| | 500 | 1000 | ± 0.490 |
| | | 800 | ± 0.411 |
| | | 630 | ± 0.099 |
| Trilinear | 100 | 1000 | ± 0.381 |
| | | 800 | ± 0.082 |
| | 500 | 1000 | ± 0.500 |
| | | 800 | ± 0.335 |
| | | 650 | ± 0.093 |

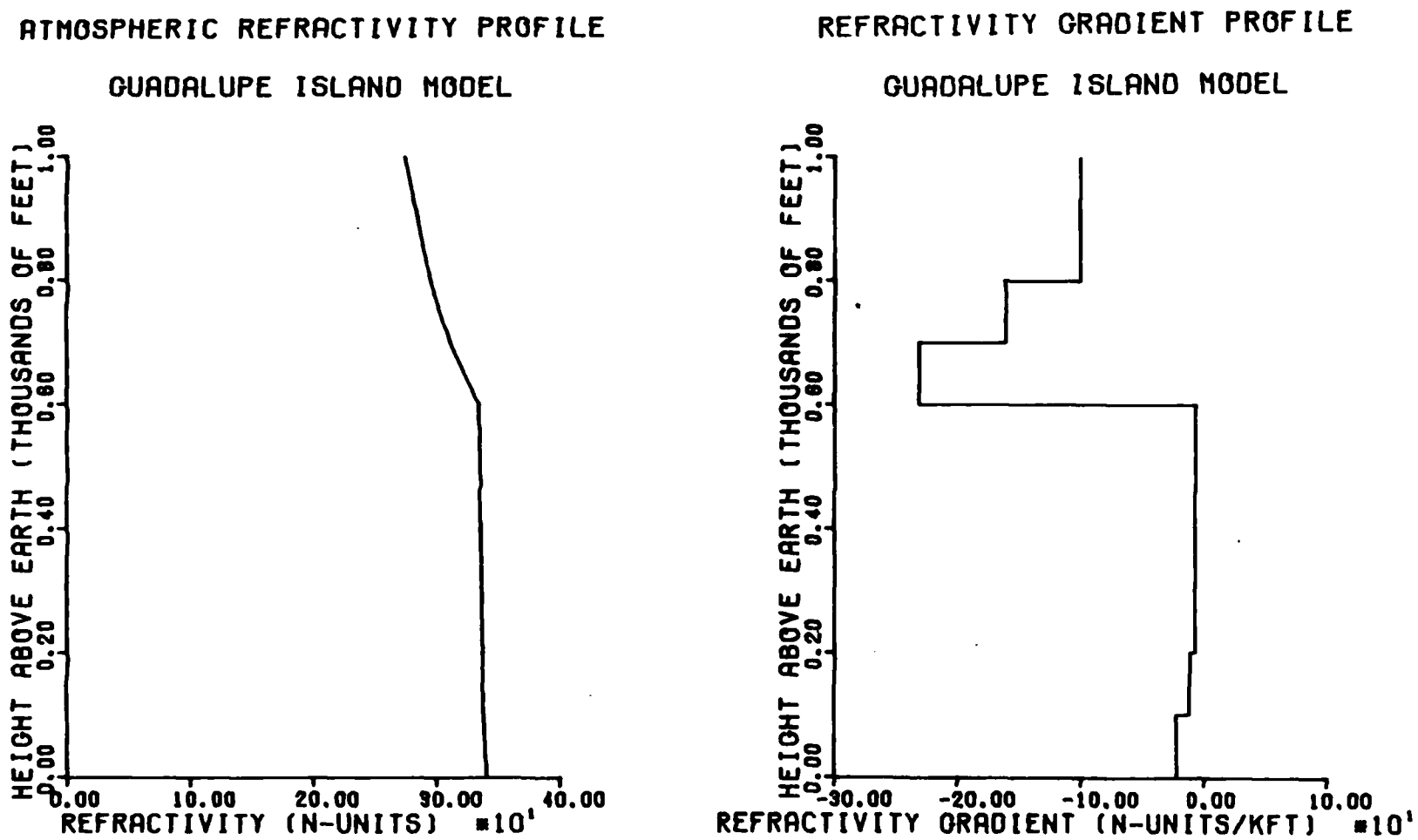


(a) (b)

Fig. 28. N and dN/dh profiles for the Guadalupe Island duct (expanded from Fig. (21a))

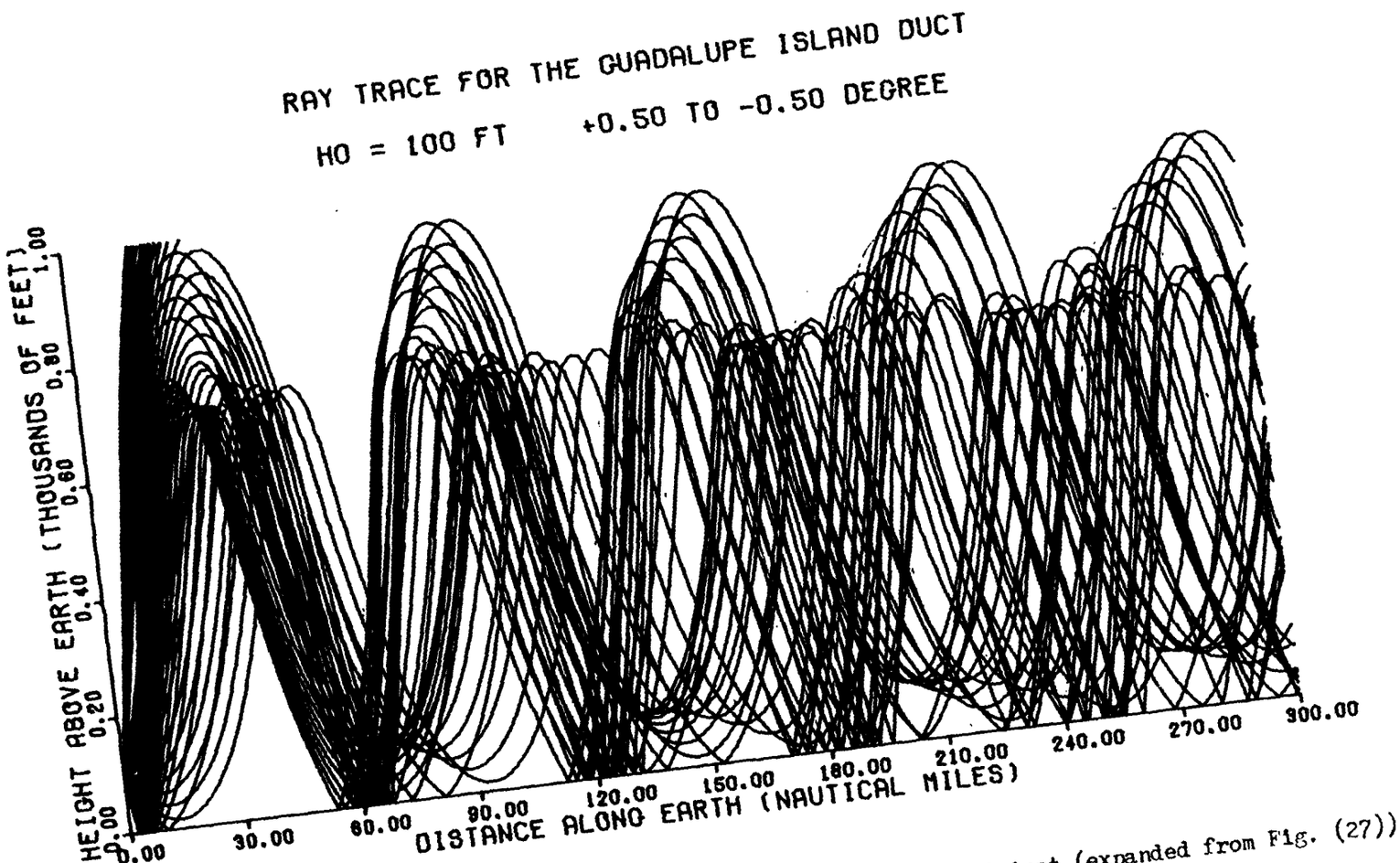


Fig. 29. Ray trace for the 100 ft emitter in the Guadalupe Island duct (expanded from Fig. (27))

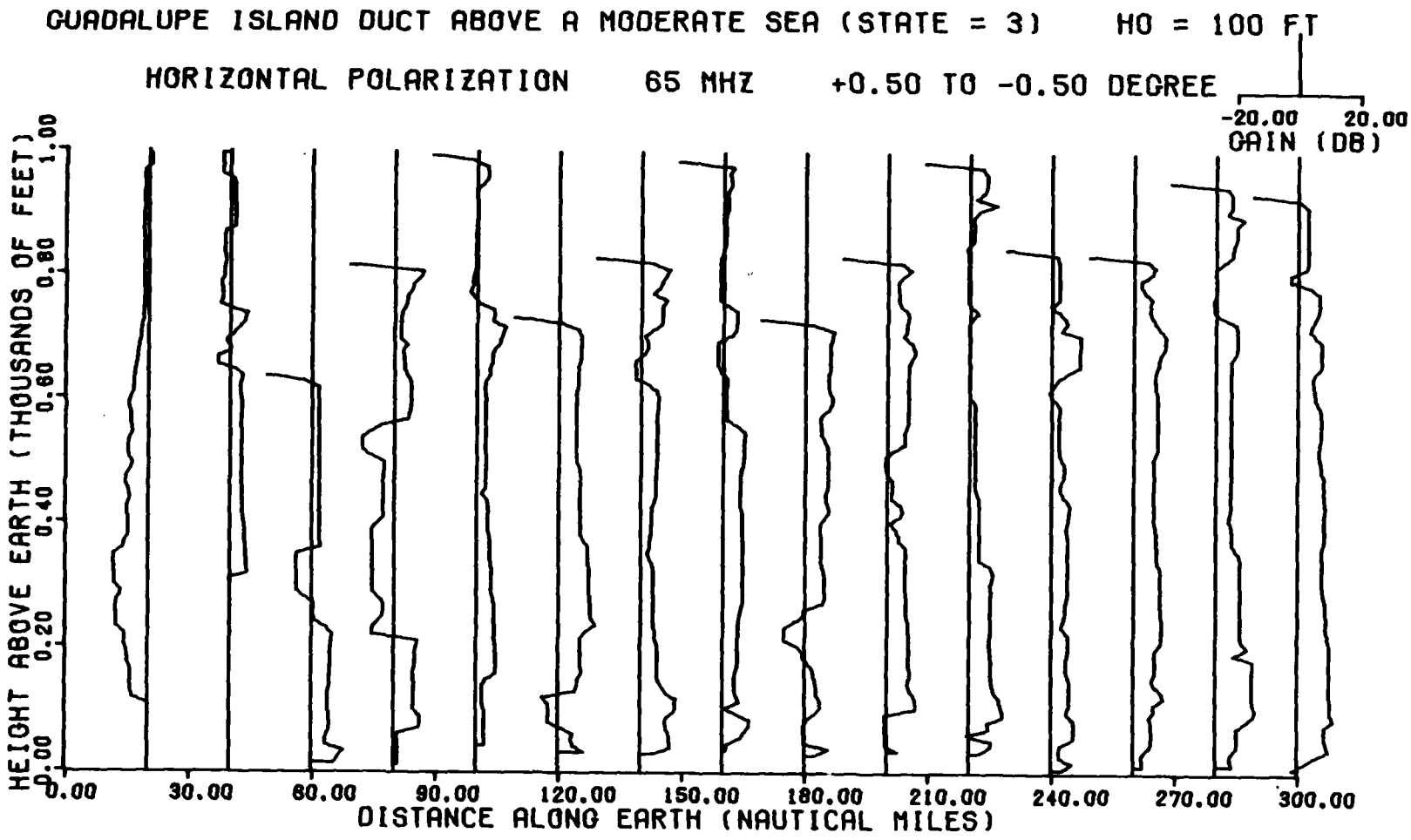


Fig. 30. Height gain curves at 65 MHz, from Figs. (28) and (29)

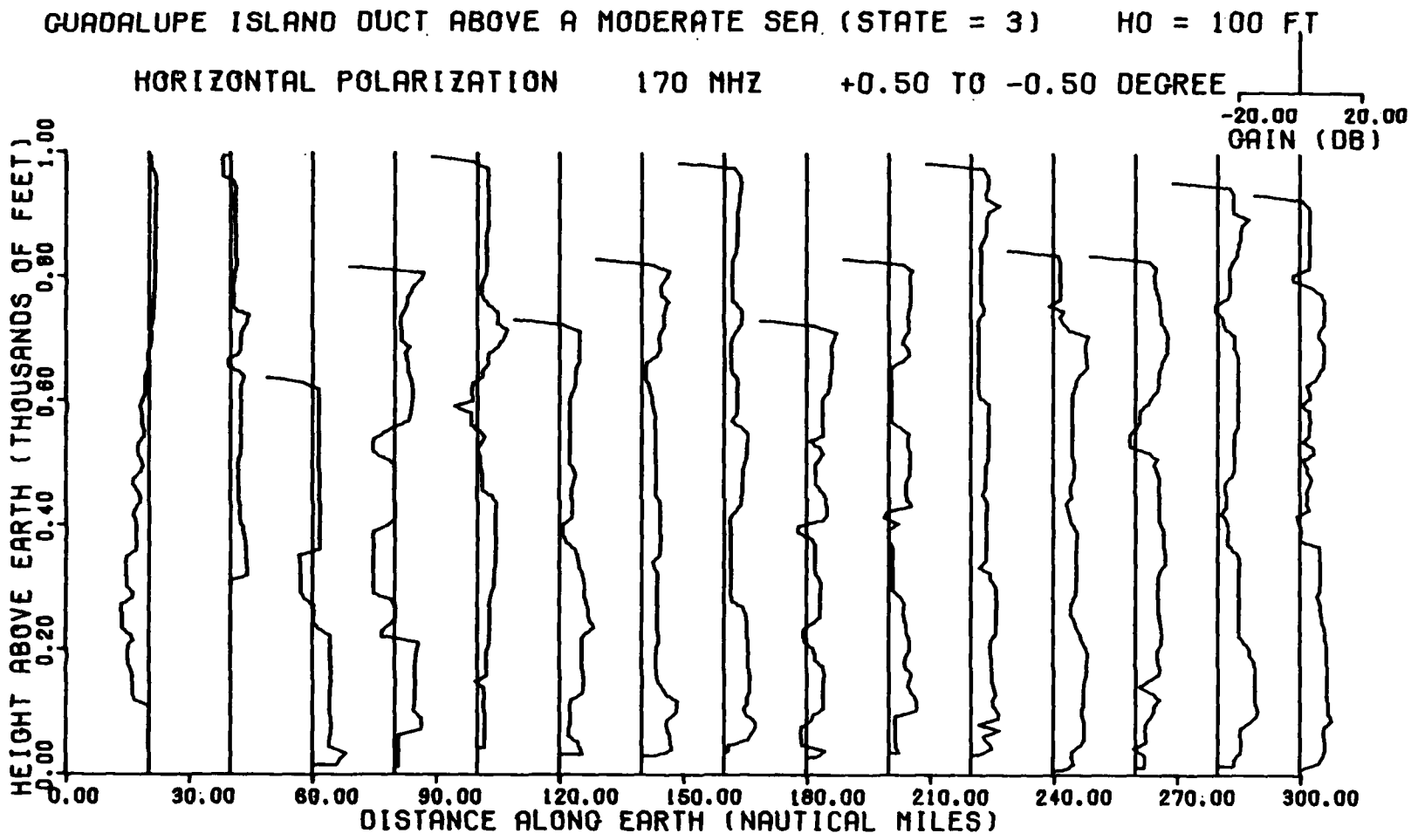


Fig. 31. Height gain curves at 170 MHz, from Figs. (28) and (29)

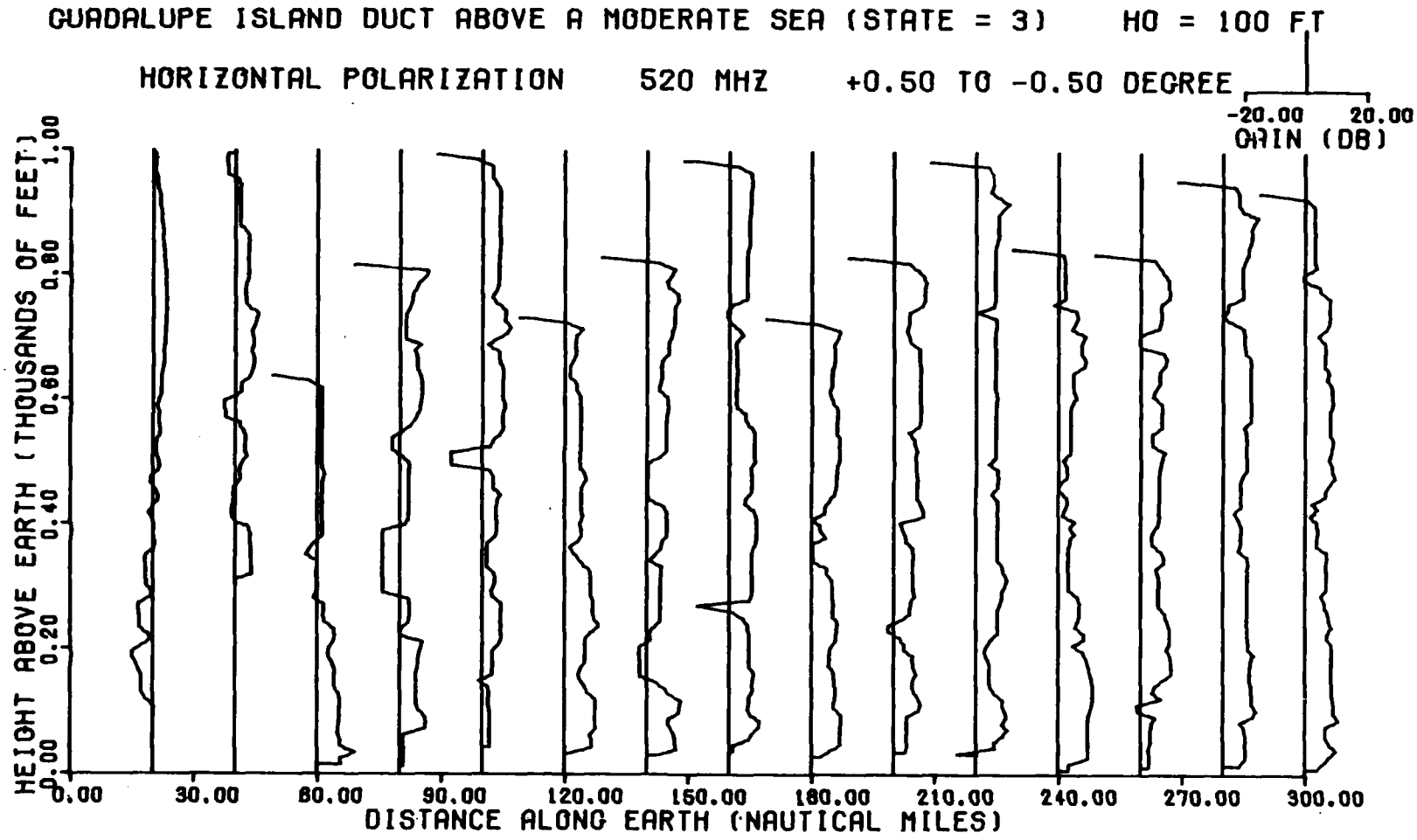


Fig. 32. Height gain curves at 520 MHz, from Figs. (28) and (29)

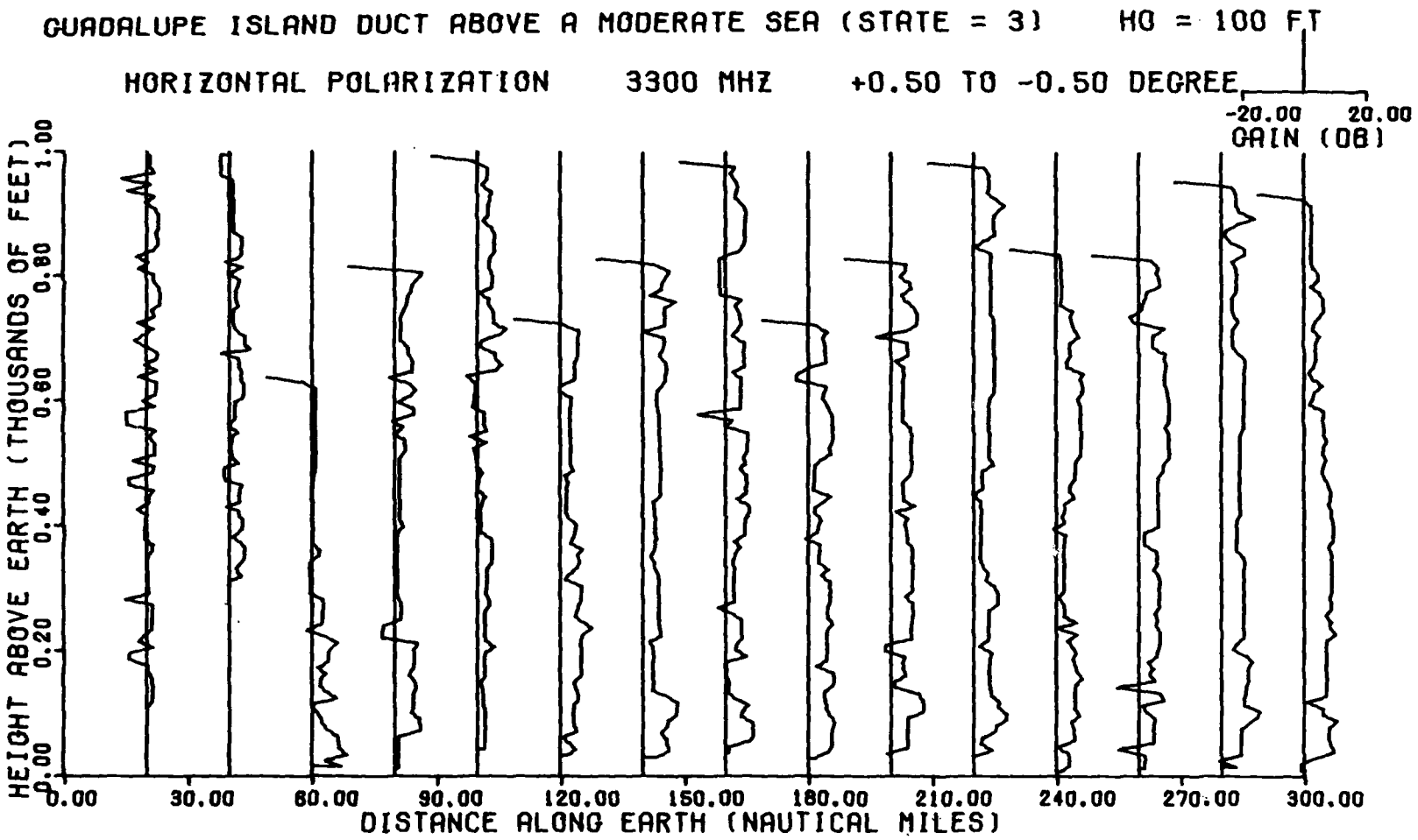


Fig. 33. Height gain curves at 3300 MHz, from Figs. (28) and (29)

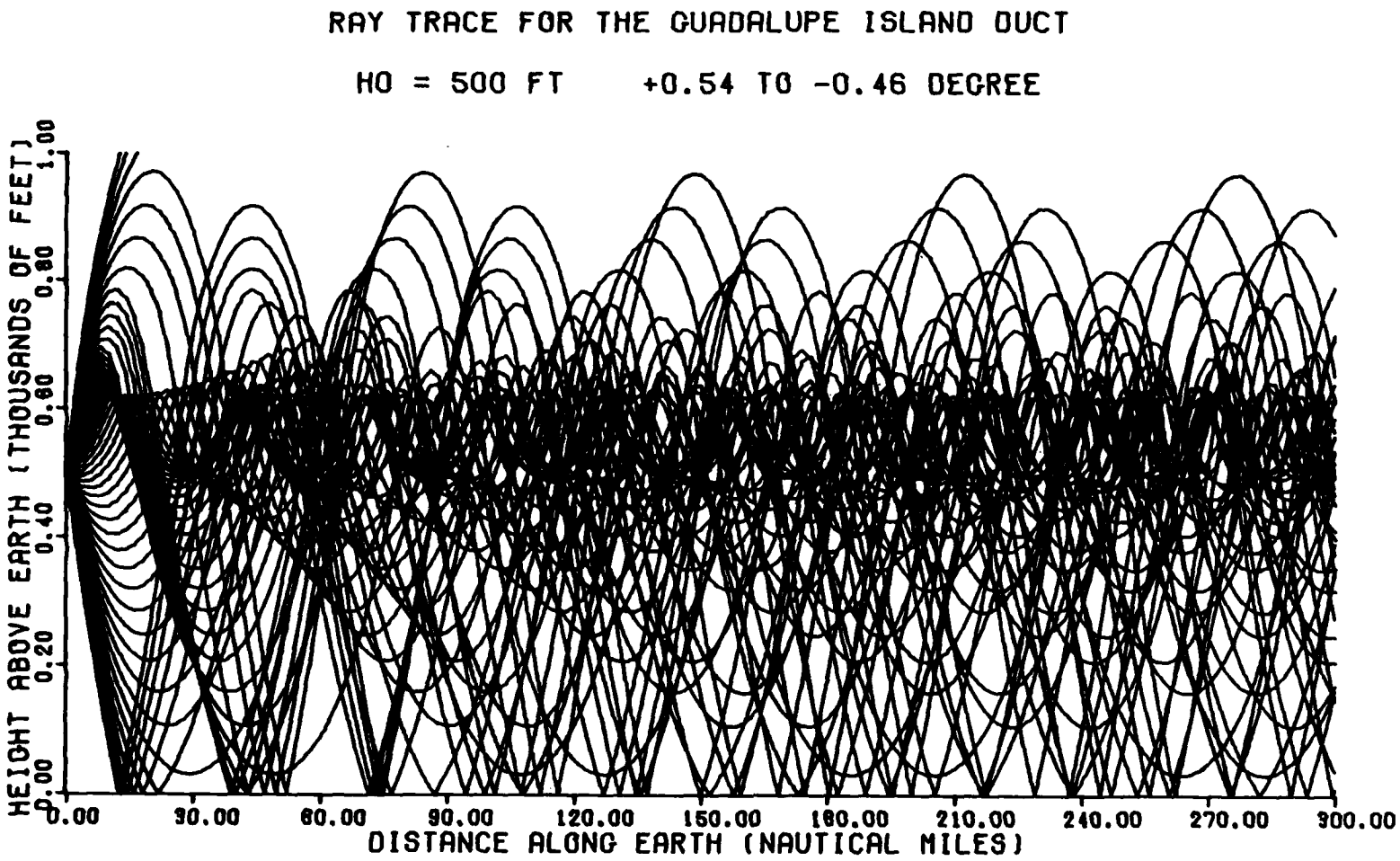


Fig. 34. Ray trace for the 500 ft emitter in the Guadalupe Island duct

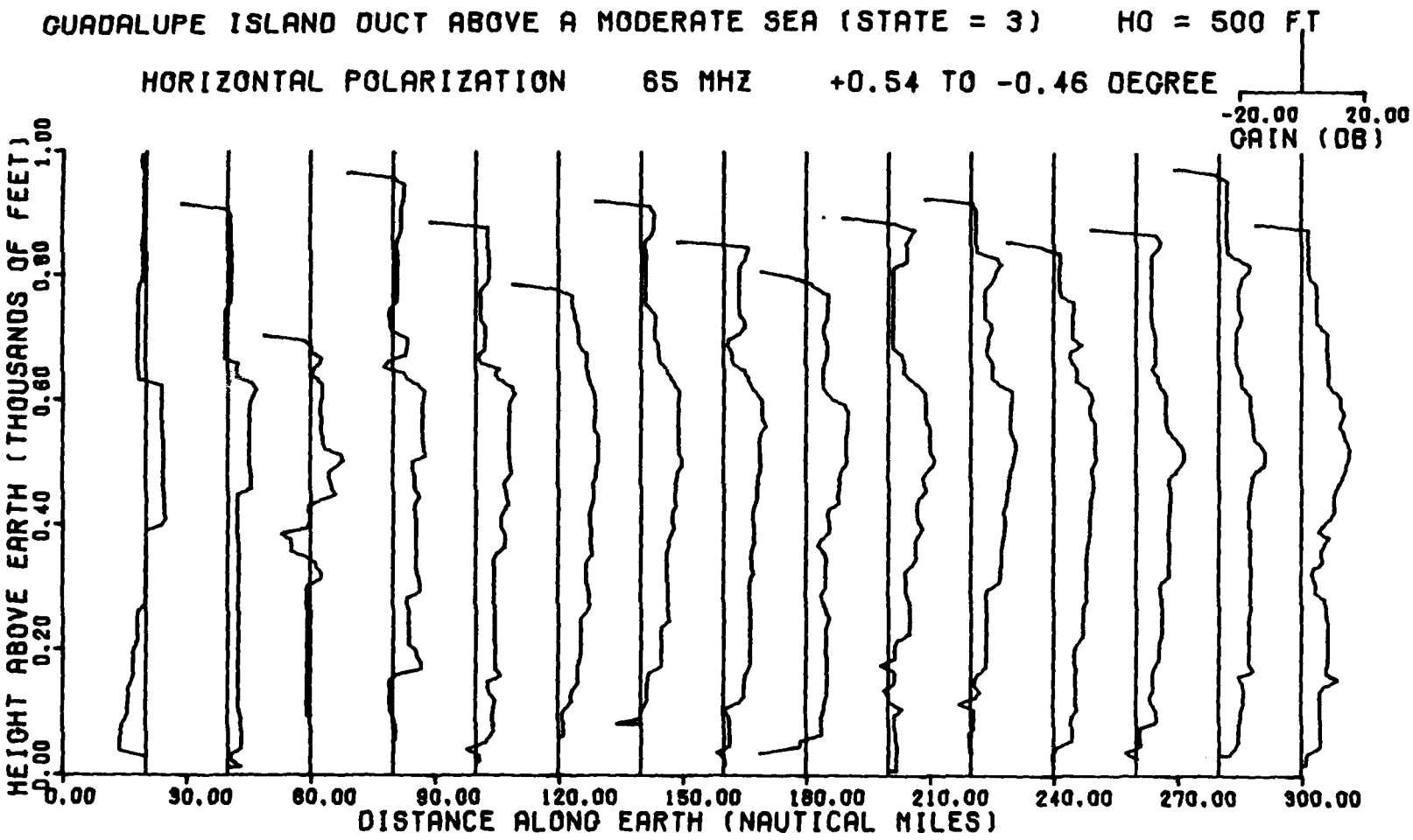


Fig. 35. Height gain curves at 65 MHz, from Figs. (28) and (34)

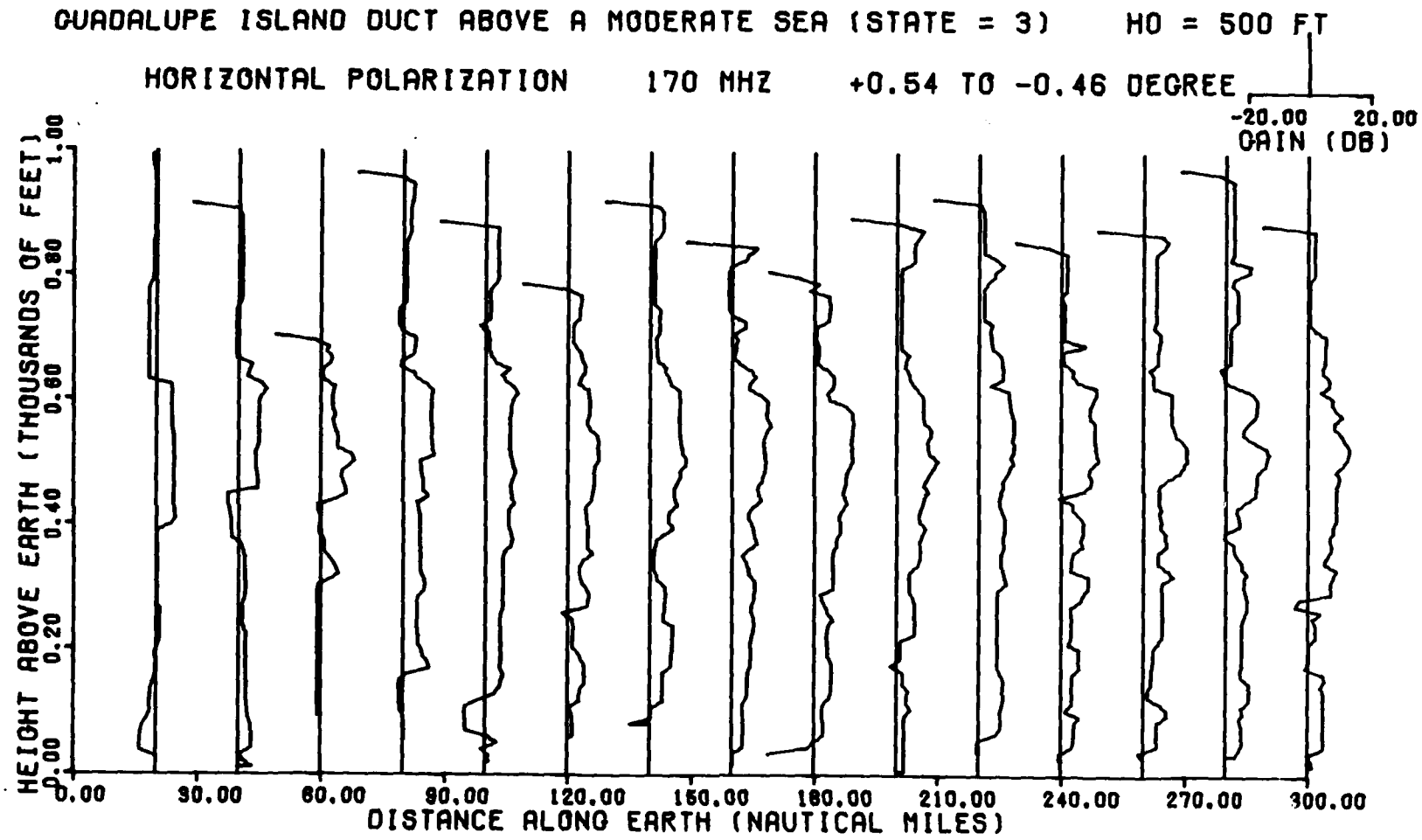


Fig. 36. Height gain curves at 170 MHz, from Figs. (28) and (34)

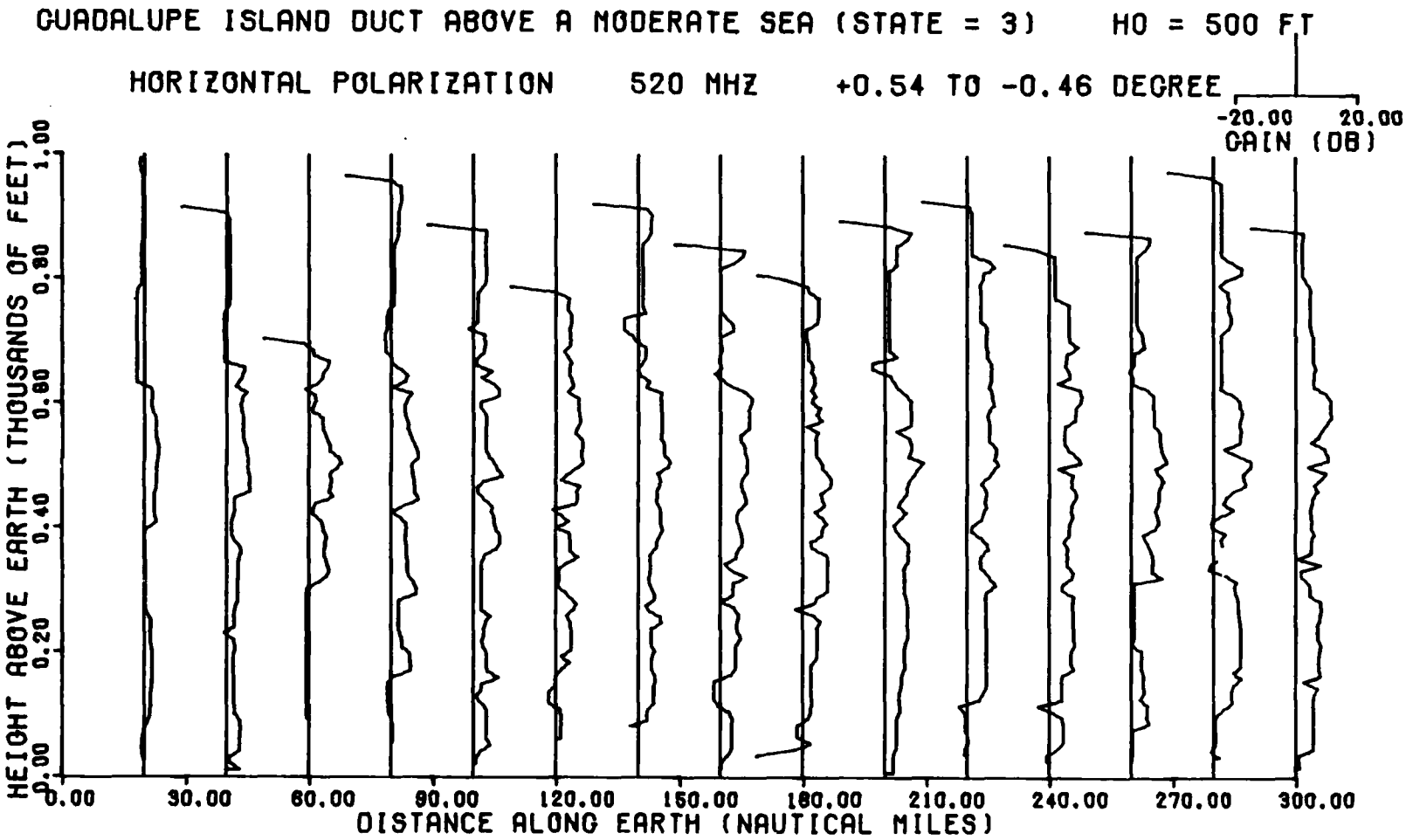


Fig. 37. Height gain curves at 520 MHz, from Figs. (28) and (34)

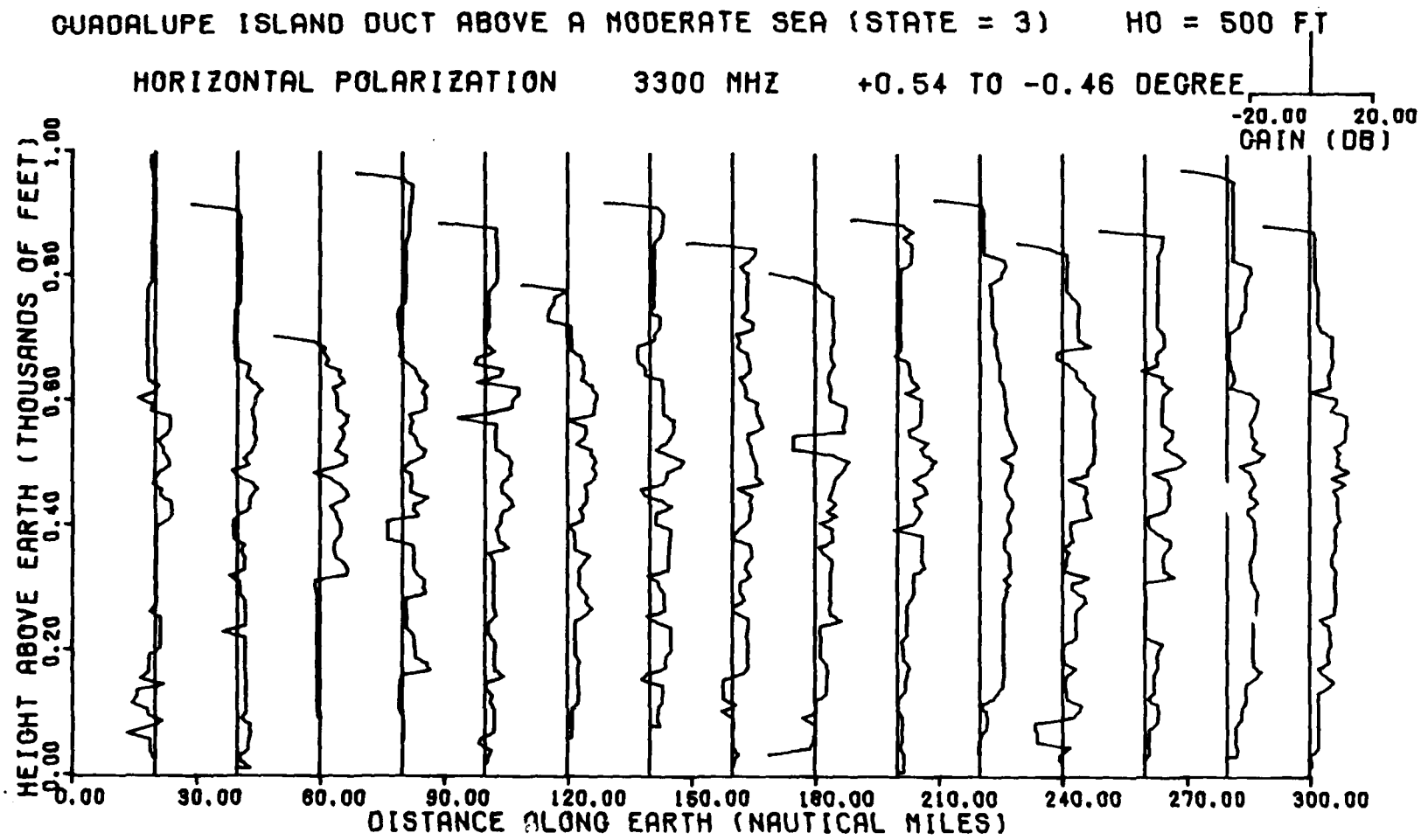


Fig. 38. Height gain curves at 3300 MHz, from Figs. (28) and (34)

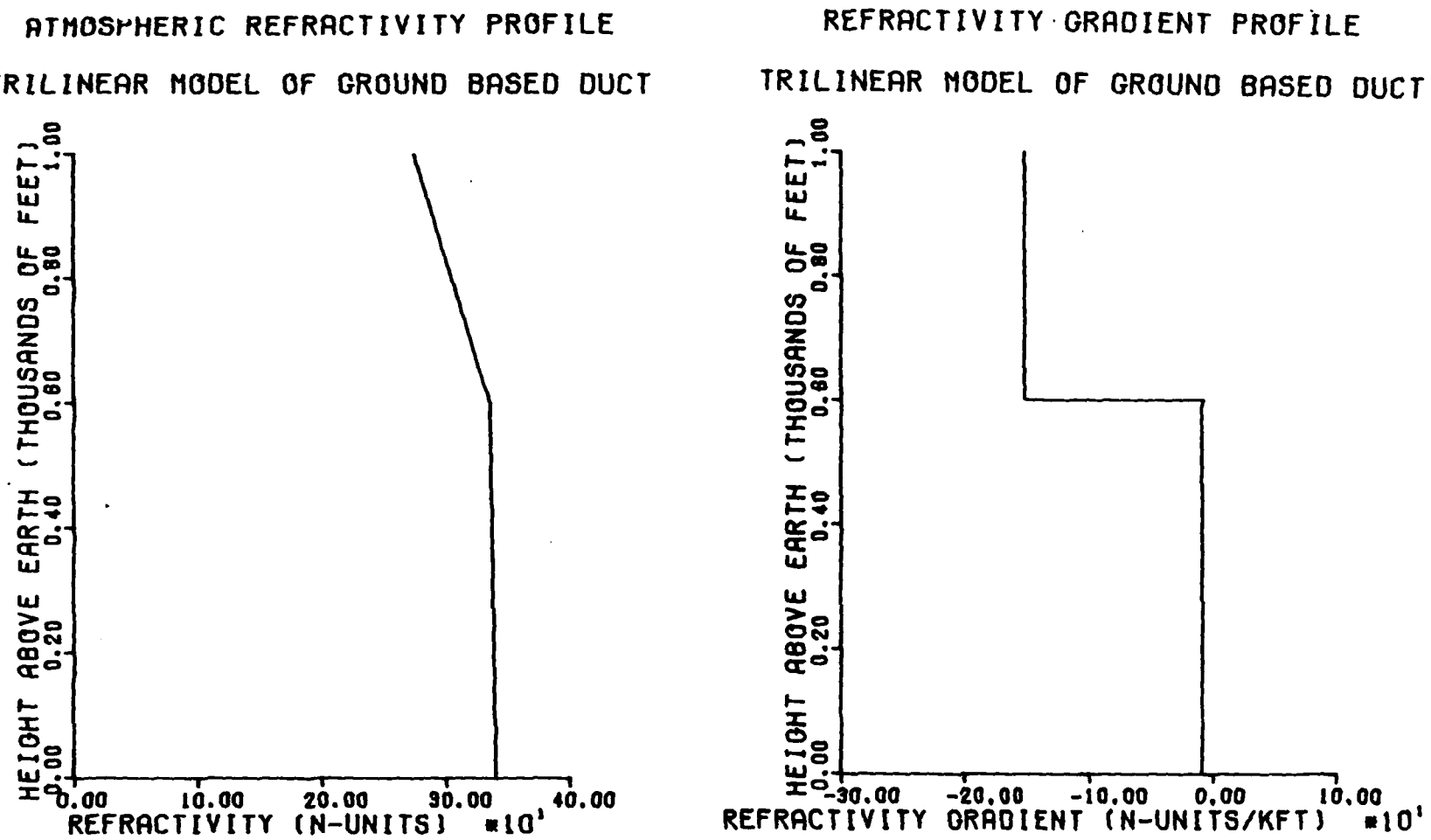


(a) (b)

Fig. 32. N and dN/dh profiles for the trilinear ground based duct (expanded from Fig. (21b))

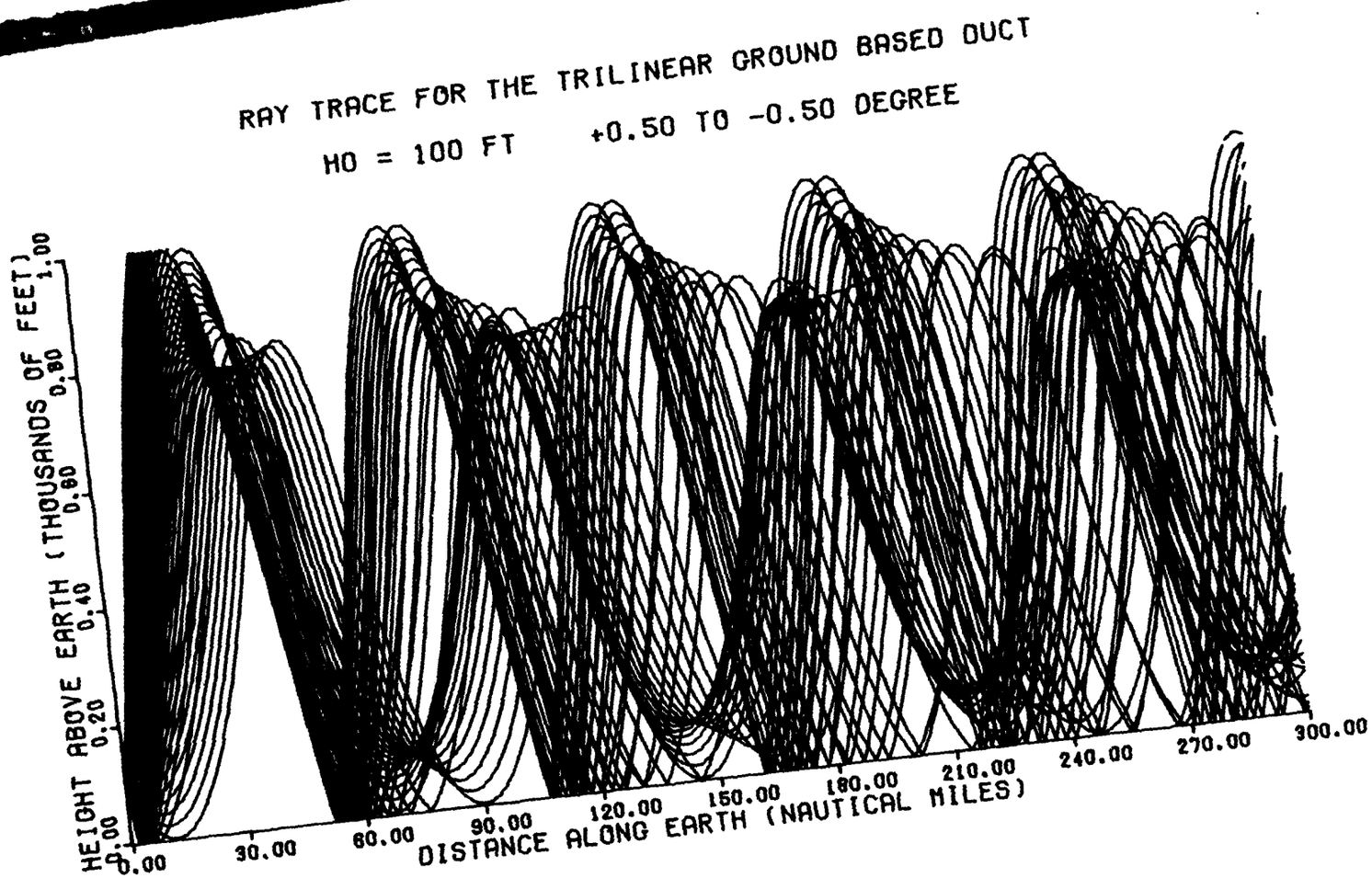


Fig. 40. Ray trace for the 100 ft emitter in the trilinear duct

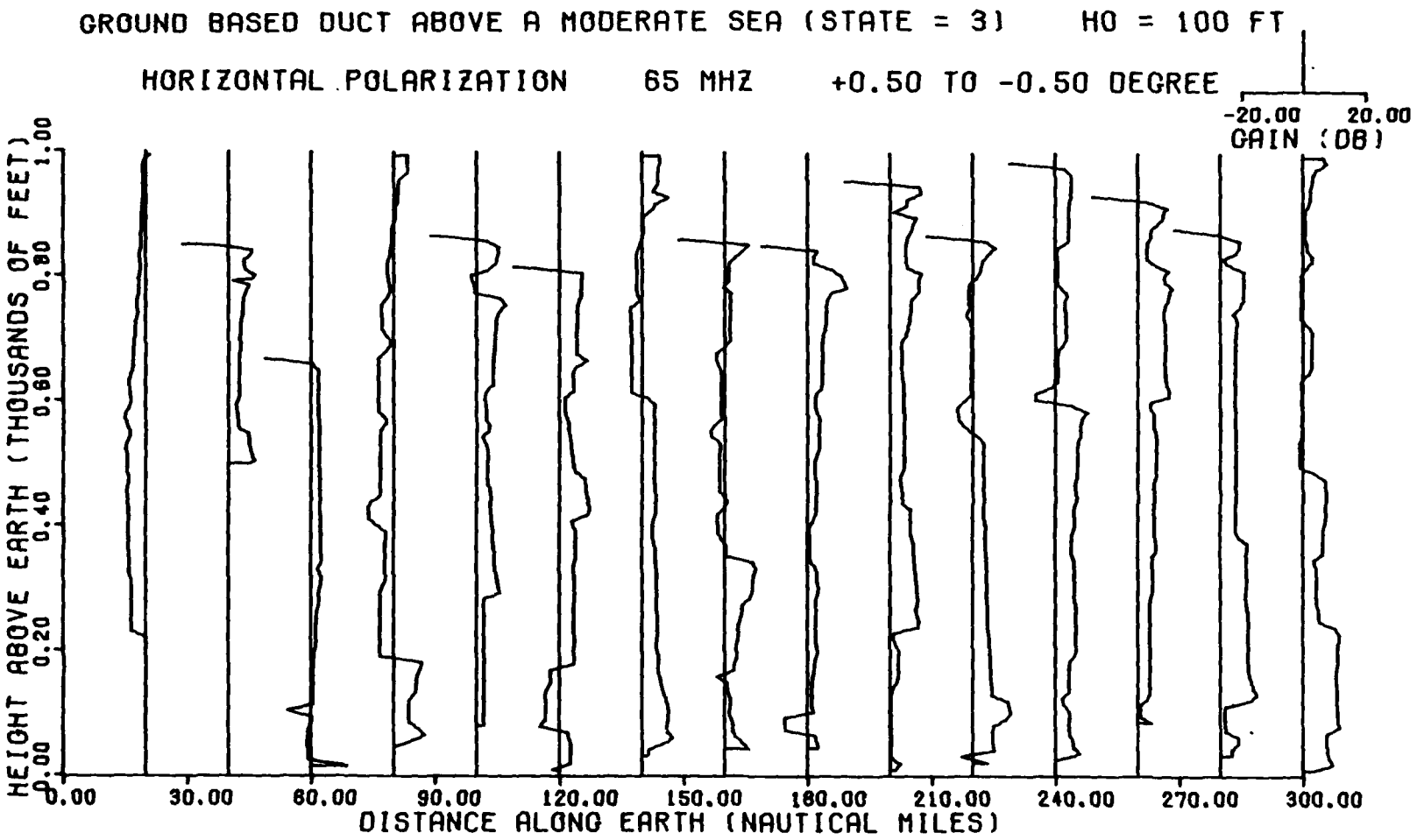


Fig. 41. Height gain curves at 65 MHz, from Figs. (39) and (40)

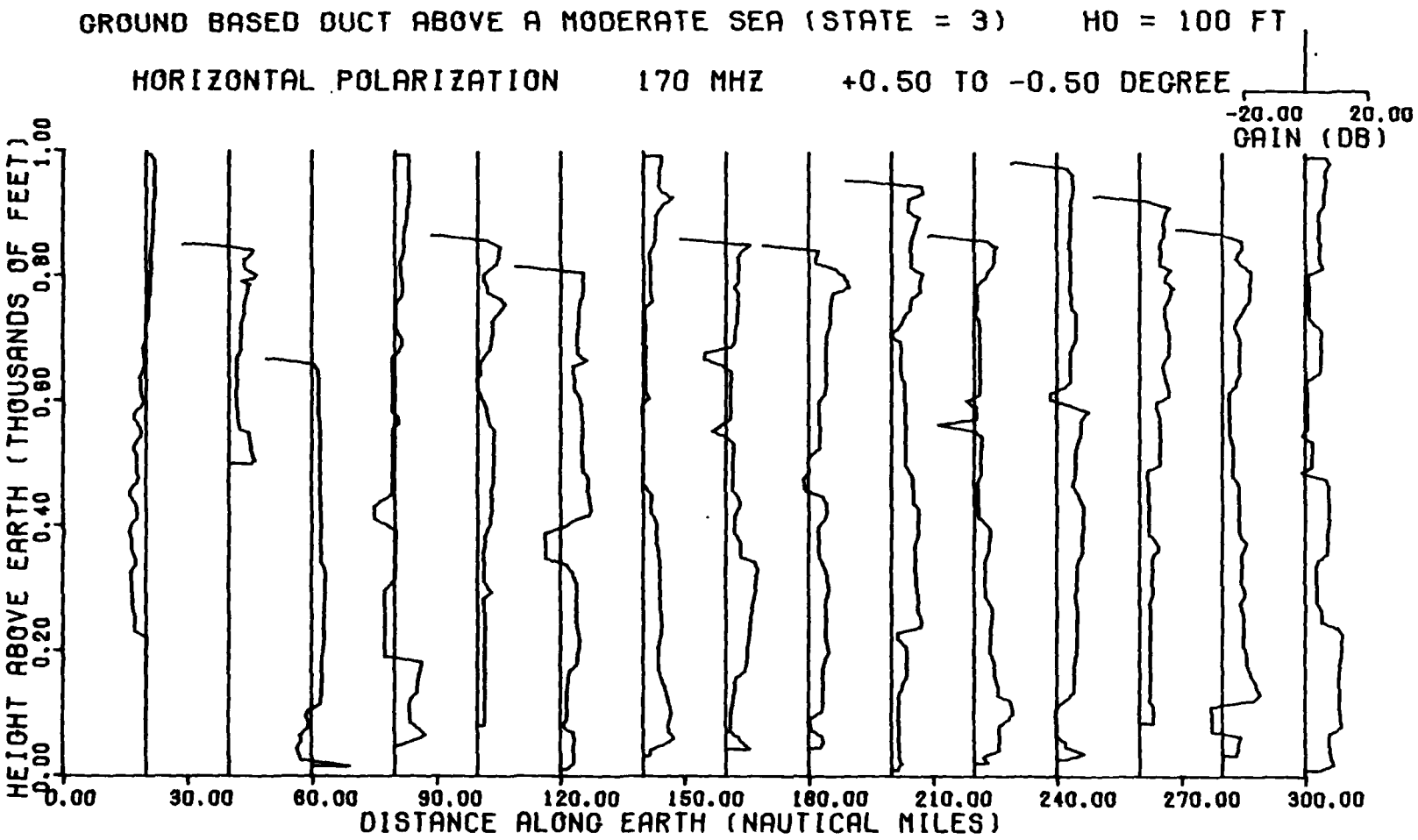


Fig. 42. Height gain curves at 170 MHz, from Figs. (39) and (40)

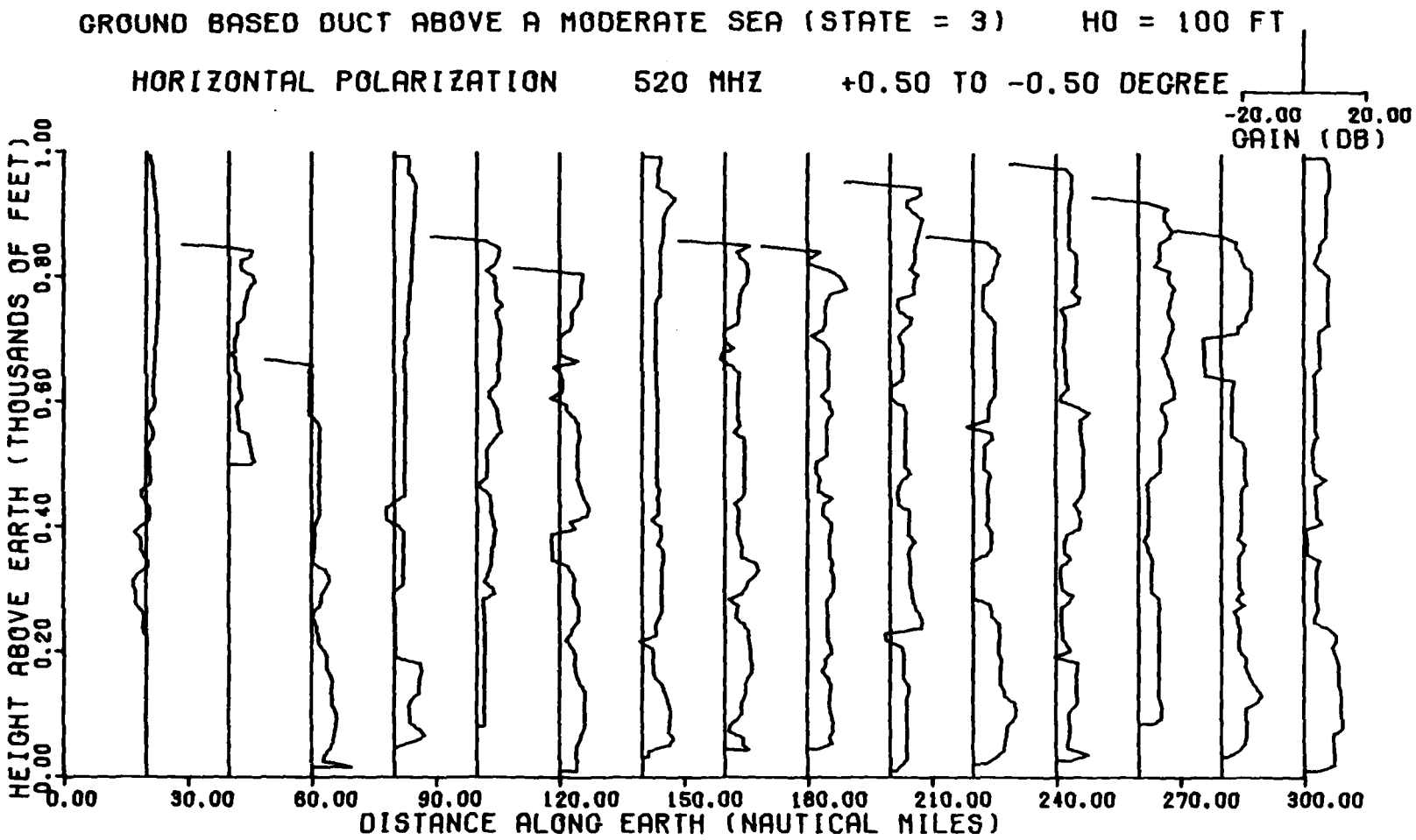


Fig. 43. Height gain curves at 520 MHz, from Figs. (39) and (40)

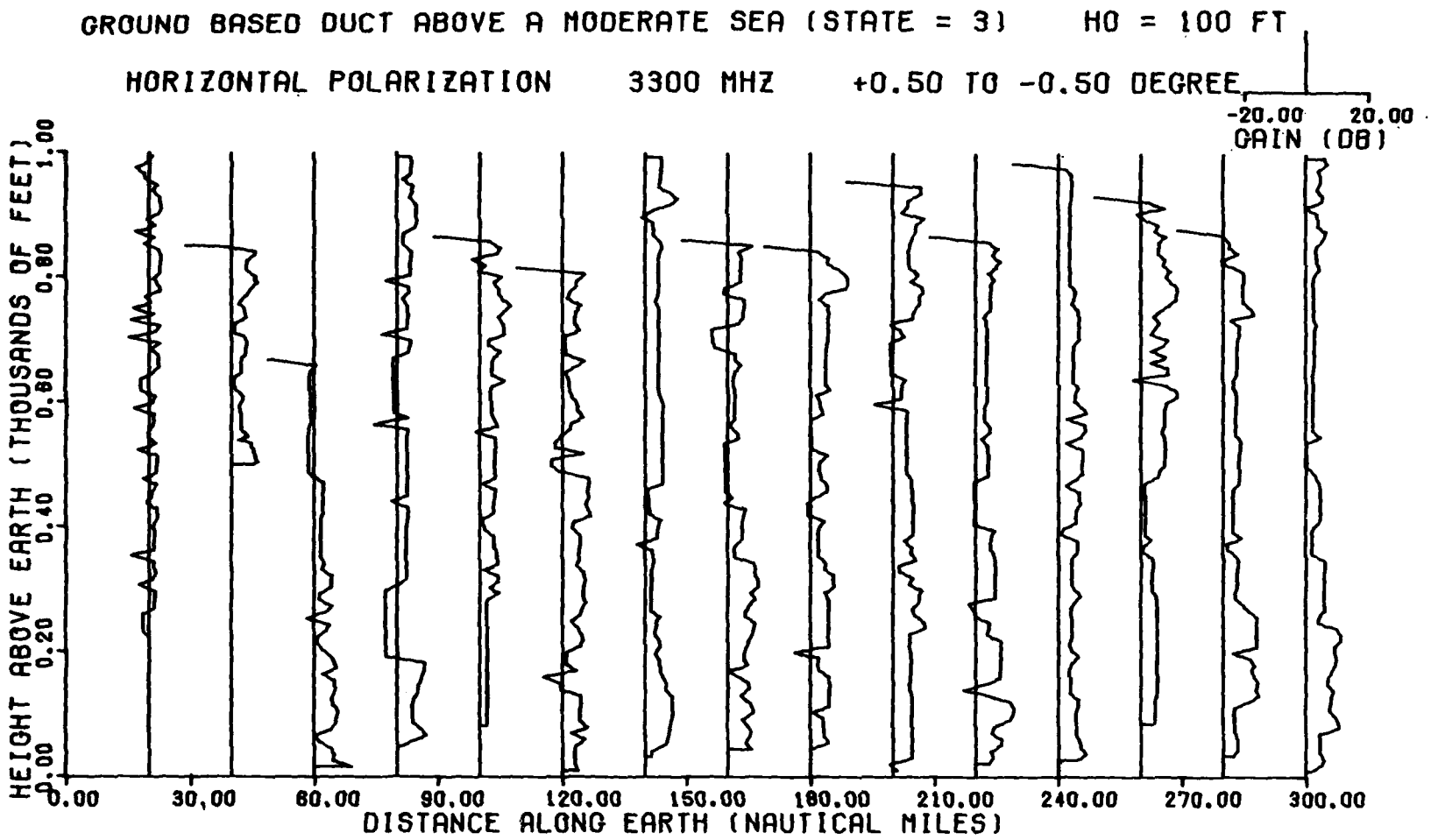


Fig. 44. Height gain curves at 3300 MHz, from Figs. (39) and (40)

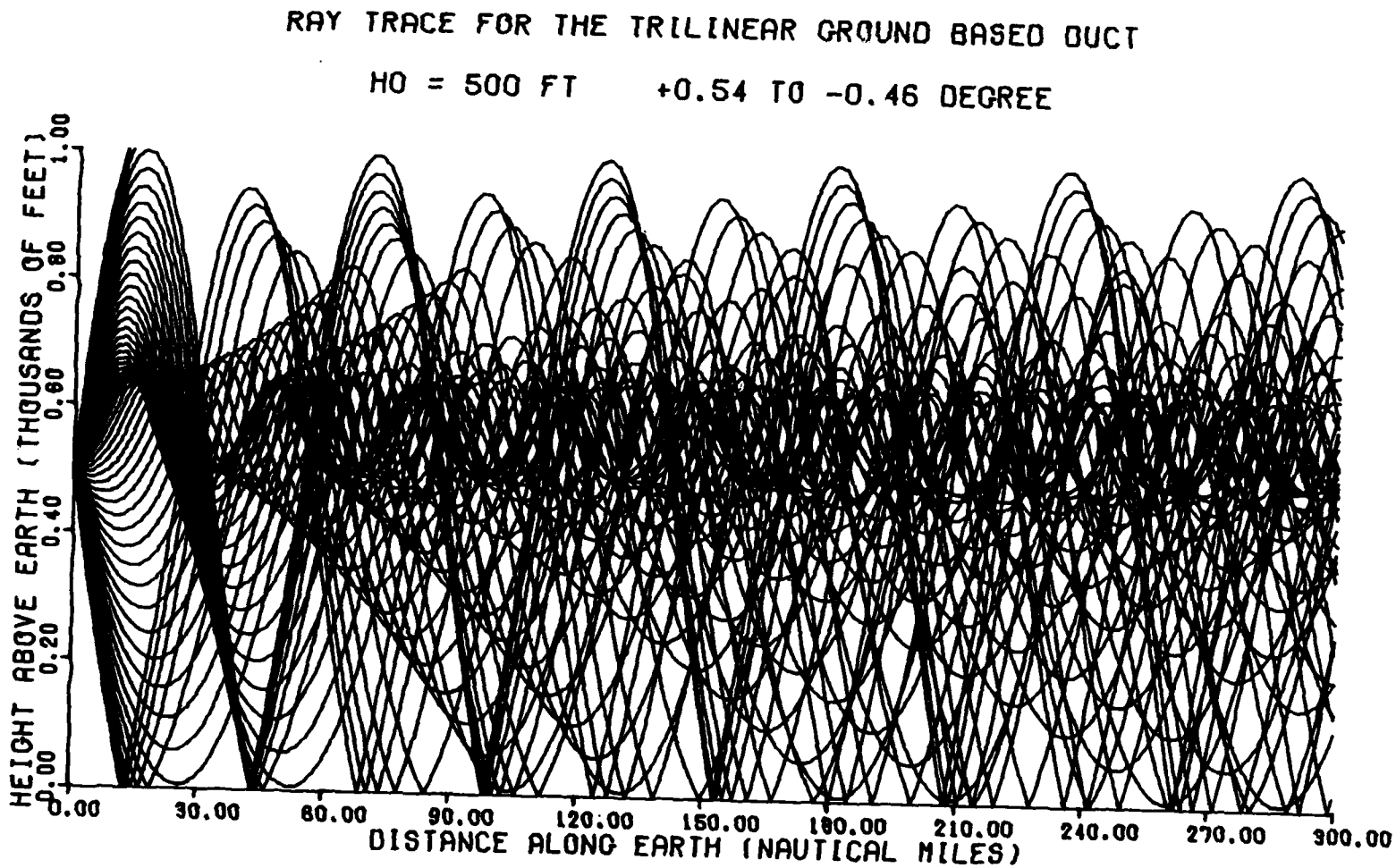


Fig. 45. Ray trace for the 500 ft emitter in the trilinear duct

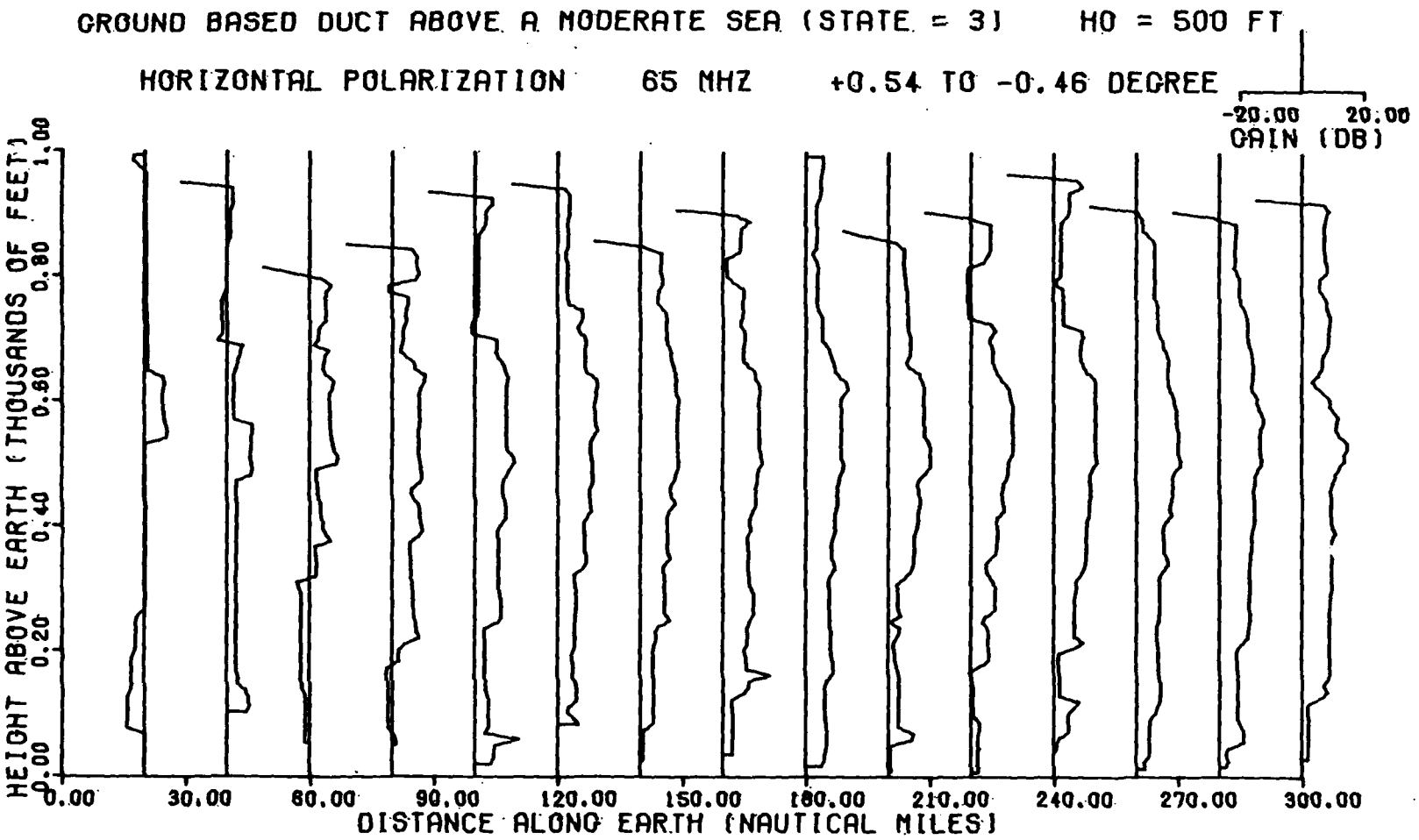


Fig. 46. Height gain curves at 65 MHz, from Figs. (39) and (45)

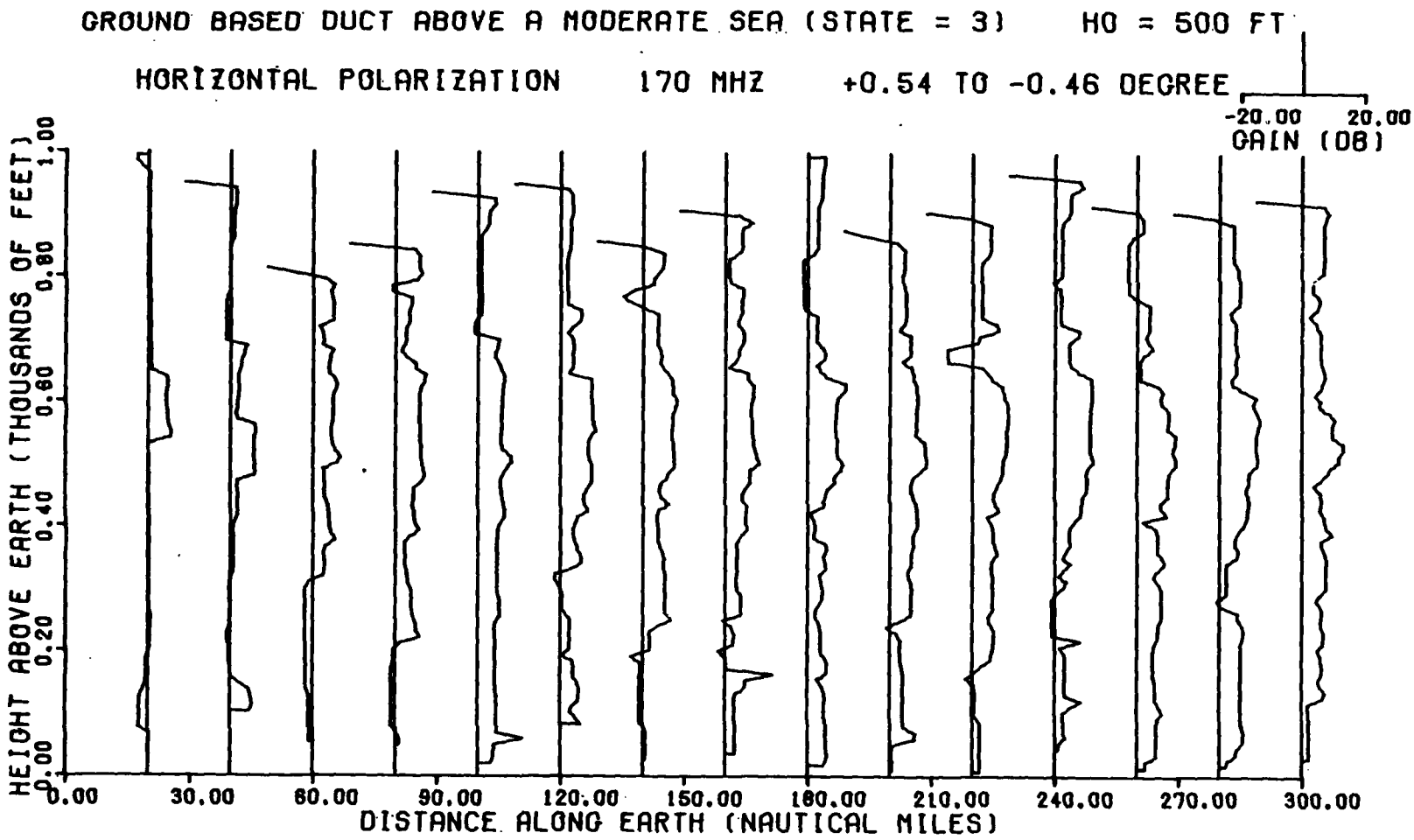


Fig. 47. Height gain curves at 170 MHz, from Figs. (39) and (45)

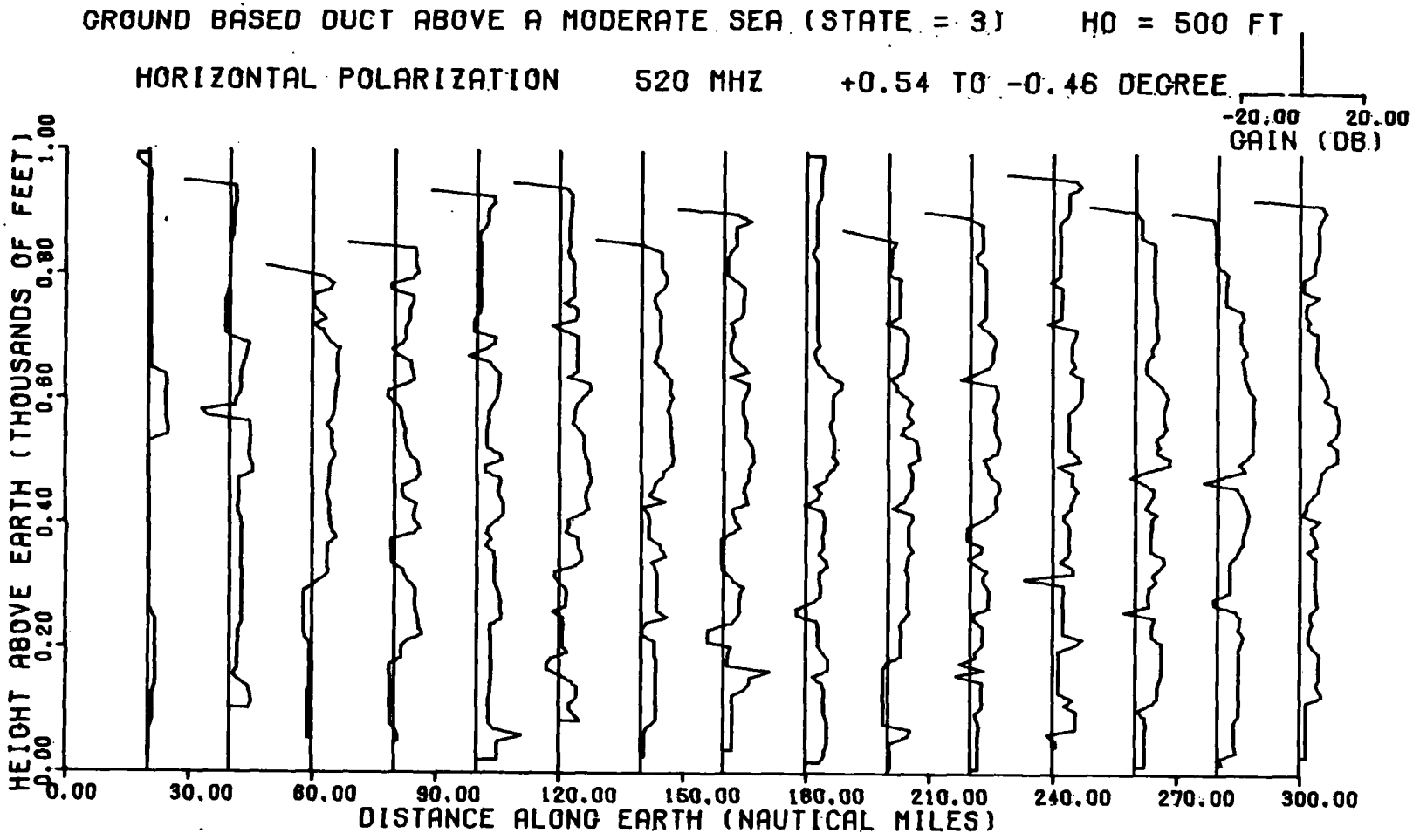


Fig. 48. Height gain curves at 520 MHz, from Figs. (39) and (45)

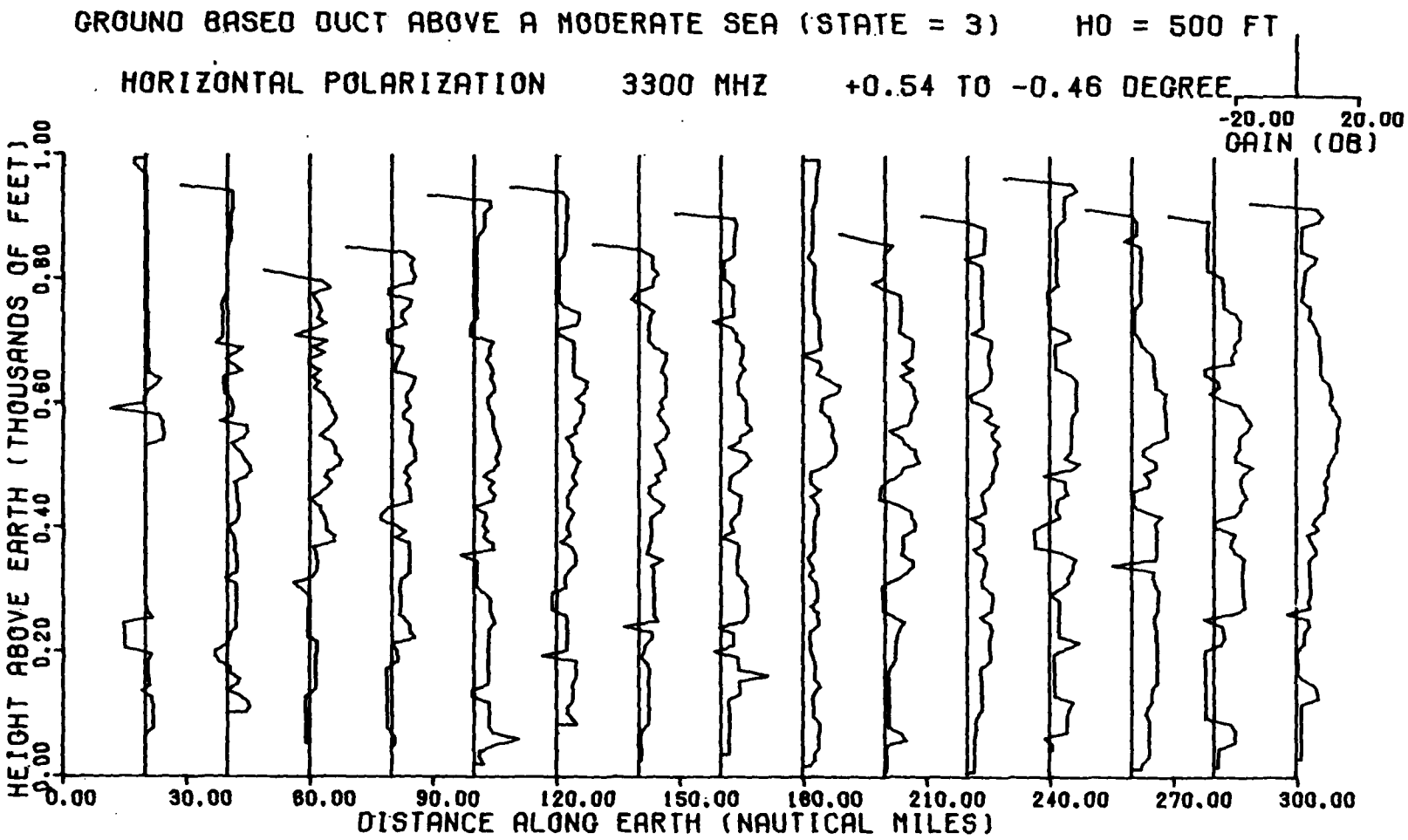


Fig. 49. Height gain curves at 3300 MHz, from Figs. (39) and (45)

## Comparison of Results

The preceding simulation results are compared in this section to the experimental and calculated height gains presented by Pappert and Goodhart for the ground based Guadalupe Island duct. The experimental data for the 100 ft high emitter are from Fig. (20) and the waveguide mode theory calculations are based upon the trilinear refractivity profile of Table (8) and Fig. (21b). The height gain curves from Pappert and Goodhart, shown in Figs. (50) through (59), are for fixed receiver heights of 100 and 500 ft at a distance of 120 naut mi from the transmitter (measured along the earth's surface), with selected results given at a distance of 60 naut mi. Applying the principle of reciprocity for a linear isotropic medium, these results are compared to the simulation height gain curves where the transmitter and receiver have been interchanged. As mentioned previously, all calculations assume a sea surface of moderate roughness ($\Delta h$ equals 1 ft and 1.1 ft in the respective waveguide and geometric optics results) over the entire path between San Diego and Guadalupe Island.

Fig. (50) shows measured and calculated height gain profiles at 65 MHz for a transmitter to receiver separation of 60 naut mi with the receiver (or simulation transmitter) at 500 ft above mean sea level. Shown are the experimental and calculated results obtained from waveguide theory, plus calculated height gains for the earth diffracted field[1, 14] and the field scattered by the troposphere.[14, 41] The diffracted and troposcatter fields, which are labeled "normal" in the figure legends, are nonducted fields which are present when the transmitter is below the horizon (in this case at a height less than 2200 ft). These fields will be shown to be consistently weak, usually ranging from 20 to 60 db below the ducted field. The experimental, waveguide theory, and normal height gain

curves are all repeated in Figs. (50a) and (50b) to avoid congestion when plotting the simulated height gains obtained from the Guadalupe Island and trilinear refractivity profiles, shown in Figs. (50a) and (50b), respectively. The simulation results shown in this case are from the height gain curves at 60 naut mi given in Figs. (35) and (46).

In examining the results of Fig. (50) it is apparent that geometric optics yields a height gain profile that is much more irregular than the curves obtained experimentally or from waveguide theory. This may be due to the fact that the geometric optics simulation calculates only the fields that are specularly reflected at the sea surface, and thus omits diffusely scattered fields which may tend to "fill in" the height gain profile. A second explanation may be that the specular reflection coefficient of the sea is in error because of incorrect electrical properties assigned to the sea surface in Table (2). Another possibility may lie with the conditions of Eqs. (77) and (78) given in Chapter IV which state that geometric optics becomes a better propagation model as frequency increases. A final reason may be that since geometric optics does not make explicit use of wavelength and phase, it is incapable of predicting the existence of certain types of modes which are accounted for in waveguide mode theory. It will be shown that the latter two explanations are the most likely since the geometric optics results do improve considerably at higher frequencies and since geometric optics is unable to calculate the field above the duct which is due to the presence of "leaky" modes in this region. If the lack of a diffusely reflected field were a suitable reason, then the simulation error would be expected to increase rather than decrease at higher frequencies, since the sea would appear to be a rougher surface and thus a more diffuse reflector at shorter wavelengths. Also, an incorrect choice of electrical properties

for the sea would not be expected to produce a significant error in the Fresnel reflection coefficient of Eq. (180) for horizontally polarized fields. Little change occurs in the reflection coefficient over the range of small grazing angles encountered (0 to 0.359 deg) even for extremely large variations in surface electrical characteristics as evidenced by Figs. (12) through (17) in Chapter V.

While both the experimental data and waveguide calculations indicate that a relatively constant field is measured at the receiver when the transmitter is above the duct, the reciprocal height gain curve obtained from geometric optics shows no field present for this condition. Waveguide mode theory predicts that such a field does exist which is the result of the coupling of energy from the transmitted signal into the duct by means of "leaky" modes.[1, 14] If the transmitter and receiver were reversed, as they are in the simulation, then this field would exist above the duct because of energy leakage by the same types of modes. However as the ray traces of Figs. (29), (34), (40), and (45) show, there is nothing in the geometric optics solution to suggest energy leakage along the top of the duct.

To aid in describing energy leakage through a ducting layer, consider the comparison of a tropospheric duct to a dielectric slab waveguide. In the case of the dielectric waveguide, the field may be resolved into a sum of elementary waves or modes which are guided along the slab boundaries with little or no attenuation in the direction of propagation and with an exponential decay in the direction normal to the outside of either boundary. However a duct has no well defined upper boundary, such as a discontinuity in the refractive index, and consequently has propagation characteristics which are different from those of a simple dielectric waveguide. Mode theory predicts that two types of modes, commonly referred

to as "trapped" and "leaky" modes, may exist within a meteorological duct. Trapped modes are unattenuated modes of propagation which are analogous to those of the dielectric slab. Leaky modes, while guided within the duct along the earth's surface, are allowed to propagate obliquely to the duct in the region above the superrefractive layer. Energy is then coupled into or out of a duct when one or more leaky modes is strongly excited by a nearby transmitter.[1, 12, 16]

Figs. (51) and (52) show results at 65 MHz for a 120 naut mi transmitter to receiver separation with the receiver at 100 and 500 ft heights. Again Figs. (51a) and (52a) give simulated height gain curves using the Guadalupe Island refractivity profile, and Figs. (51b) and (52b) show simulation results obtained with the trilinear duct profile. As before, the geometric optics height gain curves are highly irregular, especially those using the trilinear refractivity profile. Also, the simulated height gains shown in these figures are generally 5 to 20 db greater than those of either the experimental or waveguide curves. It is quite evident that waveguide mode theory has a far better agreement with the experimental measurements at 65 MHz than does geometric optics.

Pappert and Goodhart indicate that equipment calibration errors have sometimes affected the measured data, resulting in this instance in a larger than expected difference between the experimental and mode theory height gain curves shown in Fig. (52). Evidence of equipment error appears in Figs. (51) and (52), where the measured field at 500 ft in Fig. (51) is not the same as the field at 100 ft in Fig. (52), thus indicating a violation of reciprocity.

Figs. (53) and (54) show experimental and calculated height gain curves at 170 MHz for a distance of 120 naut mi with the receiver height

at 100 and 500 ft. The simulation results are still in much poorer agreement with the measured data than are the waveguide calculations. However the geometric optics results of Fig. (53) do show a two mode interference structure which is slightly displaced from the same two mode pattern given by waveguide theory. Pappert and Goodhart note that the number of modes required in the waveguide calculations ranges from a single mode at 65 MHz and two modes at 170 MHz, to nearly a hundred modes at 3300 MHz. They also explain that the sharp null at 1200 ft in the experimental data of Fig. (53) is most likely the result of a transmitter and receiver antenna misalignment, and is therefore not to be interpreted as a real null.

Figs. (55) and (56) show height gain curves at 520 MHz for a range of 120 naut mi with receiver heights of 100 and 500 ft. The simulation results give field strengths that are within 5 to 10 db of the experimental and mode theory results, which is a considerable improvement over the previous cases at the lower frequencies. Agreement is generally best between the simulation results using the Guadalupe Island profile and mode theory results, although as Fig. (55a) shows, some of the interference lobes do not appear in the geometric optics height gain curve between the altitudes of 400 and 600 ft. The deep null at 1100 ft is again considered to be the result of antenna misalignment.

Fig. (56) shows waveguide calculations for cases where the modal equation is solved at the ground ($D = 0$) and at the bottom edge of the ducting layer which is at a height of 600 ft ($D = 600$). Pappert and Goodhart state that at this frequency modes exist which are either earth detached or evanescent at the ground. The height gain curve for $D = 600$ includes these additional modes and is in better agreement with experimental results by eliminating the fine structure of the $D = 0$ curve.

While the mode calculations in Fig. (55) are for D = 600, deep nulls appear in the waveguide height gain curve since the additional modes are sufficiently evanescent at the 100 ft receiver height so as not to affect the mode sum by any appreciable amount.

Since geometric optics solves for the direction of energy propagation through a medium, it is unable to model the distribution of energy contained in the nonpropagating evanescent modes existing within a duct. However ray optics is capable of describing earth detached propagation as evidenced by the ray traces of Figs. (29), (34), (40), and (45). These figures all show a number of rays which travel below the ducting layer without intersecting the earth's surface. Such elevated rays represent earth detached propagation which begins to appear in the simulated height gain curves at higher frequencies. In the 520 MHz case, geometric optics produces results which lie between the mode theory height gains for D = 0 and D = 600. It should be noted that neither ray optics nor mode theory gives results that are in very good agreement with the experimental data in Figs. (55) and (56). This discrepancy, which is mentioned by Pappert and Goodhart for the waveguide calculations, is suspected to be due to temporal or spatial fluctuations in the duct layer at the time of measurement.

Fig. (57) shows results at 3300 MHz for a range of 60 naut mi and a receiver height of 100 ft. The pair of solid curves for the experimental data represent the envelope of measured field strength at this range. The results obtained from geometric optics are in very good agreement with both the experimental and waveguide theory height gain curves. Mode theory predicts a large decrease in the field above 800 ft because of the destructive interference in this region of nearly 100 modes. Pappert and Goodhart point out that this phasing would be eliminated, however, by a

turbulence in the ducting layer of the trilinear refractivity model.

Figs. (58) and (59) show results at 3300 MHz for a transmitter to receiver separation of 120 naut mi with the receiver at 100 and 500 ft. While the simulation results fall between the experimental and waveguide height gain curves for the 100 ft receiver of Fig. (58), both geometric optics and mode theory predict fields that are 5 to 10 db higher than the field measured at this altitude. Unless both mode theory and geometric optics are in error, the most likely explanations are that either an antenna alignment error still continued to exist or the duct did not remain stationary and horizontally homogeneous at the time of measurement. In the case of the 500 ft high receiver the simulated height gain curves given for the Guadalupe Island profile in Fig. (59a) again appear to be in better agreement with the mode theory calculations than those simulated with the trilinear profile in Fig. (59b). The experimental results, while lacking the fine structure of either the ray optics or waveguide height gain curves, are shown to be an approximate average of the calculated curves in Fig. (59). This may be due to either a change in the duct refractivity which is not accounted for in either duct profile model or the existence of other earth detached or evanescent modes which were not included in either the mode theory or geometric optics results.

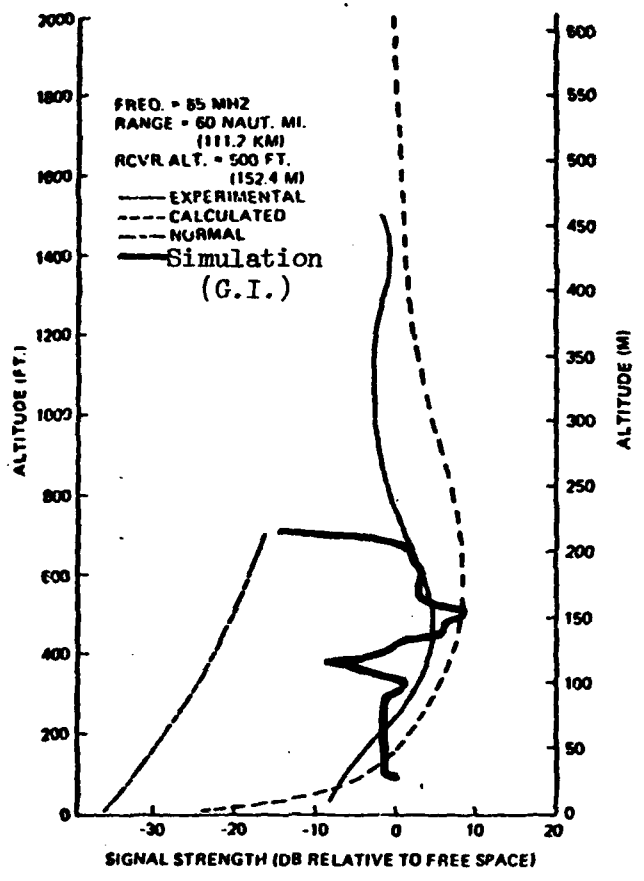


(a)

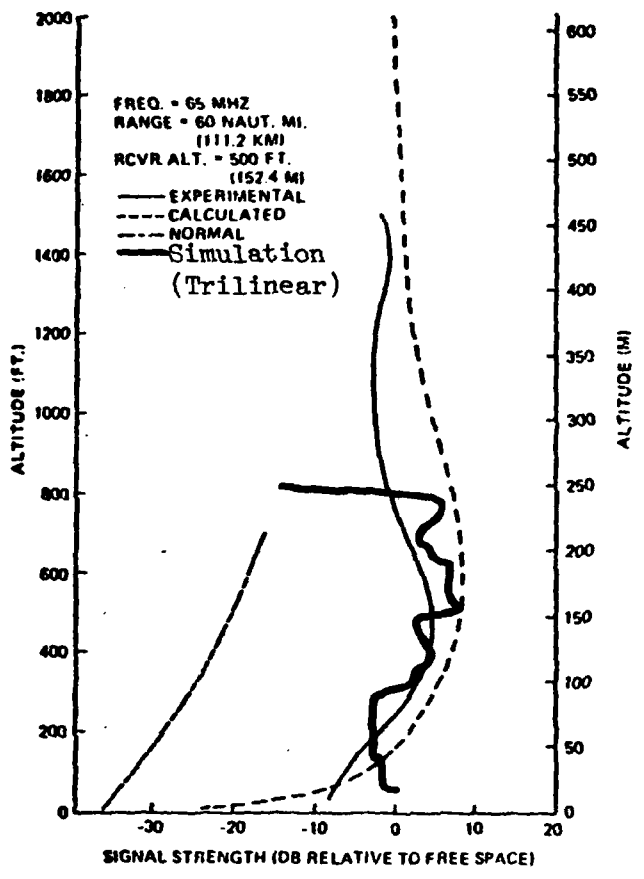


(b)

Fig. 50. Height gain curves at 65 MHz, for $h_o$ = 500 ft and x = 60 naut mi

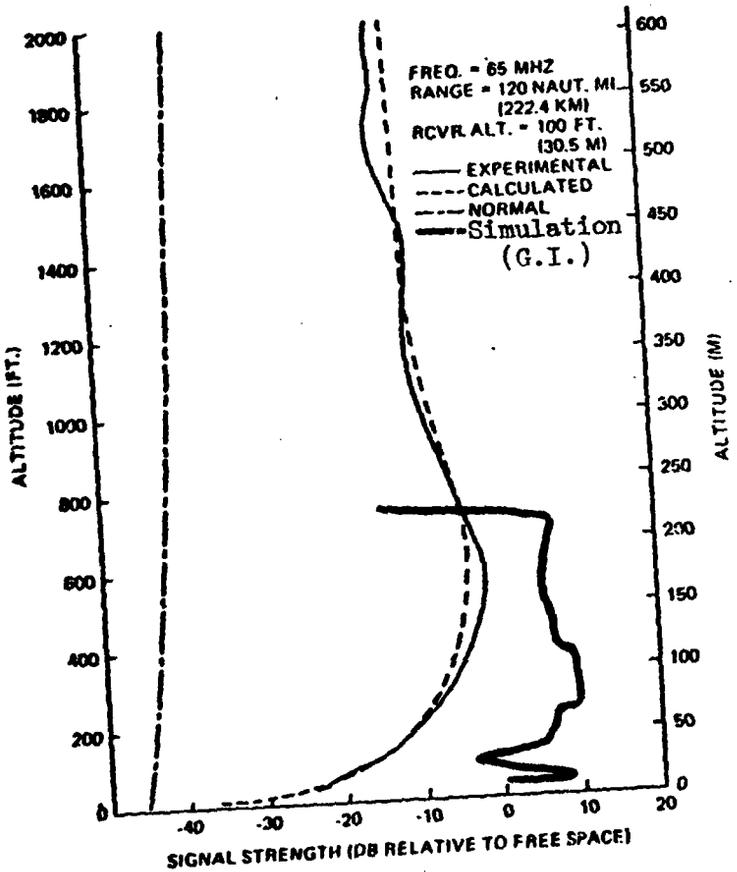


(a)

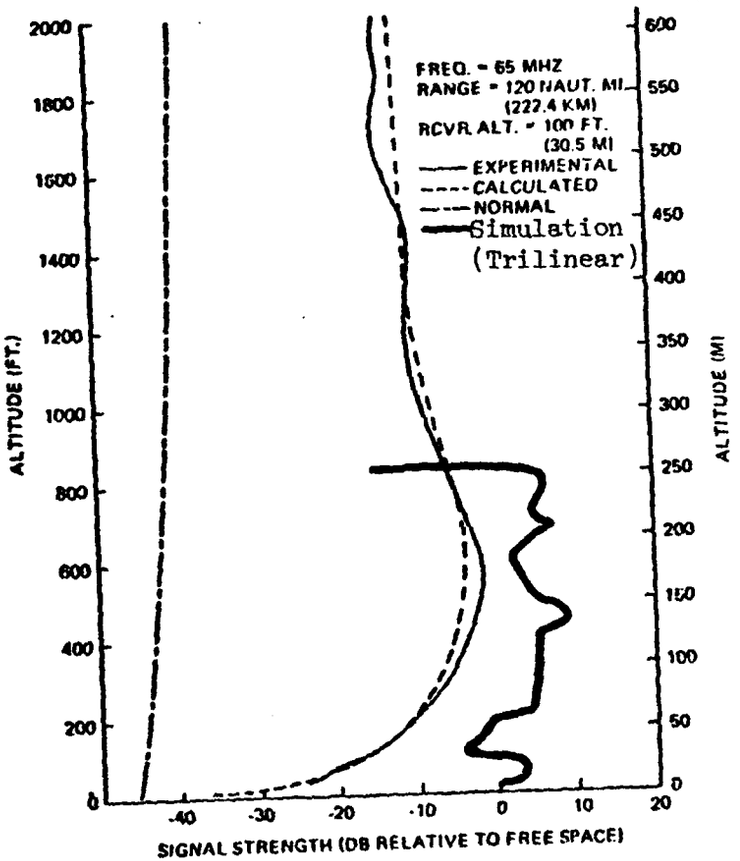


(b)

Fig. 51. Height gain curves at 65 MHz, for $h_o$ = 100 ft and x = 120 naut mi

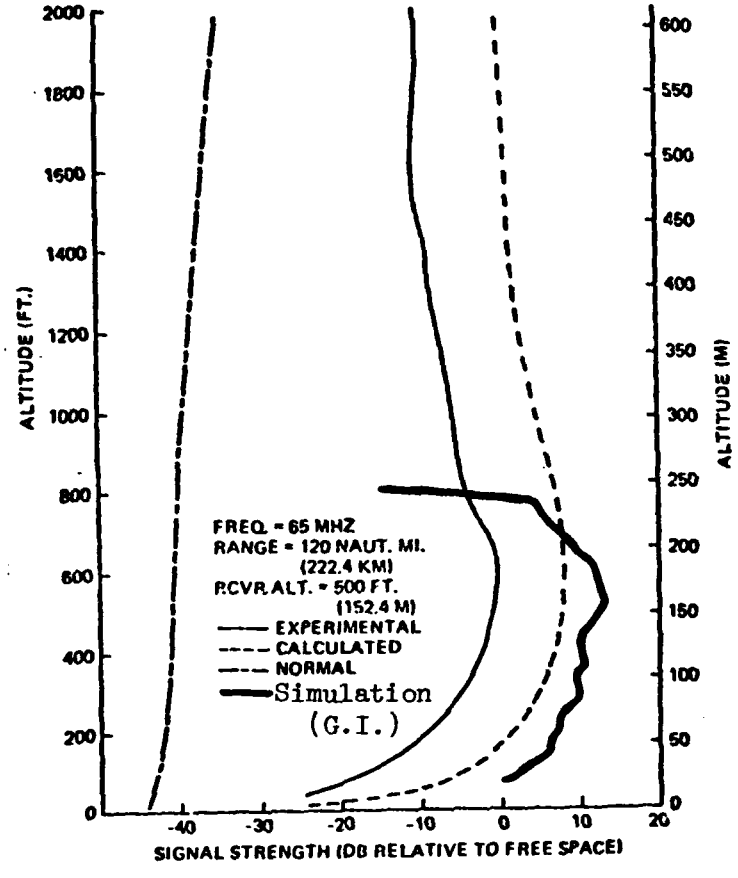


(a)

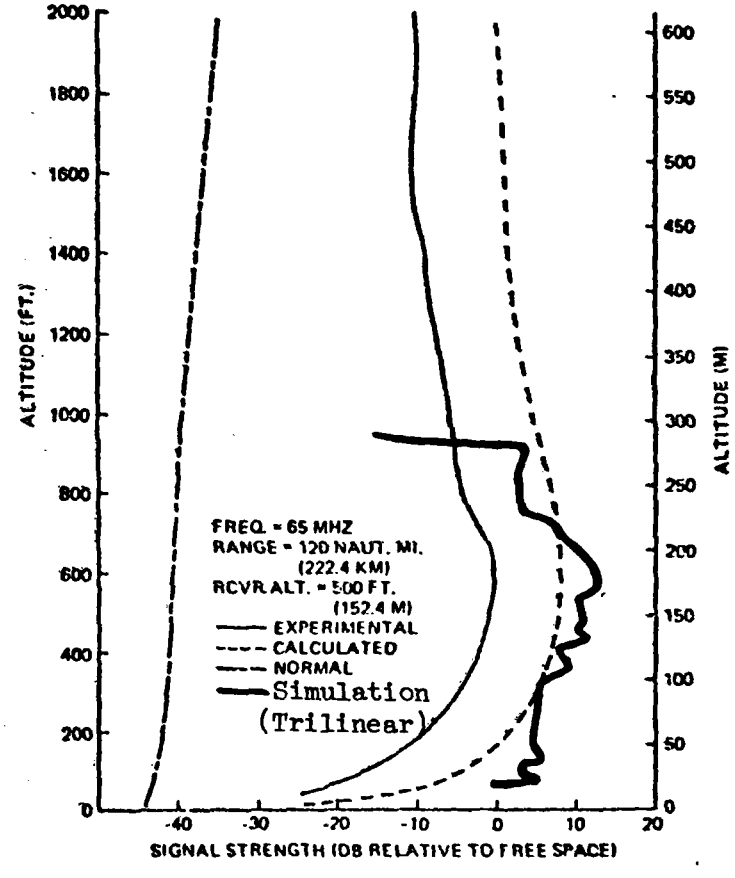


(b)

Fig. 52. Height gain curves at 65 MHz, for $h_o$ = 500 ft and x = 120 naut mi

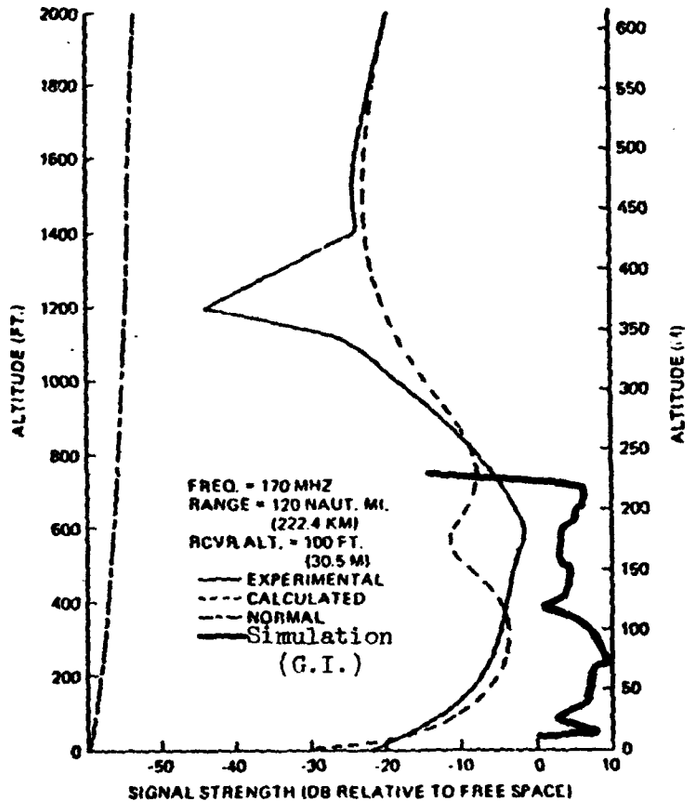


(a)

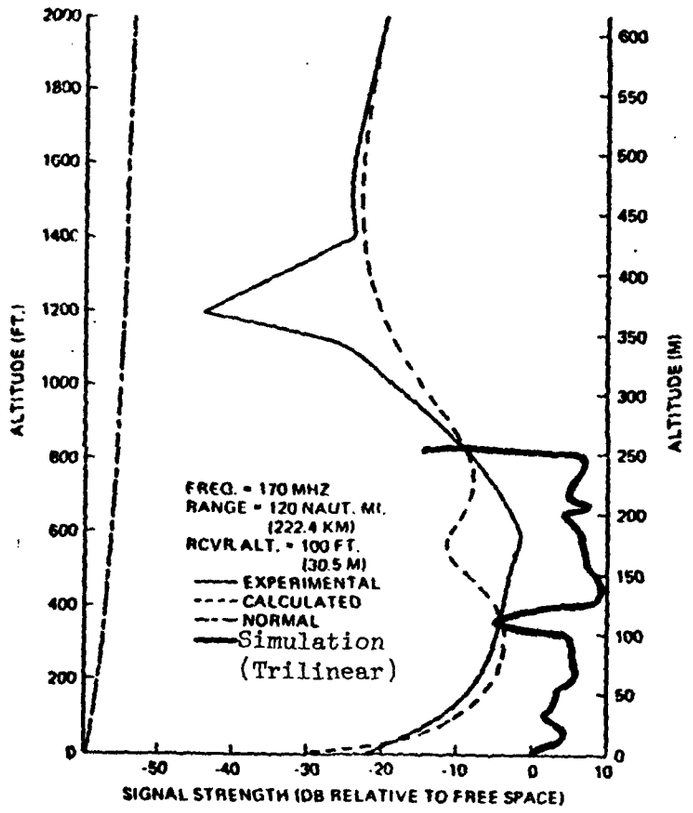


(b)

Fig. 53. Height gain curves at 170 MHz, for $h_o$ = 100 ft and x = 120 naut mi

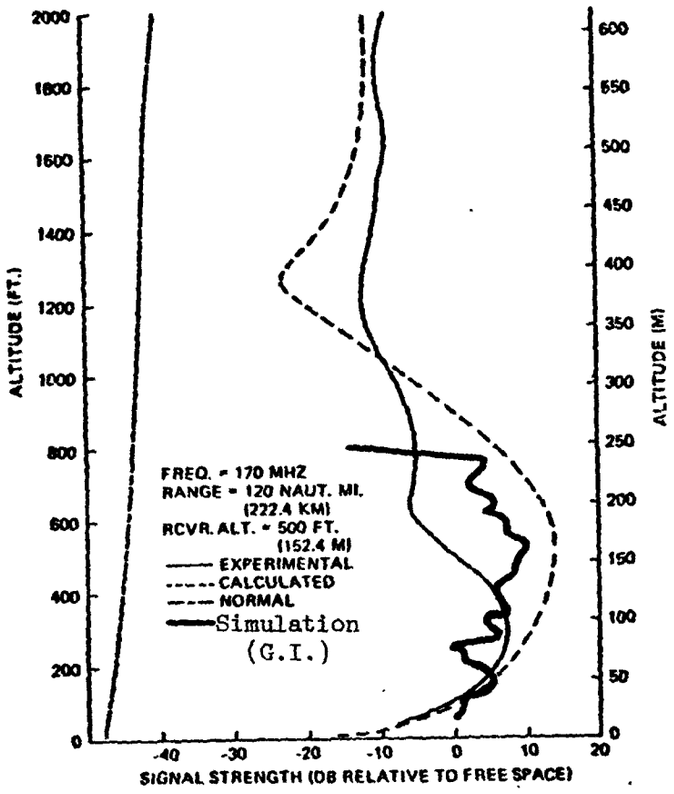


(a)

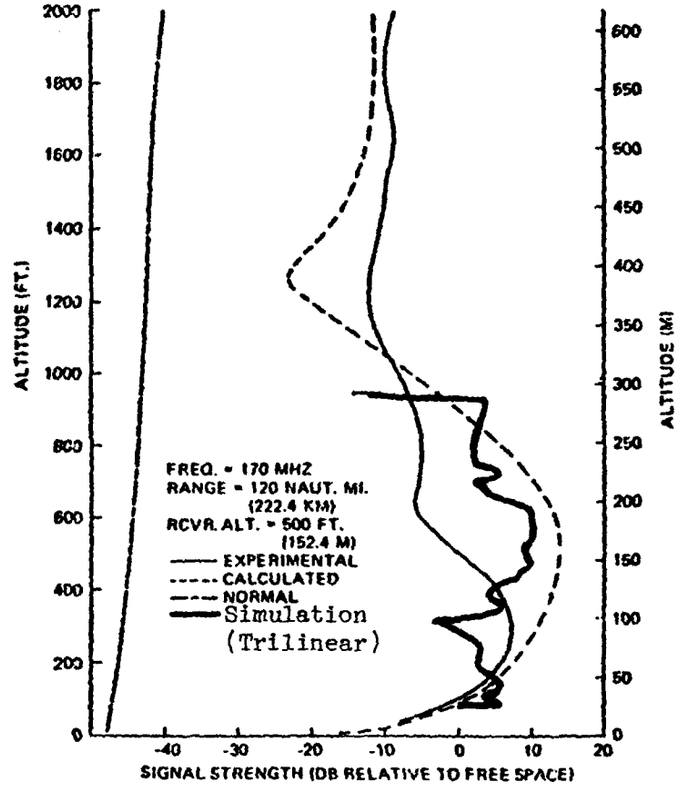


(b)

Fig. 54. Height gain curves at 170 MHz, for $h_o$ = 500 ft and x = 120 naut mi

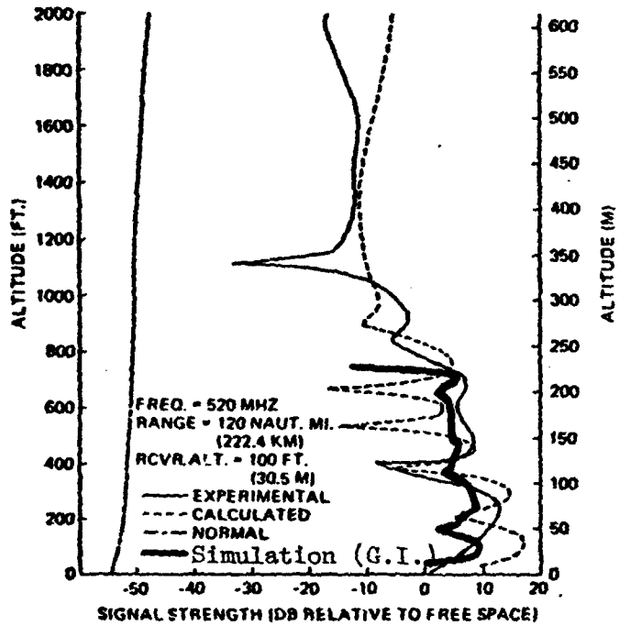


(a)

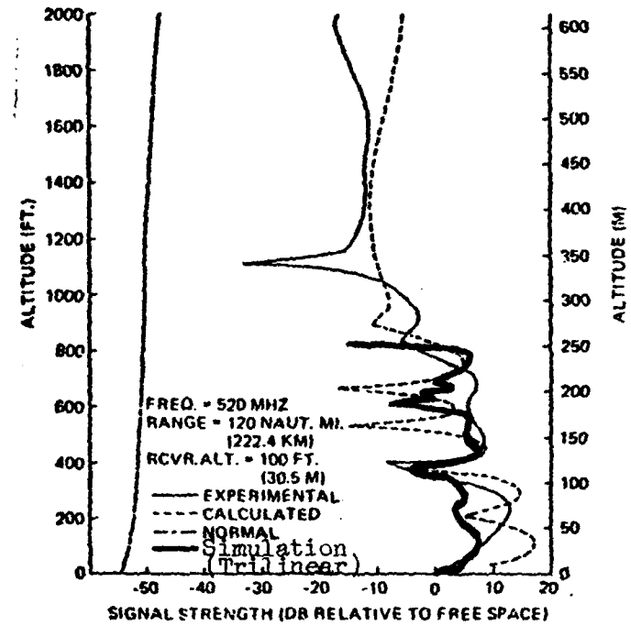


(b)

Fig. 55. Height gain curves at 520 MHz, for $h_o$ = 100 ft and x = 120 naut mi

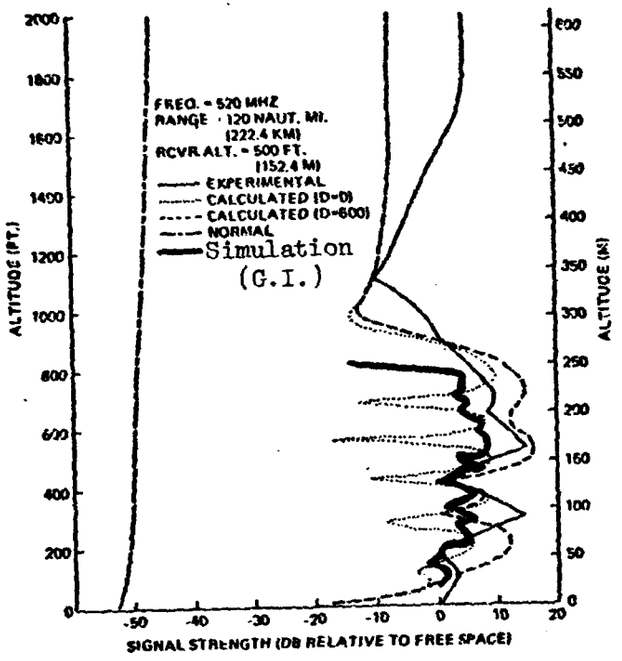


(a)

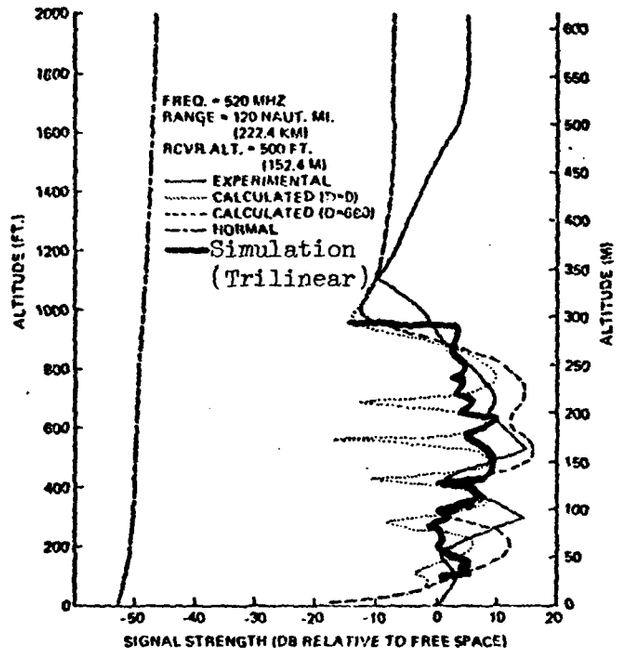


(b)

Fig. 56. Height gain curves at 520 MHz, for $h_o$ = 500 ft and x = 120 naut mi

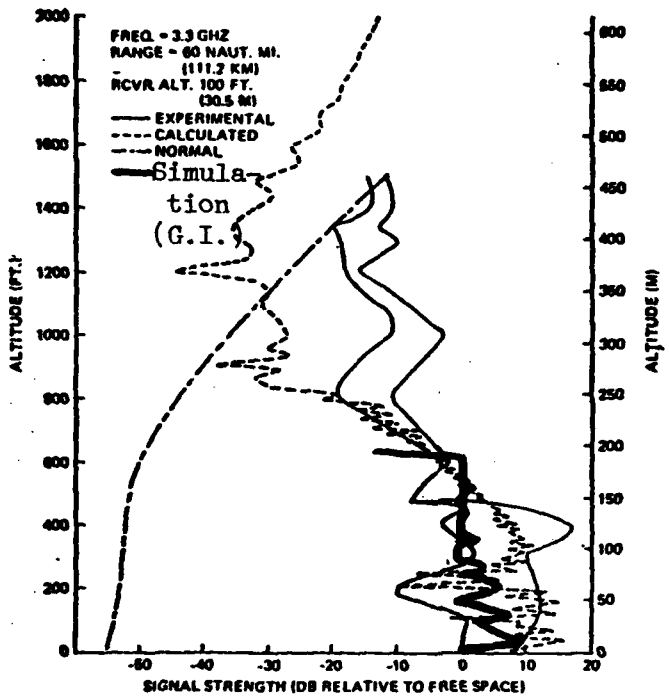


(a)

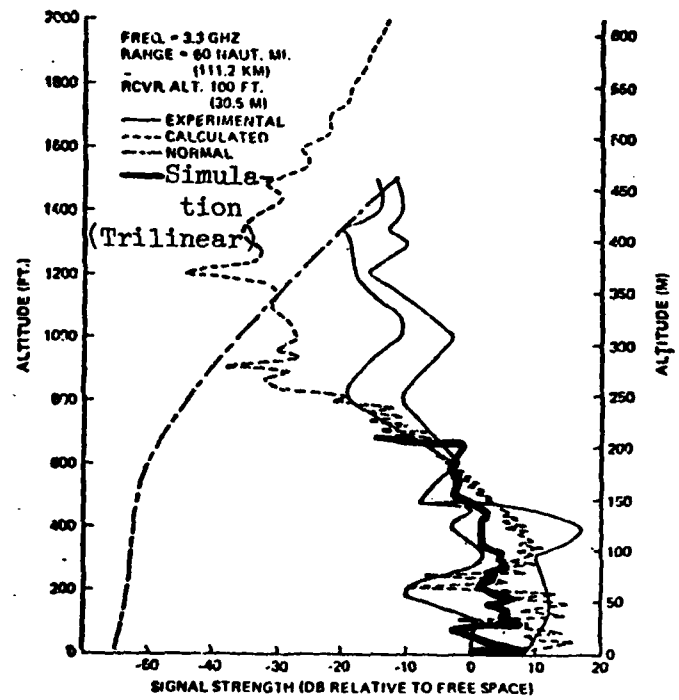


(b)

Fig. 57. Height gain curves at 3.3 GHz, for $h_o$ = 100 ft and x = 60 naut mi

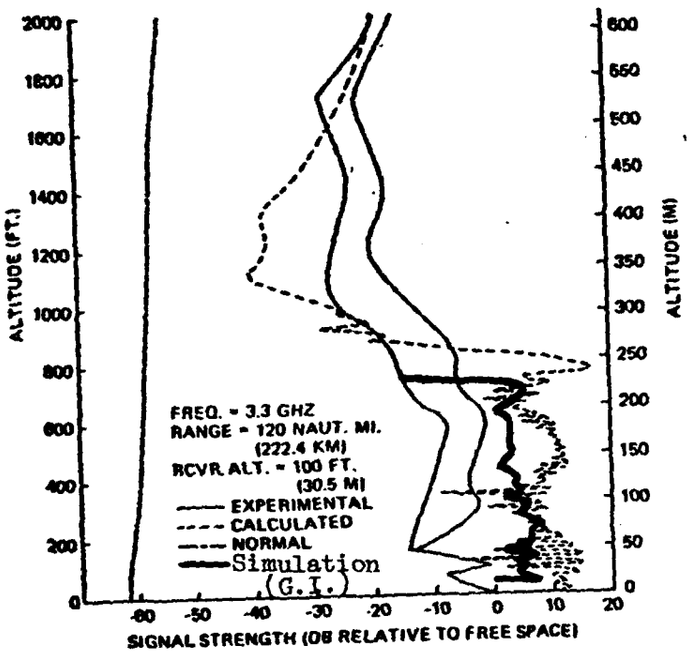


(a)

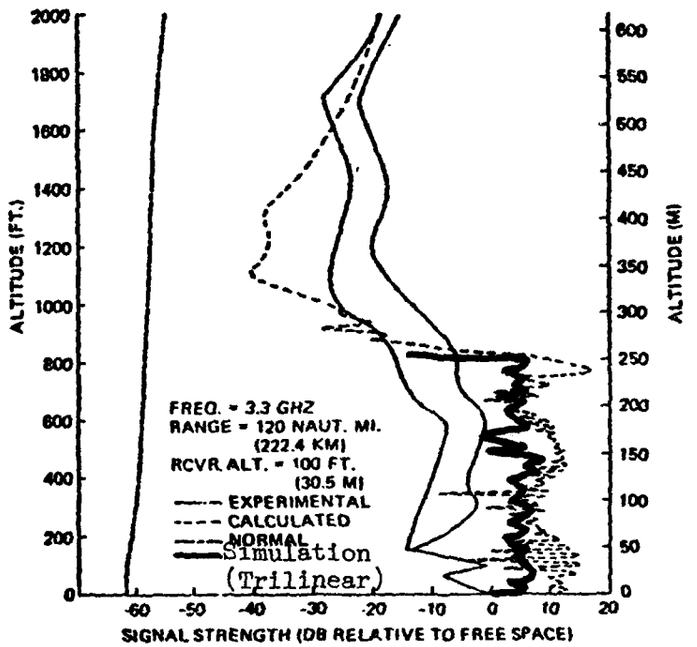


(b)

Fig. 58. Height gain curves at 3.3 GHz, for $h_o$ = 100 ft and x = 120 naut mi

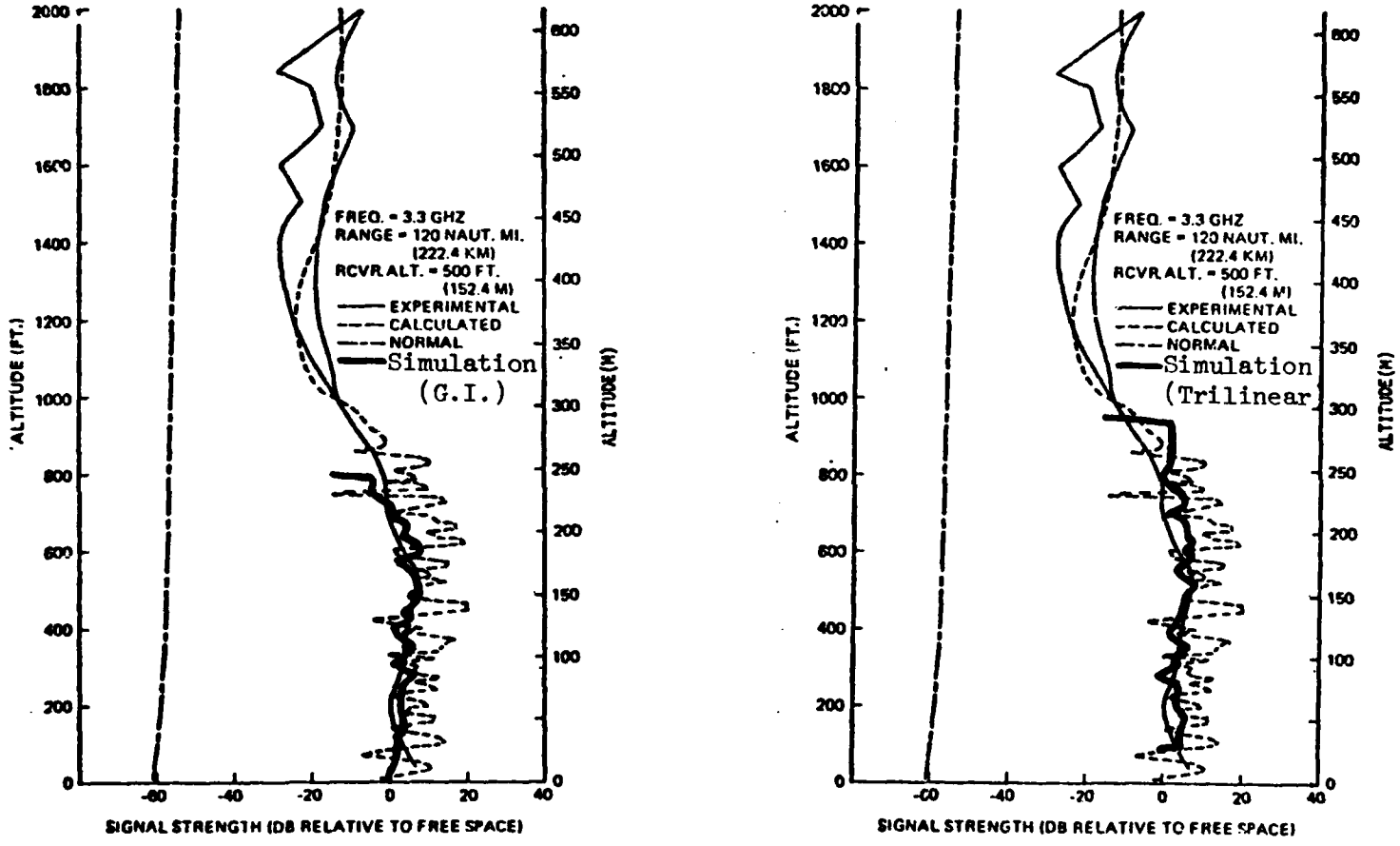


(a) (b)

Fig. 59. Height gain curves at 3.3 GHz, for $h_o$ = 500 ft and x = 120 naut mi

# CHAPTER VII

## SUMMARY AND CONCLUSIONS

The results presented in this paper indicate that classical geometric optics yields moderately fair predictions of the strength of a tropospherically ducted field at frequencies below 100 to 200 MHz, and reasonably good estimates at frequencies above 500 MHz. The fields calculated from geometric optics were generally higher and more irregular than those obtained experimentally or from waveguide mode theory at 65 and 170 MHz, although at 170 MHz both mode and ray theories differed at times from the measured field by as much as 20 db. These errors may be related to problems in the alignment and calibration of the measurement equipment or in temporal and spatial fluctuations in the ducting layer. In the case of the geometric optics results a further explanation may lie with the restrictions of Eqs. (77) and (78) in Chapter IV, which state that ray theory is useful as a propagation model only at high frequencies. Nonetheless, ray optics appears to provide an order of magnitude approximation to the field as low as 65 MHz, which could conceivably be extended down to 30 MHz where atmospheric refraction becomes the primary mechanism for long distance radio propagation.

By contrast, the fields calculated from geometric optics at 520 and 3300 MHz were generally within 5 to 10 db of both the experimental and waveguide theory results. In some of the examples shown at these higher frequencies, ray theory was in better agreement with waveguide theory than with the experimental data. Again this difference may have resulted from

equipment error or inhomogeneities in the duct layer. Finally, the ray theory calculations which had the closest agreement with either experimental or mode theory results were those derived from the Guadalupe Island refractivity profile. The only plausible reason for this outcome is that the Guadalupe Island profile, by including several variations in the refractivity structure both within the ducting layer and near the earth surface which were not modeled by the trilinear profile, simply was more representative of the Guadalupe Island duct.

Limitations that are inherent to classical ray theory have been noted throughout this paper. These include the inability to model diffracted fields and certain propagating (leaky) and nonpropagating (evanescent) modes which are present in a tropospheric duct. Regions in which these effects are of concern, such as the earth shadow region and the area above a duct, must then be treated by the diffraction and waveguide mode theories of physical optics.

Despite its obvious limitations, geometric optics provides a useful qualitative as well as quantitative description of the effects of atmospheric refraction on wave propagation. Given a distribution of atmospheric refractive index, the ray trajectories of geometric optics yield an easily understood representation of wavefront propagation through layered atmospheres with a minimum of computational effort. Furthermore, unlike waveguide mode theory where large numbers of modes may be required to obtain a field solution, geometric optics is able to make rapid and efficient field calculations for different frequencies, polarizations, and surface properties based upon a single set of ray trajectories. This ability to lend a physical interpretation to refraction effects plus the ease and efficiency of computation, make ray theory an attractive alternative to the more laborious mode theory of propagation, especially when

several layers are present in the atmosphere. Moreover, the results presented in this thesis indicate that geometric optics, when properly understood and applied, offers a reasonably accurate method for determining the strength of a field in an inhomogeneous atmospheric structure, such as a tropospheric duct, which is comparable in realism to that of waveguide mode theory.

# APPENDIX

This Appendix provides a description plus instructions for use of the atmospheric refractivity computer simulation (ATREF) discussed in Chapter V. Program ATREF is written in Extended FORTRAN language for the CDC 6600 digital computer system and requires approximately 65,000 octal words of memory. Approximately 12 to 15 seconds of central processor time are required to calculate the ray trajectories and height gains for an emitter at one frequency. Program input is given in standard card image form and output is provided in both printed and on-line CALCOMP plotted formats, depending on user selection. A description of the executive program and seven subroutines of the computer simulation is given below.

ATREF is the main executive program which controls the input/output functions, refractivity model selection, and calculation of the ray trajectories and height gain curves. Refractivity profiles may consist of either the stored free space or exponential CRPL models given by Eqs. (16), (129), and (130), or an input profile. Input profiles are stored as piecewise linear functions connecting the data points of the profiles.

REFRCT performs the printing and plotting of the refractivity and refractivity gradient profiles.

RKINTC sets up the integration of the ray trajectory and time of propagation differential equations given by Eqs. (131) through (133). When a ray crosses a boundary between two piecewise linear segments of

an input refractivity profile or when a ray intersects the earth, RKINTG integrates to the boundary by means of a variable step size interpolation algorithm. The ray equations are then reinitialized at the boundary and integration continues until another boundary is crossed, repeating the interpolation process.

RK integrates the ray equations by means of a fourth order Runge-Kutta algorithm using either an integration step size of DELX=XDELTA/10, where XDELTA is the distance interval along the earth's surface for printing and plotting the height gain curves, or a step size computed by the interpolation operation in subroutine RKINTG.

ATMOS computes atmospheric refractivity at the ray height and sets up the ray equations for use in subroutine RK.

SCATT calculates the complex Fresnel reflection coefficient and surface roughness factor for use in Eqs. (158), (159), and (187).

HGAIN computes the relative field strength and power density by means of Eqs. (137) through (160) in Chapter V. The height gain is obtained from field calculations at 100 overlapping "window" or altitude increments (of height $dl_v$ in Chapter V) between the highest and lowest rays. Regions that are not correctly modeled by geometric optics, such as earth shadow regions and caustics, are omitted in the height gain plots and represented in the printed output by asterisks (*).

PLOTTR draws and labels all plot axes and prints two lines for labeling above each plot. PLOTTR also prints a one line banner preceding the plots for additional descriptive purposes (e.g., the date), and provides for scaling the plots from their normal sizes (4x5 inches for N and dN/dh profiles plots and 10x5 inches for ray traces and height gain curves).

A flow diagram and program listing are given in Figs. (60) and (61), with input specifications, sample input and sample output shown in Tables (10), (11), and (12), respectively.

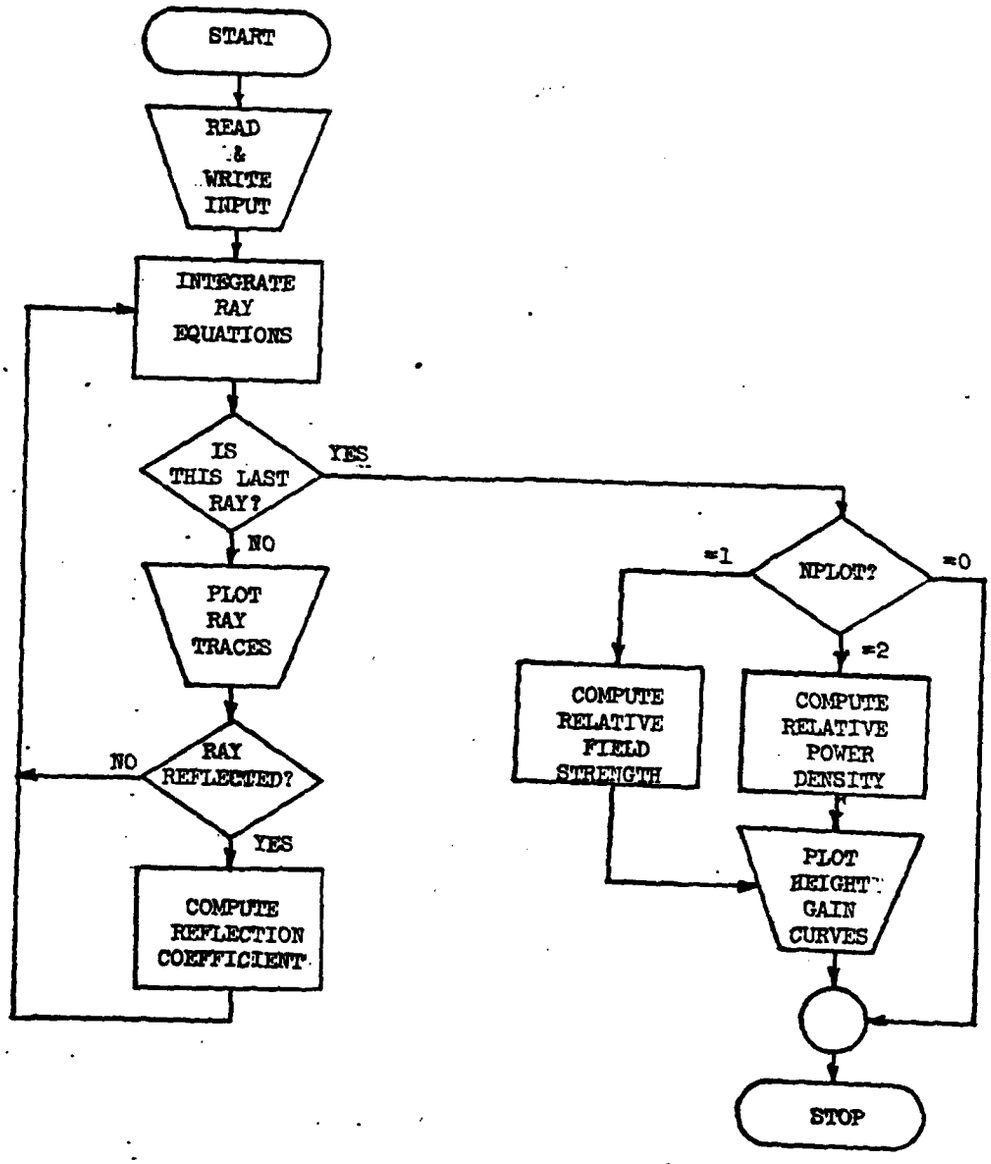


Fig. 60. Computer program flow diagram

```
      PROGRAM ATREF (INPUT,OUTPUT,PLOT)
C
C-----THIS PROGRAM IS A GEOMETRIC OPTICS MODEL OF WAVE PROPAGATION
C-----THROUGH AN INHOMOGENEOUS ATMOSPHERE HAVING A VERTICALLY
C-----STRATIFIED INDEX OF REFRACTION.  THE PROGRAM CALCULATES THE
C-----DIRECTION OF WAVEFRONT PROPAGATION BY SOLVING THE EULER-
C-----LAGRANGE EQUATIONS OF RAYS NORMAL TO INCREMENTAL WAVEFRONT
C-----SURFACES.  THE RAY TRAJECTORIES ARE THEN USED TO COMPUTE
C-----THE RELATIVE EMITTER FIELD STRENGTH OR POWER DENSITY
C-----(NORMALIZED TO FREE SPACE) AS A FUNCTION OF ALTITUDE AND
C-----DISTANCE ALONG THE EARTH'S SURFACE.  FIELDS WHICH ARE
C-----REFLECTED FROM THE EARTH ARE ATTENUATED BY A FRESNEL
C-----REFLECTION COEFFICIENT AND A SURFACE ROUGHNESS FACTOR.
C-----THE ELEVATION ANGLE AND TIME OF PROPAGATION ARE CALCULATED
C-----ALONG EACH RAY PATH TO DETERMINE THE DIRECTION OF THE
C-----WAVEFRONT PROPAGATION VECTOR AND THE PHASE RELATIONSHIP
C-----BETWEEN INTERFERING WAVEFRONTS FOR THE FIELD STRENGTH AND
C-----POWER DENSITY COMPUTATIONS.
C
      COMMON /ONECOM/ CRH,CRX,CRG,DTR,JAREA,NDATA,C,C1,C2
     1      ,RHO(51,30),PHI(51,30),PI,CMF,CNAUT,AHS
     2      ,FRQ,TPW,NHV,NSL,NRMS,ABSRH,PHASE,THETA
      COMMON /TWOCOM/ RA,DELX,AHO,ELO(51),JRAY,EXMAX,AHMAX,XFINAL
      COMMON /THRCOM/ NELD,JPLOT,IPLACE,VX(30),JCASE
     1      ,H(51,30),G(51,30),HN(50),RN(50),S(51,30)
     2      ,KSIZ,YSIZ,JPLT,XMIN,YMIN,XDIV,YDIV
     3      ,XMAX,YMAX,NREF,NRAY,NPRO,NPLOT,NGRAD
     4      ,KREF,KGRAD,KPLOT
      DIMENSION POL(2),TER(4),REFMOD(2,3)
      DATA POL/10HHORIZONTAL,10HVERTICAL  /
      DATA TER/10HSEA WATER ,10HDRY GROUND,10HAVG GROUND,10HWET GROUND/
      DATA REFMOD/10HFREE SPACE,10H MODEL    ,10HEXPONENTIA,
     1            10HL MODEL    ,10HINPUT PROF,10HILE MODEL /
      DATA DTR,RA,CM,PI/1.7453E-02,2.0925E+07,2.998E+08,3.14159/
      DATA CMF,CNAUT/3.281,6076.0/
C
C     SET UP THE NUMBER OF PROGRAM RUNS
      READ 300,NCASE
      DO 200 ICASE=1,NCASE
C
C     READ AND PRINT THE INPUT DATA
      READ 300,NPRO
      READ 300,NDATA
      READ 310,((HN(ID),RN(ID)),ID=1,NDATA)
      READ 320,AHS,AHO,AHMAX
      READ 320,XDELTA,XFINAL
      READ 320,ELOS1,ELOS2
      READ 320,FRQ,PW
      READ 300,NHV,NSL,NRMS
      READ 300,KREF,KGRAD,KRAY,KPLOT
      READ 300,NREF,NGRAD,NRAY,NPLOT
      PRINT 330
      PRINT 340,NCASE,NPRO,(REFMOD(IRM,NPRO+1),IRM=1,2)
      PRINT 350,AHS,AHO,AHMAX
      PRINT 360,XDELTA,XFINAL
      PRINT 370,ELOS1,ELOS2
      PRINT 380,FRQ,PW,POL(NHV),TER(NSL),NRMS
```

Fig. 61. Program listing

```
      PRINT 390,KREF,KGRAD,KRAY,KPLOT
      PRINT 400,NREF,NGRAD,NRAY,NPLOT
C
C     CALCULATE ZERO MEAN SEA LEVEL REFRACTIVITY IF NOT ALREADY KNOWN
      NTEMP=NDATA
      IF (HN(NDATA)) 8,8,5
    6 SLOPE=(RN(NDATA-1)-RN(NDATA))/(HN(NDATA-1)-HN(NDATA))
      RN(NDATA+1)=RN(NDATA)-SLOPE*HN(NDATA)
      HN(NDATA+1)=0.0
      NTEMP=NDATA+1
C
C     SET UP INITIAL ATMOSPHERIC REFRACTIVITY CONSTANTS
    8 IF (NPRO-1) 10,15,20
C
C     FREE SPACE MODEL
   10 C1=0.0
      C2=0.0
      GO TO 25
C
C     EXPONENTIAL MODEL
   15 C1=313.0
      C2=0.00004386
      GO TO 25
C
C     PIECE-WISE LINEAR MODEL
   20 C1=RN(NTEMP)
      C2=(ALOG(RN(NTEMP))-ALOG(RN(1)))/HN(1)
C
C     SET UP INITIAL CONDITIONS
   25 C=CMF*CM
      NELO=50
      CNELO=(ELOS1-ELOS2)*FLOAT(NELO)
      DENOT=1./FLOAT(NELO)
      DELX=CNAUT*XDELTA/10.
      EXMAX=CNAUT*XFINAL
      FRQ=1000000.0*FRQ
      PLACE=EXMAX/DELX
      TPW=PW/1000000.0
      ICALC=KPLOT+NRAY+NPLOT
      IPLACE=IFIX(PLACE)+1
      IPLOT=NREF+NGRAD+NRAY+NPLOT
      JCASE=ICASE
      JPLT=0
      NELO=IFIX(CNELO)+1
C
C     CALL ROUTINES IF THERE IS A PRINTOUT OR PLOT OF THE
C     REFRACTIVITY PROFILE
      JPLOT=1
      IF (NREF) 30,30,31
   30 IF (KREF) 33,33,32
   31 CALL PLOTTR
   32 CALL REFRCT
C
C     CALL ROUTINES IF THERE IS A PRINTOUT OR PLOT OF THE
C     REFRACTIVITY GRADIENT
   33 JPLOT=2
      IF (NGRAD) 34,34,35
```

Fig. 61. (continued)

```
   34 IF (KGRAD) 37,37,36
   35 CALL PLOTTR
   36 CALL REFRCT
C
C     CHECK IF THERE ARE ANY FURTHER CALCULATIONS
   37 IF (ICALC) 200,200,40
C
C     CHECK IF THERE IS TO BE A PLOT OF THE RAY TRACES.  IF SO,
C     CALL ROUTINE TO SET UP THE PLOT AXES
   40 IF (NRAY) 44,44,42
   42 JPLOT=3
      CALL PLOTTR
   44 CONTINUE
C
C     SET UP A LOOP TO CALCULATE THE ALTITUDE PROFILE OF EACH RAY
      DO 100 I=1,NELO
C
C     INITIALIZE FOR INTEGRATION
      CRH=AHO
      CRK=0.0
      ICCC=I-1
      ELO(I)=ELOS1-DENOT*FLOAT(ICCC)
      EANG=DTR*ELO(I)
      CRG=((RA+CRH)/RA)*SIN(EANG)/COS(EANG)
      JRAY=I
C
C     CALL ROUTINE TO COMPUTE RAY TRACES AND PROPAGATION TIMES
      CALL RKINTG
  100 CONTINUE
C
C     RESET PARAMETER VALUES
      DELX=10.*DELX
      IPLACE=IPLACE/10+1
C
C     CALL ROUTINES IF THERE IS A PRINTOUT OR PLOT OF THE
C     RELATIVE FIELD STRENGTH OR RELATIVE POWER DENSITY
  120 JPLOT=4
      IF (NPLOT) 130,130,140
  130 IF (KPLOT) 200,200,150
  140 CALL PLOTTR
  150 CALL HGAIN
  200 CONTINUE
C
C     CALL LIBRARY ROUTINE FOR ON-LINE PLOTTING
      IF (IPLOT) 220,220,210
  210 CALL PLOTE
      PRINT 430
  220 CONTINUE
C
  300 FORMAT (6I5)
  310 FORMAT (2F15.7)
  320 FORMAT (5F15.7)
  330 FORMAT (1H1,2X,*ATMOSPHERIC RADIO REFRACTIVITY COMPUTATIONS*//)
  340 FORMAT (2X,*   NCASE=*,I6/
     1         2X,*    NPRO=*,I6/
     2         2X,*   MODEL=*,5X,2A10)
  350 FORMAT (2X,*     AHS=*,F10.2,4X,*FEET*/
```

Fig. 61. (continued)

```
    1          2X,*      AHD=*,F10.2,4X,*FEET*/
    2          2X,*    AHMAX=*,F10.2,4X,*FEET*)
360 FORMAT (2X,*   XDELTA=*,F10.2,4X,*NAUT MI*/
    1          2X,*   XFINAL=*,F10.2,4X,*NAUT MI*)
370 FORMAT (2X,*    ELOS1=*,F10.2,4X,*DEG*/
    1          2X,*    ELOS2=*,F10.2,4X,*DEG*)
380 FORMAT (2X,*      FRQ=*,F10.2,4X,*MHZ*/
    1          2X,*       PW=*,F10.2,4X,*MICROSEC*/
    2          2X,*    POLAR=*,5X,A10/
    3          2X,* TERRAIN=*,5X,A10/
    4          2X,*     NRMS=*,I6)
390 FORMAT (2X,*     KREF=*,I6/
    1          2X,*    KGRAD=*,I6/
    2          2X,*     KRAY=*,I6/
    3          2X,*    KPLOT=*,I6)
400 FORMAT (2X,*     NREF=*,I6/
    1          2X,*    NGRAD=*,I6/
    2          2X,*     NRAY=*,I6/
    3          2X,*    NPLOT=*,I6)
430 FORMAT (5X,*END OF FILE ON PLOTTER TAPE*)
    END
```

Fig. 61. (continued)

```
      SUBROUTINE REFRCT
C
C-----THIS ROUTINE CALCULATES AND PLOTS THE REFRACTIVITY AND
C-----REFRACTIVITY GRADIENT PROFILES
C
      COMMON /ONECOM/ CRH,CRX,CRG,DTR,JAREA,NDATA,C,C1,C2
     1      ,RHO(51,30),PHI(51,30),PI,CMF,CNAUT,AHS
     2      ,FRQ,TPW,NHV,NSL,NRMS,ABSRH,PHASE,THETA
      COMMON /TWOCOM/ RA,DELX,AHO,ELO(51),JRAY,EXMAX,AHMAX,XFINAL
      COMMON /THRCOM/ NELD,JPLOT,IPLACE,VX(30),JCASE
     1      ,H(51,30),G(51,30),HN(50),RN(50),S(51,30)
     2      ,XSIZ,YSIZ,JPLT,XMIN,YMIN,XDIV,YDIV
     3      ,XMAX,YMAX,NREF,NRAY,NPRO,NPLOT,NGRAD
     4      ,KREF,KGRAD,KPLOT
      DIMENSION X(150),Y(150)
C
C     PRINT HEADING IF THERE IS A PRINTOUT
      IF (JPLOT-1) 10,10,14
   10 IF (KREF) 18,18,12
   12 PRINT 110
      GO TO 18
   14 IF (KGRAD) 18,18,16
   16 PRINT 120
C
C     SET UP INITIAL CONDITIONS TO CALCULATE REFRACTIVITY AND
C     REFRACTIVITY GRADIENT VERSUS ALTITUDE
   18 IF (NPRO-1) 20,20,30
   20 ID=51
      DELH=AHMAX/50.
      A=AHMAX+DELH
      GO TO 40
   30 ID=NDATA
      L=0
      M=0
      IF (HN(1)-AHMAX) 35,60,60
   35 DELH=(AHMAX-HN(1))/25.
      A=AHMAX+DELH
      ID=24
      M=ID-1
C
C     SET UP A LOOP TO PRINT AND PLOT THE FREE SPACE AND EXPONENTIAL PROFILES
   40 CONTINUE
      DO 55 I=1,ID
      A=A-DELH
      X(I)=C1*EXP(-C2*A)
      Y(I)=A
      IF (JPLOT-1) 42,42,46
C
C     PRINT THE REFRACTIVITY PROFILE
   42 X1=X(I)
      Y1=Y(I)
      IF (KREF) 44,44,43
   43 PRINT 140,I,Y1,X1
   44 IF (NREF) 54,54,50
C
C     PRINT THE REFRACTIVITY GRADIENT PROFILE
   46 IF (I-ID) 47,54,54
```

Fig. 61. (continued)

```
   47 X1=1000.*(X(I)-X(I+1))/(Y(I)-Y(I+1))
      Y1=(Y(I)+Y(I+1))/2.0
      IF (KGRAD) 49,49,48
   48 PRINT 140,I,Y1,X1
   49 IF (NGRAD) 54,54,50
C
C     PLOT THE REFRACTIVITY AND REFRACTIVITY GRADIENT PROFILES
   50 X1=X1/XDIV
      Y1=Y(I)/YDIV
      Y2=Y(I+1)/YDIV
      IF (I-1) 52,52,53
   52 CALL PLOT (X1,Y1,3)
   53 CALL PLOT (X1,Y1,2)
      CALL PLOT (X1,Y2,2)
   54 CONTINUE
   55 CONTINUE
      IF (NPRO-1) 80,80,55
C
C     SET UP A LOOP TO PRINT AND PLOT THE PIECE-WISE LINEAR PROFILES
   56 L=ID
   60 LP=0
      DO 75 I=1,NDATA
      IF (HN(I)-AHMAX) 61,61,74
   61 L=L+1
      LP=LP+1
      M=M+1
      X(L)=RN(I)
      Y(L)=HN(I)
      IF (JPLOT-1) 62,62,55
C
C     PRINT THE REFRACTIVITY PROFILE
   62 X1=X(L)
      Y1=Y(L)
      IF (KREF) 64,64,63
   63 PRINT 140,L,Y1,X1
   64 IF (NREF) 74,74,70
C
C     PRINT THE REFRACTIVITY GRADIENT PROFILE
   65 IF (I-NDATA) 67,66,56
   66 IF (NPRO-1) 67,67,74
   67 X1=1000.*(X(M)-X(M+1))/(Y(M)-Y(M+1))
      Y1=(Y(M)+Y(M+1))/2.0
      IF (KGRAD) 69,69,68
   68 PRINT 140,M,Y1,X1
   69 IF (NGRAD) 74,74,70
C
C     PLOT THE REFRACTIVITY AND REFRACTIVITY GRADIENT PROFILES
   70 X1=X1/XDIV
      Y1=Y(M)/YDIV
      Y2=Y(M+1)/YDIV
      IF (LP-1) 72,72,73
   72 CALL PLOT (X1,Y1,3)
   73 CALL PLOT (X1,Y1,2)
      CALL PLOT (X1,Y2,2)
   74 CONTINUE
   75 CONTINUE
C
```

Fig. 61. (continued)

```
C     POSITION THE PEN IF THERE HAS BEEN A PLOT
   80 IF (JPLOT-1) 90,90,92
   90 IF (NREF) 96,96,94
   92 IF (NGRAD) 96,96,94
   94 CALL PLOT (0.0,0.0,3)
      CALL PLOT (8.0,-30.0,-3)
      CALL PLOT (0.0,2.0,-3)
   96 CONTINUE
      RETURN
C
  110 FORMAT (///23X,*REFRACTIVITY PROFILE*/10X,*I*,8X,
     1*ALTITUDE*,8X,*REFRACTIVITY*/21X,*(FT)*,11X,*(N-UNITS)*)
  120 FORMAT (///18X,*REFRACTIVITY GRADIENT PROFILE*/10X,*I*,8X,
     1*ALTITUDE*,7X,*REFR GRADIENT*/21X,*(FT)*,9X,*(N-UNITS/KFT)*)
  140 FORMAT (8X,I3,2(6X,F10.2))
      END
```

Fig. 61. (continued)

```
      SUBROUTINE RKINTG
C
C-----THIS ROUTINE SETS UP THE INTEGRATION OF THE RAY TRAJECTORY
C-----AND TIME OF PROPAGATION EQUATIONS FOR EACH RAY.  WHEN A RAY
C-----CROSSES A BOUNDARY BETWEEN THE PIECE-WISE LINEAR SEGMENTS
C-----OF THE REFRACTIVITY PROFILE OR THE BOUNDARY AT THE EARTH'S
C-----SURFACE, THE RAY EQUATIONS ARE INTEGRATED TO THE BOUNDARY
C-----BY MEANS OF A VARIABLE STEP SIZE INTERPOLATION ALGORITHM.
C-----THE RAY EQUATIONS ARE THEN RE-INITIALIZED AT THE BOUNDARY
C-----AND INTEGRATED TO THE NEXT BOUNDARY, WHERE THE INTERPOLATION
C-----IS REPEATED.
C
      COMMON /ONECOM/ CRH,CRX,CRG,DTR,JAREA,NDATA,C,C1,C2
     1      ,RHO(51,30),PHI(51,30),PI,CMF,CNAUT,AHS
     2      ,FRQ,TPW,NHY,NSL,NRMS,ABSRH,PHASE,THETA
      COMMON /TWOCOM/ RA,DELX,AHO,ELO(51),JRAY,EXMAX,AHMAX,XFINAL
      COMMON /THRCOM/ NELO,JPLOT,IPLACE,VX(30),JCASE
     1      ,H(51,30),G(51,30),HN(50),RN(50),S(51,30)
     2      ,XSIZ,YSIZ,JPLT,XMIN,YMIN,XDIV,YDIV
     3      ,XMAX,YMAX,NREF,NRAY,NPRO,NPLOT,NGRAD
     4      ,KREF,KGRAD,KPLOT
      DIMENSION YINT(10),DELXX(5),PINT(10)
      DATA DELXX,NEQ/10000.,1000.,100.,10.,0.,2/
C
C     SET UP INITIAL CONDITIONS
      DO 10 I=1,10
      PINT(I)=0.0
   10 YINT(I)=0.0
      L=1
      ANGLE=0.0
      RHMAG=1.0
      STPX=DELX
      VX(L)=CRX
      H(JRAY,L)=CRH
      S(JRAY,L)=ATAN(CRG*RA/(RA+CRH))
      G(JRAY,L)=PINT(1)
      RHO(JRAY,L)=RHMAG
      PHI(JRAY,L)=ANGLE
      YINT(1)=CRH
      YINT(2)=CRG
      VALG=YINT(2)
      VGTEMP=PINT(1)
      VHTEMP=YINT(1)
      VXTEMP=CRX
      ICODE=3
      II=0
C
C     CHECK IF A RAY TRACE IS TO BE MADE
      IF (NRAY) 14,14,11
C
C     TEST FOR MAXIMUM ALTITUDE
   11 IF (CRH-AHMAX) 12,12,13
C
C     MAXIMUM ALTITUDE NOT EXCEEDED. POSITION PEN AT EMITTER COORDINATES
   12 X=0.0
      Y=CRH/YDIV
      CALL PLOT (X,Y,ICODE)
```

Fig. 61. (continued)

```
      ICODE=2
      GO TO 14
C
C     MAXIMUM ALTITIDE EXCEEDED. POSITION PEN AT UPPER LEFT HAND GRAPH CORNER
   13 X=0.0
      Y=AHMAX/YDIV
      CALL PLOT (X,Y,ICODE)
   14 IF (JRAY-1) 15,15,22
C
C     FIND WHICH LAYER THE EMITTER IS IN
   15 CONTINUE
      DO 20 I=1,NDATA
      IF (CRH-HN(I)) 20,20,16
   16 JAREA=I
      JXMTR=I
      GO TO 25
   20 CONTINUE
      GO TO 25
   22 JAREA=JXMTR
   25 CONTINUE
C
C     SET UP A LOOP FOR INTEGRATION OF THE ARRAYS "YINT" AND "PINT"
      DO 200 I=2,IPLACE
      II=II+1
C
C     CALL ROUTINE TO INTEGRATE "YINT" AND "PINT"
      CALL RK (NEQ,CRX,STPX,YINT,PINT)
C
C     CHECK WHICH LAYER THE RAY IS IN
  100 KAREA=JAREA
      DO 120 J=1,NDATA
      IF (YINT(1)-HN(J)) 120,120,110
  110 KAREA=J
      GO TO 125
  120 CONTINUE
C
C     SET UP LAYER IF RAY HAS INTERSECTED EARTH'S SURFACE
      IF (YINT(1)-AHS) 122,122,125
  122 KAREA=NDATA+1
  125 CONTINUE
C
C     CHECK WHICH LAYER BOUNDARY, IF ANY, HAS BEEN CROSSED FIRST
      IF (JAREA-KAREA) 140,145,130
C
C     AN UPPER BOUNDARY HAS BEEN CROSSED
  130 BNDRY=HN(JAREA-1)
      KAREA=JAREA-1
      GO TO 160
C
C     A LOWER BOUNDARY HAS BEEN CROSSED
  140 BNDRY=HN(JAREA)
      KAREA=JAREA+1
      GO TO 160
C
C     NO BOUNDARY HAS BEEN CROSSED.  STORE ARRAY VALUES EVERY
C     TENTH INTEGRATION STEP
  145 IF (II-10) 148,146,146
```

Fig. 61. (continued)

```
  146 II=0
      L=L+1
      VX(L)=CRX
      H(JRAY,L)=YINT(1)
      S(JRAY,L)=ATAN(YINT(2)*RA/(RA+YINT(1)))
      G(JRAY,L)=PINT(1)
      RHO(JRAY,L)=RHMAG
      PHI(JRAY,L)=ANGLE
  148 VALG=YINT(2)
      VXTEMP=CRX
      VHTEMP=YINT(1)
      VGTEMP=PINT(1)
      STPX=DELX
C
C     CHECK IF A RAY TRACE IS TO BE MADE
      IF (NRAY) 200,200,152
C
C     A RAY TRACE IS TO BE MADE.  CHECK FOR MAXIMUM ALTITJDE
  152 IF (YINT(1)-AHMAX) 154,154,156
C
C     MAXIMUM ALTITUDE NOT EXCEEDED.  CALL ROUTINE TO PLOT THE RAY
  154 X=CRX/XDIV
      Y=YINT(1)/YDIV
      CALL PLOT (X,Y,ICODE)
      ICODE=2
      GO TO 158
C
C     MAXIMUM ALTITUDE EXCEEDED. TURN OFF PLOTTER
  156 ICODE=3
  158 IF (JAREA-KAREA) 170,200,170
C
C     THE LAYER BOUNDARY HAS BEEN FOUND.  SET UP FOR LINEAR INTERPOLTION SCHEME
  160 DXTOT=0.
      HTEMP=YINT(1)
      CRX=VXTEMP
      YINT(1)=VHTEMP
      YINT(2)=VALG
      PINT(1)=VGTEMP
C
C     SET UP VARIABLE INTEGRATION STEP SIZE AND INTERPOLATE TO THE BOUNDARY
      DO 165 IJK=1,5
      XX=-YINT(2)/YINT(3)
      XYCHK=XX*XX-2.*(YINT(1)-BNDRY)/YINT(3)
      IF(XYCHK.LT.0.) XYCHK=0.
      YY=SQRT(XYCHK)
      CHGX=XX+YY
      IF (XX.GT.YY) CHGX=XX-YY
      IF (IJK.GT.4) CHGX=(BNDRY-YINT(1))/YINT(2)
      SD=STPX-DXTOT
      IF ((CHGX.LE.0.).OR.(CHGX.GE.SD        )) CHGX=
     1       (STPX-DXTOT)*(BNDRY-YINT(1))/(HTEMP-YINT(1))
      CHGX=CHGX-DELXX(IJK)
      IF (CHGX.LE.0.) GO TO 165
C
C     CALL ROUTINE TO INTEGRATE TO THE BOUNDARY
      CALL RK (NEQ,CRX,CHGX,YINT,PINT)
      DXTOT=DXTOT+CHGX
```

Fig. 61. (continued)

```
  165 CONTINUE
C
C     CHECK IF A RAY TRACE IS TO BE MADE
      IF (NRAY-1) 170,152,152
C
C     CHECK IF RAY HAS INTERSECTED EARTH'S SURFACE
  170 IF (KAREA-(NDATA+1)) 190,180,180
C
C     RAY HAS CROSSED ZERO ALTITUDE BOUNDARY. FIND INCIDENT GRAZING ANGLE
  180 THETA=ABS(ATAN(YINT(2)))
C
C     CALL ROUTINE TO CALCULATE COMPLEX SCATTERING COEFFICIENT
      CALL SCATT
C
C     SET UP COMPLEX SCATTERING COEFFICIENT
      RHMAG=RHMAG*ABSRH
      ANGLE=ANGLE+PHASE
C
C     ADD MULTIPATH RAY
      DO 185 LL=2,10
  185 YINT(LL)=-YINT(LL)
      KAREA=NDATA
C
C     SET UP TO INTEGRATE FROM THE BOUNDARY TO THE NEXT "DELX"
  190 JAREA=KAREA
      VXTEMP=CRX
      VHTEMP=YINT(1)
      VALG=YINT(2)
      VGTEMP=PINT(1)
      STPX=STPX-DXTOT
C
C     CALL ROUTINE TO INTEGRATE FROM THE BOUNDARY TO THE NEXT "DELX"
      CALL RK (NEQ,CRX,STPX,YINT,PINT)
C
C     CHECK FOR MORE BOUNDARY CROSSINGS
      GO TO 100
  200 CONTINUE
C
C     TURN OFF THE PLOTTER IF THERE IS A RAY TRACE PLOT
      ICODE=3
      IF (NRAY) 230,230,210
  210 CALL PLOT (X,Y,ICODE)
C
C     CHECK IF THIS IS A PLOT OF THE LAST RAY.  IF SO,
C     POSITION THE PEN FOR THE NEXT PLOT.
      IF (JRAY-NELO) 230,220,220
  220 CALL PLOT (0.0,0.0,3)
      CALL PLOT (16.0,-30.0,-3)
      CALL PLOT (0.0,2.0,-3)
  230 CONTINUE
      RETURN
      END
```

Fig. 61. (continued)

```
      SUBROUTINE RK (N,XN,H,Y,P)
C
C-----THIS ROUTINE INTEGRATES THE RAY TRAJECTORY AND TIME OF
C-----PROPAGATION DIFFERENTIAL EQUATIONS BY MEANS OF A FOURTH
C-----ORDER RUNGE-KUTTA ALGORITHM USING AN INTEGRATION STEP
C-----SIZE OF H = XDELTA/10, WHERE XDELTA IS THE DISTANCE INTERVAL
C-----ALONG THE EARTH'S SURFACE FOR PRINTING AND PLOTTING THE
C-----HEIGHT GAIN CURVES, OR H = CHGX WHERE CHGX IS A VARIABLE
C-----STEP SIZE SET BY THE INTERPOLATION ALGORITHM IN
C-----SUBROUTINE RKINTG.
C
      DIMENSION Y(10),P(10),YDOT(10),PDOT(10),Q(10,4),R(10,4)
     1,YN(10),PN(10)
C
C     SET UP INITIAL CONDITIONS
      DO 5 I=1,N
      YN(I)=Y(I)
    5 PN(I)=P(I)
C
C     SET UP A LOOP TO INTEGRATE THE DIFFERENTIAL EQUATIONS
      DO 60 L=1,4
C
C     CALL ROUTINE TO SET UP THE DIFFERENTIAL EQUATIONS
      CALL ATMOS (Y,P,YDOT,PDOT)
C
C     INTEGRATE THE DIFFERENTIAL EQUATIONS
      GO TO (10,20,30,40),L
   10 DO 15 K=1,N
      Q(K,L)=H*YDOT(K)
   15 Y(K)=YN(K)+Q(K,L)/2.
      R(1,L)=H*PDOT(1)
      P(1)=PN(1)+R(1,L)/2.
      X=XN+H/2.
      GO TO 50
   20 DO 25 K=1,N
      Q(K,L)=H*YDOT(K)
   25 Y(K)=YN(K)+Q(K,L)/2.
      R(1,L)=H*PDOT(1)
      P(1)=PN(1)+R(1,L)/2.
      X=XN+H/2.
      GO TO 50
   30 DO 35 K=1,N
      Q(K,L)=H*YDOT(K)
   35 Y(K)=YN(K)+Q(K,L)
      R(1,L)=H*PDOT(1)
      P(1)=PN(1)+R(1,L)
      X=XN+H
      GO TO 50
   40 DO 45 K=1,N
      Q(K,L)=H*YDOT(K)
   45 Y(K)=YN(K)+(Q(K,1)+2.0*Q(K,2)+2.0*Q(K,3)+Q(K,4))/6.0
      R(1,L)=H*PDOT(1)
      P(1)=PN(1)+(R(1,1)+2.0*R(1,2)+2.0*R(1,3)+R(1,4))/6.0
      XN=XN+H
   50 CONTINUE
   60 CONTINUE
C
```

Fig. 61. (continued)

```
C       CALL ROUTINE TO FIND THE VALUES OF THE DIFFERENTIAL EQUATIONS
C       AT THE END OF THE INTEGRATION STEP
        CALL ATMOS (Y,P,YDOT,PDOT)
C
C       STORE THE NEW DERIVATIVE OF THE RAY SLOPE
        Y(3)=YDOT(2)
        RETURN
        END
```

Fig. 61. (continued)

```
      SUBROUTINE ATMOS (Y,P,YDOT,PDOT)
C
C-----THIS ROUTINE COMPUTES ATMOSPHERIC REFRACTIVITY AT THE
C-----RAY ALTITUDE AND SETS UP THE RAY DIFFERENTIAL EQUATIONS
C
      COMMON /ONECOM/ CRH,CRX,CRG,DTR,JAREA,NDATA,C,C1,C2
     1      ,RHO(51,30),PHI(51,30),PI,CMF,CNAUT,AHS
     2      ,FRQ,TPW,NHV,NSL,NRMS,ABSRH,PHASE,THETA
      COMMON /TWOCOM/ RA,DELX,AHO,ELO(51),JRAY,EXMAX,AHMAX,XFINAL
      COMMON /THRCOM/ NELD,JPLOT,IPLACE,VX(30),JCASE
     1      ,H(51,30),G(51,30),HN(50),RN(50),S(51,30)
     2      ,KSIZ,YSIZ,JPLT,XMIN,YMIN,KDIV,YDIV
     3      ,XMAX,YMAX,NREF,NRAY,NPRO,NPLOT,NGRAD
     4      ,KREF,KGRAD,KPLOT
      DIMENSION Y(10),P(13),YDOT(10),PDOT(10)
C
C     SET UP INITIAL CONDITIONS
      CH=Y(1)
      CG=Y(2)
C
C     TEST FOR THE APPROPRIATE ATMOSPHERIC MODEL
      IF (NPRO-1) 10,10,20
C
C     FREE SPACE AND EXPONENTIAL MODELS
   10 REFR=C1*EXP(-C2*CH)
      DLNDH=-C2*REFR*1.0E-06/(REFR*1.0E-06 + 1.0)
      GO TO 100
C
C     THE ATMOSPHERE IS STRATIFIED.  SELECT THE APPROPRIATE MODEL
   20 IF (JAREA-1) 50,50,60
C
C     ALTITUDE IS ABOVE THE HIGHEST REFRACTIVITY PROFILE DATA POINT.
C     USE AN EXPONENTIAL MODEL WHICH FITS THE DATA
   50 REFR=C1*EXP(-C2*CH)
      DLNDH=-C2*REFR*1.0E-06/(REFR*1.0E-06 + 1.0)
      GO TO 100
C
C     ALTITUDE IS BELOW THE HIGHEST REFRACTIVITY PROFILE DATA POINT.
C     USE A PIECE-WISE LINEAR MODEL
   60 SLOPE=(RN(JAREA-1)-RN(JAREA))/(HN(JAREA-1)-HN(JAREA))
      B=RN(JAREA)-SLOPE*HN(JAREA)
C
C     COMPUTE REFRACTIVITY FOR THE PIECE-WISE LINEAR MODEL
   80 REFR=SLOPE*CH + B
      DLNDH=(SLOPE*1.0E-05)/(REFR*1.0E-06 + 1.0)
C
C     COMPUTE THE DERIVATIVES FOR RAY TRACES
  100 RAD=RA+CH
      YDOT(2)=RAD*(2.0*(RA*CG/RAD)**2 +
     1      DLNDH*RAD*((RA*CG/RAD)**2 + 1.0)**2 + 1.0)/RA**2
      YDOT(1)=CG
C
C     COMPUTE THE DERIVATIVE FOR TIME OF PROPAGATION
      PDOT(1)=RAD*(REFR*1.0E-06+1.0)
     1*SQRT(1.0+(RA*CG/RAD)**2)/(C*RA)
      RETURN
      END
```

Fig. 61. (continued)

```
      SUBROUTINE SCATT
C
C-----THIS ROUTINE CALCULATES THE COMPLEX SPECULAR SCATTERING
C-----COEFFICIENT FOR WAVEFRONT REFLECTION FROM SMOOTH OR ROUGH
C-----LAND AND SEA SURFACES
C
      COMMON /ONECOM/ CRH,CRX,CRG,DTR,JAREA,NDATA,C,C1,C2
     1      ,RHO(51,30),PHI(51,30),PI,CMF,CNAUT,AHS
     2      ,FRQ,TPW,NHV,NSL,NRMS,ABSRH,PHASE,THETA
      DIMENSION EPS(3,2),SIGMA(3,2),DELHSL(9,2)
      REAL NI,NR
      DATA EPS,IC/80.,69.,65.,4.,10.,30.,0/
      DATA SIGMA/4.3,6.5,15.0,.0001,.0016,.01/
      DATA DELHSL/0.,.2,.5,1.1,1.7,2.5,4.3,8.6,12.9
     1,0.,9.,30.,56.,112.,214.,429.,1288.,2146./
C
C     SET UP INITIAL CONDITIONS
      IF (IC) 10,10,50
   10 IC=1
      JJ=NRMS+1
      IF (NSL-1) 12,12,30
   12 KK=1
      IF (FRQ-1500000000.) 14,16,16
   14 II=1
      GO TO 40
   16 IF (FRQ-5000000000.) 18,20,20
   18 II=2
      GO TO 40
   20 II=3
      GO TO 40
   30 KK=2
      II=NSL-1
C
C     CALCULATE THE COMPLEX DIELECTRIC CONSTANT
   40 ER=EPS(II,KK)
      EI=60.0*SIGMA(II,KK)*C/(CMF*FRQ)
      A=SQRT(ER**2+EI**2)
      ALPHA=ATAN2(EI,ER)
      DELTAH=DELHSL(JJ,KK)
C
C     CHECK WHICH POLARIZATION IS BEING USED
   50 IF (NHV-1) 60,60,70
C
C     HORIZONTAL POLARIZATION
   60 NR=SIN(THETA)-SQRT(A)*COS(ALPHA/2.)
      NI=SQRT(A)*SIN(ALPHA/2.)
      DR=SIN(THETA)+SQRT(A)*COS(ALPHA/2.)
      DI=SQRT(A)*SIN(ALPHA/2.)
      GR=(NR*DR-NI*DI)/(DR**2+DI**2)
      GI=(NR*DI+NI*DR)/(DR**2+DI**2)
      GO TO 80
C
C     VERTICAL POLARIZATION
   70 NR=SQRT(A)*COS(ALPHA/2.)*SIN(THETA)-1.0
      NI=SQRT(A)*SIN(ALPHA/2.)*SIN(THETA)
      DR=SQRT(A)*COS(ALPHA/2.)*SIN(THETA)+1.0
      DI=SQRT(A)*SIN(ALPHA/2.)*SIN(THETA)
```

Fig. 61. (continued)

```
      GR=(NR*DR+NI*DI)/(DR**2+DI**2)
      GI=(NR*DI-NI*DR)/(DR**2+DI**2)
C
C     CALCULATE THE COMPLEX FRESNEL REFLECTION COEFFICIENT
   80 ABSRH=SQRT(GR**2+GI**2)
      PHASE=ATAN2(-GI,GR)
C
C     CALCULATE THE TOTAL SPECULAR REFLECTION COEFFICIENT
      ABSRH=ABSRH*EXP(-0.5*(4.0*PI*DELTAH*SIN(THETA)*FRQ/C)**2)
      RETURN
      END
```

Fig. 61. (continued)

```
      SUBROUTINE HGAIN
C
C-----THIS ROUTINE COMPUTES RELATIVE FIELD STRENGTH AND POWER
C-----DENSITY (NORMALIZED TO FREE SPACE VALUES).  HEIGHT GAINS
C-----ARE OBTAINED FROM CALCULATIONS AT 100 "WINDOWS" OR ALTITUDE
C-----INCREMENTS EXTENDING VERTICALLY BETWEEN THE HIGHEST AND
C-----LOWEST RAYS.
C
      COMMON /ONECOM/ CRH,CRX,CRG,DTR,JAREA,NDATA,C,C1,C2
     1      ,RHO(51,30),PHI(51,30),PI,CMF,CNAUT,AHS
     2      ,FRQ,TPW,NHV,NSL,NRMS,ABSRH,PHASE,THETA
      COMMON /TWOCOM/ RA,DELX,AHO,ELO(51),JRAY,EXMAX,AHMAX,XFINAL
      COMMON /THRCOM/ NELO,JPLOT,IPLACE,VX(30),JCASE
     1      ,H(51,30),G(51,30),HN(50),RN(50),S(51,30)
     2      ,KSIZ,YSIZ,JPLT,XMIN,YMIN,XDIV,YDIV
     3      ,XMAX,YMAX,NREF,NRAY,NPRO,NPLOT,NGRAD
     4      ,KREF,KGRAD,KPLOT
      DIMENSION L(51),TDIFF(30),ESIG(30),PSC(30)
     1,TSIG(30),ESIGT(30),PSCT(30),TSIGT(30)
      DATA ZDIV/40.0/
C
C     SET UP INITIAL CONDITIONS
      R1=RA+AHO
      XN=DELX/XDIV
      YN=AHMAX/YDIV
      YS=AHS/YDIV
      NP=100
C
C     SET UP A LOOP TO CALCULATE RELATIVE FIELD STRENGTH OR
C     POWER DENSITY AT EACH INCREMENT OF DISTANCE
      DO 1000 K=2,IPLACE
      HLO=AHMAX
      U=VX(K)/RA
C
C     FIND HIGHEST AND LOWEST RAYS
      DO 100 I=1,NELO
      HLO=AMIN1(HLO,H(I,K))
      IF (HLO.EQ.H(I,K)) IRA=I
  100 CONTINUE
      HHI=AMIN1(H(1,K),AHMAX)
      HDIFF=HHI-HLO
      HTB=ABS(H(1,K)-H(2,K))
C
C     EXIT IF ALL RAYS EQUAL OR EXCEED THE MAXIMUM ALTITUDE
      IF (HLO-AHMAX) 200,1100,1100
C
C     SET UP WINDOW SIZE AND WINDOW POSITIONS TO EXCLUDE THE
C     HIGHEST AND LOWEST RAYS
  200 WINDOW=HDIFF/95.
      HNOW=HHI-WINDOW/10.
      HFINAL=HLO+WINDOW/10.
      RWP=HNOW-HFINAL
C
C     FIND THE ALTITUDE INCREMENT FOR EACH NEW WINDOW POSITION
      DH=RWP/FLOAT(NP)
      HNOW=HNOW+DH
C
```

Fig. 61. (continued)

```
C     SET UP A LOOP TO POSITION THE WINDOW EVERY "DH" FEET IN ALTITUDE
      DO 900 J=1,NP
      HNOW=HNOW-DH
C
C     CALCULATE THE UPPER ANGLE LIMIT SUBTENDED BY THE WINDOW IN
C     FREE SPACE
      R2=RA+HNOW
      DSQ=R1**2 + R2**2 - 2.0*R1*R2*COS(U)
      E1=ACOS((DSQ + (R1*TAN(U))**2 - (R1/COS(U)-R2)**2)
     1/(2.0*R1*TAN(U)*SQRT(DSQ)))
      IF (R1/COS(U).GT.R2) E1=-E1
C
C     CALCULATE THE LOWER ANGLE LIMIT SUBTENDED BY THE WINDOW IN
C     FREE SPACE
      R2=RA+HNOW-WINDOW
      DSQ=R1**2 + R2**2 - 2.0*R1*R2*COS(U)
      E2=ACOS((DSQ + (R1*TAN(U))**2 - (R1/COS(U)-R2)**2)
     1/(2.0*R1*TAN(U)*SQRT(DSQ)))
      IF (R1/COS(U).GT.R2) E2=-E2
      EDIFF=SQRT(ABS(E1-E2)/DTR)
C
C     CALCULATE THE ELEVATION ANGLE OF THE EMITTER AT THE WINDOW
      R1=RA+HNOW-WINDOW/2.
      R2=RA+AHO
      DSQ=R1**2 + R2**2 - 2.0*R1*R2*COS(U)
      AO=ACOS((DSQ + (R1*TAN(U))**2 - (R1/COS(U)-R2)**2)
     1/(2.0*R1*TAN(U)*SQRT(DSQ)))
      IF (R1/COS(U).GT.R2) AO=-AO
C
C     SET UP THE WINDOW ALTITUDE PLUS ITS UPPER AND LOWER BOUNDARIES
      HUP=HNOW
      HH=HNOW-WINDOW/2.
      HDN=HNOW-WINDOW
C
C     SET UP CONTROL INTEGERS FOR EACH RAY
      DO 220 I=1,NELO
      IF (H(I,K).GT.HUP) GO TO 210
      IF (H(I,K).LT.HDN) GO TO 215
      L(I)=2
      GO TO 220
  210 L(I)=3
      GO TO 220
  215 L(I)=1
  220 CONTINUE
C
C     SET UP INITIAL CONDITIONS
      E=0.0
      JSLOPE=0
      JREV=0
      JSTART=0
      JSTOP=0
      LC=0
      TMAX=0.0
      KTOT=0
      MEL=NELO-1
      DO 222 IFS=1,2
      TDIFF(IFS)=0.0
```

Fig. 61. (continued)

```
  222 ESIG(IFS)=0.0
      IF (L(1).NE.2) GO TO 225
C
C     INITIAL CONDITIONS IF FIRST RAY IS INSIDE THE WINDOW
      JSTART=1
      LC=1
      J1=1
  225 CONTINUE
C
C     SET UP A LOOP WHICH SCANS RAY HEIGHT VERSUS ELEVATION ANGLE
      DO 600 I=1,MEL
  230 JLAST=JSLOPE
      JC=IABS(L(I)-L(I+1))
      IF (L(I)-L(I+1)) 260,400,240
C
C     NORMAL RAY ORDER
  240 JSLOPE=1
      IF (JLAST.EQ.2) GO TO 310
      GO TO 270
C
C     INVERTED RAY ORDER
  260 JSLOPE=2
      IF (JLAST.EQ.1) GO TO 310
C
C     CHECK IF NEXT RAY IS THE LOWEST
  270 IF (I+1-IRA) 280,272,280
C
C     NEXT RAY IS THE LOWEST.  CHECK IF IT HAS BEEN REFLECTED FROM THE EARTH
  272 IF (RHO(IRA,K)-1.0) 274,290,290
C
C     LOWEST RAY HAS BEEN REFLECTED.  SET ITS IMAGE ALTITUDE BELOW THE EARTH
  274 H(I+1,K)=AHS-H(I+1,K)
      GO TO 290
C
C     CHECK IF THIS RAY IS THE LOWEST
  280 IF (I-IRA) 290,600,290
C
C     EITHER ONE OR TWO WINDOW LIMIT CROSSINGS
  290 IF (JC-1) 300,300,350
C
C     ONE WINDOW LIMIT CROSSING
  300 LC=LC+1
      IF (LC-1) 340,340,350
C
C     RAY ORDER REVERAL OCCURS.  CHECK IF RAY BUNDLE EXISTS INSIDE WINDOW
  310 IF (JC-1) 320,320,230
C
C     CHECK IF RAY REVERSAL OCCURS INSIDE OR OUTSIDE THE WINDOW
  320 IF (LC) 230,230,330
C
C     RAY ORDER REVERSAL OCCURS WITHIN THE WINDOW
  330 J2=I
      JREV=1
      GO TO 440
C
C     FIRST WINDOW LIMIT CROSSING
  340 J1=I+1
```

Fig. 61. (continued)

```
      J2=I+1
      IF (I.EQ.MEL.AND.L(NELO).EQ.2) GO TO 420
      GO TO 500
C
C     SECOND WINDOW CROSSING
  360 J2=I
      GO TO 440
C
C     BOTH WINDOW LIMITS CROSSED.  CHECK FOR NEARBY CAUSTICS
  380 IF (ABS(H(I,K)-H(I+1,K))-5.0*HTB) 390,390,560
C
C     BOTH WINDOW LIMITS CROSSED.  NO CAUSTIC HAS BEEN FOUND
  390 J1=I+1
      J2=I
      GO TO 440
C
C     NO WINDOW LIMIT CROSSINGS
  400 IF (I.EQ.MEL.AND.L(NELO).EQ.2) GO TO 420
      GO TO 500
C
C     LAST RAY IS INSIDE WINDOW
  420 J2=NELO
      JSTOP=1
C
C     THE INCREMENT OF RAYS AT THE WINDOW HAS BEEN FOUND.
C     CHECK IF RAY ORDER IS NORMAL OR INVERTED.
  440 IF (JLAST-1) 460,460,480
C
C     NORMAL RAY ORDER.  CALCULATE THE UPPER AND LOWER ANGLES
C     SUBTENDED BY THE WINDOW.
  460 EUP=ELO(J1)
      EDN=ELO(J2)
      IF (JSTART.EQ.0) EUP=
     1ELO(J1-1)-(ELO(J1-1)-ELO(J1))*(H(J1-1,K)-HUP)/(H(J1-1,K)-H(J1,K))
      IF (JSTOP.EQ.0.AND.JREV.EQ.0) EDN=
     1ELO(J2)-(ELO(J2)-ELO(J2+1))*(H(J2,K)-HDN)/(H(J2,K)-H(J2+1,K))
      E=SQRT(EUP-EDN)
      PSCAT=PHI(J2,K)
      RSCAT=RHO(J2,K)
      GO TO 500
C
C     INVERTED RAY ORDER.  CALCULATE THE UPPER AND LOWER ANGLES
C     SUBTENDED BY THE WINDOW.
  480 EDN=ELO(J1)
      EUP=ELO(J2)
      IF (JSTART.EQ.0) EDN=
     1ELO(J1-1)-(ELO(J1-1)-ELO(J1))*(H(J1-1,K)-HDN)/(H(J1-1,K)-H(J1,K))
      IF (JSTOP.EQ.0.AND.JREV.EQ.0) EUP=
     1ELO(J2)-(ELO(J2)-ELO(J2+1))*(H(J2,K)-HUP)/(H(J2,K)-H(J2+1,K))
      E=SQRT(EDN-EUP)
      PSCAT=PHI(J1,K)
      RSCAT=RHO(J1,K)
C
C     SET UP INITIAL CONDITIONS TO CALCULATE MEAN ELEVATION ANGLE
C     AND MEAN TIME OF ARRIVAL
  500 KTOT=KTOT+1
      JA=J1
```

Fig. 61 (continued)

```
      JB=J2
      JCOUNT=0
      IF (J1-J2) 520,520,510
  510 JA=J2
      JB=J1
C
C     CALCULATE MEAN ELEVATION ANGLE AND TIME OF ARRIVAL FOR EACH
C     WAVEFRONT
  520 SNEW=0.0
      TNEW=0.0
      DO 540 JAB=JA,JB
      JCOUNT=JCOUNT+1
      SNEW=SNEW+S(JAB,K)
  540 TNEW=TNEW+G(JAB,K)
      ALPH=-SNEW/FLOAT(JCOUNT)
      TSIGT(KTOT)=TNEW/FLOAT(JCOUNT)
C
C     CALCULATE ANGLE INCREMENT OF EACH WAVEFRONT
      ESIGT(KTOT)=E*RSCAT*COS(A0)/COS(ALPH)
      PSCT(KTOT)=PSCAT
C
C     RESET INITIAL CONDITIONS TO CONTINUE SCAN OF HEIGHT VS ANGLE
  560 H(IRA,K)=ABS(H(IRA,K))
      LC=0
      JREV=0
      JSTART=0
  600 CONTINUE
C
C     CHECK IF WINDOW IS IN A SHADOW REGION RESULTING FROM A CAUSTIC
      IF (KTOT) 780,780,610
C
C     WINDOW IS NOT IN A SHADOW REGION.  PUT WAVEFRONTS IN ORDER
C     OF THEIR TIMES-OF-ARRIVAL
  610 CONTINUE
      DO 660 IS=1,KTOT
      TMIN=10.0
      DO 650 IR=1,KTOT
      TMIN=AMIN1(TMIN,TSIGT(IR))
      IF (TMIN.EQ.TSIGT(IR)) IMIN=IR
  650 CONTINUE
      TSIG(IS)=TSIGT(IMIN)
      ESIG(IS)=ESIGT(IMIN)
      PSC(IS)=PSCT(IMIN)
      TSIGT(IMIN)=20.0
  660 CONTINUE
C
C     CHECK IF MORE THAN ONE WAVEFRONT IS PRESENT IN THE WINDOW
      IF (KTOT.EQ.1) GO TO 700
C
C     CALCULATE TIME DIFFERENCE OF ARRIVAL (T.D.O.A.) BETWEEN WAVEFRONTS
      DO 670 IT=2,KTOT
      TDIFF(IT)=TSIG(IT)-TSIG(1)
  670 TMAX=AMAX1(TMAX,TDIFF(IT))
C
C     SET UP A LOOP TO CALCULATE TOTAL FIELD STRENGTH OR POWER
C     DENSITY IF WAVEFRONTS OVERLAP IN TIME
  700 ESUMR=0.0
```

Fig. 61. (continued)

```
      ESUMI=0.0
      DO 720 IFI=1,KTOT
      IF (TDIFF(IFI).GT.TPW) GO TO 710
      ESUMR=ESUMR+ESIG(IFI)*COS(PSC(IFI)+2.0*PI*FRQ*TDIFF(IFI))
      ESUMI=ESUMI+ESIG(IFI)*SIN(PSC(IFI)+2.0*PI*FRQ*TDIFF(IFI))
  710 CONTINUE
  720 CONTINUE
      ESUM=SQRT(ESUMR**2+ESUMI**2)
C
C     CHECK IF FIELD STRENGTH OR POWER DENSITY IS TO BE COMPUTED
      IF (NPLOT-1) 730,740,760
  730 IF (KPLOT-1) 740,740,760
C
C     CALCULATE RELATIVE FIELD STRENGTH OF EACH WAVEFRONT
  740 CONTINUE
      DO 750 IFS=1,KTOT
  750 ESIG(IFS)=10.*ALOG10(ESIG(IFS)/EDIFF)
C
C     CALCULATE TOTAL RELATIVE FIELD STRENGTH
      SP=10.*ALOG10(ESUM/EDIFF)
      GO TO 800
C
C     CALCULATE RELATIVE POWER DENSITY OF EACH WAVEFRONT
  760 CONTINUE
      DO 770 IFS=1,KTOT
  770 ESIG(IFS)=20.*ALOG10(ESIG(IFS)/EDIFF)
C
C     CALCULATE TOTAL RELATIVE POWER DENSITY
      SP=20.*ALOG10(ESUM/EDIFF)
      GO TO 800
C
C     SET FIELD STRENGTH AND POWER DENSITY FOR A SHADOW REGION
  780 SP=-100000.0
      ESIG(1)=-100000.0
      ESIG(2)=-100000.0
C
C     PRINT HEADING AND RAY HEIGHTS IF THIS IS A NEW DISTANCE
  800 IF (J.NE.1) GO TO 820
      XNAUT=VX(K)/CNAUT
      IF (KPLOT-1) 816,812,814
  812 PRINT 1200,XNAUT
      GO TO 816
  814 PRINT 1210,XNAUT
C
C     POSITION THE PEN AND DRAW THE NEW ORDINATE AXES IF THERE IS A PLOT
  816 IF (NPLOT) 820,820,818
  818 CALL PLOT (XN,0.0,-3)
      CALL PLOT (0.0,YS,3)
      CALL PLOT (0.0,YN,2)
      CALL PLOT (0.0,0.0,3)
  820 CONTINUE
C
C     PRINT THE RELATIVE FIELD STRENGTH OR POWER DENSITY AND
C     TIME DIFFERENCES OF ARRIVAL
      IF (KPLOT) 826,826,822
  822 PRINT 1220,J,HH,SP,ESIG(1),ESIG(2),TMAX,TDIFF(2),KTOT
      IF (KTOT-1) 826,826,824
```

Fig. 61 (continued)

```
 824  PRINT 1230,((ESIG(IFS),TDIFF(IFS)),IFS=3,KTOT)
C
C     SET PARAMETERS IF THERE IS A PLOT
  826 IF (NPLOT) 900,900,850
  850 Y=HH/YDIV
      IF (J-1) 854,854,855
C
C     SET FIRST END POINT OF PLOT
  854 X=0.0
      ICODE=3
      CALL PLOT (X,Y,ICODE)
C
C     CHECK IF FIELD STRENGTH OR POWER DENSITY IS TOO LOW FOR PLOTTING
  855 IF (SP+15.0) 856,857,857
C
C     FIELD STRENGTH OR POWER DENSITY LESS THAN -40 DB.  TURN OFF PLOTTER.
  856 X=-15.0/ZDIV
      CALL PLOT (X,Y,ICODE)
      ICODE=3
      GO TO 858
C
C     PLOT TOTAL RELATIVE FIELD STRENGTH OR POWER DENSITY
  857 X=SP/ZDIV
      ICODE=2
      CALL PLOT (X,Y,ICODE)
C
C     SET END POINT OF PLOT
  858 IF (J-NP) 900,859,859
  859 X=0.0
      ICODE=2
      IF (SP.LT.-15.0) ICODE=3
      CALL PLOT (X,Y,ICODE)
  900 CONTINUE
 1000 CONTINUE
C
C     POSITION THE PEN IF THERE HAS BEEN A PLOT
 1100 IF (NPLOT) 1120,1120,1110
 1110 CALL PLOT (0.0,0.0,3)
      CALL PLOT (8.0,-30.0,-3)
      CALL PLOT (0.0,2.0,-3)
 1120 CONTINUE
      RETURN
C
 1200 FORMAT (///,1X,*PRINTOUT OF FIELD STRENGTH AND T.D.O.A.'S AT X =*
     1,F8.2,2X,*NAUTICAL MILES*,
     2//3X,*NO.*,4X,*HEIGHT (FT)*,4X,* TOTAL FIELD (DB) *,4X,
     3*DIRECT FIELD (DB) *,4X,*MULTIPATH FLD (DB)*,4X,
     4*MINIMUM TDOA (SEC)*,4X,*TDOA (SEC)*,4X,*NS*/)
 1210 FORMAT (///,1X,*PRINTOUT OF POWER DENSITY AND T.D.O.A.'S AT X =*
     1,F8.2,2X,*NAUTICAL MILES*,
     2//3X,*NO.*,4X,*HEIGHT (FT)*,2X,*TOTAL POWER DENS (DB)*,2X,
     3*DIRECT POWER DENS (DB)*,2X,*MULTIPATH PWR (DB)*,4X,
     4*MINIMUM TDOA (SEC)*,4X,*TDOA (SEC)*,4X,*NS*/)
 1220 FORMAT (2X,I3,5X,F9.2,9X,3(F9.4,13X),1PE11.4,1PE18.4,4X,I2)
 1230 FORMAT (72X,F9.4,24X,1PE18.4)
      END
```

Fig. 61. (continued)

```
      SUBROUTINE PLOTTR
C
C-----THIS ROUTINE SETS UP THE AXES FOR ALL PLOTS
C
      COMMON /TWOCOM/ RA,DELX,AHO,ELO(51),JRAY,EXMAX,AHMAX,XFINAL
      COMMON /THRCOM/ NELO,JPLOT,IPLACE,VX(30),JCASE
     1      ,H(51,30),G(51,30),HN(50),RN(50),S(51,30)
     2      ,XSIZ,YSIZ,JPLT,XMIN,YMIN,XDIV,YDIV
     3      ,XMAX,YMAX,NREF,NRAY,NPRO,NPLOT,NGRAD
     4      ,KREF,KGRAD,KPLOT
      DIMENSION AHD(8),TTL(8),XTL(8),YTL(8),TLE(8),ZTL(1)
      DATA YMIN,YSIZ,SIZE/0.0,5.0,0.1505/
      DATA ZTL(1),IZTL,ZSIZ,ZMIN,ZDIV/10H GAIN (DB),10,1.0
     1,-20.0,40.0/
C
C     SET UP INITIAL CONDITIONS IF THIS IS THE FIRST PLOT
      IF (JPLT) 10,10,20
   10 YMAX=AHMAX
      YDIV=(YMAX-YMIN)/YSIZ
      YDIVA=YDIV/1000.0
      YPT=YSIZ+1.0
      ZPT=YSIZ+0.5
      YN=YMAX/YDIV
      YS=AHS/YDIV
      JPLT=1
C
C     READ PLOT SCALE FACTOR AND PLOT BANNER
      READ 110,SCALE
      READ 120,IAHD,(AHD(K),K=1,7)
C
C     SCALE THE PLOT SIZE
      CALL FACTOR (SCALE)
C
C     POSITION THE PEN AND PRINT THE PLOT BANNER
      IF (JCASE-1) 15,15,20
   15 YAHD=(10.0-SIZE*IAHD)/2.
      CALL PLOT (4.0,-30.0,-3)
      CALL PLOT (0.0,2.0,-3)
      CALL SYMBOL (0.0,YAHD,SIZE,AHD,90.0,IAHD)
C
C     POSITION THE PEN FOR THE NEXT PLOT
      CALL PLOT (6.0,-30.0,-3)
      CALL PLOT (0.0,2.0,-3)
C
C     READ AXIS LABELS AND TWO LINES OF PLOT TITLES
   20 READ 120,IXTL,(XTL(K),K=1,7)
      READ 120,IYTL,(YTL(K),K=1,7)
      READ 120,ITTL,(TTL(K),K=1,7)
      READ 120,ITLE,(TLE(K),K=1,7)
C
C     CHECK WHICH PLOT THIS IS
      IF (JPLOT-2) 30,40,60
C
C     SET UP INITIAL CONDITIONS FOR REFRACTIVITY PROFILE
C     AND GRADIENT PLOTS
   30 XMAX=400.0
      XMIN=0.0
```

Fig. 61. (continued)

```
      GO TO 50
   40 XMAX=100.0
      XMIN=-300.0
   50 XSIZ=4.0
      XDIV=(XMAX-XMIN)/XSIZ
      XDIVA=XDIV
      GO TO 70
C
C     SET UP INITIAL CONDITIONS FOR RAY TRACE, FIELD STRENGTH,
C     AND POWER DENSITY PLOTS
   60 XMAX=EXMAX
      XMIN=0.0
      XSIZ=10.0
      XDIV=(XMAX-XMIN)/XSIZ
      XDIVA=XFINAL/XSIZ
      XRE=XSIZ-0.5
C
C     SET UP PARAMETERS FOR AXIS LABELS AND PLOT TITLES
   70 XTTL=(XSIZ-SIZE*ITTL)/2.
      XTLE=(XSIZ-SIZE*ITLE)/2.
C
C     DRAW AND LABEL THE AXES
      CALL AXIS (0.0,0.0,YTL,IYTL,YSIZ,90.0,YMIN,YDIVA)
      CALL AXIS (0.0,0.0,XTL,-IXTL,XSIZ,0.0,XMIN,XDIVA)
C
C     PRINT THE PLOT TITLES
   74 CALL SYMBOL (XTTL,YPT,SIZE,TTL,0.0,ITTL)
      CALL SYMBOL (XTLE,ZPT,SIZE,TLE,0.0,ITLE)
C
C     DRAW THE REFERENCE SCALE FOR ALL FIELD STRENGTH AND
C     POWER DENSITY PLOTS
      IF (JPLOT-3) 82,82,80
   80 CALL AXIS (XRE,ZPT,ZTL,-IZTL,ZSIZ,0.0,ZMIN,ZDIV)
      CALL PLOT (XSIZ,ZPT,3)
      CALL PLOT (XSIZ,YPT,2)
   82 CALL PLOT (0.0,0.0,3)
C
C     DRAW THE EARTH SURFACE IF NOT AT ZERO MEAN SEA LEVEL
      IF (AHS) 86,85,84
   84 CALL PLOT (0.0,YS,3)
      CALL PLOT (XSIZ,YS,2)
      CALL PLOT (0.0,0.0,3)
C
C     POSITION THE PEN FOR THE REFRACTIVITY GRADIENT PROFILE PLOT
   86 IF (JPLOT-2) 100,90,100
   90 XN=-XMIN/XDIV
      CALL PLOT (XN,0.0,-3)
  100 CONTINUE
      RETURN
C
  110 FORMAT (3F15.7)
  120 FORMAT (I2,8X,7A10)
      END
```

Fig. 61. (continued)

TABLE 10

CARD INPUT DATA

| CARD | VARIABLE | FORMAT | DESCRIPTION |
|---|---|---|---|
| 1 | NCASE | I5 | NUMBER OF PROGRAM RUNS. |
| 2 | NREF | I5 | CODE FOR REFRACTIVITY MODEL.<br>NREF=0 FREE SPACE REFRACTIVITY MODEL<br>NREF=1 EXPONENTIAL REFRACTIVITY MODEL<br>NREF=2 INPUT REFRACTIVITY PROFILE MODEL |
| 3 | NDATA | I5 | NUMBER OF REFRACTIVITY PROFILE DATA LEVELS.<br>NDATA = 1 IF NREF=0 OR 1 |
| 2 | HN(1)<br>RN(1) | 2F15.7 | HN(1) IS THE HIGHEST ALTITUDE IN THE REFRACTIVITY PROFILE.<br>RN(1) IS REFRACTIVITY AT HN(1).<br>** (LEAVE THIS CARD BLANK IF EITHER NREF=0 OR NREF=1) |
| 3 | HN(2)<br>RN(2) | 2F15.7 | HN(2) IS SECOND HIGHEST ALTITUDE IN THE REFRACTIVITY PROFILE.<br>RN(2) IS REFRACTIVITY AT HN(2).<br>** (OMIT CARDS 5 THROUGH (NDATA+3) IF EITHER NREF=0 OR NREF=1) |
| NDATA +3 | HN(NDATA)<br>RN(NDATA) | 2F15.7 | LOWEST ALTITUDE IN PROFILE.<br>REFRACTIVITY AT HN(NDATA).<br>** (OMIT IF NREF=0 OR NREF=1) |
| NDATA +4 | AHS<br>AHO<br>AHMAX | 3F15.7 | EARTH SURFACE ALTITUDE IN FEET.<br>EMITTER ALTITUDE IN FEET.<br>MAXIMUM ALTITUDE IN FEET FOR PRINTED AND PLOTTED OUTPUT. |
| NDATA +5 | XDELTA<br>XFINAL | 2F15.7 | DISTANCE INTERVAL IN NAUTICAL MI FOR PRINT AND PLOT OUTPUT.<br>MAXIMUM DISTANCE IN NAUT MI FOR PRINTED AND PLOTTED OUTPUT. |
| NDATA +6 | ELOS1<br>ELOS2 | 2F15.7 | HIGHEST RAY ELEVATION ANGLE IN DEGREES.<br>LOWEST RAY ELEVATION ANGLE IN DEGREES. |

TABLE 10 (continued)

| | | | |
|---|---|---|---|
| | | | ** THE QUANTITY (ELOS1-ELOS2) SHOULD NOT EXCEED 1.0 DEGREE. |
| NDATA +7 | FRQ | 2F15.7 | EMITTER FREQUENCY IN MEGAHERTZ. |
| | PW | | EMITTER PULSE WIDTH IN MICROSEC. SET PW=1000000.0 IF EMITTER IS CONTINUOUS WAVE (C.W.) |
| NDATA +8 | NHV | 3I5 | CODE FOR EMITTER POLARIZATION. NHV=1 HORIZONTAL POLARIZATION NHV=2 VERTICAL POLARIZATION |
| | NSL | | CODE FOR EARTH SURFACE TYPE. NSL=1 SEA WATER NSL=2 VERY DRY LAND NSL=3 "AVERAGE" LAND NSL=4 VERY MOIST LAND |
| | NRMS | | CODE FOR SURFACE ROUGHNESS. SEE TABLE BELOW. |

TABLE OF EARTH ROUGHNESS CODES

(FROM MAURICE LONG, "RADAR REFLECTION FROM LAND AND SEA", REF. (35), AND THE OFFICE OF TELECOMMUNICATIONS, U.S. DEPT. OF COMMERCE, REF. (39) )

| CODE | STANDARD DEVIATIONS OF HEIGHT FOR SEA AND LAND SURFACES | |
|---|---|---|
| NRMS | (SEA) | (LAND) |
| 0 | 0.0 | 0 |
| 1 | 0.2 | 9 |
| 2 | 0.6 | 30 |
| 3 | 1.1 | 56 |
| 4 | 1.7 | 112 |
| 5 | 2.6 | 214 |
| 6 | 4.3 | 429 |
| 7 | 8.6 | 1288 |
| 8 | 12.9 | 2146 |

| | | | |
|---|---|---|---|
| NDATA +9 | KPRO | 4I5 | CODE FOR REFRACTIVITY PROFILE PRINTOUT. KPRO=0 NO PRINTOUT KPRO=1 PRINTOUT |
| | KGRAD | | CODE FOR REFRACTIVITY GRADIENT PROFILE PRINTOUT. KGRAD=0 NO PRINTOUT KGRAD=1 PRINTOUT |
| | KRAY | | ** THIS VARIABLE IS NOT USED. SET KRAY=0 |
| | KPLOT | | CODE FOR RELATIVE FIELD STRENGTH OR POWER DENSITY PRINTOUT. KPLOT=0 NO PRINTOUT |

TABLE 10 (continued)

| | | | |
|---|---|---|---|
| | | | KPLOT=1 RELATIVE FIELD STRENGTH PRINTOUT |
| | | | KPLOT=2 RELATIVE POWER DENSITY PRINTOUT |
| NDATA +10 | NPRO | 4I5 | CODE FOR REFRACTIVITY PROFILE PLOT. |
| | | | NPRO=0 NO PLOT |
| | | | NPRO=1 PLOT |
| | NGRAD | | CODE FOR REFRACTIVITY GRADIENT PROFILE PLOT. |
| | | | NGRAD=0 NO PLOT |
| | | | NGRAD=1 PLOT |
| | NRAY | | CODE FOR RAY TRACE PLOT. |
| | | | NRAY=0 NO PLOT |
| | | | NRAY=1 PLOT |
| | NPLOT | | CODE FOR RELATIVE FIELD STRENGTH OR POWER DENSITY PLOT. |
| | | | NPLOT=0 NO PLOT |
| | | | NPLOT=1 RELATIVE FIELD STRENGTH PLOT |
| | | | NPLOT=2 RELATIVE POWER DENSITY PLOT |
| NDATA +11 | SCALE | F15.7 | SCALE FACTOR FOR ENLARGING OR REDUCING PLOT SIZE FROM ITS NORMAL 5 X 10 INCH FORMAT. NORMAL PLOT SIZE GIVEN WITH SCALE=1.0 |
| | | | ** (OMIT THIS CARD AND ALL CARDS THAT FOLLOW IF THERE ARE NO PLOTS) |
| NDATA +12 | IAHD | I2 | NUMBER OF CHARACTERS IN PLOT BANNER. |
| | AHD | 7A10 | CHARACTERS IN PLOT BANNER. ** (THIS CARD IS ALWAYS READ WHEN THERE ARE ANY PLOTS) |
| NDATA +13 | IXTL | I2 | NUMBER OF CHARACTERS IN X-AXIS LABEL. |
| | XTL | 7A10 | CHARACTERS IN X-AXIS LABEL. **(THIS CARD READ FOR ALL PLOTS) |
| NDATA +14 | IYTL | I2 | NUMBER OF CHARACTERS IN Y-AXIS LABEL. |
| | YTL | 7A10 | CHARACTERS IN Y-AXIS LABEL. **(THIS CARD READ FOR ALL PLOTS) |
| NDATA +15 | ITTL | I2 | NUMBER OF CHARACTERS IN FIRST LINE OF PLOT TITLE. |

TABLE 10 (continued)

| | | | |
|---|---|---|---|
| | TTL | 7A10 | CHARACTERS IN FIRST LINE OF PLOT TITLE. **(THIS CARD READ FOR ALL PLOTS) |
| NDATA +16 | ITLE | I2 | NUMBER OF CHARACTERS IN SECOND LINE OF PLOT TITLE. |
| | TLE | 7A10 | CHARACTERS IN SECOND LINE OF PLOT TITLE. **(THIS CARD READ FOR ALL PLOTS) |

***** REPEAT CARDS (NDATA+11) THROUGH (NDATA+16) FOR EACH PLOT IN A GIVEN SIMULATION RUN.

***** REPEAT CARDS (2) THROUGH (NDATA+16) FOR EACH SIMULATION RUN.

TABLE 11

SAMPLE INPUT FOR THE 100 FT HIGH EMITTER IN THE TRILINEAR DUCT

| COMM. | STATEMENT NUMBER | CONT. | FORTRAN STATEMENT | IDENT SEQ |
|---|---|---|---|---|
| | 1 | | | |
| | 2 | | | |
| | 5 | | | |
| | | | 2000.0 275.3 | |
| | | | 1300.0 276.8 | |
| | | | 1000.0 275.1 | |
| | | | 600.0 336.3 | |
| | | | 0.0 341.0 | |
| | | | 0.0 100.0 1000.0 | |
| | | | 20.0 300.0 | |
| | | | 0.5 -0.5 | |
| | | | 65.0 1000000.0 | |
| | 1 | | 1 3 | |
| | 1 | | 1 0 1 | |
| | 1 | | 1 1 1 | |
| | | | 0.75 | |
| 1 | 1 | | 23 NOV 1977 | |
| 2 | 2 | | REFRACTIVITY (N-UNITS) | |
| 3 | 8 | | HEIGHT ABOVE EARTH (THOUSANDS OF FEET) | |
| 3 | 2 | | ATMOSPHERIC REFRACTIVITY PROFILE | |
| 3 | 6 | | TRILINEAR MODEL OF GROUND BASED DUCT | |
| 3 | 5 | | REFRACTIVITY GRADIENT (N-UNITS/KFT) | |
| 3 | 8 | | HEIGHT ABOVE EARTH (THOUSANDS OF FEET) | |
| 2 | 9 | | REFRACTIVITY GRADIENT PROFILE | |

*A standard card form, IBM electro 88015/, is available for punching statements from this form

TABLE 11 (Continued)

| STATEMENT NUMBER | FORTRAN STATEMENT |
|---|---|
| 36 | TRILINEAR MODEL OF GROUND BASED DUCT |
| 37 | DISTANCE ALONG EARTH (NAUTICAL MILES) |
| 38 | HEIGHT ABOVE EARTH (THOUSANDS OF FEET) |
| 45 | RAY TRACE FOR THE TRILINEAR GROUND BASED DUCT |
| 36 | HO = 100 FT +0.50 TO -0.50 DEGREE |
| 37 | DISTANCE ALONG EARTH (NAUTICAL MILES) |
| 38 | HEIGHT ABOVE EARTH (THOUSANDS OF FEET) |
| 65 | GROUND BASED DUCT ABOVE A MODERATE SEA (STATE = 3) HO = 100 FT |
| 58 | HORIZONTAL POLARIZATION 65 MHZ +0.50 TO -0.50 DEGREE |

*A standard card form, IBM electro 888157, is available for punching statements from this form

TABLE 12

SAMPLE OUTPUT FOR THE 100 FT HIGH EMITTER IN THE TRILINEAR DUCT

```
ATMOSPHERIC RADIO REFRACTIVITY COMPUTATIONS

   NCASE=      1
    NPRO=      2
   MODEL=      INPUT PROFILE MODEL
     AHS=      0.00     FEET
     AHO=    100.00     FEET.
   AHMAX=   1000.00     FEET
  XDELTA=     20.00     NAUT MI
  XFINAL=    300.00     NAUT MI
   ELOS1=       .50     DEG
   ELOS2=      -.50     DEG
     FRQ=     65.00     MHZ
      PW=1000000.00     MICROSEC
   POLAR=      HORIZONTAL
 TERRAIN=      SEA WATER
    NPMS=      3
    KREF=      1
   KGRAD=      1
    KRAY=      0
   KPLOT=      1
    NREF=      0
   NGRAD=      0
    NRAY=      0
   NPLOT=      1
```

REFRACTIVITY PROFILE

| I | ALTITUDE (FT) | REFRACTIVITY (N-UNITS) |
|---|---|---|
| 1 | 1000.00 | 275.10 |
| 2 | 500.00 | 336.30 |
| 3 | 0.00 | 341.00 |

REFRACTIVITY GRADIENT PROFILE

| I | ALTITUDE (FT) | PEFR GRADIENT (N-UNITS/KFT) |
|---|---|---|
| 1 | 800.00 | -153.00 |
| 2 | 300.00 | -7.83 |

TABLE 12 (Continued)

PRINTOUT OF FIELD STRENGTH AND T.D.O.A.'S AT X = 20.00 NAUTICAL MILES

| NO. | HEIGHT (FT) | TOTAL FIELD (DB) | DIRECT FIELD (DB) | MULTIPATH FLD (DB) | MINIMUM TDOA (SEC) | TDOA (SEC) | NS |
|---|---|---|---|---|---|---|---|
| 1 | 994.04 | 1.3447 | 1.3447 | 0.0000 | 0. | 0. | 1 |
| 2 | 984.61 | -.9119 | 1.3446 | .5515 | 1.5559E-09 | 1.5559E-09 | 2 |
| 3 | 975.19 | -.9784 | 1.3824 | 0.0000 .5336 | 1.5053E-09 | 0. 1.5053E-09 | 2 |
| 4 | 965.77 | -.8756 | 1.3965 | 0.0000 .5335 | 1.5398E-09 | 0. 1.5398E-09 | 2 |
| 5 | 956.34 | -.9994 | 1.4150 | 0.0000 .6158 | 1.4882E-09 | 0. 1.4882E-09 | 2 |
| 6 | 946.92 | -1.1190 | 1.4450 | 0.0000 .8121 | 1.4347E-09 | 0. 1.4347E-09 | 2 |
| 7 | 937.50 | -1.0235 | 1.4485 | 0.0000 .8121 | 1.4684E-09 | 0. 1.4684E-09 | 2 |
| 8 | 928.07 | -1.1364 | 1.4878 | 0.0000 .7861 | 1.4145E-09 | 0. 1.4146E-09 | 2 |
| 9 | 918.65 | -1.3906 | 1.4878 | 0.0000 .7769 | 1.3250E-09 | 0. 1.3250E-09 | 2 |
| 10 | 909.23 | -1.2674 | 1.5143 | 0.0000 .7769 | 1.3584E-09 | 0. 1.3584E-09 | 2 |
| 11 | 899.80 | -1.4193 | 1.5219 | 0.0000 .7455 | 1.3023E-09 | 0. 1.3023E-09 | 2 |
| 12 | 890.38 | -1.5793 | 1.5341 | 0.0000 .7244 | 1.2428E-09 | 0. 1.2428E-09 | 2 |
| 13 | 880.96 | -1.4676 | 1.5438 | 0.0000 .7244 | 1.2767E-09 | 0. 1.2767E-09 | 2 |
| 14 | 871.54 | -1.6361 | 1.5437 | 0.0000 .6959 | 1.2177E-09 | 0. 1.2177E-09 | 2 |
| 15 | 862.11 | -1.8124 | 1.5432 | 0.0000 .6506 | 1.1548E-09 | 0. 1.1548E-09 | 2 |
| 16 | 852.69 | -1.7089 | 1.5466 | 0.0000 .6506 | 1.1898E-09 | 0. 1.1898E-09 | 2 |
| 17 | 843.27 | -1.9128 | 1.5331 | 0.0000 .6434 | 1.1286E-09 | 0. 1.1286E-09 | 2 |
| 18 | 833.84 | -2.2087 | 1.5331 | 0.0000 .5507 | 1.0235E-09 | 0. 1.0235E-09 | 2 |
| 19 | 824.42 | -2.1472 | 1.4949 | 0.0000 .5507 | 1.0603E-09 | 0. 1.0603E-09 | 2 |
| 20 | 815.00 | -2.0283 | 1.4904 | 0.0000 .5507 | 1.0998E-09 | 0. 1.0998E-09 | 2 |
| 21 | 805.57 | -2.2740 | 1.4429 | 0.0000 .4787 | 1.0342E-09 | 0. 1.0342E-09 | 2 |

## REFERENCES


1. Kerr, D. E., Propagation of Short Radio Waves, vol. 13, M.I.T. Radiation Laboratory Series. New York: McGraw-Hill, 1951.

2. Booker, H. G., Developments in the theory of radio propagation, 1900-1950, Radio Sci., vol. 10, no. 7, pp. 665-668, Jul. 1975.

3. Saxton, J. A., Propagation of metre waves beyond the normal horizon, Proc. IEE, vol. 69, pp. 360-369, Sep. 1951.

4. Gossard, E. E., Refractive index variance and its height distribution in various air masses, Radio Sci., vol. 12, no. 1, pp. 89-105, Jan.-Feb. 1977.

5. Richter, J. H., and H. V. Hitney, The Effect of the Evaporation Duct on Microwave Propagation, Naval Electronics Laboratory Center, San Diego, California, NELC Tech. Rep., 1949, Apr. 1975.

6. Booker, H. G., Elements of radio meteorology: How weather and climate cause unorthodox radar vision beyond the geometrical horizon, J. IEE, vol. 93, pt. IIIA, pp. 69-78, 1946.

7. Skolnik, M. I., Radar Systems. New York: McGraw-Hill, 1962, pp. 501-512.

8. Smyth, J. B., and L. G. Trolese, Propagation of radio waves in the lower troposphere, Proc. IRE, vol. 35, pp. 1198-1202, Nov. 1947.

9. Guinard, N. W., J. Ransone, D. Randall, C. Purves, and P. Watkins, Propsagation through an elevated duct: Tradewinds III, IEEE Trans. Antennas and Propagation, vol. AP-12, pp. 479-490, Dec. 1964.

10. Schelleng, J. C., C. R. Burrows, and E. B. Ferrell, Ultra-short wave propagation, Proc. IRE, vol. 21, pp. 427-463, Mar. 1933.

11. Norton, K. A., P. L. Rice, and L. E. Vogler, Use of angular distance in estimating transmission loss and fading range for propagation through a turbulent atmosphere over irregular terrain, Proc. IRE, vol. 43, pp. 1488-1526, Oct. 1955.

12. Wait, J. R., Electromagnetic Waves in Stratified Media. New York: Macmillan, 1962.

13. Booker, H. G., and W. Walkinshaw, The mode theory of tropospheric refraction and its relation to waveguides and diffraction, in Meteorological Factors in Radio Wave Propagation. London: The Physical Society, 1946, pp. 80-127.

14. Pappert, R. A., and C. L. Goodhart, Case studies of beyond-the-horizon propagation in tropospheric ducting environments, Radio Sci., vol. 12, no. 1, pp. 75-87, Jan.-Feb. 1977.

15. Kelso, J. M., Radio Ray Propagation in the Ionosphere. New York: McGraw-Hill, 1965, pp. 189-257.

16. Budden, K. G., The Wave Guide Mode Theory of Wave Propagation. London: Logos, 1961, chaps. 7-12.

17. Beckmann, P., and A. Spizzichino, The Scattering of Electromagnetic Waves from Rough Surfaces. New York: Pergamon, 1963, chaps. 2, 5, and 14.

18. Barton, D. K., Low Angle Radar Tracking, Proc. IEEE, vol. 62, no. 6, pp. 687-704, Jun. 1974.

19. Wong, M. S., Refraction anomalies in airborne propagation, Proc. IRE, vol. 46, pp. 1628-1638, Sep. 1958.

20. Vickers, W. W., and M. E. Lopez, Low-angle radar tracking induced by nonstratified atmospheric anomalies, Radio Sci., vol. 10, no. 5, pp. 491-505, May 1975.

21. Wallace, W. L., Atmospheric Refractivity Effects on the AWACS Radar System, Air Force Electronics Systems Division, Hanscom Field, Massachusetts, ESD Tech. Rep. 72-124, Nov. 1973.

22. Hartree, D. R., J. G. L. Michel, and P. Nicholson, Practical methods for the solution of the equations of tropospheric refraction, in Meteorological Factors in Radio Wave Propagation. London: The Physical Society, 1946, pp. 127-168.

23. Bean, B. R., and E. J. Dutton, Radio Meteorology, National Bureau of Standards Monograph 92. Washington: U. S. Government Printing Office, 1966, chaps. 1-3, and 8.

24. Smith, E. K., and S. Weintraub, The constants in the equation for atmospheric refractive index at radio frequencies, Proc. IRE, vol. 41, pp. 1035-1037, Aug. 1953.

25. Bean, B. R., and G. D. Thayer, Central Radio Propagation Laboratory exponential reference atmosphere, Natl. Bur. Standards (U.S.) J. Research, vol. 63D, pp. 315-317, Nov.-Dec. 1959.

26. The Rocket Panel, Pressures, densities, and temperatures in the upper atmosphere, Phys. Rev., vol. 88, pp. 1027-1032, 1952.

27. Handbook of Geophysics for Air Force Designers, Geophysics Research Directorate, Air Force Cambridge Research Center, Air Force Research and Development Command, 1957.

AD-A127 719 A GEOMETRIC OPTICS MODEL FOR CALCULATING THE FIELD STRENGTH OF ELECTROMAG..(U) AIR FORCE WRIGHT AERONAUTICAL LABS WRIGHT-PATTERSON AFB OH R P WASKY 3/3

UNCLASSIFIED DEC 77 F/G 20/14 NL

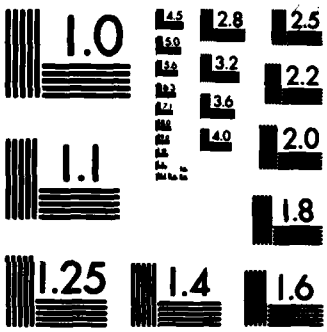


MICROCOPY RESOLUTION TEST CHART
NATIONAL BUREAU OF STANDARDS-1963-A

28. Bean, B. R., B. A. Cahoon, C. A. Samson, and G. D. Thayer, A World Atlas of Atmospheric Radio Refractivity, ESSA Monograph 1. Washington: U.S. Government Printing Office, 1966, pp. 1-25.

29. Crowder, H. K., and S. W. McCuskey, Topics in Higher Analysis. New York: Macmillan, 1964, pp. 37-38.

30. Keller, J. B., Geometrical Theory of Diffraction, J. Opt. Soc. Amer., vol. 52, no. 2, pp. 116-130, Feb. 1962.

31. Harrington, R. F., Time-Harmonic Electromagnetic Fields. New York: McGraw-Hill, 1961, pp. 54-61.

32. Jackson, J. D., Classical Electrodynamics. New York: Wiley, 1975, pp. 278-282.

33. Burrows, C. R., and S. S. Attwood, Radio Wave Propagation. New York: Academic Press, 1949, pp. 2-4 and 370-374.

34. Saxton, J. A., Electrical properties of sea water, Wireless Engineer, vol. 29, pp. 269-275, 1952.

35. Long, M. W., Radar Reflectivity of Land and Sea. Lexington: Heath, 1975, pp. 95-125.

36. Povejsil, D. J., R. S. Raven, and P. Waterman, Airborne Radar. Princeton: Van Nostrand, 1961, pp. 184-186.

37. Duncan, J. W., The effects of ground reflections and scattering on an interferometer direction finder, IEEE Trans. Aerospace and Electronic Syst., vol. AES-3, no. 6, pp. 922-932, Nov. 1967.

38. Ament, W. S., Toward a theory of reflection by a rough surface, Proc. IRE, vol. 41, pp. 142-146, Jan. 1953.

39. Computer Programs for Air/Ground Propagation and Interference Analysis (0.1 to 20 GHz), Office of Telecommunications, U.S. Dept. of Commerce, Rep. FAA-RD-73-103, Sep. 1973, pp. 16 and 214 (available from National Technical Information Service, Springfield, Virginia, Doc. AD 770 335).

40. Bullington, K., Reflection coefficients of irregular terrain, Proc. IRE, vol. 42, pp. 1258-1262, Aug. 1954.

41. Yeh, L. P., Simple methods for designing troposcatter circuits, IRE Trans. Communications Syst., vol. CS-8, pp. 193-198, 1960.

END

FILMED

6-83

DTIC